SLAC-237
UC-34d
(E)

A SEARCH FOR UNCONVENTIONAL TAU DECAYS AND MEASUREMENT OF THE TAU PRODUCTION CROSS SECTION IN e^+e^- ANNIHILATIONS AT SPEAR*

Kenneth Gregory Hayes

Stanford Linear Accelerator Center
Stanford University
Stanford, California 94305

January 1981

Prepared for the Department of Energy

under contract number DE-AC03-76SF00515

Printed in the United States of America. Available from the National Technical Information Service, U.S. Department of Commerce, 5285 Port Royal Road, Springfield, VA 22161. Price: Printed Copy A13; Microfiche A01.

---

* Ph.D. dissertation.

ABSTRACT

We present the results of an experimental study of two properties of the tau lepton performed with the MARK II detector in the SPEAR e^+e^- storage ring at SLAC.

The tau production cross section in e^+e^- annihilation between 3.85 and 6.85 Gev in the center of mass has been measured using e-μ events, and is consistent with the spin 1/2, point cross section. The branching ratio product for the electron and muon leptonic decay modes is measured to be .032±.002±.004.

Searches for 12 neutrinoless decay modes of the tau which violate lepton number conservation have been made. No evidence for lepton number violation is observed, and we set upper limits (90% C.L.) on the branching ratio for each decay mode. The branching ratio limit on the radiative decays $\tau\to\mu\gamma$ and $\tau\to e\gamma$ are .055% and .064% respectively. For the 3 charged lepton decays $\tau\to eee$, $\tau\to e\mu\mu$, $\tau\to\mu ee$, and $\tau\to\mu\mu\mu$, the branching ratio limits are .040%, .033%, .044%, and .049% respectively. Upper limits on the branching ratios are also set for the following charged lepton+neutral hadron decays of the tau: $\tau\to e\rho$ (.037%), $\tau\to\mu\rho$ (.044%), $\tau\to eK^0$ (.13%), $\tau\to\mu K^0$ (.10%), $\tau\to e\pi^0$ (.21%), and $\tau\to\mu\pi^0$ (.082%).

Acknowledgements

So many people have been important to me throughout my academic career that I can't thank them all by name. Still, several must be singled out for their special help.

First, I thank my advisor, Martin Perl. Not only did he provide inspiration and guidance in his warm an open manner, but he patiently steered me back to the path whenever I would stray. I also thank all the members of the MARK II Collaboration, particularly Group E at SLAC, whose combined efforts made this experiment possible.

The road began many years ago at Davis. I thank the members of the high energy physics group, Winston Ko, Dick Lander, Dave Pellet, and Phil Yager for including me in their activities, and thereby exposing me to the world of elementary particles.

I thank my friends, who have taught me so many things outside of physics. Together we have shared these happy days. In particular, I thank Homa and Shadi Bina, Joe Erwin, Emily and Mark Johnson, Ira Levine, Ila Montalvo, Petros Rapidis, Doug Rosner, and "R" Smith.

I thank my Mother and Father, Brother and Sisters, for doing the things families do.

Most of all, I want to thank Mamá and Papá, for their constant love, support, and encouragement, and my wife Cita for inviting me to share her world which is so full of life and love and joy.

TABLE OF CONTENTS

Chapter 1

INTRODUCTION

Our current theory of elementary particle physics represents the latest of man's attempts to understand the structure of matter as a composite of a small set of simple, fundamental units. The gauge theories of the strong, electromagnetic, and weak interactions divide these units into two classes: the elementary fermions and the gauge bosons which mediate their interactions. The fermions can be further subdivided into the strongly interacting quarks (the constituents of all strongly interacting particles), and the weakly interacting leptons. Prior to 1975, only 4 members (excluding anti-particles) of the lepton family were known: the electron, the muon, and their associated neutrinos. In that year, a new candidate for the lepton family was discovered in an experiment performed with the MARK I detector in the SPEAR electron-positron storage ring.[1-2] It was named the tau and has a mass[3] of 1782^{+3}_{-4} Mev/c^2.

This thesis is a study of two properties of the tau performed with the MARK II detector at SPEAR. 1) We present a new measurement of the tau production cross section in e+e- annhilations between 3.8 and 6.8 Gev in the center of mass. Measurements of this cross section are an important source of information on the fundamental nature of the tau.

2) To test whether the tau obeys the empirical rule of lepton flavor conservation, we have searched for 12 decay modes of the tau which violate this rule.

1.1 A NEW MEASUREMENT OF THE TAU PRODUCTION CROSS SECTION

i) Theoretical considerations:

Evidence for the classification of the tau as a lepton has come from two sources: its production cross section in e+e- annhilations[2] and studies of its observed decay modes.[4] At SPEAR energies, tau production occurs through the one photon exchange graph illustrated in Figure 1.1.

$$e^+e^- \dashrightarrow \gamma \dashrightarrow \tau^+\tau^- \qquad (1)$$

This process will occur only if the center of mass energy (ECM) is greater than twice the tau mass. Measurement of the cross section near threshold is the most sensitive way of determining the tau mass.

The production mechanism also yields information on the leptonic nature of the tau. If the tau was a hadron, we would expect the production process listed in (2)

$$e^+e^- \dashrightarrow \gamma \dashrightarrow \tau^+\tau^- + \text{hadrons} \qquad (2)$$

to dominate reaction (1) for energies where (2) is kinematically allowed. For example, the charmed $D^{+(-)}$ mesons, whose mass is only about 80 Mev/c^2 larger than the tau mass, are produced at least 5 times more often via process (2) for ECM=5.2 Gev.[5] Thus, the fact that reaction (1) is observed to dominate tau production is strong evidence for including the tau in the lepton family.

Information on the cross section can be used to determine the tau's

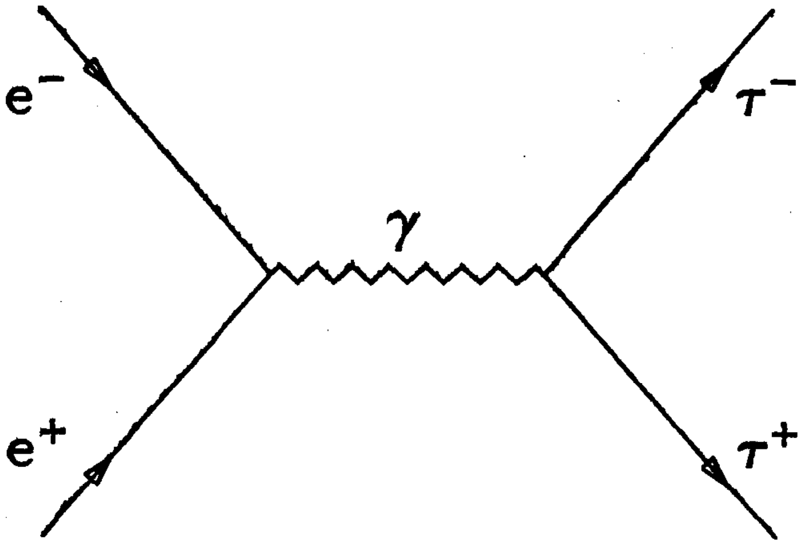

Figure 1.1. One photon exchange diagram for tau pair production in e^+e^- annihilation.

spin and to verify its point-like nature. For example, the lowest order QED point pair production cross section for spin 0 and spin 1/2 particles is

$$\text{Spin } 0 \qquad \sigma=\pi\alpha^2\beta^3/3S \qquad \beta=\sqrt{1-4m^2/S} \tag{3a}$$

$$\text{Spin } 1/2 \qquad \sigma=(4\pi\alpha^2/3S)\beta(3-\beta^2)/2 \tag{3b}$$

where $S=ECM^2$, m is the particle's mass, and β is the velocity in units of the speed of light. For large center of mass energies ($ECM>>2m$), the spin 1/2 cross section approaches the limiting value

$$\sigma=4\pi\alpha^2/3S \tag{3c}$$

In most storage rings, this condition is always satisfied for muons. Thus, (3c) is called the muon pair production cross section, and serves as a convient standard to compare against other cross sections. Such measurements are often quoted in terms of the ratio R_x

$$R_x=\sigma(e^+e^- \rightarrow X)/\sigma(e^+e^- \rightarrow \mu^+\mu^-) \tag{3d}$$

For example, the ratio R_t for the tau pair production cross section (assuming a spin 1/2, point-like tau) is

$$R_t=\sigma(e^+e^- \rightarrow \tau^+\tau^-)/\sigma(e^{+-} \rightarrow \mu^+\mu^-)=\beta(3-\beta^2)/2 \tag{3e}$$

The energy dependence of R_t is limited to just the threshold behavior of the cross section and has the simple property R_t--> 1 as β-->1.

If the tau was not point-like, the theoretical cross section would be multiplied by a form factor which would deviate from unity. We expect the deviation to increase with energy as the photon in (1) probes smaller distances. Therefore, high energy measurements of the cross section provide the most sensitive test of the point-like nature of the tau.

Because the tau has a short lifetime, it has not been possible to directly observe the taus from reaction (1). Instead, cross section measurements are performed using event signatures that are highly indicative of tau decays. The event topology consisting of a single muon with an oppositely charged electron and no other detected particles is the cleanest signature of tau pair production and decay (4).

$$\begin{array}{l} e^+e^- \text{-->}\ \tau^{+(-)} \ + \ \tau^{-(+)} \\ \qquad\qquad\qquad\qquad\quad\ \ \lfloor\text{-->}\, e^{-(+)}\nu\nu \\ \qquad\qquad\ \ \lfloor\text{-->}\, \mu^{+(-)}\nu\nu \end{array} \tag{4}$$

Tau production was first observed in events of this type.[1]

ii) Previous Measurements of the tau production cross section.

The threshold behavior of the tau cross section has been measured by several groups. The MARK I collaboration used e-μ events in their analysis.[6] Figure 1.2 shows their measurement of R_τ (equation 3d) along with the theoretical prediction for a spin 1/2, point particle for 2 mass values. The highest statistics measurement was obtained at SPEAR by the DELCO collaboration.[3] To increase the statistics, they used all events of the form

$$e^+e^- \text{-->}\ e^{+(-)} + X^{-(+)} + \text{missing energy} \tag{5}$$

where X is any particle that is not an electron. Figure 1.3 displays their measurement of R_{ex}

$$R_{ex}=\sigma(e^+e^- \to e^{+(-)}+X^{-(+)}+\text{missing energy})/\sigma(e^+e^- \to \mu^+\mu^-) \tag{6}$$

Also shown is the theoretical prediction (3b) for a particle of mass 1782 Mev/c^2.

Although both sets of data are consistent with equation (3b), the DELCO data above 5.5 Gev suggest that perhaps some process beyond statistical fluctuations could be occuring. Although the statistics are poorer, the MARK I data does not suggest any violation of (3b). To clarify this situation, Chapter 4 of this thesis presents a new

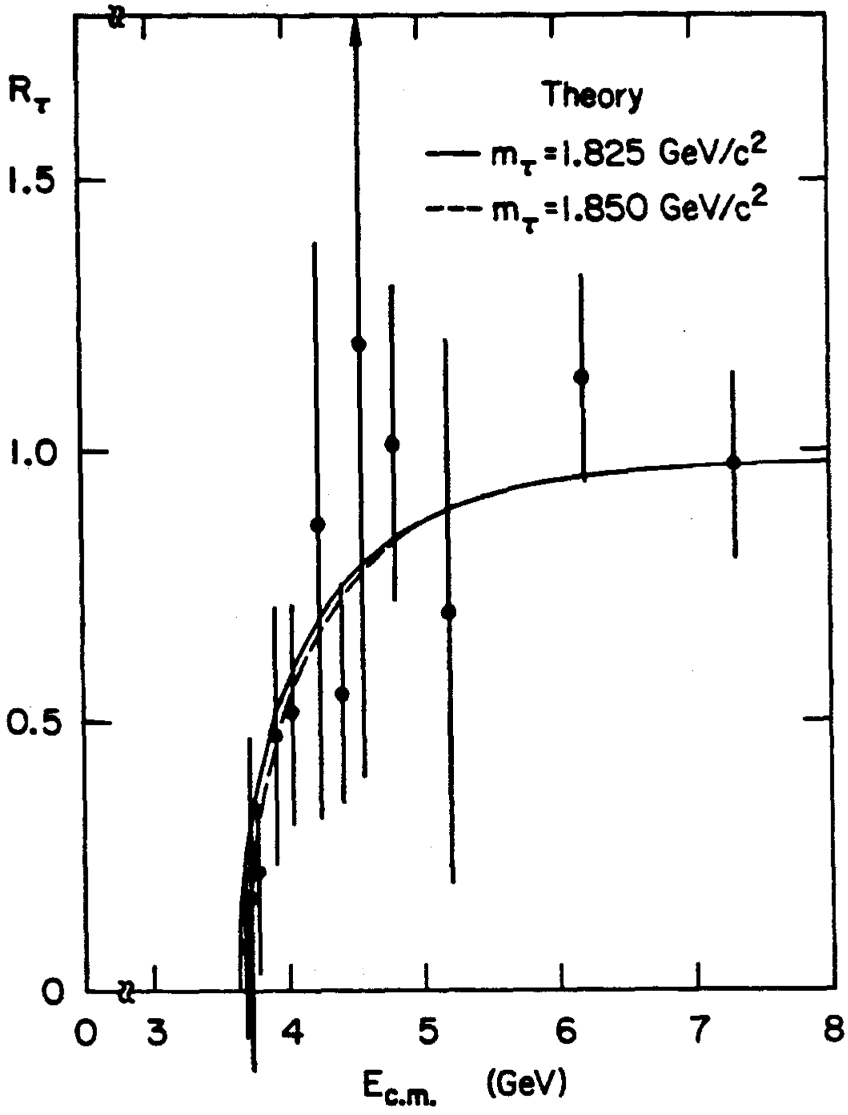

Figure 1.2. The MARK I collaboration's measurement of R_τ compared to theoretical curves for a point-like, spin 1/2 particle for two mass values. The earlier data indicated a tau mass between 1825 and 1900 Mev/c .

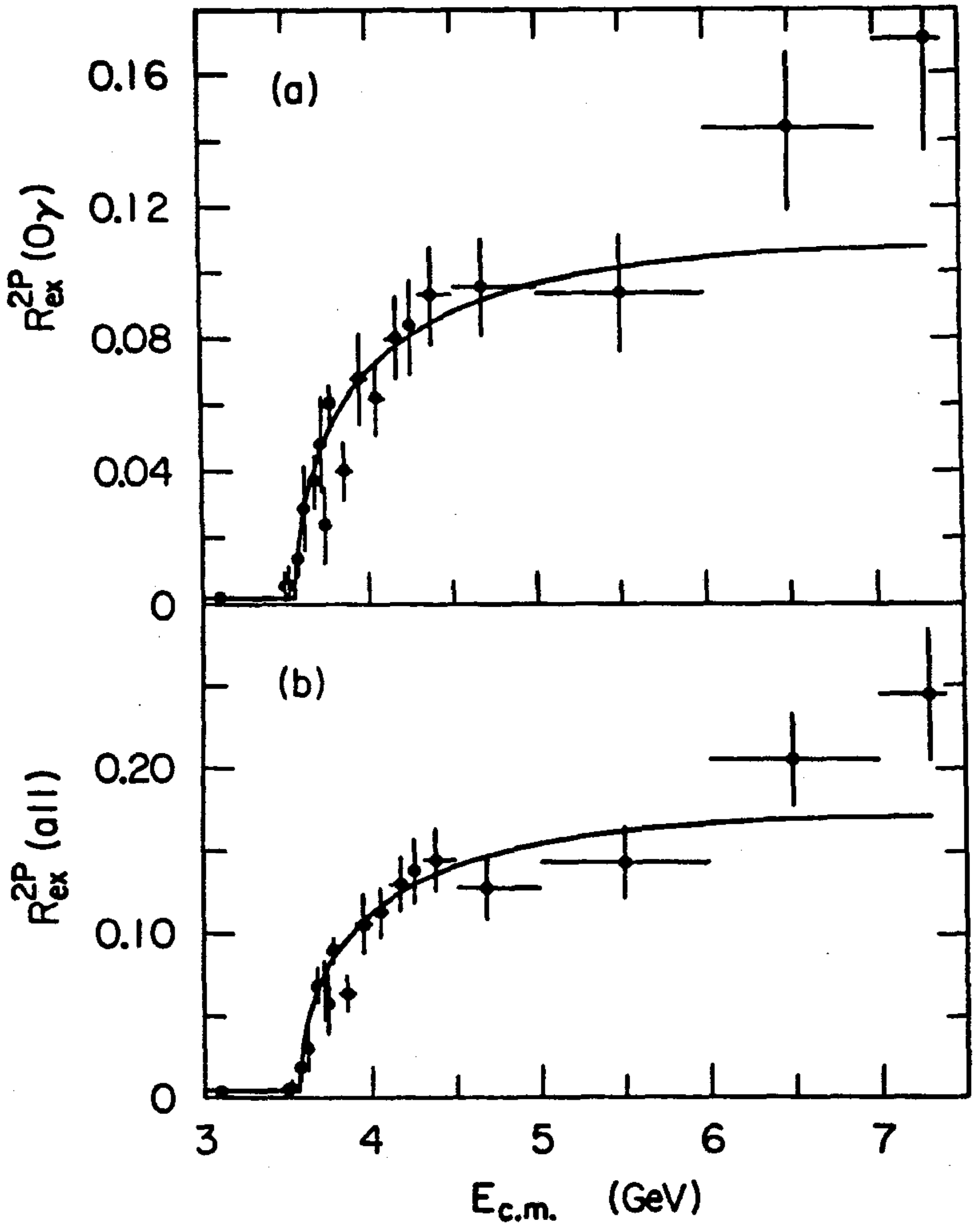

Figure 1.3. The DELCO measurement of R_Υ using e+X events: (a) with no photons detected, (b) all events.

measurement of the tau production cross section performed with the MARK II detector at SPEAR.

Experiments at the PETRA electron-positron storage ring have measured the tau cross section for energies up to 32 Gev in the center of mass.[7] These experiments are all consistent with equation (3b).

1.2 TESTS OF LEPTON FLAVOR CONSERVATION IN TAU DECAYS:

The principle of lepton flavor conservation grew out of studies on the muon and its relationship to the electron. These studies revealed that the muon and its associated neutrino, were carbon copies of the electron and its neutrino except for 2 things: 1) The muon and electron have a different mass. The muon neutrino and electron neutrino may have a different mass, but only upper limits on their masses have been measured. 2) The electron and its neutrino, and the muon and its neutrino both have a unique property, "electron-ness" or "muon-ness", which is shared with no other particle. To be more specific, we define the two quantum numbers L_e (electron number) and L_m (muon number), and assign to each particle the values listed in Table 1.1. Then the experimental results on the electron and muon can be summarized by the following rule: in any reaction, the separate sums of L_e and L_m for the outgoing particles, must equal their respective sums for the incoming particles. This rule is called "lepton flavor conservation."

We have no a priori way of knowing how a new lepton will be integrated into this picture. For example, it may have its own separately conserved lepton number. If not, it may have the lepton number of the electron or muon (the ortho-lepton model), or it may have

TABLE 1.1

Lepton number assignments.

Particle	Electron Number	Muon Number
$e^- \nu_e$	+1	0
$e^+ \bar{\nu}_e$	-1	0
$\mu^- \nu_\mu$	0	+1
$\mu^+ \bar{\nu}_\mu$	0	-1
All Hadrons	0	0

the lepton number of the positron or anti-muon (the para-lepton model). Still more complicated situations can be imagined.

Perhaps the simplest model is the sequential lepton model. This model assumes that the lepton family exists as a mass sequence of charged leptons and associated neutrinos ("generations"), each having its own separately conserved quantum number. Besides stating the experimental results on the muon and electron in concise form, the sequential lepton model suggested that perhaps there were other generations in the lepton sequence that had not yet been discovered. Furthermore, just as the muon decays to an electron and two neutrinos (7),

$$\mu^- \rightarrow e^- + \bar{\nu}_e + \nu_\mu \qquad (7)$$

other more massive leptons should decay in an analogous manner to muons or electrons. This was the motivation for the search which resulted in the discovery of the tau in e+e- annhilations through the reaction listed in (4). Once the tau was discovered, however, its status as a sequential lepton remained to be proven by experiment.

Although the sequential model is simple and elegant, we must not forget that it is a generalization based on one instance: the muon (relative to the electron). Theoretically, present day gauge theories find no a priori reason to conserve lepton flavor. Just as the quark strong interaction eigenstates are mixed by the weak interaction, thereby allowing weak transitions between quark generations, transitions between lepton generations would be perfectly natural (and possible--providing the neutrino masses are not all equal). Whether or not they are confirmed, the recent experimental claims on the observation of neutrino oscillations have vividly demonstrated the empirical nature of the lepton conservation law.[8] Studies with the tau can provide new evidence to either support or invalidate this law.

Examination of the steps which lead to the concept of lepton number conservation with the muon will reveal the reasons for the concept and provide an example of methods useful in obtaining evidence on lepton conservation with the tau. When the muon was discovered, it was mistakenly identified with the hypothesized Yukawa meson responsible for the nuclear force. As nuclear beta decay was thought to occur through the weak decay of the virtual meson, it was assumed the muon decayed into an electron and neutrino. After the muon was shown to be weakly interacting and therefore not the Yukawa particle, a search was carried out to see if it decayed into an electron plus photon.[9] Failure to observe a photon in the muon decay products led back to the assumption that it decayed into an electron plus neutrino. Only after the electron spectrum had been measured was it understood that the muon decayed into an electron and at least two other light neutral particles assumed to be the neutrinos of nuclear beta decay.[10] After the resurrection of the intermediate meson hypothesis to solve the problem of the violation of unitarity at high energy in the Fermi theory, it was recognized that the electron plus photon decay of the muon should occur through the diagrams shown in Figure 1.4.[11] As the measured upper limit on this decay was already less than the theoretical predictions, this argued strongly for the existence of two separate neutrinos. The verification of this idea came with the direct observation of separate muon neutrinos in accelerator experiments.[12]

Today, the concept of lepton conservation is supported primarily by the impressive upper limits on the lepton flavor violating processes listed below:[13-16]

$$\Gamma(\mu \to e\gamma)/\Gamma(\mu \to e\nu\nu) \lesssim 1.9 \times 10^{-10} \qquad (8a)$$

$$\Gamma(\mu \to e\gamma\gamma)/\Gamma(\mu \to e\nu\nu) \lesssim 5. \times 10^{-8} \qquad (8b)$$

$$\Gamma(\mu \to eee)/\Gamma(\mu \to e\nu\nu) \lesssim 1.9 \times 10^{-9} \qquad (8c)$$

$$\sigma(\mu^- + S \to e^- + S)/\sigma(\mu^- + S \to \text{capture}) \lesssim 7. \times 10^{-11} \qquad (8d)$$

$$\sigma(\mu^- + S \to e^+ + Si^*)/\sigma(\mu^- + S \to \text{capture}) \lesssim 9. \times 10^{-10} \qquad (8e)$$

These experiments indicate that if muon--electron flavor mixing occurs, it does so at a very tiny level. Some current theories, discussed below, predict violations that occur at rates far smaller than even these limits.

The most important tests of lepton number conservation with the tau would demonstrate that its neutrino is not identical with any of the four "old" neutrinos: $\nu_e, \nu_e, \nu_\mu, \nu_\mu$. Neutrino experiments can test the coupling of the tau to the old neutrinos via reaction (9)

$$\nu_i + \text{nucleus} \dashrightarrow \tau^{+(-)} + \text{anything} \qquad (9)$$

where τ^- tests the coupling to ν_i and τ^+ test the coupling to $\bar{\nu}_i$. This experiment has been performed using a muon neutrino beam with negative results.[17] In conjunction with the upper limits on the tau lifetime, this rules out the possibility that the tau is associated solely with the muon neutrino or muon anti-neutrino.[2]

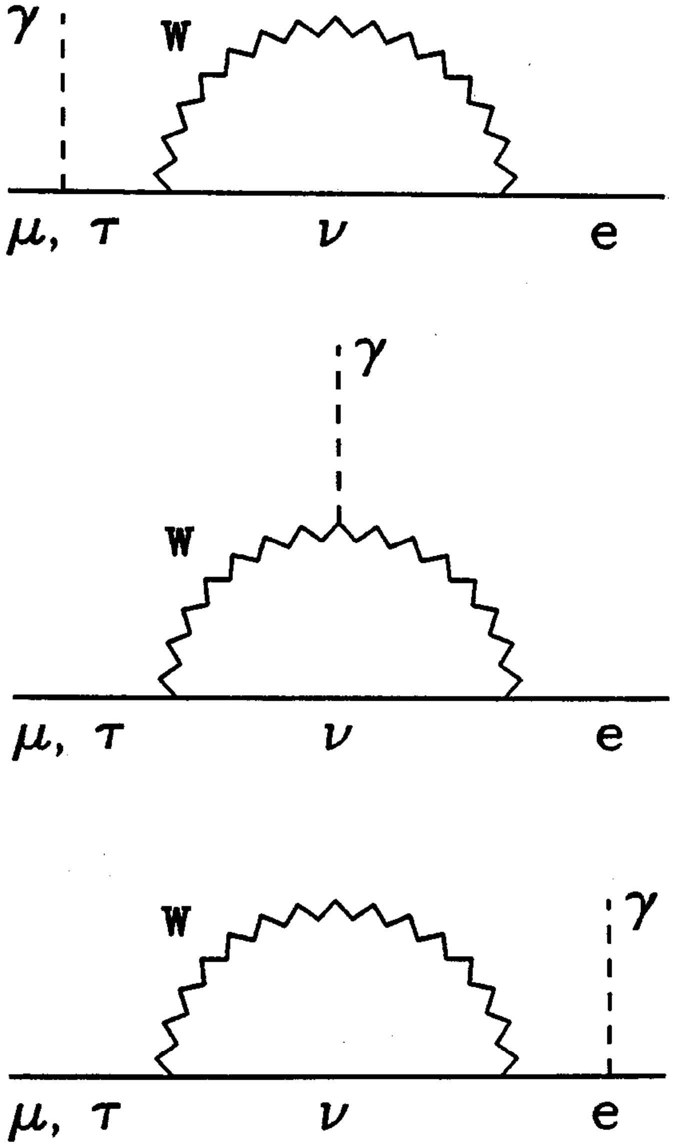

Figure 1.4. Lowest order diagrams leading to radiative muon (tau) decays in the charged intermediate vector boson model when the muon (tau) and electron share the same neutrino.

Electron neutrino beams do not exist, so other less direct ways must be found to test the tau--electron association.

If the tau were associated with the electron anti-neutrino, the ratio R of the tau decay rates

$$R=\Gamma(\tau \rightarrow e\nu_{\tau}\nu_{e})/\Gamma(\tau \rightarrow \mu\nu_{\tau}\nu_{\mu}) \tag{10}$$

would be approximately two[18] instead of the measured value of one[19], due to the identical neutrinos in the electron decay. Therefore, this can be ruled out, leaving only the association of the tau with the electron neutrino to be determined. This is, of course, the same situation that existed with regard to the muon 20 years ago, and the arguments discussed then apply now. Note that the 3 neutrino identifications which have been ruled out used model independent tests. Current experimental tests of the equality between the tau and electron neutrino are more model dependent.

As before, we might expect the tau to decay electromagnetically to an electron plus photon with a characteristic lifetime of 10^{-21} seconds.

$$\tau^{+(-)} \dashrightarrow e^{+(-)} + \gamma \tag{11}$$

However, Feinberg, Kabir, and Weinberg[20] have proven the remarkable result that for several simple types of interactions which might be expected to cause $\tau \rightarrow e$ transformations, reaction (11) is forbidden due to the similarity of the tau and electron. Only if the tau has an anamolous magnetic moment (beyond that predicted for Dirac particles with QED) would (11) be allowed. Thus, we need not expect that electromagnetic transitions would dominate tau decays. Of course, if the tau has an anamalous magnetic moment, the rate could be large.

In any given model, the rate for reaction (11) can be calculated and is non-zero in many cases if the tau and electron neutrino are identical. For example, the simplest model we can imagine simply enlarges the standard 4 lepton SU(2)XU(1) model by adding an extra left handed singlet and mixing the tau and electron in the standard left handed electron doublet and the new singlet. In this case the decay $\tau \to e\gamma$ can occur as shown in the diagrams of Figures 1.4 and 1.5 with the rate[21]

$$R=\Gamma(\tau\to e\gamma)/\Gamma(\tau\to e\nu\nu)=(3\alpha/8\pi)(1-4/3\sin^2\Theta_W)^2\simeq 4\times 10^{-4} \qquad (12)$$

where Θ_W is the Weinberg angle. Chapter 5 details the search made with the MARK II for this decay and the similiar reaction listed in (13).

$$\tau^{+(-)} \dashrightarrow \mu^{+(-)} + \gamma \qquad (13)$$

Previous searches for these decays have established upper limits on the branching ratios for (11) and (13) of 2.6% and 1.3% respectively[6]. Although no evidence for these decays is found in our search, the upper limit that we determine is still an order of magnitude larger than the rate predicted by equation (12).

The SU(2)XU(1) model described above has many other consequences. For example, the 3 charged lepton tau decay $\tau \to eee$ will occur in lowest order via the diagram shown in Figure 6b. The ratio of the rate for this decay over the normal leptonic decay rate is[22]

$$R=\Gamma(\tau\to eee)/\Gamma(\tau\to e\nu\nu)=[2(1-2\sin^2\Theta_W)^2+4\sin^4\Theta_W]\simeq .7 \qquad (14)$$

The upper limit on this branching fraction determined in chapter 6 eliminates this model. In general, it is very difficult to construct a model with no unique tau neutrino which does not violate one or more experimental results. Direct observation of a unique tau neutrino would

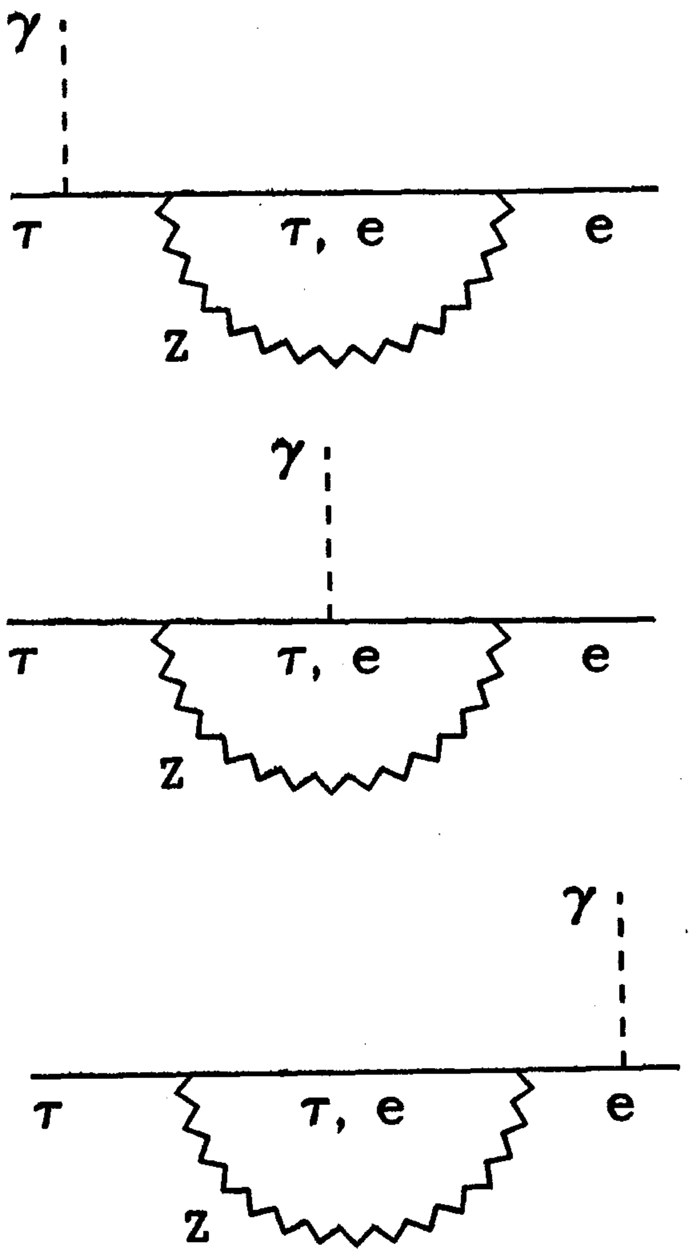

Figure 1.5. Lowest order diagrams leading to radiative tau decays in the neutral intermediate vector boson model when the tau and electron share the same neutrino.

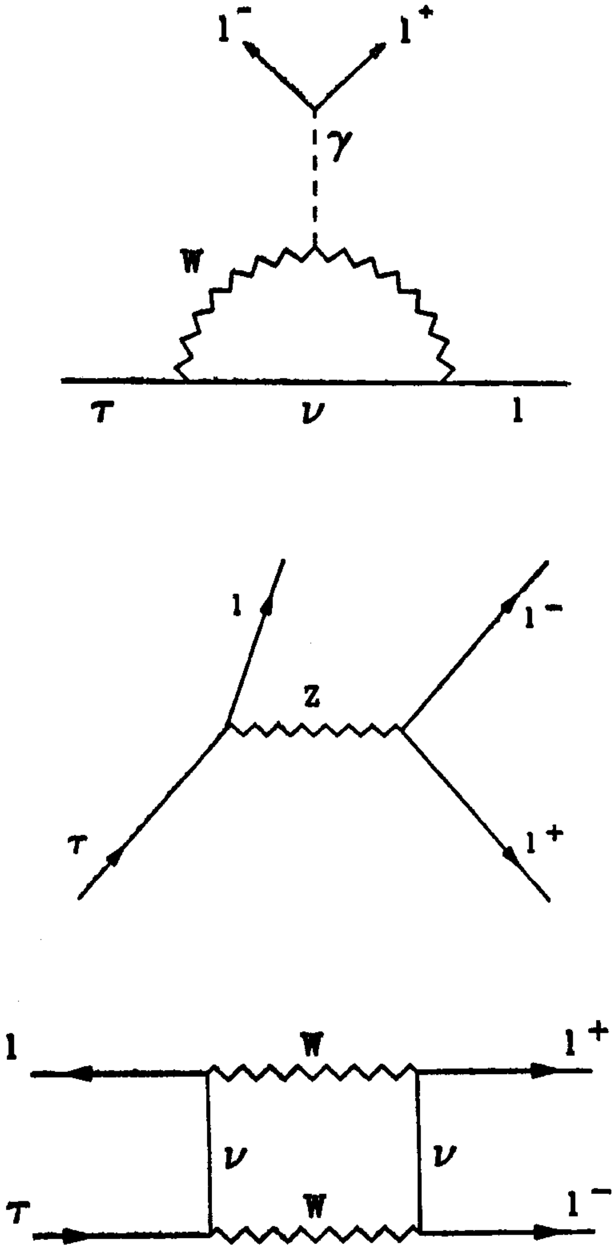

Figure 1.6. Three diagrams for the process tau --> 11^+1^- (1 is either an e or μ). (a) Internal photon conversion in the diagrams of Figure 1.4. (b) Coupling of the tau to the neutral intermediate vector boson. (c) Example of a higher order diagram.

be a model independent way of proving the non-identity of the electron and tau neutrinos. Several proposals have been made to produce a tau neutrino beam using the 1000 Gev tevatron proton beam at Fermi National Laboratory.[23] These experiments may provide direct proof in the next few years.

Other models exist which allow radiative decays of one lepton to another even if each lepton has its own neutrino. If mass differences exist between the neutrinos in different generations, it is possible that the neutrino mass eigenstates will be different than the eigenstates of the weak interaction. Thus, weak transitions can occur between generations leading to lepton flavor violation. Several experiments are currently being performed to test this hypothesis using the large flux of neutrinos available at nuclear reactors.[8] Assuming for simplicity that only the tau and electron neutrino mix, the relative rate for the decay listed in (11) is

$$R=\Gamma(\tau\rightarrow e\gamma)/\Gamma(\tau\rightarrow e\nu\nu)=(3\alpha/32\pi)(\sin2\Theta/2M_W^2)^2(m_{\nu_\tau}^2-m_{\nu_e}^2)^2 \qquad (15)$$

where Θ is the mixing angle, and M_W is the intermediate vector boson mass. Assuming the mass of the tau neutrino is equal to its current upper limit (250 Mev/c^2) and that mixing is maximal, the value of R is 5×10^{-15} --a completely academic value.

If neutral heavy leptons exist which couple to both the tau and electron, then the significant mass difference would not be the neutrino mass difference, but instead would be the mass difference between the neutral heavy leptons. Presumably this could be large, thereby giving a much higher rate.[24-25] Other models have been suggested that achieve high rates (relative to (12)) by introducing additional particles such as new Higgs particles,[26] or massive singly or doubly charged heavy leptons.[27] The interested reader is directed to the references.

Searches for other tau decay modes which would violate lepton number conservation have been made. Table 1.2 summarizes the results of these experiments.

TABLE 1.2

Previous experimental limits on branching ratios for lepton flavor violating tau decay modes.

MODE	LIMIT (%)	C.L.(%)	REFERENCE
$\tau \rightarrow e + \gamma$ or $\tau \rightarrow \mu + \gamma$	12	90	28
$\tau \rightarrow e + \gamma$	2.6	90	6
$\tau \rightarrow \mu + \gamma$	1.3	90	6
$\tau \rightarrow$(3 charged leptons)	1.	95	28
$\tau \rightarrow$(3 charged leptons)	.6	90	6
$\tau \rightarrow$(3 charged particles)	1.0	95	28
$\tau \rightarrow \rho + \pi^0$	2.4	90	6

The tau decays to three charged leptons (16)

$$\tau \rightarrow e e^+ e^-, \quad \tau \rightarrow \mu e^+ e^-, \quad \tau \rightarrow e \mu^+ \mu^-, \quad \tau \rightarrow \mu \mu^+ \mu^- \qquad (16)$$

are analogous to the muon decay to three electrons (5.b). If the tau decayed via the modes listed in (11) or (13), the 3 charged lepton decay would also be expected, although suppressed by order α/π, simply from internal conversion of the photon (Figure 1.6a)[11]. However, this decay is interesting in its own right because it tests the coupling of the tau to the neutral vector boson as discussed above. Other classes of diagrams can also contribute (e.g. Figure 1.6c). Models created to explain the $\mu \rightarrow e + \gamma$ transition will also predict non-zero rates for $\mu \rightarrow eee$ decay. These results apply directly to the three charged lepton decays of the tau. In particular, the model with doubly charged leptons predicts an enhancement of the three lepton rate relative to the radiative decay[27].

Chapter 6 of this thesis reports on a search for the three charged lepton decays of the tau listed in (16). Our experiment is an order of magnitude more sensitive than previous searches.

Other lepton flavor violating decays of the tau can be imagined besides those analogous to the neutrinoless muon decays listed in (8). The large mass of the tau dramatically increases the number of decays which are kinematically allowed. Chapter 7 reports on our search for the lepton violating tau decays listed in (17).

$$\tau^{+(-)} \dashrightarrow l^{+(-)} + h^0 \quad l=e,\ \mu \qquad h=\pi,\ K,\ \rho \tag{17}$$

These decays, to a charged lepton plus neutral hadron, are the simplest tau decays which conserve angular momentum that are possible to detect with the MARK II. If the tau were some strange object which coupled to both leptons and quarks in unconventional ways, we might uncover evidence in these decays. Little theoretical work has been done in this area[29].

It is hard to imagine how very large improvements in the sensitivity of any of the above searches will be obtained. Assuming other backgrounds are not important, the limiting factor in any search is simply the number of taus which are available to decay. If they are produced in an electron positron storage ring (the only place where taus have currently been observed), with the center of mass energy near the maximum of the tau production cross section (4.2 Gev), one could hope to produce at most 5×10^5 taus/year. Assuming the experiment runs for 2 years with a detection efficiency of 50%, the 90% confidence level upper limit on any branching ratio would be at least 5×10^{-6}. If lepton number violation occurs at levels much below this limit, we may never be able to observe it.

References:

1.) M.L. Perl, Proc. of Summer Institute on Particle Physics, SLAC-191, Stanford Linear Accelerator Center, Stanford University, Stanford, California, (1975), p. 333;
M.L. Perl et al., Phys. Rev. Lett. 35:1489, (1975).

2.) M.L. Perl, SLAC-PUB-2446, (submitted to Ann. Rev. Nuc. and Part. Sc.) and references therein.

3.) J. Kirkby, Proc. of 1979 Int. Sym. on Lepton and Photon Interactions at High Energy, Fermi National Laboratory, Batavia Ill. (1979);
W. Bacino et al., Phys. Rev. Lett. 41:013, (1978).

4.) C.A. Blocker, Ph.D. Thesis, LBL Report LBL-10801 (1980).

5.) M.W. Coles, Ph.D. Thesis, LBL Report LBL-11513 (1980).

6.) M.L. Perl, Proc. of 1977 Int. Symp. on Lepton and Photon Interactions at High Energies, Deutsches Elektronen-Synchrotron, Hamburg, Germany, (1977), p.145.

7.) R. Brandelik et. al., Phys. Lett 92B:199, (1980);
H. Spitzer, DESY Preprint DESY 80/46, (1980);
D.P. Barber et al., Phys. Rev Lett. 43:1915, (1979).

8.) F. Reines, H.W. Sobel, and E. Pasierb, Phys. Rev. Lett. 45:1307, (1980).

9.) B. Pontecorvo, Phys. Rev. 72:246, (1947);
E.P. Hincks and B. Pontecorvo, Phys. Rev. 73:257, (1948).

10.) R.B. Leighton, C.D. Anderson, and A.J. Seriff, Phys. Rev. 75:1432, (1949).

11.) G. Feinberg, Phys. Rev. 110:1482, (1958).
12.) G. Danby et al., Phys. Rev. Lett. 9:36, (1962).

13.) J.D. Bowman et al., Phys. Rev. Lett. 42:556, (1979).

14.) J.D. Bowman, T.P. Cheng, L.-F. Li, and H.S. Matis, Phys. Rev. Lett. 41:442, (1978).

15.) S.M. Korenchenko et al., Zh. Eksp. Teor. Fiz. 70:3, (1976) [Sov. Phys. JETP 43:1, (1976)].

16.) A Badertscher et al., Nuovo Cim. Lett. 28:401, (1980).

17.) A. M. Cnops et al., Phys. Rev Lett. 40:144, (1978).

18.) A. Ali and T.C. Yang, Phys. Rev. D14:3052, (1976).

19.) F.J. Heile et al., Nuc. Phys. B138:189, (1978).

20.) G. Feinberg, P. Kabir, S. Weinberg, Phys. Rev. Lett 3:527, (1959).

21.) G. Altarelli et. al., Phys. Lett. 67B:463, (1977).

22.) D. Horn and G.G. Ross, Phys. Lett. 67B:460, (1977).

23.) The following proposals were submitted to Fermi National Laboratory in 1980: V.F. Kaftanor et al., Proposal P633; I. Pless et al., P636; M. Longo et al., P644; C. Baltay et al., P646; W. Lee et al. P654; S. Whitaker et al. P656.

24.) T.P. Cheng and L.-F. Li, Deeper Pathways in High-Energy Physics; Pro. Coral Gables Conf. 1977, Ed: A. Perlmutter and L.F. Scott, Plenum Press, 1977, p. 659.

25.) J.D. Bjorken, K. Lane, and S. Weinberg, Phys. Rev. D16:1474, (1977).

26.) J.D. Bjorken and S. Weinberg, Phys. Rev. Lett. 38:622, (1977).

27.) W.J. Marciano and A.I. Sanda, Phys. Lett. 67B:303, (1977); F. Wilczek and A. Zee, Phys. Rev. Lett. 38:531, (1977); B.W. Lee et al., Phys. Rev. Lett. 38:937, (1977).

28.) G. Flugge, Proc. of 1977 Experimental Meson Spectroscopy Conference, Northeastern University, Boston, Mass.

29.) E. Derman, Phys. Rev. D19:317, (1979).

Chapter 2

The MARK II Detector

The similarity observed between general purpose detectors for single ring e+e- colliding beam experiments is not accidental. The physics of single photon electron positron annhilation coupled with the current state of detector technology impose strong constraints on detector design. The low event rate and identity between the laboratory and center of mass systems demand a large solid angle detector. The low rate also makes it desirable to measure as much as possible for each event. Given that non-destructive instruments must be placed before destructive ones, the following design is prescribed: first, a charged particle detector and momentum analizer, followed by 2) an electromagnetic shower detector, 3) a hadronic shower detector, and 4) muon range counters. The MARK II follows this general prescription. It is basically a cylindrically symmetric detector with elements 1, 2, and 4.

Figures 2.1 and 2.2 show a cross sectional slice and an isometric projection of the MARK II. As a particle leaves the interaction region, it passes through the beam pipe and pipe counter, before entering the drift chamber. After traversing the drift chamber, it next crosses the time of flight (TOF) counters, the 1.3 radiation length thick aluminum solenoid coil, and the lead--liquid argon electromagnetic shower detectors. The muon range counters surround the inner detector and are sensitive to muons with momentum above 700 Mev/c. Large angle tracks which exit through the ends of the drift chamber are detected by

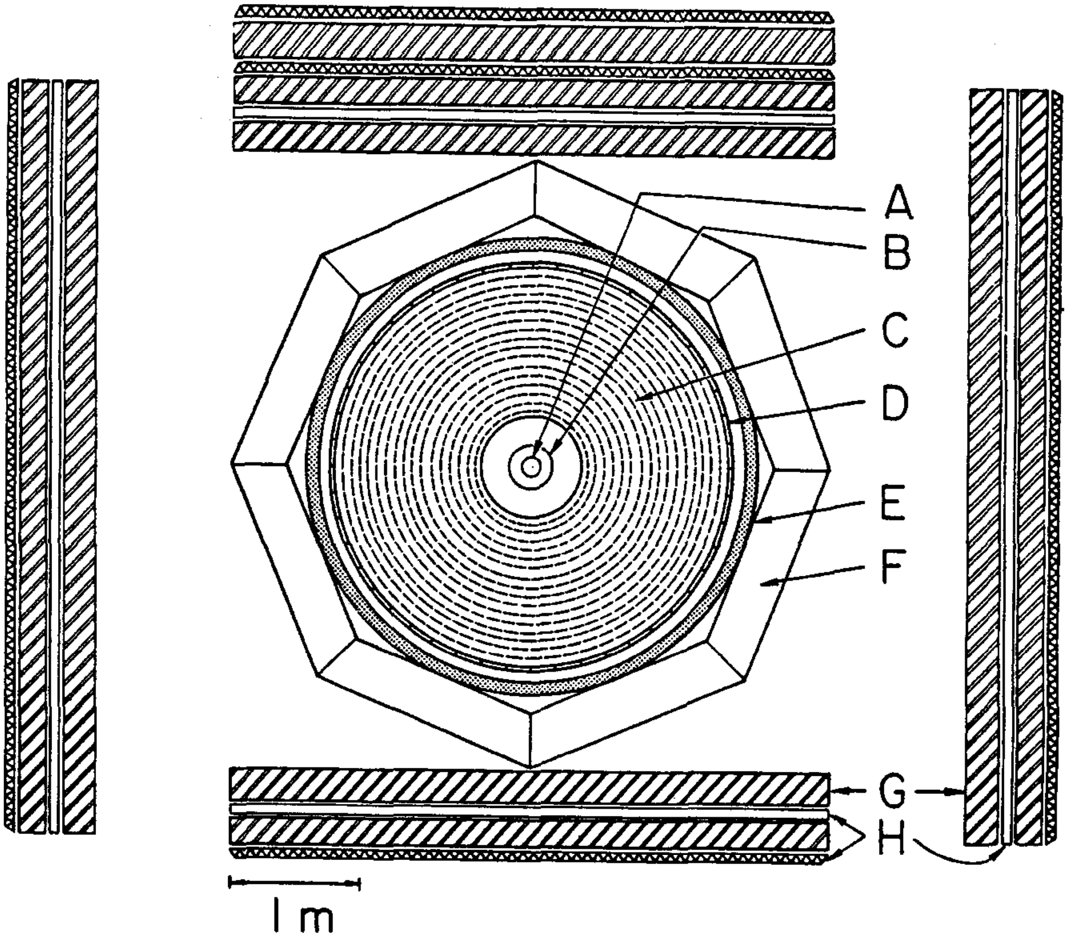

Figure 2.1. Cross sectional view of the MARK II detector. A) Vacuum chamber, B) Pipe counter, C) 16 layer drift chamber, D) Time of flight counters, E) Solenoid coil, F) Lead-liquid argon shower detectors, G) Iron flux return and range counter absorbers, H) Muon proportional tubes.

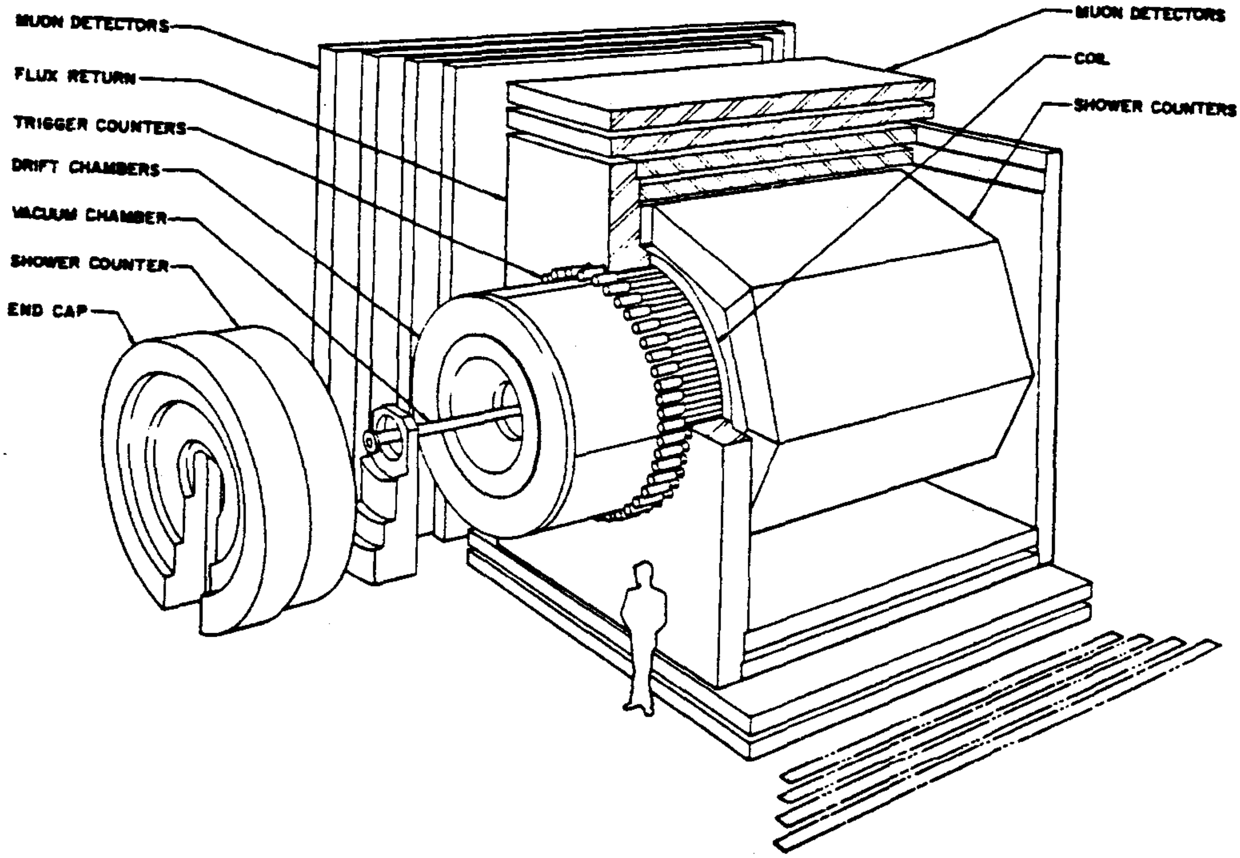

Figure 2.2. Isometric projection of the MARK II detector.

counters attached to the pole faces of the magnetic flux return steel. These "endcap" counters are not used in this analysis, and will not be mentioned further. The muon system is described in chapter 3. A brief description of the other major detector elements follows.

2.1 DRIFT CHAMBER:

Charged particles are detected in over 80% of the solid angle with a 16 layer cylindrical drift chamber.[1] Six layers are parallel to the beam axis, while the other 10 have one end rotated by roughly 3 degrees to allow 3 dimensional reconstruction. The z axis of the right-handed rectangular coordinate system points along the direction of the positron beam, while the y axis lies in the vertical direction. The radii of the first (innermost) and last layers are 41 cm and 1.45 meters respectively, and the active length of the sense wires in the outermost layer is 2.78 meters.

The average momentum resolution is given by (1)

$$\Delta P/P = .01\sqrt{(1.5)^2 + P^2} \qquad (1)$$

where the constant term represents the effects of multiple coulomb scattering, and the momentum dependent term accounts for the 200 micron single cell resolution.

2.2 TIME OF FLIGHT SYSTEM:

The time of flight counters are located between the drift chamber outer skin and the solenoid coil, at a 1.5 meter radius from the beam axis. The scintillator is viewed at both ends to give a time resolution of 300 picoseconds. This allows separation (1-sigma) of electrons from pions below 300 Mev/c, kaons from pions below 1.3 Gev/c, and protons from pions below 2.0 Gev/c. The separation procedure is described in more detail in section 4.2.

2.3 EVENT TRIGGER:

The event trigger[2] is a two level system composed of a fast (500 nanosecond) and simple "primary" trigger whose output sets off the more sophisticated but slower (30 microsecond) "secondary" trigger. The primary trigger demands the coincidence of a beam crossing signal from a pickup electrode with the pipe counter, and hits in at least 4 of 9 selected drift chamber layers. The pipe counter limits the cosmic ray background to tracks which pass within 12 cm of the beam axis. The loose requirement on the drift chamber data results in near perfect efficiency for tracks which pass through all of the drift chamber layers. Typical trigger rates are below 100 hz for low energy runs, but can approach 2 khz at high energy.

The secondary trigger is a hardware track finder and track counter. It works by rotating crescent shaped masks axially around the drift chamber and defining tracks if a minimum number of layers have hits within the mask boundaries. Twenty-four masks are used, allowing tracks of different momenta and charge to be recognized. The criteria used for most of the experiment was at least 1 track with 4 out of 6 axial layers hit, and 1 track with at least 3 hits in the five innermost layers. This resulted in a trigger rate of a few hertz. The combination drift chamber/trigger logic system works so well that the trigger efficiency for event topologies used in this analysis (ie, tracks which enter the shower counter or muon system solid angle) is nearly 100%.

2.4 LEAD-LIQUID ARGON SHOWER COUNTERS:

Located just outside the solenoid coil, the 8 lead-liquid argon electromagnetic shower counters are used for photon detection and electron identification. Appendix B describes the counters in more detail. Here we will discuss the general performance characteristics.

The energy resolution for electromagnetic showers is given approximately by (2)

$$\Delta E/E = .13/\sqrt{E(\mathrm{Gev})} \tag{2}$$

Figure 2.3 shows the counter response to electrons and muons. This figure plots the total energy deposited in the counters divided by the track momentum, for tracks from 2 prong total charge zero events with ECM=6.6 Gev, where the momentum of each track is within 10% of the beam energy. These tracks are also required to be inside the shower counter fiducial volume, defined by extrapolating the measured drift chamber trajectory to the rear of the module, and demanding it be at least 3.8 cm inside all edges.

The photon detection efficiency (Figure 2.4) was measured using constrained fits to the processes $\Psi\to\pi^+\pi^-\pi^0$ and $\Psi\to2\pi^+2\pi^-\pi^0$. Upward fluctuations in the electronic noise can cause fake photons to be found by the photon detection software. The threshold in the efficiency is caused by the cuts required to keep the fake rate acceptable. Figure 2.5 shows the energy distribution of fakes in muon pair events. The fake rate depends on the state of the hardware, but is

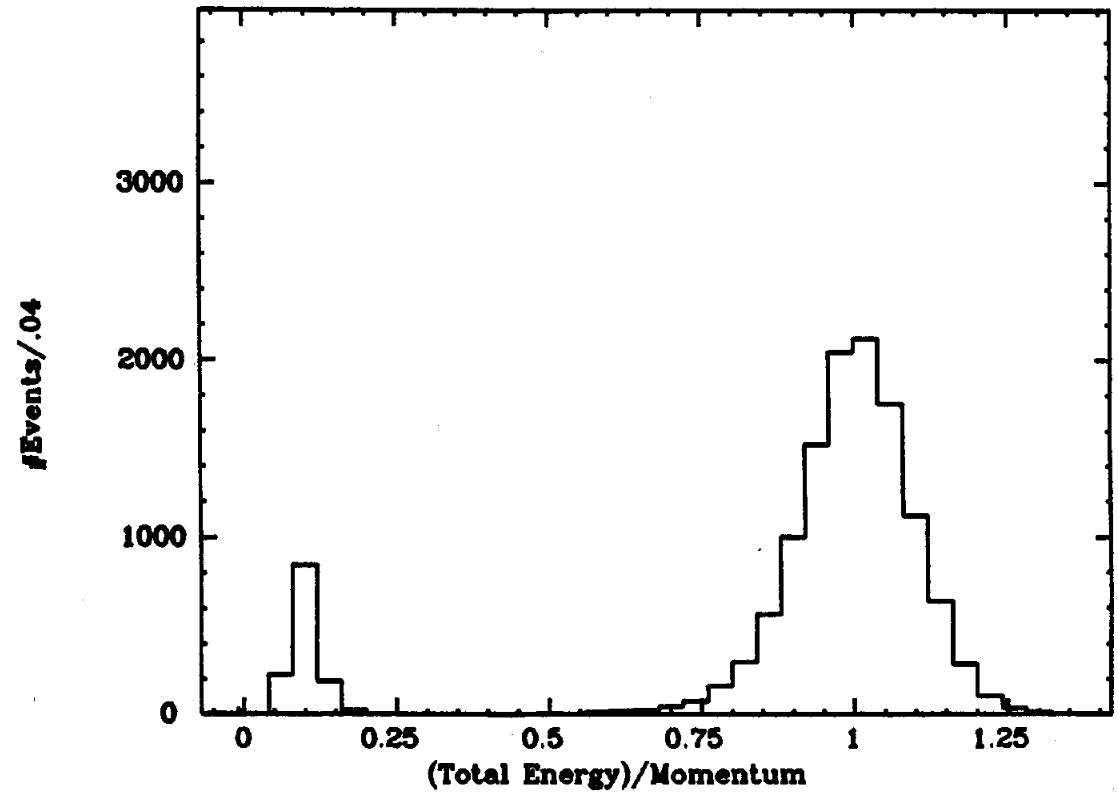

Figure 2.3. Total shower energy divided by particle momentum for electrons and muons from bhabha and muon-pair events at 6.6 GeV.

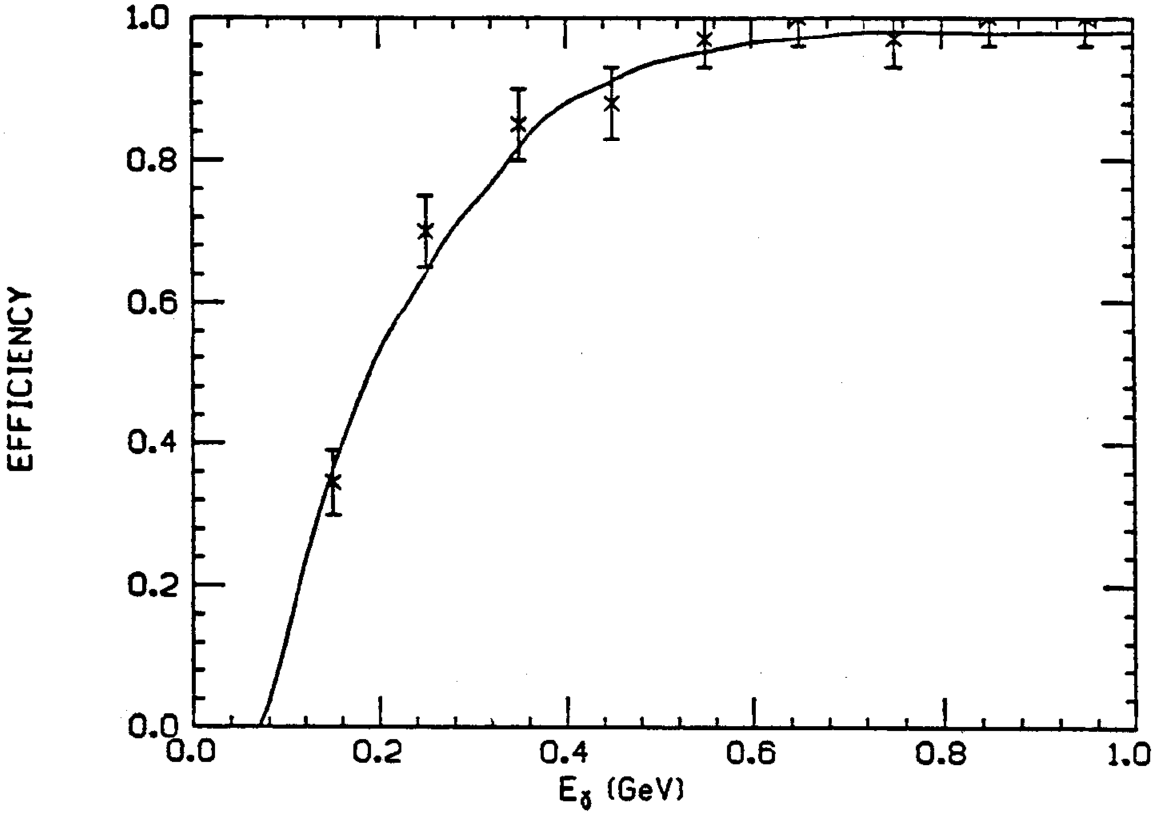

Figure 2.4. Measured shower counter photon detection efficiency for photons within the counter volume. The curve shows an EGS Monte Carlo calculation.

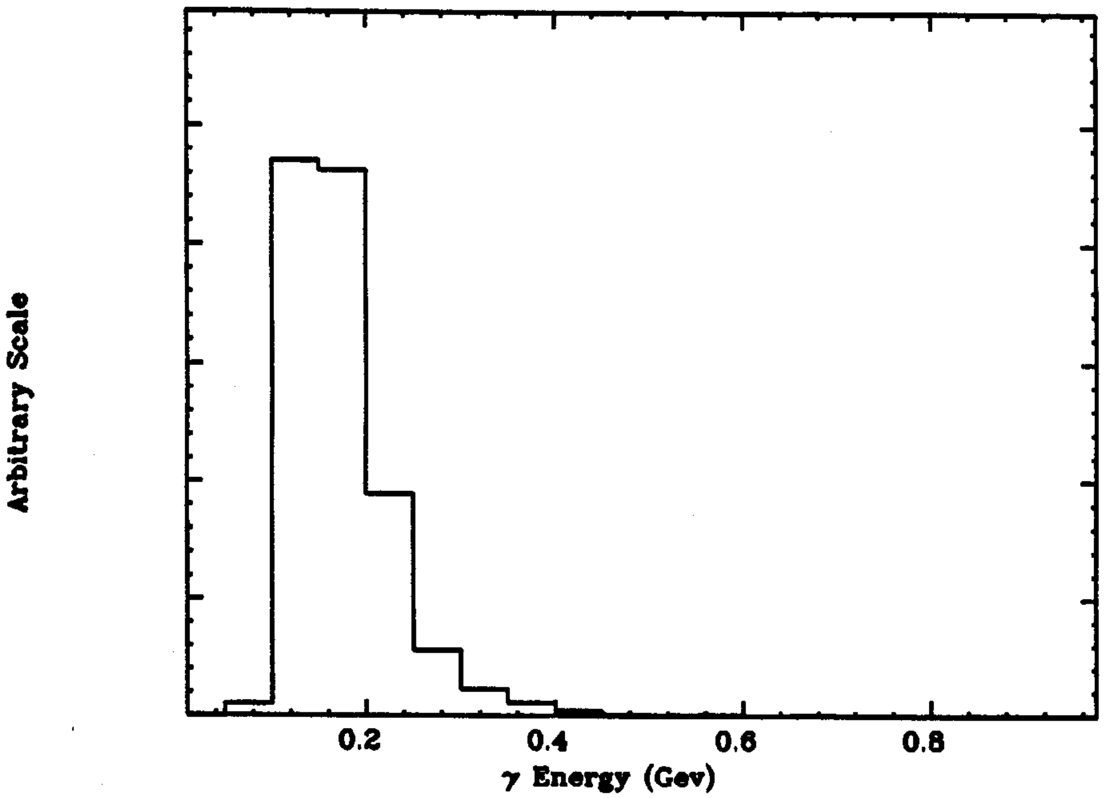

Figure 2.5. Fake photon energy distribution from muon-pair events.

typically .16 photons/event.

The shower counter information can be used to separate electrons from other particles. The algorithm used to achieve the separation is known as "Recursive Partitioning for Non-Parametric Classification" which exists as a program at the SLAC computer center.[3] Briefly, the algorithm works as follows:

By independent means, obtain unbiased samples of electrons and the other particles (we use pions). For each member of both samples, form an N dimensional vector constructed from the measured values of all variables to be used in the separation process (ie, the TOF electron weight, the 7 shower counter layer energies and widths, and some compound 'physical' variables formed from these). This is the input to the program.

The program builds a binary decision tree by iterating on the following proceedure. By comparing the input samples, determine the one variable which is the most sensitive separator, and fix a cut at the value which achieves the maximum separation. The separation ability (S) of a particular variable (X), is determined by running through all values of the variable existing in the input vectors $(x_k \epsilon x_1, x_2, \ldots)$, and measuring the fraction of elements in each sample whose X value is below x_k. Call the fractions $F_e(x_k)$ and $F_{pi}(x_k)$. The value of X which maximizes $S(x)=|F_e(x)-F_{pi}(x)|$ is the value which achieves the maximum separation, $S_{max}(x)$. The variable with the largest S_{max} is the most sensitive separation variable.

The program then divides each sample into two sub-samples: those which are below, and those which are above the cut. This process is continued until 1) perfect separation is achieved, 2) the number of input vectors is too small to make statistically significant cuts, or 3) no variable has any separating power left. These stopping points on the decision tree are called "terminal nodes."

When using the resultant decision tree for particle identification, the candidate particle's input vector is constructed, and stepped down the tree until a terminal node is reached. Depending on the relative number of original training vectors which landed at the node, the particle is called electron, not-electron, or ambiguous, depending on the users' requirements on the identification and mis-identification efficiencies.

Separate decision trees are made for different momentum intervals using training samples obtained from several sources. Different samples were used to measure the resulting identification efficiencies. Below 1.0 Gev/c, pions from tightly constrained reconstructed neutral kaon decays are used (see section 7.4), while pions from multiprong decays of the $\Psi(3095)$ are used above. Electrons are obtained from converted photons and Bhabha events. Table 2.1 lists the measured identification and mis-identification probabilites for pions and electrons as a function of momentum.

Table 2.1

Electron and pion identification and misidentification efficiencies. P(i→j) means the probability a particle of type i is called type j.

Momentum	P(e→e)	P(e→not-e)	P(π→not-e)	P(π→e)
.3-.4	.730+-.007	.077+-.004	.565+-.012	.098+-.007
.4-.5	.760+-.009	.060+-.005	.651+-.011	.111+-.007
.5-.6	.833+-.011	.042+-.006	.712+-.011	.069+-.006
.6-.7	.866+-.012	.032+-.006	.736+-.012	.056+-.006
.7-.8	.823+-.017	.047+-.010	.870+-.011	.032+-.006
.8-.9	.857+-.018	.024+-.008	.810+-.015	.052+-.009
.9-1.1	.848+-.015	.035+-.008	.895+-.004	.031+-.002
1.1-1.3	.918+-.015	.022+-.008	.896+-.006	.036+-.004
1.3-1.5	.968+-.008	.009+-.004	.871+-.014	.056+-.010
2.0-2.1	.981+-.002	.004+-.001	-----	-----
2.6	.987+-.001	.004+-.001	-----	-----
3.3	.991+-.001	.003+-.001	-----	-----

References:

1.) R.H. Schindler, Ph.D. Thesis, SLAC Report No. 219 (1979).

2.) T.M. Himel, Ph.D. Thesis, SLAC Report No. 223 (1979).

3.) J.H. Friedman, IEEE Transactions on Computers, April 1977, p. 404.

CHAPTER 3

The Muon Detection System

3.1 INTRODUCTION:

Muon identification is accomplished by exploiting their non-participation in the strong interaction. By forcing the particle sample to traverse an absorbing material, strongly interacting particles will be attenuated while muons (aside from dE/dx losses and multiple coulomb scattering) will be unaffected and can be detected with simple counters sensitive to charged particles. Although a thicker absorber gives better separation due to the increased attenuation, demanding that the muons do not range out in the absorbing material determines a maximum absorber thickness which depends on the muon momentum. To provide muon identification over a wide range of momenta, practical systems usually consist of several consecutive layers of absorbing material and particle detectors. The probability that a hadron is misidentified as a muon depends not only on the absorber thickness, but also on the fraction of pions and kaons which decay to muons before entering the absorber, and the ability of other detector elements to discriminate against such decays.

The MARK II muon detection system consists of 4 walls that surround the central detector, each wall being made of alternate layers of steel plates and planes of proportional tubes. During the time the data used in this analysis was collected, the system had three absorbing plates on the top wall and two on each of the other walls. The first two steel layers on the top and bottom walls double as the magnetic flux return for the spectrometer magnet. The first layer of the system subtends approximately 51% of the total solid angle, and has a momentum threshold for muon penetration of approximately 700 Mev/c. We will discuss below the physical construction, the tracking and identification algorithm, and measurements of the detection efficiency and hadron misidentification probabilities.

3.2 PHYSICAL CONSTRUCTION:

Before a particle can reach the first absorbing plate, it must traverse inner detector material (ie, the magnet coil and shower counters) equivalent to 20 cm of iron. The steel absorbing plates are 23 cm thick in the first two layers and 30 cm thick in the third layer of the top wall. The first layer is located approximately 3 meters from the interaction region, and subtends 51% of the solid angle, while the second layer is approximately of equal area and covers 90% of the solid angle subtended by the first. The top wall's third layer subtends 9% of the total solid angle.

Behind each absorbing plate there is a plane of proportional tubes which run the full width of the wall and which measure one of the two orthogonal coordinates. The tubes are oriented so that the second and third layers measure the coordinate orthogonal to that measured by the first. The 1672 tubes used in the system are actually built in the form of 8 tube modules made of extruded aluminum. The system uses modules of different lengths, the longest being 19 feet long, but they all have the cross section displayed in Figure 3.1. The 25 mm wire spacing is well suited to the tracking errors caused by multiple coulomb scattering. The triangular design of the tubes result in a module of great strength which suffers little mechanical deformation even in the longest versions. This is important as it insures the modules pack together with no gaps or irregularities over their entire length.

The forty-five micron diameter gold plated tungsten sense wires are held under 200 grams of tension and terminate in 100 ohm resistors located in an electronics enclosure welded to one end of the module. Gas is supplied through 2 fittings located at the opposite end and flows serially through the eight tubes. Signals on the sense wires are discriminated and sent via line drivers (also located in the electronic enclosure) to the electronics trailer where they trigger a 3 microsecond one-shot whose output is loaded into a long shift register. When the detector secondary trigger requirement is satisfied, the contents of the shift register are read out and saved on the data tape.

After testing several gas mixtures, a 95% argon 5% carbon dioxide mixture was chosen due to the relaxed timing and gain requirements for this application, and due to safety considerations for a system with such a large gas volume and distribution network. The response of a typical module as a function of high voltage is shown in Figure 3.2 for one of the tested mixtures. Here we plot the efficiency for any tube in the module to detect a track and the "doubles" efficiency for two adjacent tubes to simultaneously detect the track measured with normally incident cosmic rays. The average counting rate per wire (for 16 foot tubes) is also shown. The module efficiency is greater than 99.5% and has a plateau of several hundred volts before the background singles

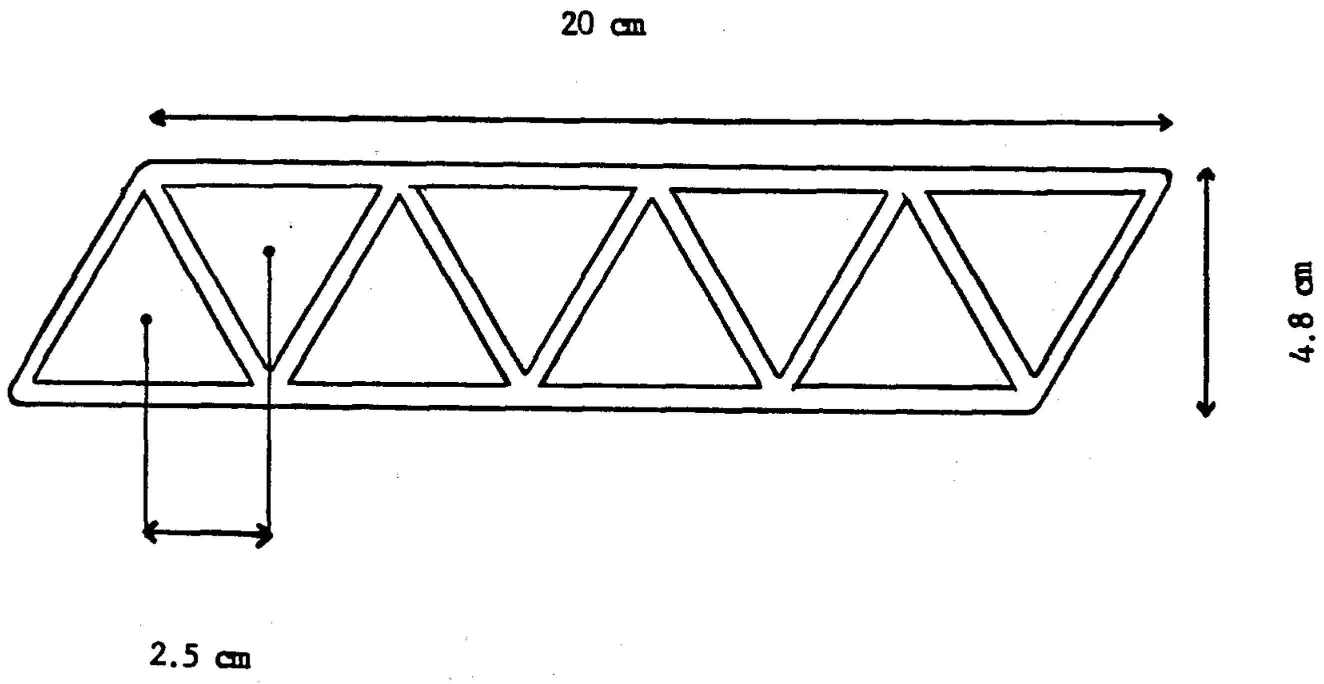

Figure 3.1. Cross sectional view of muon system proportional counter module.

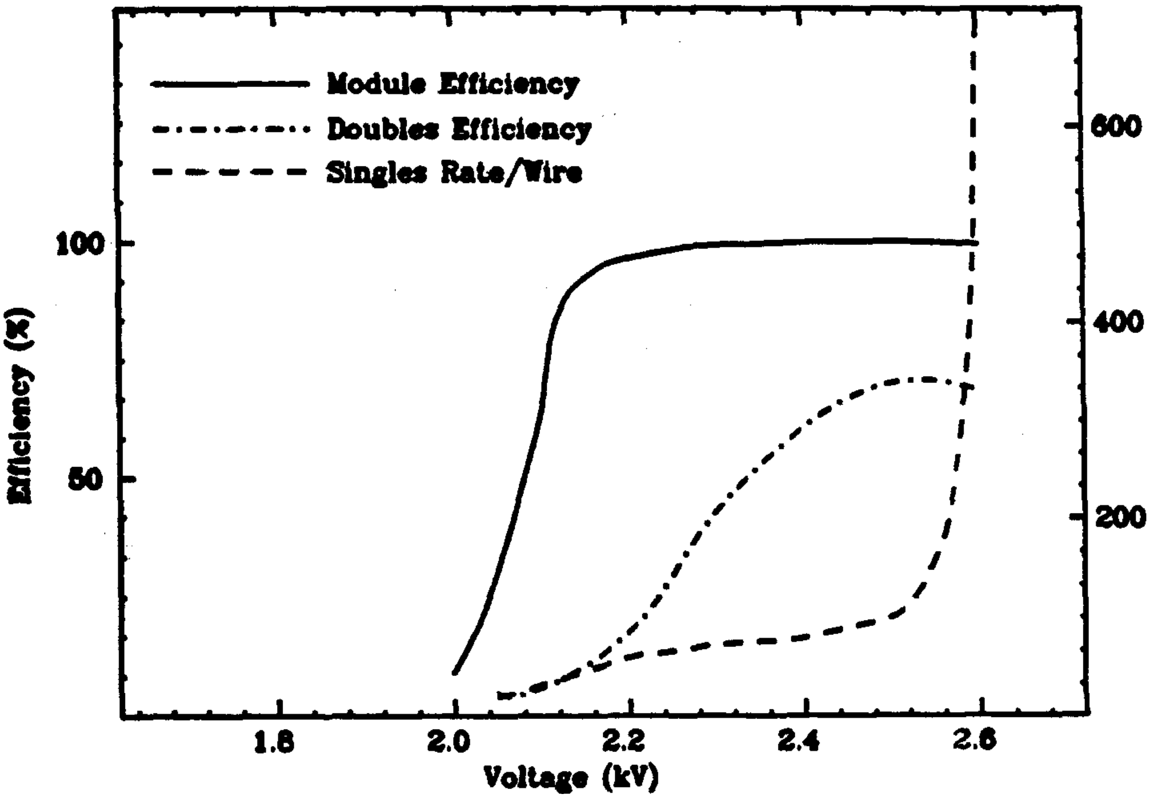

Figure 3.2. Muon system proportional tube operating characteristics as a function of applied voltage.

rate begins to rapidly increase. Note that in the plateau region, the singles rate is determined almost entirely by the cosmic ray flux. The doubles efficiency rises more slowly, plateauing near the maximum value expected from geometrical considerations approximately 100 volts below the background threshold. Thus it is possible to operate the tubes so as to achieve good efficiency throughout the entire gas volume.

Several hardware subsystems were developed to monitor the system reliability. Shift register operation was confirmed by shifting through an 8 bit fixed pattern at the end of each read cycle. At the start of each run, every electronic channel was tested by forcing a small charge onto the wire via the high voltage isolation resistor. The actual wire performance was checked with cosmic rays. The output of all tubes in a plane were 'ored' together, and the coincidence of this signal from all horizontal or vertical planes was used to define a cosmic trigger. In a matter of minutes the efficiency and background counting rate of every tube could be measured. The system modularity allowed easy replacement of defective tubes, but this proved unnecessary except for a few replacements during the installation and shake-down phase of the experiment.

3.3 THE MUON IDENTIFICATION ALGORITHM:

The muon identification routine analyzes all charged tracks individually and is conceptually very straightforward: extrapolate the measured drift chamber trajectory out through the absorbing wall keeping track of dE/dx losses, bending in the magnetic field inside the flux return iron (where applicable), and the average multiple coulomb scattering. If a proportional tube fired near the predicted track position (i.e, within 3 sigma of the deviation expected from multiple scattering) in each plane traversed before the particle ranges out, call it a muon. Edge effects and range straggling complicate this simple picture, so before examining the detailed algorithm, the range straggling and multiple coulomb scattering will be discussed.

3.3a Multiple Coulomb Scattering:

Before reaching a plane of proportional tubes, a particle must first traverse several massive detector elements--the coil, shower counters, and iron absorbing walls upstream of the detector plane--which can significantly change its direction due to multiple coulomb scattering. As an estimate of the RMS deviation from the predicted position at the detector plane (σ_x), the deviation arising from each element is calculated and added in quadrature (Equation 1)

$$\sigma_x = [\sum_i \Theta_i^2(D_i^2 + T_i^2/12)]^{1/2} \tag{1}$$

where Θ_i, D_i, and T_i are the RMSD multiple scattering angle, distance to the detector plane, and thickness of the scattering element respectively. Θ_i is calculated using the simple formula given in appendix A. Although the approximations contained in equation 1 will be poor for tracks which exit an absorber element with low momentum, thereby suffering a large amount of multiple scattering, the geometry is such that the largest contribution to σ_x arises from the scattering elements located far upstream for which the approximations are valid. For example, Figure 3.3 plots σ_x, as a function of momentum, for normally incident tracks in the first and second layers of the bottom

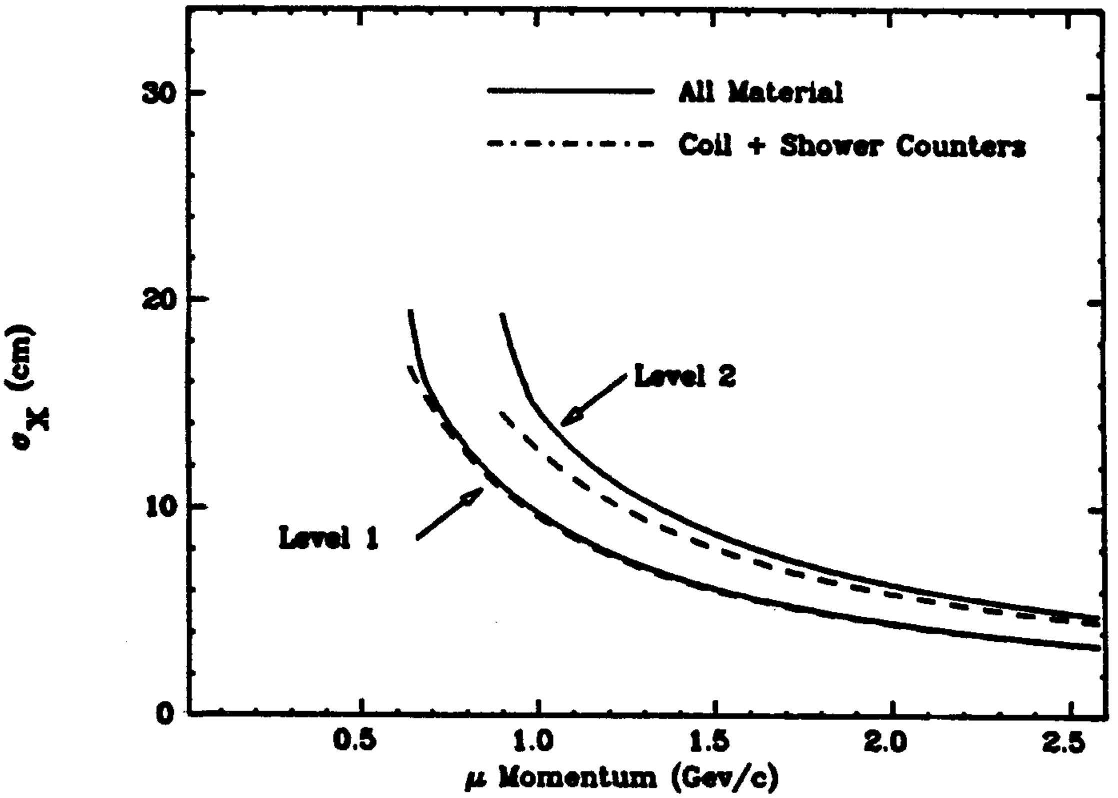

Figure 3.3. Projected multiple scattering (sigma) for normally incident muons at first and second levels. The contribution from the solenoid coil + shower counters is also shown.

wall. Also shown is the σ_x that would result considering the multiple scattering in the coil and shower counters alone. Note that σ_x is on the order of 10 cm and is dominated by the scattering in the coil and shower counters. The error in the extrapolated position arising from the drift chamber resolution is typically 3 cm (sigma) depending on the depth and orientation of the layer, and is added in quadrature with σ_x to obtain the total deviation. Figure 3.4 shows a typical distribution, made with cosmics rays, of the measured deviation in units of σ_x for the first plane in the bottom wall.

3.3b Range Straggling:

Fluctuations in the dE/dx losses when a particle traverses an absorbing medium result in fluctuations in its range. Thus, there is no sharp momentum threshold for muon penetration of a given layer. The relative range straggling is between 2 and 3 percent for muons with momentum of interest in this analysis (See Appendix A). Of concern here, however, is the projected range straggling along the axis perpendicular to the absorbing plane. Multiple scattering contributes to this projected straggling as the particle can be bent towards or away from the normal, thereby traversing a greater or lesser amount of material before exiting.

One way to describe the situation is to consider the fraction of incident muons of momentum P which traverse the material preceeding a given detecter plane, as a function of the variable Q

$$Q = (R(P)-R_0)/R(P)$$

where R_0 is the total amount of material the particle would have to

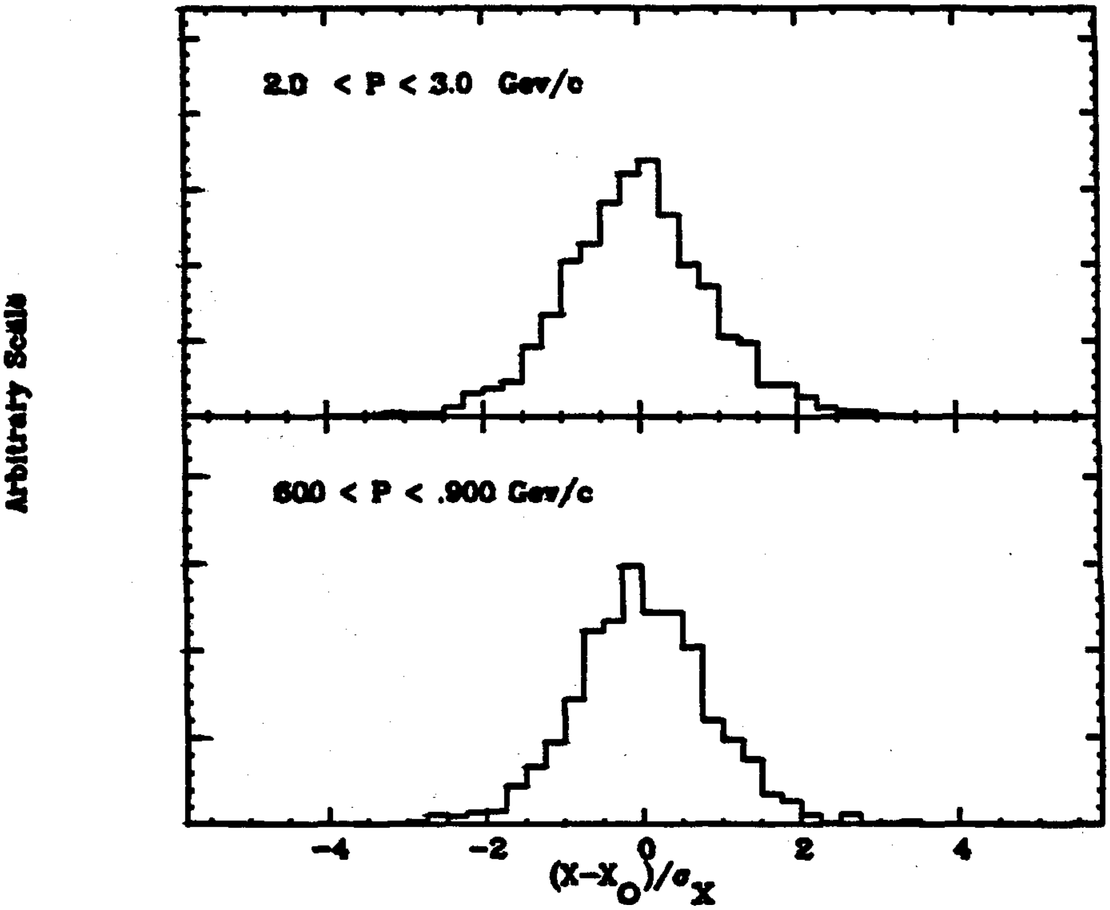

Figure 3.4. Measured deviation from extrapolated position divided by the expected multiple scattering for cosmic ray muons at level 1.

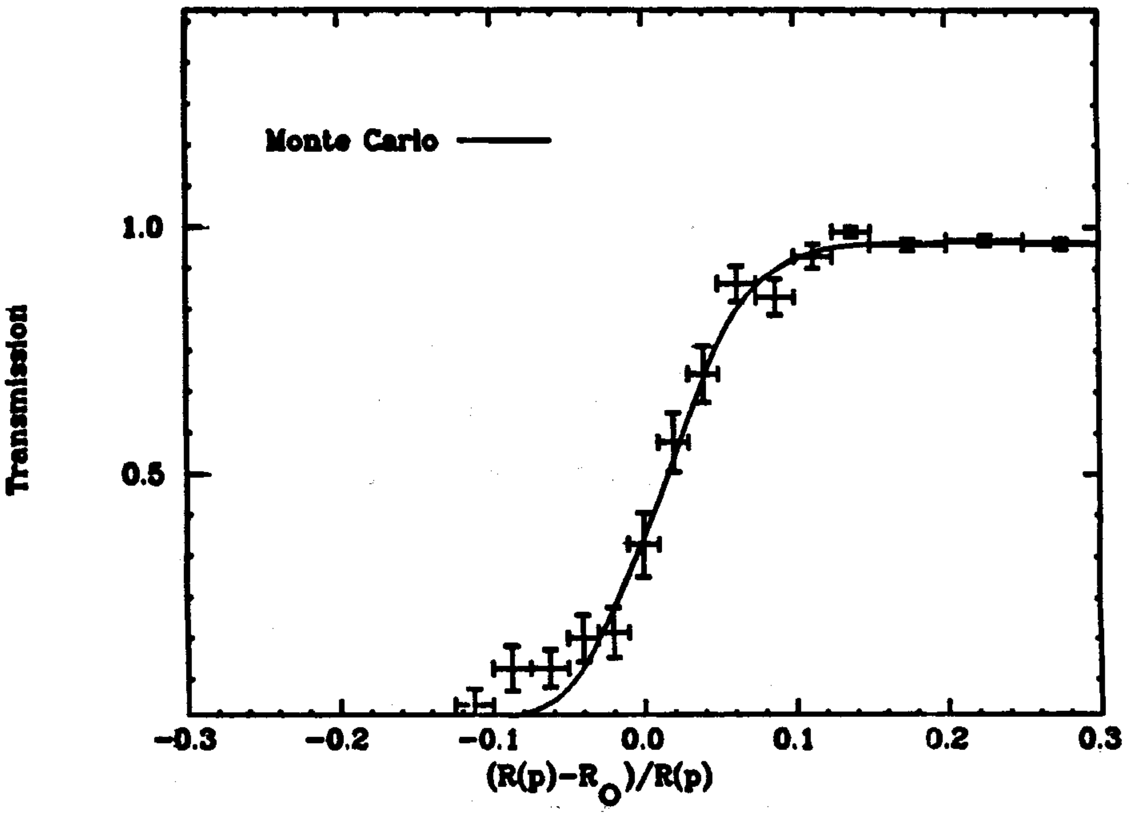

Figure 3.5. Level 1 muon transmission curve measured with cosmic ray muons. The monte carlo calculation is also shown.

traverse if it experienced no mutiple scattering, and R(P) is the tabulated range for a particle with momentum P. In an absorber with no magnetic field, $R_0 = R_n/\cos(\theta)$ where R_n is just the absorber thickness and θ is the angle of the incident track to the normal. For example, Figure 3.5 shows, as a function of Q, the measured detection probability for cosmic ray muons with $\cos(\theta) > .90$ in the first layer of the bottom wall. To eliminate confusion arising from the shower counter boundaries, those tracks within 2 degrees (azimuth) of a module edge are not used in the plot.

To determine the projected range straggling for muons as a function of momentum and incidence angle, a Monte Carlo program was developed which simulated the detector geometry and did the transport in small steps allowing for dE/dx losses and fluctuations, multiple coulomb scattering, and magnetized materials. For each layer, the generated transmission plot was fit to an integrated gaussian with adjustable width (σ_r) and offset. As an illustration of the relative importance of the various physical processes, in Figure 3.6 we plot as a function of incidence angle, σ_r for the first detector plane allowing for energy loss fluctuations only, multiple scattering only, both energy loss fluctuations and multiple scattering, and both in magnetized iron equivalent to the MARK II flux return. Although the relative projected range straggling due to energy loss fluctuations is independent of incidence angle, the multiple scattering contribution increases sharply with increasing incidence angle becoming the dominate effect for angles larger than 18 degrees ($\cos(\theta) < .95$). Calculations with both effects included indicate they effectively add in quadrature. Inclusion of the magnetic field increases the straggling especially at

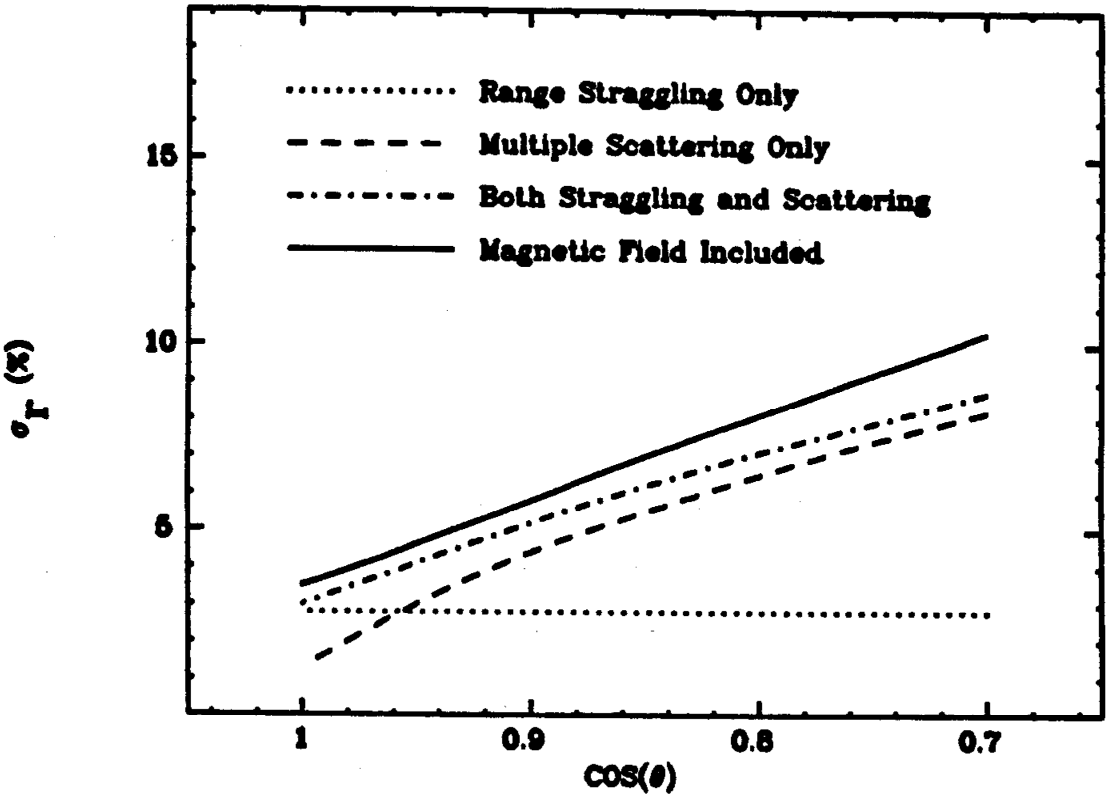

Figure 3.6. Level 1 projected range straggling (sigma) as a function of incidence angle.

large incidence angles. The calculations also indicate that multiple scattering causes a more or less constant offset of roughly 9 grm/cm^2 equivalent to 2.2% for the first detector plane and 1.7% for the second.

Averaging the Monte Carlo results over the incident angle distribution measured with the cosmic ray sample of Figure 3.5 yields the curve shown in the figure. The data and calcualations agree well. Both the analysis program and the MARK II Monte Carlo program assume a gaussian distribution for the projected range straggling, and use the calculated results for the width and offset described here.

3.4 FIDUCIAL VOLUME CONSIDERATIONS:

Multiple scattering and range straggling sufficiently smear the edges of the muon system acceptance that simple fiducial volume or momentum threshold cuts are expensive to use. Therefore, a somewhat different concept has been implemented to take into account edge effects. A given detector layer is said to be "required" if the extrapolated particle trajectory is within the layer edges by more than 3 sigma of the projected multiple scattering (σ_x), and if the particle has excess range greater than 3 sigma of the expected range straggling (σ_r). The layer is "expected" if the particle trajectory is within the edges and the excess range is greater than zero. If the trajectory is no more than $3\sigma_x$ outside the layer edges, and the excess range is no less than $-3\sigma_r$, the level is called a "possible" level. No layer is allowed to have a higher status (required > expected > possible) than the status of the preceeding layers. We indicate status classes with the notation MULEVX > N where N is the number of levels and X is P, E, or R for possible, expected, or required respectively.

The "status acceptance," defined as the fraction of isotropically produced muons which satisfy a particular status class, is shown in Figures 3.7a,b as a function of muon momentum. For the status MULEVE > 0, the acceptance plateaus at the geometrical acceptance of the system (51% for level 1, 46% for level 2). The threshold region reflects the system's planar geometry in that the effective absorber thickness increases like the inverse cosine of the incident angle. Raising the status to MULEVR > 0 decreases the acceptance due to the imposition of fiducial volume cuts (see Figure 3.3), and increases and broadens the momentum threshold due to the range straggling restriction. Lowering the status to MULEVP > 0 has exactly the opposite effect.

3.5 MUON IDENTIFICATION EFFICIENCY:

Given the status classes described above, the following rules are used to determine the identification of a given track. Three choices are allowed: muon, not muon, and can't tell.

The efficiency for a muon of a given status class to be properly identified depends on several factors. The individual tube efficiency is high (>99.5%), but in our large system a few tubes were usually malfunctioning, thus reducing the average tube efficiency by some fraction of one percent. A more intrinsic inefficiency results from those tracks which scatter by more than three sigma in position or range, but is no larger than 1 to 2 percent. Tracks which are improperly measured by the drift chamber due to hardware or software

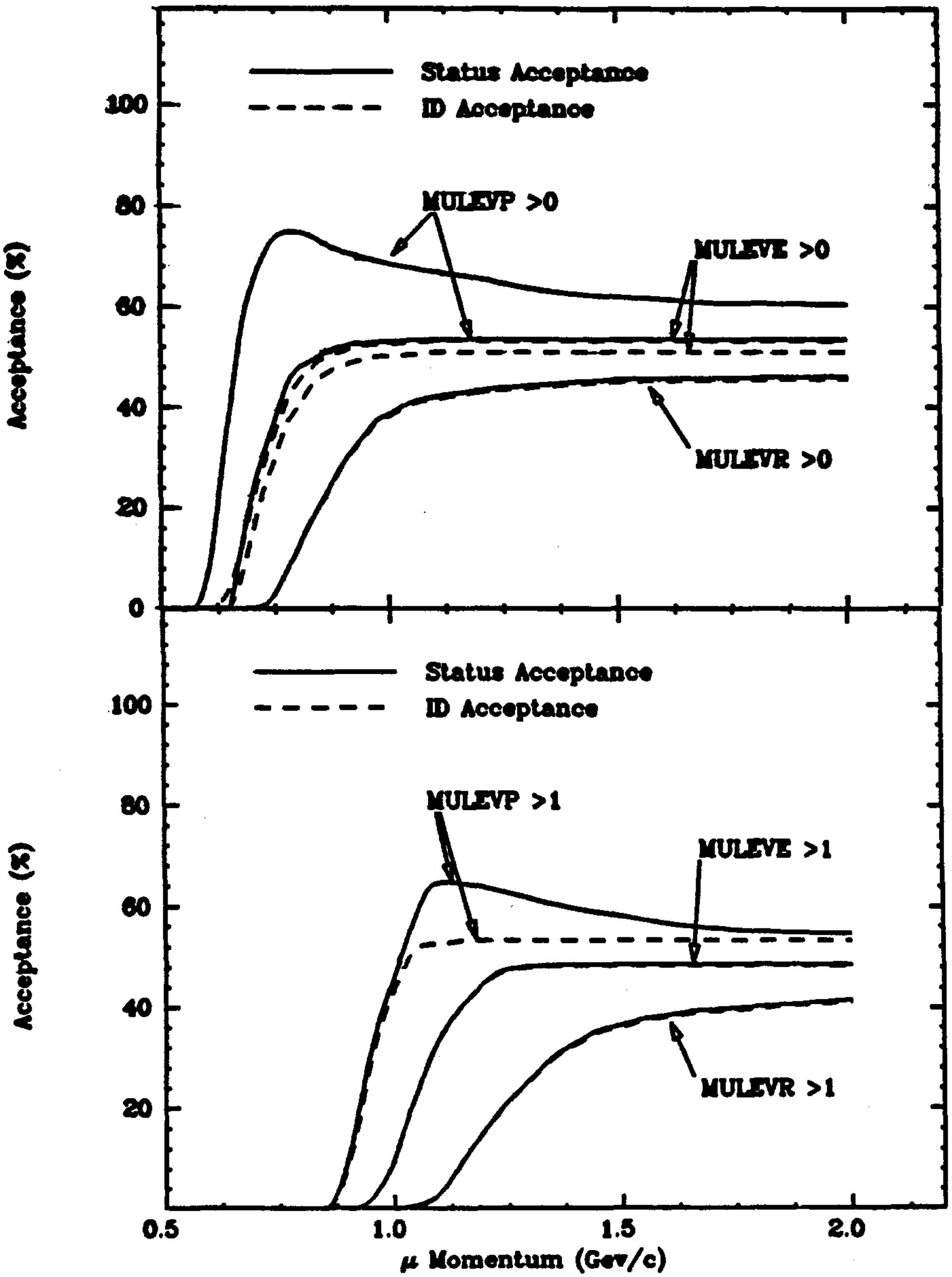

Figure 3.7. Muon system acceptance for various status classes. (a) Level 1. (b) Level 2.

TABLE 3.1

Muon system particle identification rules.

STATUS CLASS	RULE
MULEVP>0 + MULEVE=0	If a signal is detected in either of the first two detector levels, call it a muon; otherwise--can't tell.
MULEVE>0 + MULEVR=0 or MULEVR=1	If a signal is detected in either of the first two detector levels, call it a muon; otherwise--not muon.
MULEVR>1	If a signal is detected in the highest or next highest level and in at least one other level, and not more than one level is missed, call it a muon; otherwise--not muon.

deficiencies, will not project to the proper coordinates. This causes an additional inefficiency.

These inefficiencies can be measured in the momentum intervals where unambiguous muon candidate tracks can be collected from the data sample. Muon pair events provide a clean source. These events are identified only through the charged track momenta, colinearity, and shower counter pulse heights, but to guarantee sample purity, tracks are considered muon candidates only if the opposite track is identified as a muon in at least two muon levels. For a given level, only those candidates which are "required" are used in the efficiency measurement. To isolate the inefficiency due to tracking errors, the efficiency is also measured with a subset of the candidate events which have high quality drift chamber information (i.e., the tracks are detected in at least 12 of the 16 drift chamber layers and have a chi-square/dof from the track fit less than 6.25, are colinear within 30 mR, and have a Z coordinate difference at the origin less than 3 cm). To isolate the multiple scattering contribution, the efficiency is also measured with the scattering limits increased to 5 sigma from the usual 3. Table 3.2 lists the measured efficiencies.

TABLE 3.2

Muon system layer efficiencies. Statistical errors are less than .001.

	LAYER 1		LAYER 2		Correct ID	
	3s	5s	3s	5s	3s	5s
Normal Data	.977	.984	.984	.988	.968	.974
High Quality	.980	.984	.986	.989	.971	.975

Enlarging the multiple scattering limits increases the efficiency for the high quality tracks approximately .4% to 98.4% and 98.9% for layer 1 and layer 2 respectively. These values can be taken as the average efficiencies for the detector planes. Essentially no difference in the 5s efficiency is observed between the normal and high quality data, although a .2% to .3% improvement is measured for the 3s efficiency. Thus, drift chamber errors account for no more than 10% to 15% of the total inefficiency. Table 2 also lists the efficiency for the muons to be properly identified using the rules of table 3.1.

The identification efficiency for tracks which have no required levels is considerably less than 100% as they are more likely to scatter outside the system boundaries. For isotropically produced muons, the identification efficiency is roughly 86% for the status class MULEVE>0 + MULEVR=0, and is only 13% for the status MULEVP>0 + MULEVE=0. The muon "identification acceptance," defined as the fraction of isotropically produced muons which are properly identified, is also shown in Figure 3.7 for different status classes. The identification acceptance for the class MULEVP>0 is about equal to the status acceptance for the class MULEVE>0 since as many 'possible' tracks scatter inside the boundary as 'expected' ones scatter out. Raising the status class to MULEVE>0 reduces the identification acceptance only slightly. For the status class MULEVR>0, the two acceptances are nearly equal due to the the small identification inefficiency.

3.6 MISIDENTIFICATION PROBABILITIES:

Non-muons may be misidentified as muons for several reasons, the simplest being the random background counting in the detector tubes. This misidentification rate has been measured using "imaginary" tracks obtained by rotating 90 degrees in azimuth, real tracks from coplanar two prong events. The rate depends on the status class and decreases with increasing momentum proportionally to the width of the projected search region in the detector layer (see Figure 3.3). Table 3.3 lists the misidentification probabilities averaged over the momentum distribution in the sample.

TABLE 3.3

Muon misidentification probability (%)
for random tracks and electrons.

STATUS CLASS	RANDOM-TRACKS	ELECTRONS
MULEVP>0 + MULEVE=0	.78+-.10	.59+-.09
MULEVE>0 + MULEVR=0	.94+-.13	.90+-.11
MULEVR=1	.97+-.14	1.19+-.12
MULEVR=2	.01+-.01	.04+-.01

For status classes requiring a signal in only 1 detector plane, the misidentification probability is roughly 1%. For MULEVR=2, the probability is consistent with .01 squared. Also listed in Table 3.3 are the electron misidentification probabilities measured with electrons from Bhabha events. They are consistent with the random background values although a small signal could be expected from Compton scattering in the proportional tubes of the low energy photons that are the remnants of the electromagnetic shower.

Hadrons can be misidentified as muons from "punch through" where the hadron escapes experiencing a strong interaction in the absorbing wall, or where a secondary track from the strong interaction cascade succeeds in penetrating the detector plane. Alternatively, the hadron can "decay" in flight to a muon which is then detected in the proportional counters.

The probability that a pion is misidentified as a muon due to decay is easily calculated with the Monte Carlo program, and leads to the results shown in Figure 3.8. This figure shows as a function of momentum, the pion rejection ratio defined as the probability that isotropically produced pions are identified as muons ("pion misidentification acceptance"), divided by the muon identification acceptance (MULEVP >0) measured at the pion momentum (i.e., if the pions were actually muons, the ratio would be 1). The pion time dilation factor causes the misidentification to decrease with increasing momentum. However, the misidentification is also a function of the status class. The structure apparent near 1100 Mev/c is due to the transition from MULEVR=1 to MULEVR=2.

Pions which decay in the drift chamber volume will often be poorly

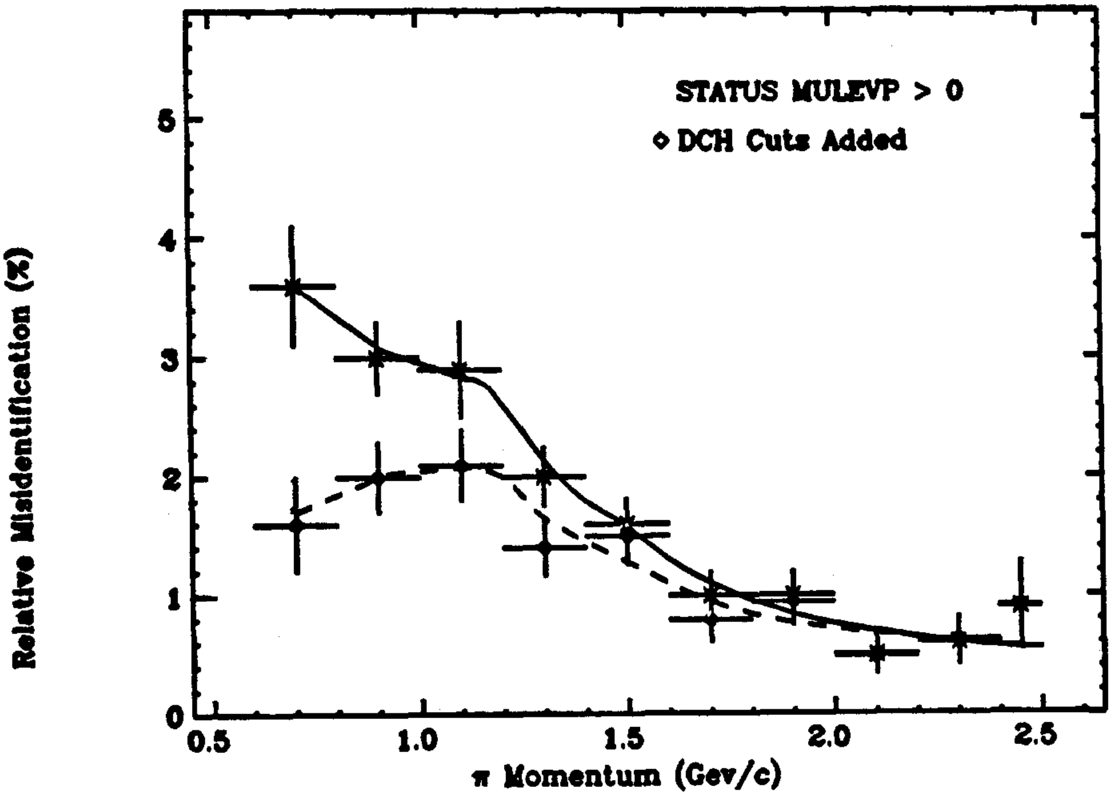

Figure 3.8. Contribution to pion misidentification probability from decay divided by muon identification efficiency for the status class MULEVP>0. The lower curve illustrates the effects of including cuts on the track fit parameters.

fit by the tracking program, and this can be exploited to decrease the misidentification probability. For example, Figure 3.8 also shows the rejection ratio obtained if all tracks are required to have at least 12 drift chamber layers used in the fit, a chi-square/dof for the track fit less than 12, and be no farther from the interaction region than .6 cm in the radial projection. These cuts reduce the misidentification by a factor of two near threshold while decreasing the muon identification acceptance by no more than 3%. The cuts have less effect as the pion momenta increases.

Determining, by a Monte Carlo calculation, the probability that a pion is misidentified due to punch through is a more difficult problem as one must reliably simulate the hadronic cascade in the absorber. Therefore, we measure directly the pion misidentification probability using pions extracted from the data sample. For this purpose, multiprong hadron events ($3<\#prongs<11$) from the $\Psi(3096)$ resonance are used. Interaction region cuts are applied, and events with converted photons are rejected. Events with identified MULEVR>1 muons were hand scanned, and only two background events were found: a $\mu\mu\gamma$ event where the photon converted but was not identified due to a grossly mismeasured track, and a hadron event with a coincident cosmic ray. Unless the Ψ has an undiscovered multiprong (>3) muon decay, the muon contamination is negligible. Within the muon system acceptance, the candidates have an isotropic angular distribution.

Figure 3.9 plots, as a function of momentum, the fraction of pion candidates which have a signal in the muon dectector plane within 3 σ_x of the extrapolated position. Only candidates whose normal angle to the absorbing wall is less than 26 degrees (cos > .90) and are within

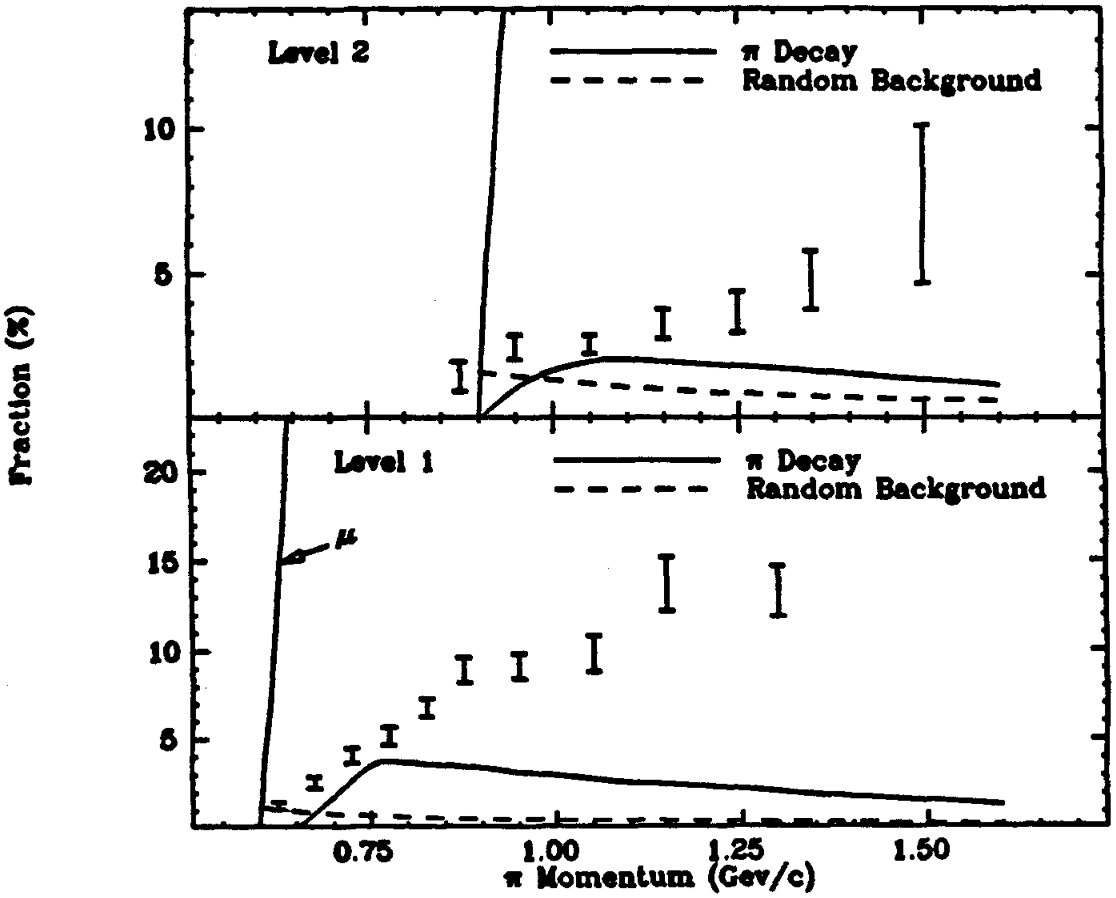

Figure 3.9. Measured fraction of pion candidates which have a signal in the muon counters within 3 sigma (MS) of the extrapolated position. The contributions from random background and pion decay are also shown.

the layer's spatial fiducial volume (3 σ_x from all edges) are used. The transmission plot for muon candidates near threshold is shown for comparison, as are the contributions to the signal from random background and pion decay. Punch through begins to dominate the misidentification approximately 200 Mev/c and 400 Mev/c above the momentum threshold in layers 1 and 2 respectively. For layer 1, the detection probability rises smoothly from threshold and reaches a value near 15% at 1.5 Gev/c, while for layer two, the probability remains constant near 3% until punch through becomes important.

Figure 3.10 plots the relative pion misidentification probability as a function of momentum for several status classes. This is the ratio (for isotropically produced and successfully tracked pions and muons) of the pion misidentification efficiency to the muon identification efficiency. If we remove the requirement that the particles be successfully tracked, the ratio would decrease by 5 to 10% as more pions than muons fail to be tracked. The misidentification varies with the status class and is smallest for the class MULEVR>1. Note that it is considerably smaller for the class MULEVE>0+MULEVR=0 than for the class MULEVR=1. This is because the candidate tracks are either near the edge of the momentum acceptance where punch through is at a minimum, or are near the plane edges and therefore have a large incidence angle relative to the absorber.

How the muon system information should be used depends on the type of analysis being done. If one wishes to have the largest possible muon acceptance independent of pion misidentification, using the status class MULEVP>0 would be appropriate. If one wishes to minimize the pion misidentification at the expense of the muon acceptance, the class

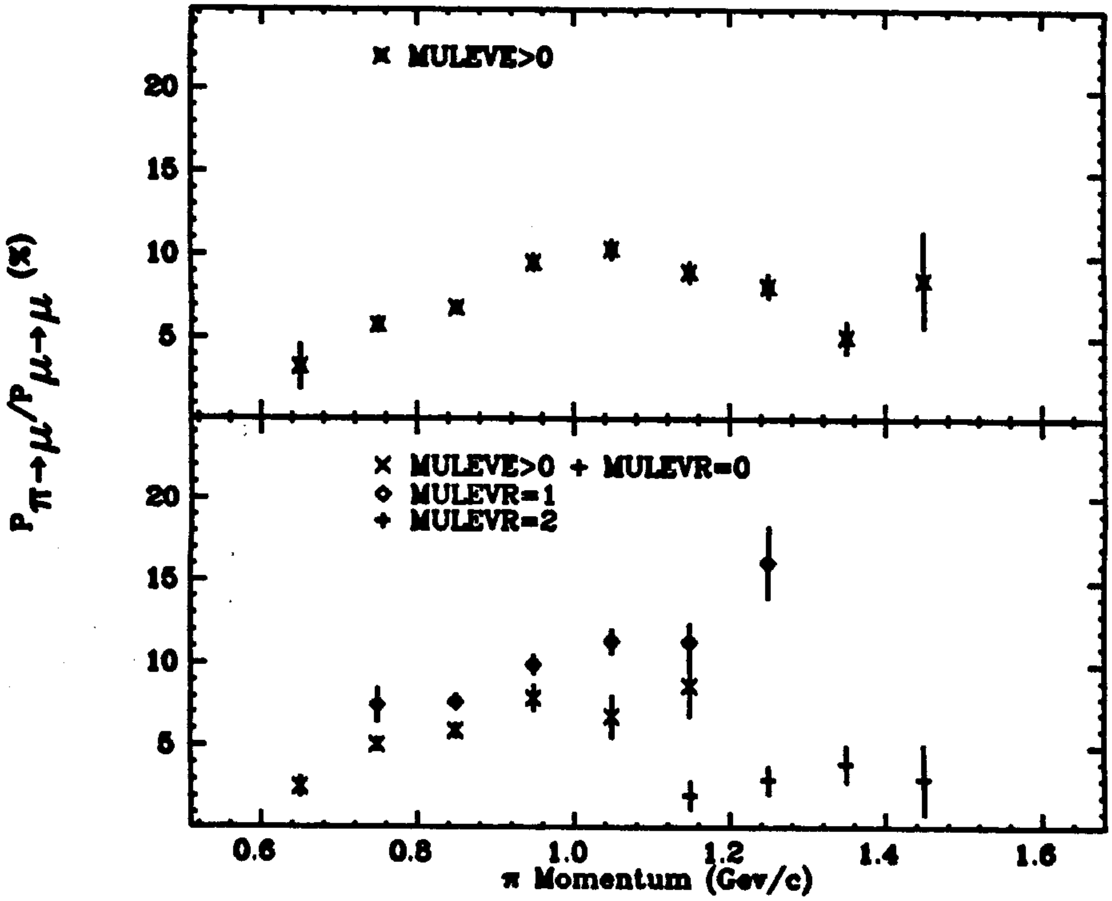

Figure 3.10. Probability that a pion is misidentified as a muon divided by the muon identification efficiency for several status classes.

MULEVR>1 could be used. To insure the cleanest separation of pions from a muon background, the class MULEVR>1 should be used with the requirement that no signals are present within the tracking region in any muon plane.

Chapter 4

Measurement of the Tau Production Cross Section

4.1 INTRODUCTION:

Tau production in e+e- annhilation was first observed using e-μ events from the reaction listed in (1).

$$\begin{array}{lll} e^+e^- \dashrightarrow & \tau^{+(-)} & + \quad \tau^{-(+)} \\ & | & \quad \llcorner\dashrightarrow e^{-(+)}\nu\nu \\ & \llcorner\dashrightarrow \mu^{+(-)}\nu\nu & \end{array} \qquad (1)$$

Because there is little background from other sources, these events provide a clean signature through which to study tau production. This chapter reports on an analysis of the e-μ events measured with the MARK II at SPEAR. Assuming the tau obeys the point pair production cross section given in equation (2),

$$\sigma_0 = 4\pi\alpha^2\beta(3-\beta^2)/(6S) \qquad (2)$$

the measurements can be used to determine the branching ratio product B_eB_μ as shown in (3)

$$N_{e\mu} = 2B_eB_\mu\sum_E L(E)\sigma(E)A(E) \qquad (3)$$

where $N_{e\mu}$ is the number of observed e-μ events, A is the detector acceptance, L is the integrated luminosity, and where the sum runs over the center of mass energies spanned by the data. Conversely, the tau production cross section can be measured and compared to the point cross section by assuming theoretical values for B_e and $B\mu$.

All data collected during the fall of 1978 and spring of 1979 which had good shower counter information are used in this analysis, except for the fixed energy runs at the $\Psi(3095)$ and $\Psi'(3684)$. Equation (2) and the measured luminosity can be used to calculate the number of produced tau pairs. Figure 4.1 plots the number of produced pairs as a function of center of mass energy. For the cross section analysis, the data is binned in energy to give roughly equal numbers of produced taus. Table 4.1 lists the integrated luminosity and number of produced tau pairs for each energy interval. The systematic error in the luminosity is estimated to be 6%.

TABLE 4.1

Tau pair production vs. center of mass energy.

Interval (Gev)	Integrated Luminosity (nb)	#Produced Pairs
3.85-4.25	2129	7348
4.25-4.65	1788	6248
4.65-5.05	1866	6006
5.05-5.45	6176	18136
5.45-6.35	1221	2922
6.35-6.85	3783	7448
Total:	16963	48108

4.2 EVENT SELECTION:

We begin by selecting all two prong, total charge zero events in the data sample. A minimum charged track acoplanarity cut of 5 degrees is applied to eliminate bhabha and muon pair events, and most events from two photon processes. A maximum acoplanarity cut of 175 degrees is imposed to eliminate converted photons. Each charged track is required

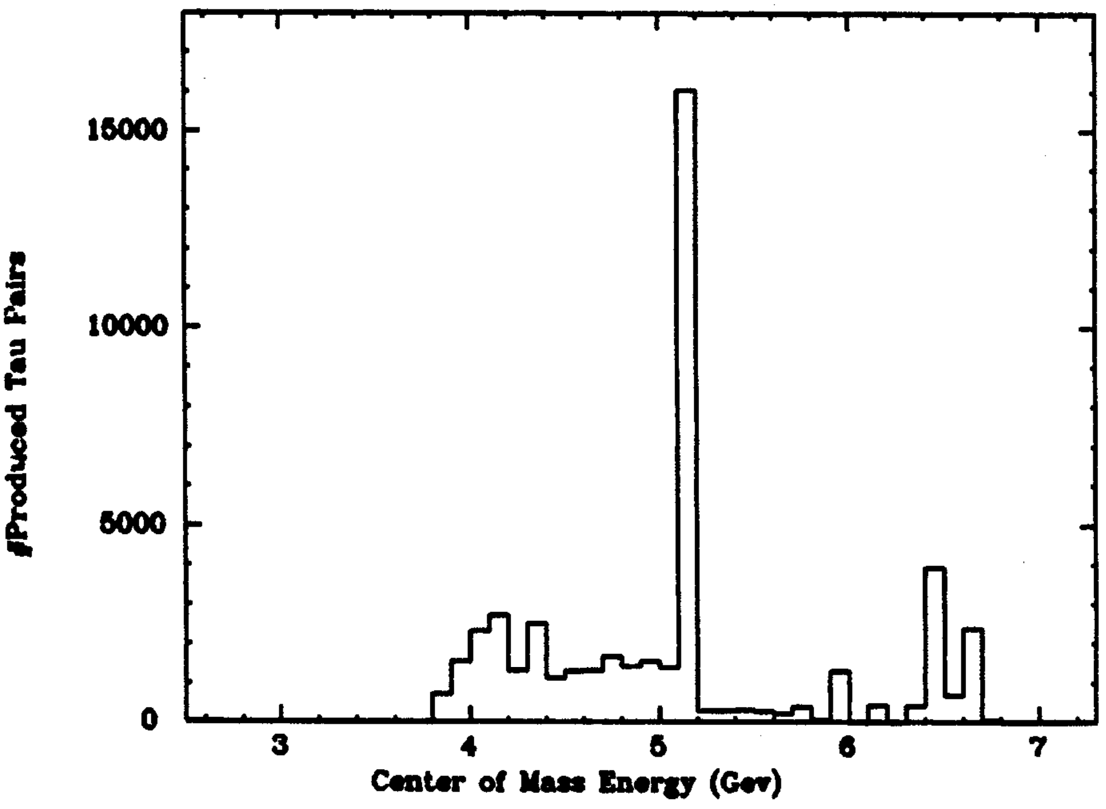

Figure 4.1. Number of produced tau pairs as a function of the center of mass energy.

to originate near the interaction region, and have a Chi-square/DOF from the track fit no larger than 16. The interaction point determined by the vertex of the two charged tracks must be no farther from the center of the interaction region than 4 cm in radial projection and 8 cm along the beam direction. All tracks are required to enter the shower counter fiducial volume as discussed in Chapter 2. Tracks with momentum less than 1.3 Gev/c that have good time of flight information are required to have a TOF less than 1.5 ns (5 sigma) from that predicted assuming it is an electron or muon. Events with barrel module photons with energy greater than 250 Mev and which have an opening angle with both charged tracks larger than 9.6 degrees are rejected. Measurements with muon-pair events indicate that 1.6% of real e-μ events will fail this photon cut due to spurious noise photons in the barrel modules.

4.3 PARTICLE IDENTIFICATION:

Misidentification of non-eμ events is the only large background in the e-μ signal. To determine this background, all events which satisfy the topology cuts are collected. Using the known misidentification probabilities, the data is inverted to determine the number of produced events in each identification catagory (ee,eμ,eπ, etc.). This can then be used to calculate the misidentification background in the measured e-μ candidates. In the analysis, it is assumed that all candidate tracks are either electrons, muons, or pions. This is a good assumption since most of the hadrons in the selected sample are the products of tau decays.

The method used to determine a particles' ID depends on its momentum. Below 300 Mev/c, the time-of-flight information is used. The relative probability that the measured TOF is consistent with an electron hypothesis or pion hypothesis is calculated and used to form the electron-pion weight (WTEPI) given in (4).

$$\mathrm{WTEPI} \equiv P(e)/(P(\pi)+P(e)) \tag{4}$$

Particles are identified as electrons if WTEPI>.80, or as pions if WTEPI<.40; otherwise, they are called ambiguous. Figure 4.2a shows the electron and pion identification and misidentification efficiencies as a function of particle momentum. These values were calculated with the monte carlo assuming a .3 ns TOF resolution.

Because the TOF system is not useful in separating muons from pions or electrons, no attempt is made to do so. Instead, we reclassify pions and muons together as non-electrons and accept a large misidentification probability for muons to be called electrons as shown in Figure 4.2b.

Above 300 Mev/c, the liquid argon counters become useful in separating electrons from muons and pions. However, pions and muons cannot be separated until the muon system momentum threshold is passed (700 Mev/c). Therefore, between 300 and 700 Mev/c, a track is identified as electron, not-electron, or ambiguous according to its shower counter identification (LAID) as discussed in chapter 2.

Above 700 Mev/c, particles are still called electrons if identified as such by LAID. If LAID is not-electron and the muon class is at least MULEVE>0, the particles are called muon or pion depending on the muon system identification (MUID) as discussed in chapter 3. If LAID is not-electron and MULEVE=0, the track is not considered to be in the fiducial volume. All other combinations of LAID and MUID are labeled ambiguous.

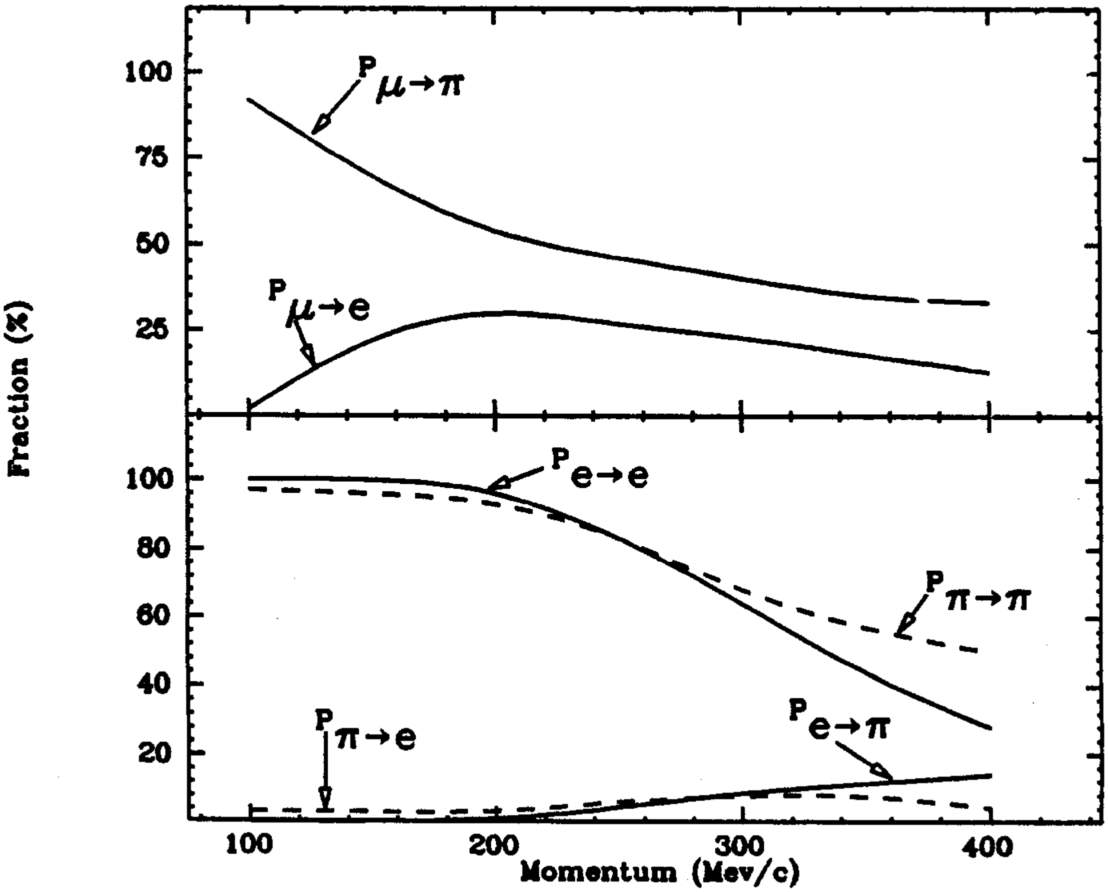

Figure 4.2. TOF identification and misidentification probabilities as a function of momentum: (a) for pions and electrons; (b) for muons.

The particle identification and misidentification efficiencies are shown in Figures 4.3a, b, and c. The muon data is derived from a combination of monte carlo calculations and measurements. The muon system detection efficiency measured with muons from muon-pair events, and the shower counter response determined with low momentum muons from cosmic rays, provide input to the monte carlo. Electrons from converted gammas and specially selected bhabha events are used as electron candidates, while pion candidates from reconstructed $K^0{}_{short}$ decays and multiprong Ψ events are used to determine the pion efficiencies. The electron sample is selected so as to approximate a uniform angular distribution within the solid angle of the shower counters. Systematic errors are estimated to be 10 percent and include effects from sample contamination, long term variations in detector response, and non-isotropy in the candidate and data sample.

Events with neither track above the muon momentum threshold cannot possibly be identified as e-μ events and are discarded. If both tracks are above 700 Mev/c, the event can be classified as ee, eμ, eπ, μμ, μπ, ππ, or ambiguous, while if one track is below the threshold, the classifications are ee, eμ, eπ, not-e/e, not-e/μ, not-e/π or ambiguous. In the following discusssions, these types will be referred to as class A and class B events respectively.

4.4 SPECIAL BACKGROUNDS:

To minimize the effect on the inversion procedure of errors in the particle identification and misidentification efficiencies, two cuts are employed to reduce the large number of ee and μμ events arising from

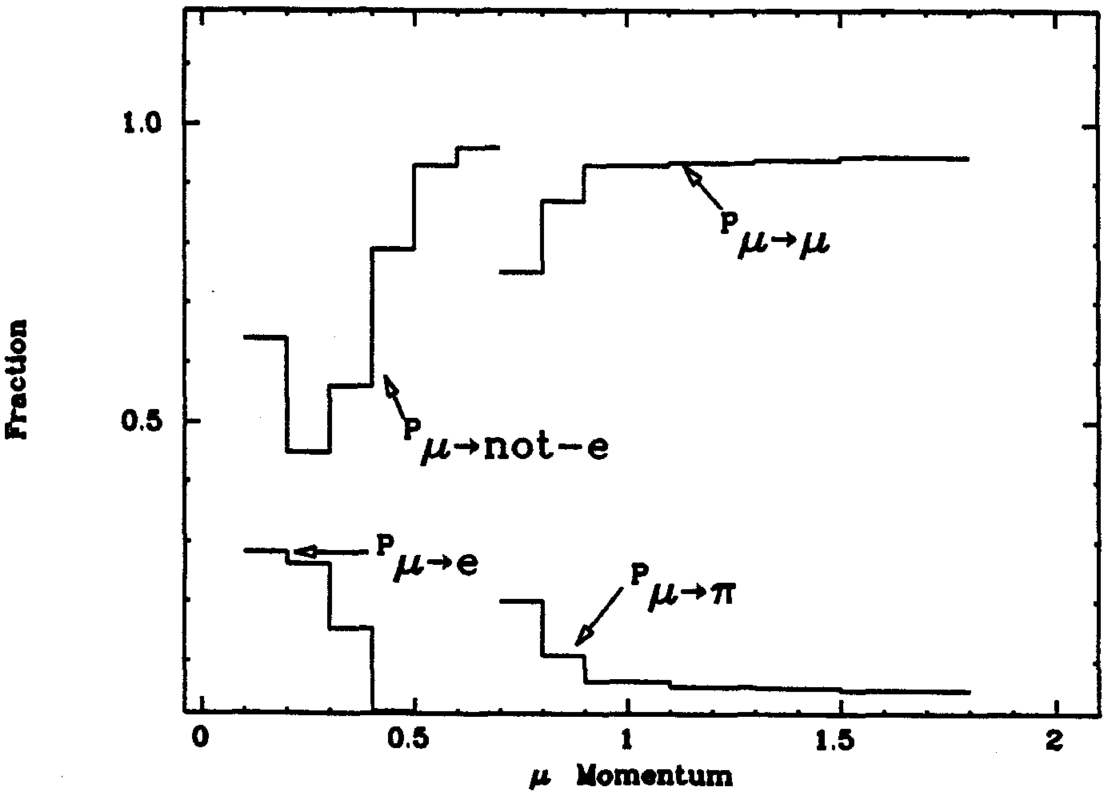

Figure 4.3a. Muon identification and mis-identification probabilities as a function of momentum.

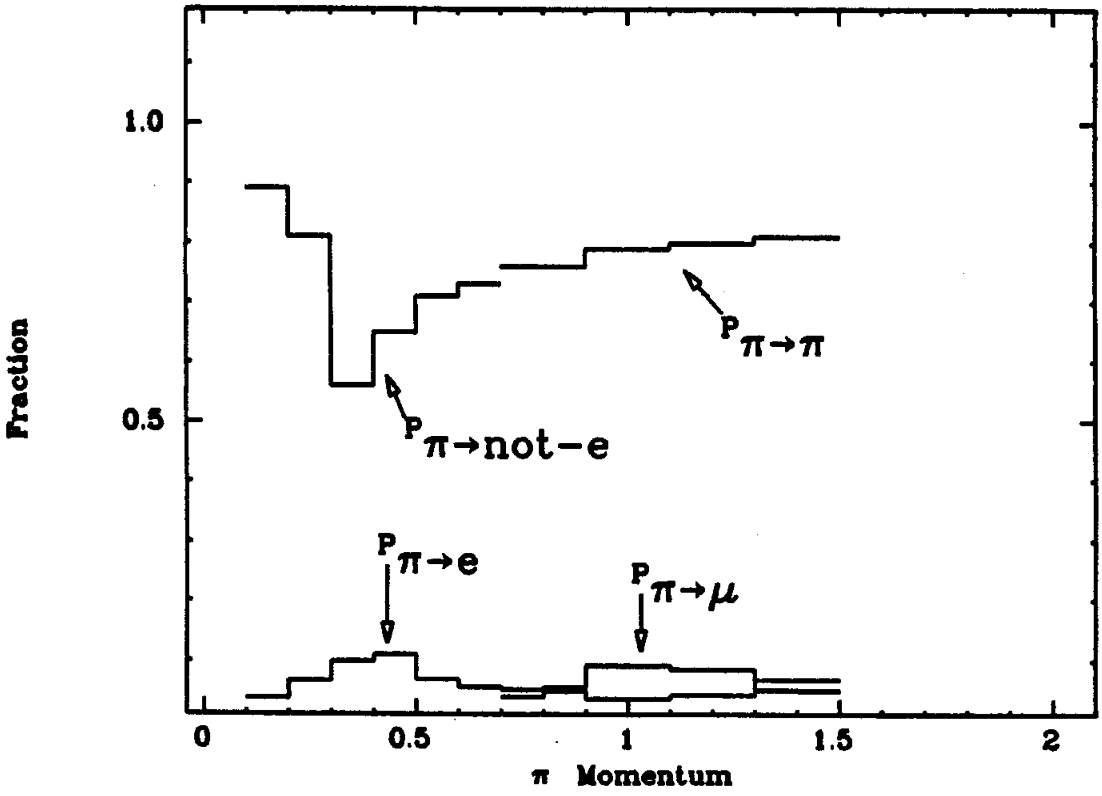

Figure 4.3b. Pion identification and mis-identification probabilities as a function of momentum.

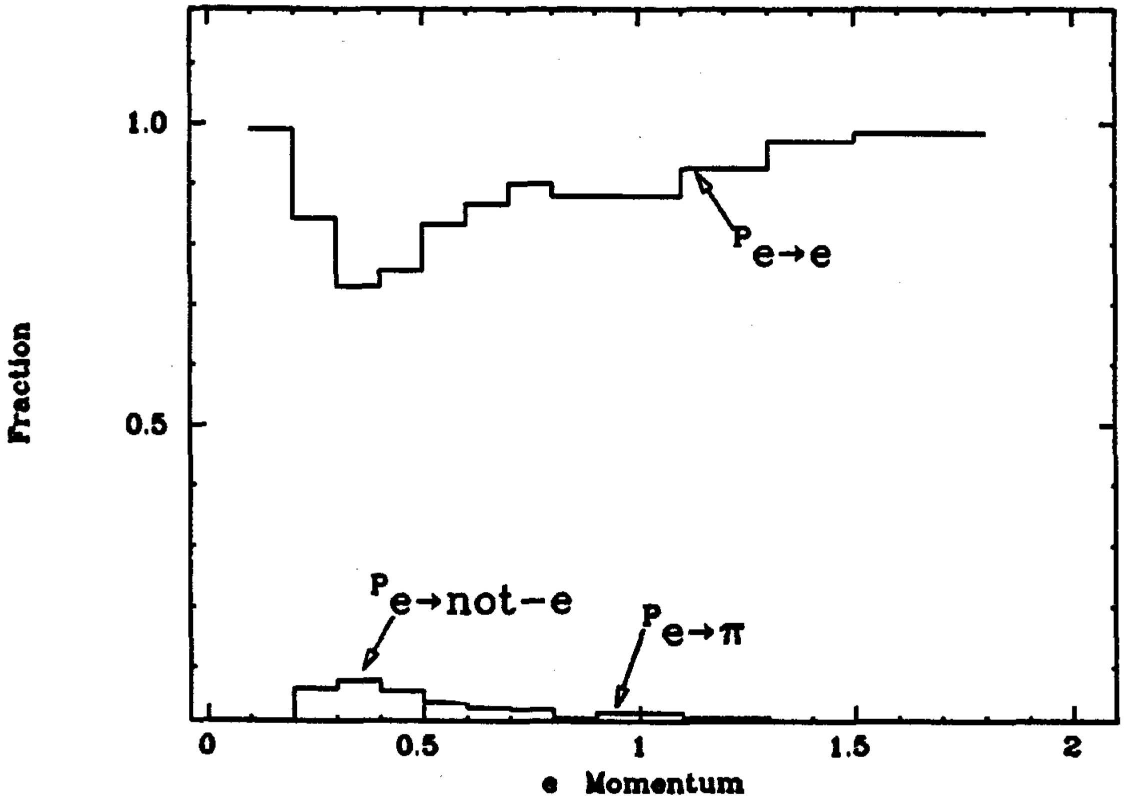

Figure 4.3c. Electron identification and mis-identification probabilities as a function of momentum.

purely electromagnetic processes. Electron pair and muon pair events which have experienced initial or final state radiation can be discriminated against by applying a cut on the invariant mass recoiling from the charged tracks. Figure 4.4 plots the squared recoiling mass distribution from ee and $\mu\mu$ events. By requiring the recoiling mass to be larger than 1 Gev/c^2, a large fraction of the events can be eliminated at a cost of no more than 1% in the e-μ acceptance.

Bhabha events where one electron has suffered a large bremstrahlung emission in the pipe counter, can survive the acoplanarity cut because the low momentum track has been incorrectly projected to the interaction region. These events constitute roughly 20% of the ee events, and are removed by retracking the low momentum track back out to the pipe counter and reapplying the acoplanarity cut.

4.5 RAW DATA:

Table 4.2 lists the number of class A and class B events which survive the analysis cuts. There are 227 class A and 227 class B e-μ events. Figure 4.5 shows the electron and muon momentum distributions for these events.

4.6 MISIDENTIFICATION BACKGROUND:

The unfold procedure is straightforward and unambiguous for class A events. Let M(i,j;p1,p2) represent the number of measured events of type ij (i,j = e,μ,π), with particle i having momentum p1 and particle j having momentum p2, and let R(i,j;p1,p2) be the number of

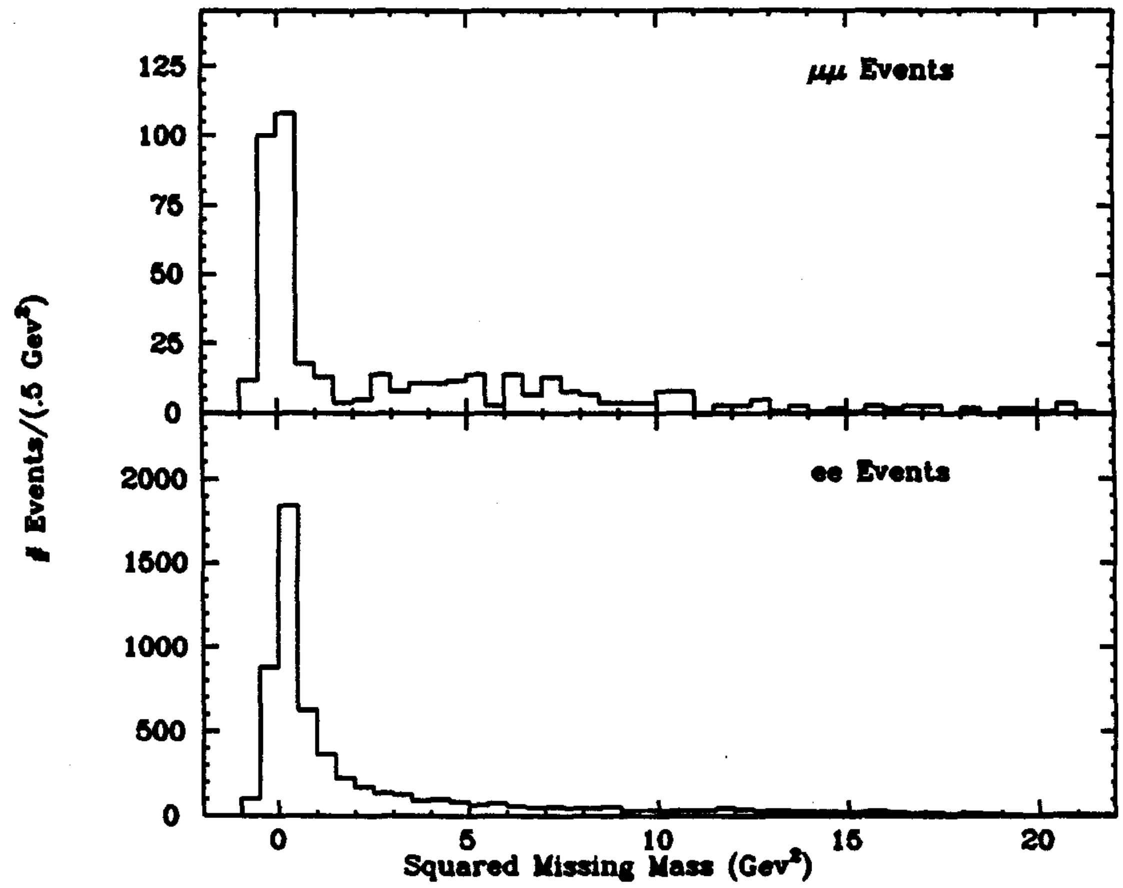

Figure 4.4. Squared invariant mass recoiling against the two charged tracks in ee and $\mu\mu$ events.

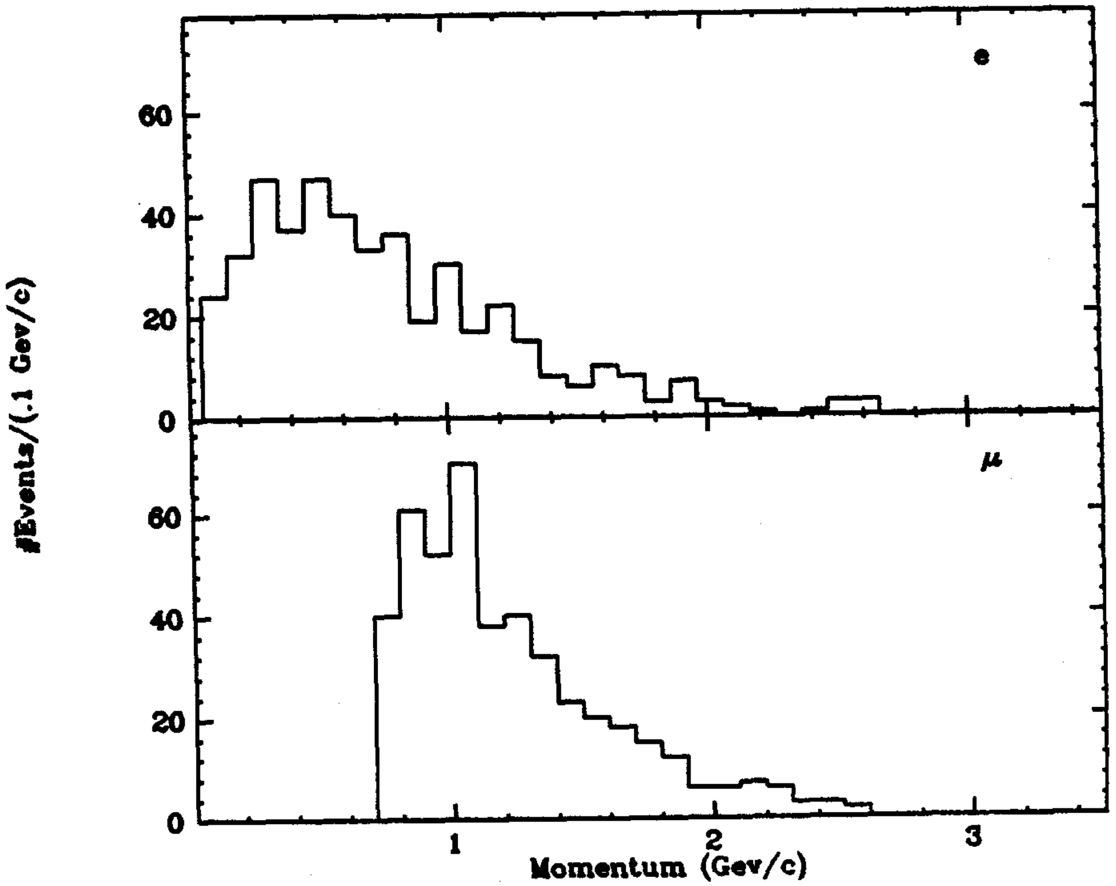

Figure 4.5. Measured momentum distribution for electrons and muons in e-μ events. No background subtractions have been made.

TABLE 4.2

Number of events by ID surviving
topology and background cuts.
n signifies non-electron.

Class A		Class B	
Type	Number	Type	Number
ee	1485	ee	969
eμ	227	eμ	227
eπ	304	eπ	283
μμ	221	ne	352
μπ	295	nμ	391
ππ	210	nπ	616
Ambiguous	269	Ambiguous	754
Total	3011		3592

real events. Measured events with an ambiguous ID are ignored; they represent an inefficiency in the measurement process. If P(i,j;p1) is the probability that a particle of type i, with momentum p1, is called type j, then M and R are related by

$$M(i,j;p1,p2) = \sum_{k,l} R(k,l;p1,p2)P(k,i;p1)P(l,j;p2) \qquad (5)$$

Equation (5) can be solved to determined R(k,l;p1,p2).

This procedure is implemented by collecting the measured events in an array by type and momentum (100 Mev/c bins). The misidentification matrices are inverted, and the number of real events by type and momentum is determined. R(i,j;p1,p2) is then summed over the two momentum indices to determine the total number of real events. Table 4.3 lists the number of measured and real class A events in vector form along with the momentum averaged misidentification matrix that relates them. The fact that electrons are not misidentified as muons (and vice versa), insures that many off diagonal elements are zero. The errors are statistical only and do not include errors in the identification probabilities.

TABLE 4.3

The number of measured and real class A events, and the momentum averaged misidentification matrix.

Type	#Measured	Identification Matrix						#Real
(ee)	(1485±38.5)	(.892	.000	.054	.000	.000	.003)	(1645.8±43.4)
(eμ)	(227±15.1)	(.000	.840	.059	.000	.050	.007)	(228.0±18.3)
(eπ)	(304±17.4)	(.022	.069	.734	.000	.004	.091)	(306.9±24.1)
(μμ)	(221±14.9)	(.000	.000	.000	.827	.061	.004)	(243.2±18.4)
(μπ)	(295±17.2)	(.000	.016	.001	.148	.737	.103)	(306.2±24.3)
(ππ)	(210±14.5)	(.000	.001	.014	.007	.064	.641)	(286.5±23.2)

From Table 4.3, one can read off the misidentification background in the measured e-μ events. The largest contributions are from misidentified e-π and μ-π events that come from other tau decays. Adding all contributions yields a total misidentification background of 35.6±1.9 events. The systematic error depends on the errors in the identification efficiencies and is taken to be 25%. Thus, the corrected number of class A e-μ events is 191.4±15.1±9.1 where the errors are statistical and systematic respectively.

For class B events, an ambiguity enters the unfold procedure as the low momentum track is identified only as electron or not-electron, and it is impossible to determine the number of real electrons, muons, and pions given only this information. Since we only wish to know the number of low momentum tracks which are electrons, there would be no problem if muons and pions had the same identification and misidentifcation probabilities below 700 Mev/c. But they don't. To overcome this problem, one can assume a fixed ratio of muons to pions and check how the background subtraction depends on this assumption. Therefore, we assume real events come only in the flavors electron and not-electron below 700 Mev/c, and the 2X2 identification matrix P(i,j;p1) is determined by averaging the muon and pion identification probabilities according to the assumed muon/pion ratio. The analysis is now performed in exactly the same way as for class A events. Since the probability of misidentifying a muon as an electron is large below 400 Mev/c, and depends very strongly on the quality of the TOF data, class B events where the low momentum track is below 400 Mev/c are excluded from the remainder of this analysis.

Figure 4.6 plots the calculated background to the e-μ class B events as a function of the assumed muon fraction. It varies smoothly between 35 and 15 events as the fraction changes from 0 to 1. The muon/pion ratio for tracks above 700 Mev/c can be measured, and is approximately constant at a value of .6 between 700 and 1200 Mev/c. Therefore, we use the background value calculated for a muon fraction of .4, and give an extra systematic error of 5 events to account for this extrapolation. The resulting background subtraction is 26±1.5±8.2 events where the first error is statistical, and the second is systematic obtained by adding in quadrature the basic 25% systematic error from identification efficiency uncertainties with the systematic error from the extrapolation. The corrected number of class B e-μ events is 98.±11.7±8.2 where the errors are statistical and systematic respectively. Table 4.4 lists the number of measured and real events, and the momentum averaged misidentification matrix connecting them.

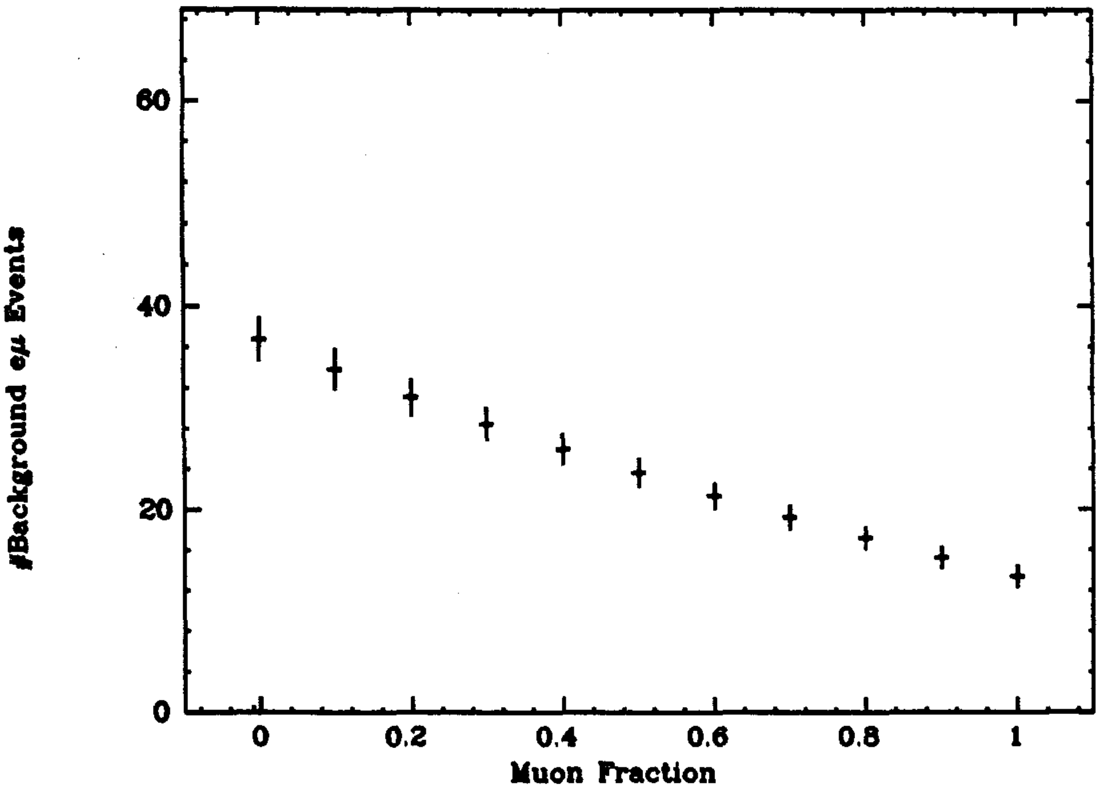

Figure 4.6. Calculated background to e-μ events with p_e<700 Mev/c as a function of assumed muon fraction.

TABLE 4.4

The number of measured and real class B events, and the momentum averaged misidentification matrix. n stands for non-electron.

Type	#Measured	Identification Matrix						#Real
(ee)	(468±521.6)	(.765	.000	.047	.045	.000	.003)	(585.1±528.6)
(eμ)	(124±511.6)	(.000	.742	.053	.000	.043	.003)	(132.2±515.5)
(eπ)	(162±512.7)	(.012	.073	.644	.001	.005	.040)	(184.3±520.3)
(ne)	(218±514.8)	(.041	.000	.003	.719	.000	.042)	(233.6±520.9)
(nμ)	(265±516.3)	(.000	.040	.003	.000	.692	.050)	(330.2±524.1)
(nπ)	(415±520.4)	(.001	.004	.038	.013	.079	.620)	(610.1±533.7)

To determine the background subtraction in the subset of events in a specific energy interval, the same background procedure is applied. Table 4.5 lists the number of detected e-μ events and the background subtraction by center of mass interval.

TABLE 4.5

The number of measured e-μ events and calculated backgrounds for specified center of mass energies.

Interval	Detected Events		Background Subtraction	
(Gev)	Class B	Class A	Class B	Class A
3.85-4.25	22±4.7	23±4.8	4.0±0.6±1.2	3.2±0.6±0.8
4.25-4.65	23±4.8	27±5.3	3.4±0.6±1.0	3.1±0.6±0.8
4.65-5.05	12±3.5	25±5.0	2.8±0.5±0.9	3.6±0.6±0.9
5.05-5.45	37±6.1	89±9.4	9.4±0.9±3.0	17.±1.3±4.1
5.45-6.35	7±2.6	12±3.4	1.7±0.4±0.7	2.6±0.5±0.6
6.35-6.86	23±4.8	51±7.1	4.6±0.6±1.2	6.5±0.8±1.6
Total	124±11.	227±15.	26.0±1.5±8.2	35.6±1.9±9.1

4.7 ACCEPTANCE:

The acceptance for detecting produced e-μ events has been determined using the full monte carlo simulation program. The muons system monte carlo simulation routines accurately calculate the muon identification efficiency, while the shower counter simulation uses a look up table of measured identification and misidentification efficiencies. Figure 4.7 plots the measured acceptance as a function of the center of mass energy. The energy dependence is mainly a function of the muon system momentum threshold.

4.8 RADIATIVE CORRECTIONS:

The actual tau production cross section (σ_{prod}) has contributions both from the lowest order expression given in equation (2) and from higher order terms. Because the lowest order expression accounts for nearly all the production and has such a simple form, it is customary to keep this expression for the cross section and multiply it by a small correction term (δ) to correct for the higher order contributions:

$$\sigma_{prod} = \sigma_0(1+\delta) \tag{6}$$

To calculate δ, we use the result of Bonneau and Martin[1] given in equation (9)

$$\delta = \frac{2\alpha}{\pi}\left\{\frac{\pi^2}{6}-\frac{17}{36}+(2\ln(2E/m_e)-1)\left[\frac{13}{12}+\int_0^E \frac{dk}{k}\left[(1-\frac{k}{E}+\frac{k^2}{2E^2})\frac{\sigma(S)\epsilon(S)}{\sigma(S_0)\epsilon(S_0)}-1\right]\right]\right\} \tag{9}$$

where the integral includes corrections for initial state radiation and runs over the phase space of the emitted photon. σ_0 is the point cross section, E is the beam energy, S and S_0 are the center of mass energy with and without radiation ($S=4E(E-k)$), and $\epsilon(S)$ and $\epsilon(S_0)$

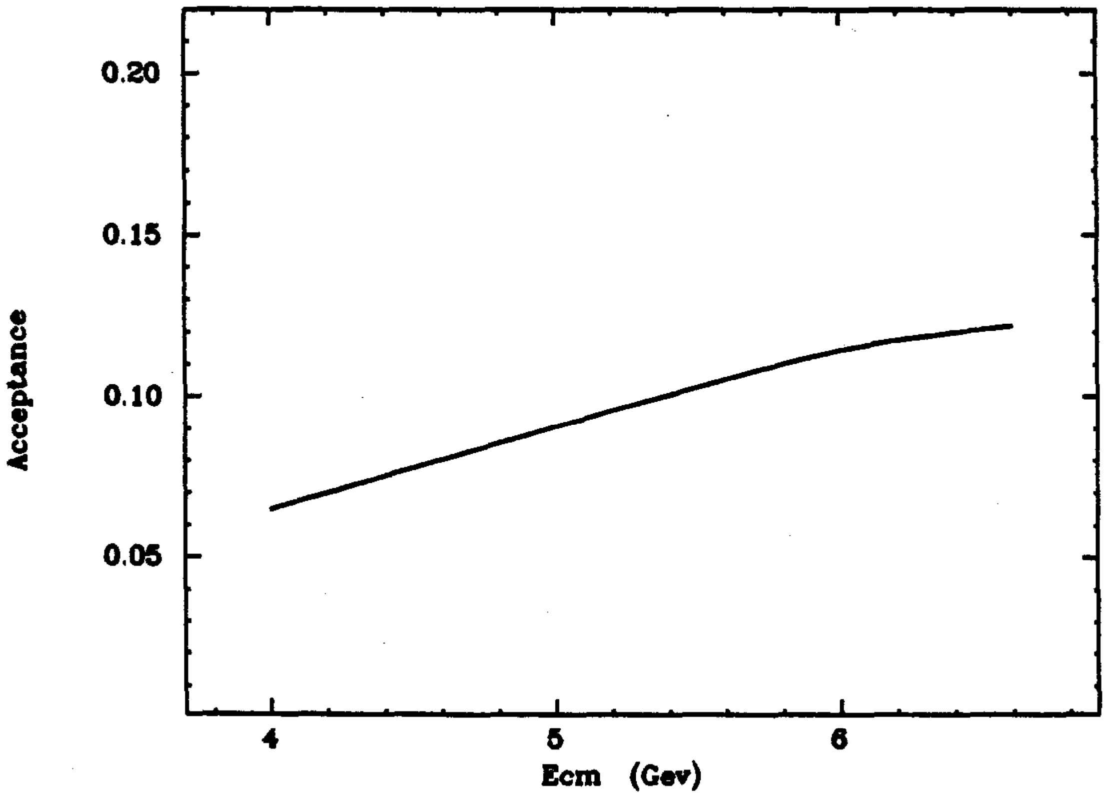

Figure 4.7. Detector acceptance for $\tau\tau$ --> $(e\nu\nu) + (\mu\nu\nu)$ as a function of the center of mass energy.

are the detection efficiency with and without radiation. The threshold in the tau production cross section cuts off the integral at a point $k_{kmx}=E(1-4m^2/S)$. The detection efficiency $\epsilon(S)$ was measured by generating monte carlo events which had photons emitted by either the electron or positron along the beam axis. Figure 4.8 plots $\epsilon(S)/\epsilon(S_0)$ as a function of k/k_{kmx} for several center of mass energies. The decrease in the detection efficiency for large k is mainly a function of the muon system momentum threshold. Linear interpolation between these values was performed to estimate the efficiency at intermeadiate energies. The resulting correction (δ) is nearly independent of the center of mass energy, ranging from 4.9% at 4.0 Gev to 5.6% at 6.6 Gev. This correction effectively increases the number of produced tau pairs over that calculated with the lowest order cross section.

4.9 DETERMINATION OF BRANCHING RATIO PRODUCT:

Assuming all produced e-μ events arise from tau decays, the branching ratio product $B_e B_\mu$ can be determined from equation (3). After applying radiative corrections, making background subtractions, and correcting for the 1.6% loss from spurious photons, the result is:

$$B_e B_\mu = .032 \pm 0.002 \pm 0.004 \qquad (10)$$

where the first error is statistical, and the second is systematic obtained by adding in quadrature the systematic errors in the background subtraction, 6% error for the integrated luminosity, and a 10% error in the calculated acceptance. Assuming the theoretical value for the ratio of the branching fractions, $B_\mu/B_e = .973$, the individual branching

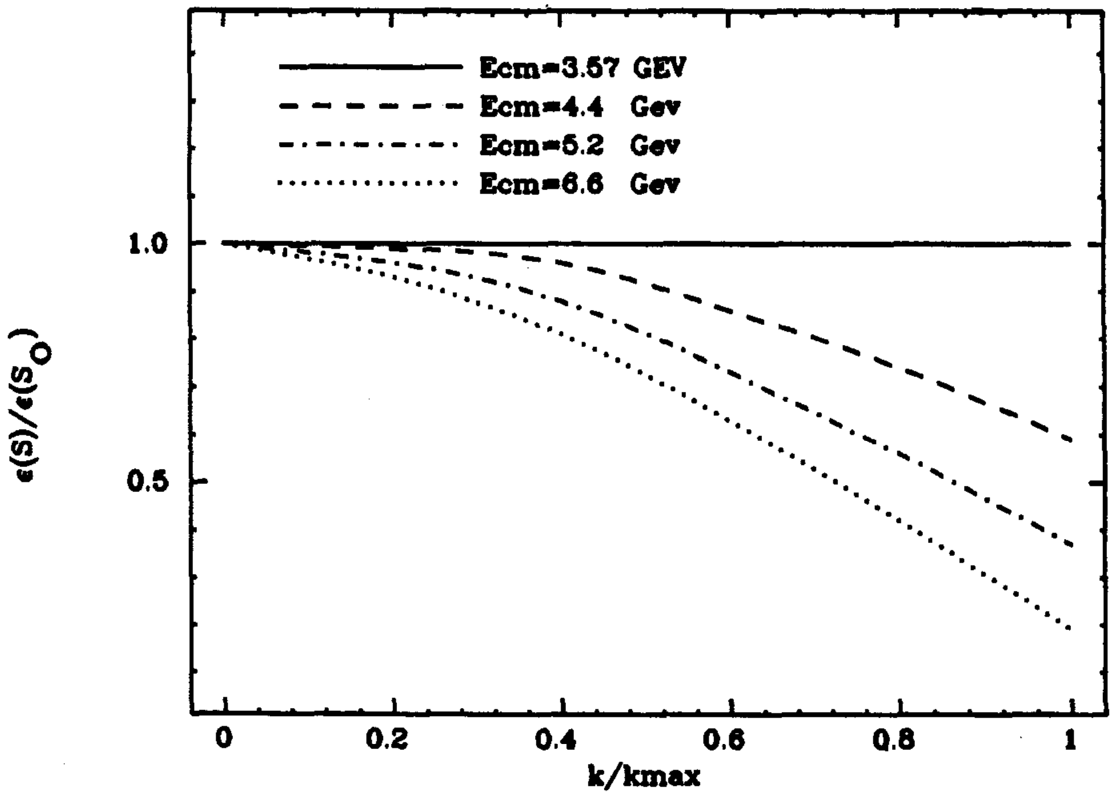

Figure 4.8. Relative detection efficiency for events with initial state radiation as a function of the radiated photon energy divided by the maximum allowed photon energy.

ratios are

$$B_e = .181 \pm 0.006 \pm .011 \qquad (11a)$$

$$B_\mu = .176 \pm 0.006 \pm .011 \qquad (11b)$$

Assuming the value for the branching ratio product given in (10), the shape of the measured cross section can be compared to the point cross section of equation (3). Figure 4.9 plots the ratio of the number of detected e-μ events (after background subtractions) to the number expected from equation (3) for the 6 center of mass energy intervals. Alternatively, if we assume the middle value in the range of theoretical predictions for the branching ratio product, B_eB_μ=.029, the data shown in Figure 4.10 result. The measured cross section is consistant with the spin 1/2 point cross section.

References:

1.) G. Bonneau and F. Martin, Nucl. Phys. B27:381 (1971).

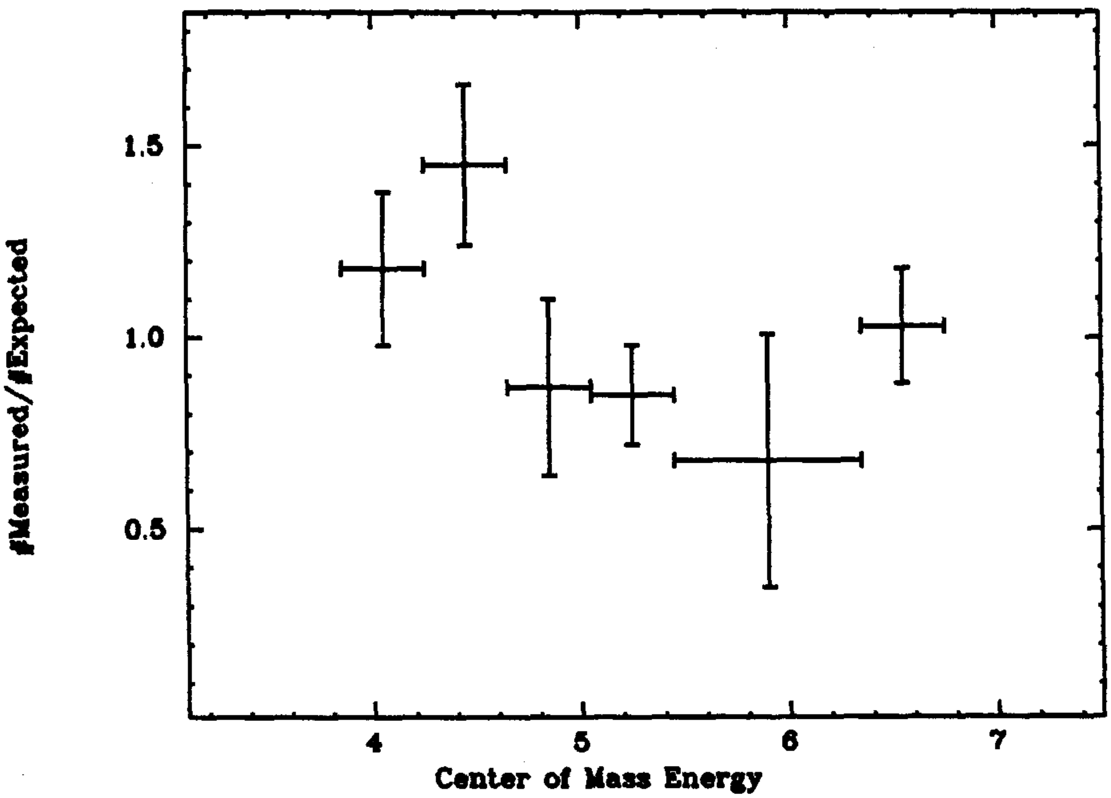

Figure 4.9. Ratio of the number of measured e-μ events to the expected number given the spin 1/2 point pair production cross section as a function of center of mass energy. The measured branching ratio product has been used to calculate the expected number of events.

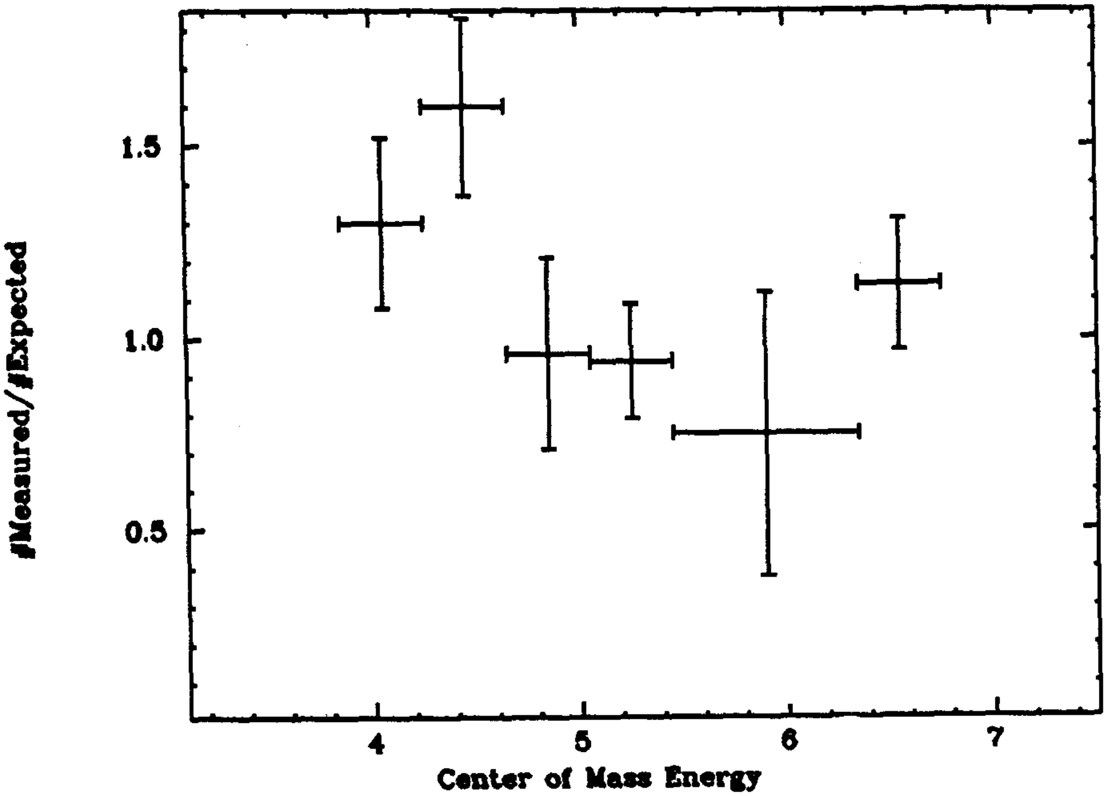

Figure 4.10. Ratio of the number of measured e-μ events to the expected number given the spin 1/2 point pair production cross section as a function of the center of mass energy. The theoretical calculation of the branching ratio product has been used to calculate the expected number of events.

Chapter 5

A Search for Radiative Tau Decays

5.1 INTRODUCTION:

The search for particles which undergo radiative transitions to one of the known leptons has been long and fruitless. In particular, the search for the electromagnetic decay of the muon (1) has been so

$$\mu \dashrightarrow e + \gamma \qquad (1)$$

refined that an upper limit of 1.1×10^{-10} has been set on the branching ratio for this process.[1] In this chapter, we present the analysis of a search for the radiative decays of the tau lepton (2).

$$\tau \dashrightarrow \mu + \gamma \qquad\qquad \tau \dashrightarrow e + \gamma \qquad (2)$$

As it requires little effort to enlarge the scope of the search to all states whose mass is within the limits determined by the center of mass energy, we will include the results of the general search herein and will refer to such states as "excited leptons". We will assume the excited leptons are pair produced (3) so that each lepton is generated

$$e^+e^- \dashrightarrow L^{*+} + L^{*-} \qquad (3)$$

with the beam energy. The discussion will focus on the radiative decays of the tau but will expand to include the general case of pair produced excited leptons where necessary.

The method of analysis will be to search for structure in the invariant mass plot of all lepton-photon combinations which satisfy certain background removing cuts detailed in the text. The data sample covers the center of mass energy range from 3.9 to 6.7 Gev with an integrated luminosity (see Figure 5.1) of 17,000 inverse nanobarns and contains 48,000 produced tau pairs.

5.2 EVENT TOPOLOGY:

Experimental studies of the tau have verified that its major decay modes are those predicted by standard weak interaction theory,[2] and have determined an upper limit near the 1% level for either radiative decay branching fraction. Therefore, we will search for radiative tau decays assuming the other tau from the produced pair decays via a standard channel. Because more than 70% of all standard mode decays have only 1 charged particle in the decay products, the event topology we use in the search are 2 prong, total charge zero events with 1 or more photons (4).

$$e^+e^- \dashrightarrow l^{+(-)} + X^{-(+)} + \gamma + (\geq 0 \text{ neutrals}) \qquad (4)$$

To reduce the contamination from beam-pipe or beam-gas events, the reconstructed vertex of the two charged prongs must lie within a cylinder 16 cm long with a 4 cm radius centered around the interaction region. To eliminate mis-measured tracks, the vertex finding algorithm must use both tracks, and the chi-square from the vertex fit must be less than 100. A minimum momentum cut of 100 Mev/c is applied to the charged tracks to insure a well defined cutoff in the detectors response to low momentum tracks.

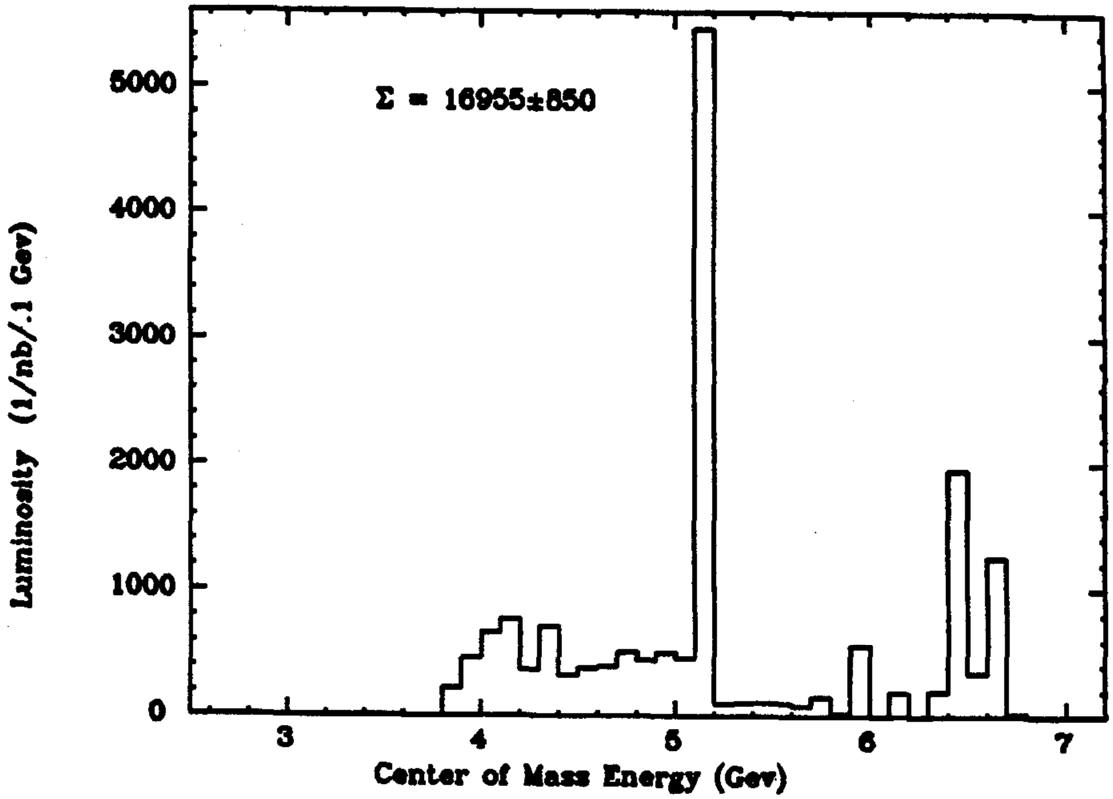

Figure 5.1. Integrated luminosity as a function of center of mass energy.

5.3 DECAY KINEMATICS AND RESOLUTION:

The kinematics of a two body decay are extremely simple. In the tau's rest frame, the decay products recoil with fixed momenta, and if we ignore any alignment of the tau, the fixed energies yield a uniformly populated distribution in the lab with limits given by equation (5).

$$E(\gamma)^{max}_{min} = .5E_{beam}(1 \pm \beta_{tau})(1-(m_l/m_{tau})^2) \qquad (5a)$$

$$E(lepton)^{max}_{min} = E(\gamma)^{max}_{min} + E_{beam}(m_l/m_{tau})^2 \qquad (5b)$$

The invariant mass of the photon-lepton system is calculated using the energy of the photon and lepton, and the angle between them as given by equation (6).

$$m = [m_l^2 + 2E(\gamma)(E_l - P_l\cos\theta)]^{1/2} \qquad (6)$$

The resolution in this measurement is dominated by the photon energy resolution and is on the order of 100 Mev/c^2. Since the tau is pair produced, the sum of the energies of its decay products equals the beam energy, and this constraint can be used to improve the resolution of the invariant mass measurement.

The proper realization of the beam constraint adjusts both the measured photon and lepton energies depending on their relative measurement errors, but in practice is nearly identical to the straight replacement of the photon energy with $E_p(\gamma)=E_{beam}-E(lepton)$. In this case, the contribution to the invariant mass resolution from measurement errors in the lepton momentum is given by (ignoring secondary lepton masses) Equation (7).

$$\begin{aligned} \Delta m &= .5m_{tau}[1/E_l - 1/(E_{beam}-E_l)]\Delta E_l \\ \Delta E_l &= .01E_l\sqrt{1.5^2+E_l^2} \end{aligned} \qquad (7)$$

The error becomes large when the lepton energy approaches the beam energy as can be seen in Figure 5.2. Here we show the mass resolution as a function of $x = E(\text{lepton})/E_{beam}$ for three beam energies. If the correct constraint procedure is applied, the resolution levels off as x approaches 1 at a value reflecting the photon energy resolution, but it is so poor that this kinematical region is useless. Consequently, lepton-gamma combinations where x is larger than .77 are rejected.

In the allowed x region, the error in the predicted photon energy is small relative to the error in the photon energy measurement. Therefore, a cut on the chi-square of the 1 constraint fit is equivalent to a cut on the photon energy resolution D

$$D = |E_p - E_m|/E_p \tag{8}$$

where E_p and E_m are the predicted and measured photon energy. To a good approximation this variable is normally distributed with a sigma of $.13/\sqrt{E_p(\text{Gev})}$. In Figure 5.3a, we show the measured distribution in $Z=D\sqrt{E_p}$ for all muon-photon candidates satisfying the above cuts along with a distribution calculated with the Monte Carlo. The signal to noise ratio improves if a cut is made at a low value of Z but at the cost of decreased acceptance. To balance these two factors, we chose to use only those photons which have Z less than .20. Note that at this stage, any signal is masked by the large background.

The same distribution is shown in Figure 5.3b for all electron-photon candidates. Bhabha events where one electron radiates a hard photon in the material preceding the drift chamber satisfy the beam constraint and constitute most of the signal that is observed.

The requirement that $E(\text{lepton})/E_{beam} < .77$ is equivalent to a cut on the predicted photon energy: $E_p(\gamma) > .23 * E_{beam}$.

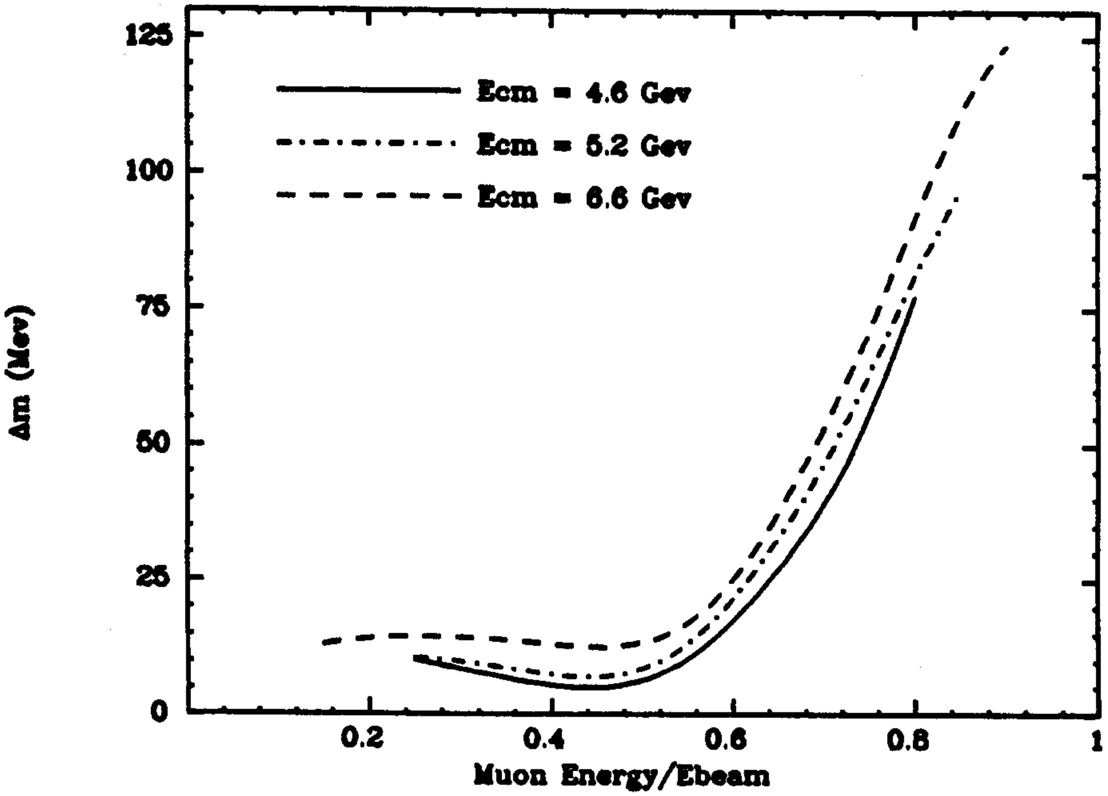

Figure 5.2. μ-γ beam constrained mass resolution as a function of E(muon)/E(beam) for several ECM values.

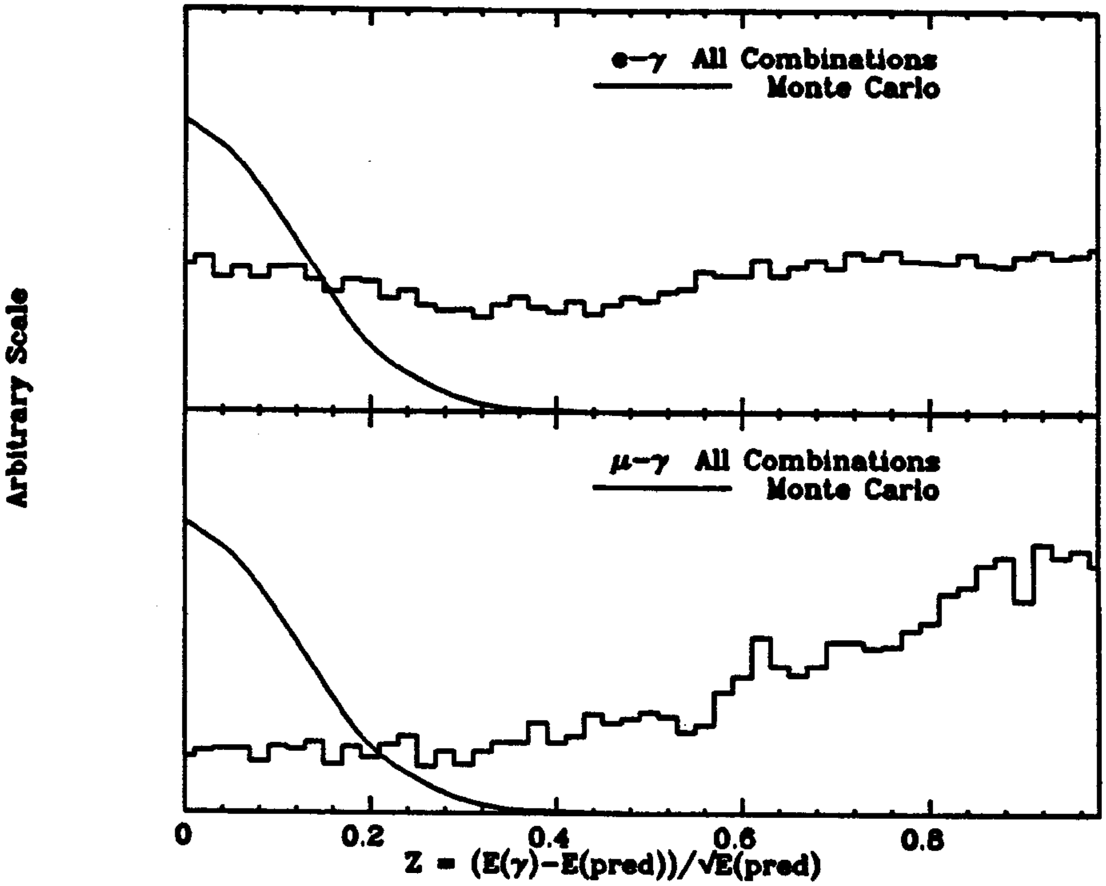

Figure 5.3. Photon Z distribution for tau-->lepton+photon candidates. The curve shows the monte carlo calculation.

In conjunction with the photon energy resolution cut, these cuts greatly reduce the random background from noise photons in the liquid argon modules.

5.4 ACCEPTANCE:

We will now address the issue of the MARK II's acceptance for detecting both decay products from the radiative tau decay. Although the proper analysis requires the full Monte Carlo simulation, a simple discussion will reveal the essential factors.

First, there is roughly a factor of .75 to account for the normal tau decay to one charged particle. Assuming no correlation between the charged tracks from the two tau decays, the drift chamber solid angle limits ($.80*4\pi$) adds a factor of .64. Restricting ourselves to the μ-γ decay, the muon system solid angle adds a factor (.50/.80) while its low momentum cutoff adds a factor which depends on the center of mass energy. Considering the case ECM=5.2 Gev, we can estimate this factor to be $(.700-E_\mu^{min})/(E_\mu^{max}-E_\mu^{min})=.82$. An addition factor of .88 arises from the cut on E(lepton)/E_{beam}.

At threshold, the tau is produced at rest, and the muon and photon recoil in opposite directions. Given that we identify the muon, the photon will be within the shower counter solid angle (except for the cracks between the modules). As the beam energy increases, the opening angle between the muon and photon decreases. For ECM=5.2 Gev, the minimum opening angle is near 90 degrees and the average is not much greater (see Figure 5.4). Therefore, requiring the photon to impact a barrel module adds a factor which is approximately the fraction of the

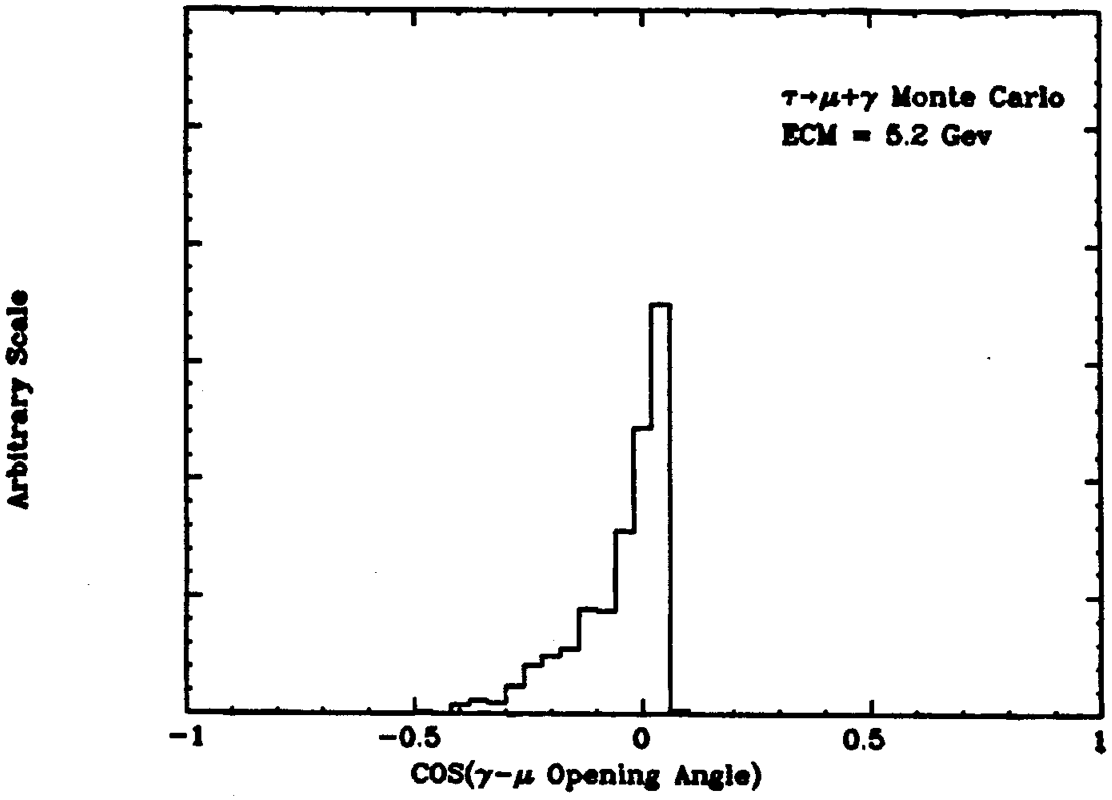

Figure 5.4. Cosine of the muon-photon opening angle for $\tau \dashrightarrow \mu + \gamma$ with ECM=5.2 Gev.

polar angle intercepted by the shower counters (i.e., .60). The detection efficiency is nearly 100% for these photons, and approximately 88% survive the resolution cut ($Z < .20$).

Putting all the factors together yields a 11% acceptance for detecting the radiative decay $\tau \rightarrow \mu + \gamma$ at 5.2 Gev. In Figures 5.5 and 5.6 we plot, as a function of center of mass energy, the acceptance calculated with the Monte Carlo to detect the muon and electron radiative decays given the cuts specified above. The acceptance is largest near the tau production threshold (15% for electron case) and steadily decreases as the center of mass energy is increased.

5.5 BACKGROUNDS:

If we now examine the measured lepton-gamma invariant mass distribution, we discover a large background which greatly impairs the sensitivity of the search. Figure 5.7 shows the invariant mass spectrum obtained using the entire data sample with the addition of a 5 degree acoplanarity cut applied to the charged tracks. This cut is necessary as the background from purely electromagnetic processes (e.g. $e^+e^- \rightarrow e^+e^-$ or $e^+e^- + \gamma$) becomes extremely large as the acoplanarity approaches zero. For example, the acoplanarity distribution (after the cut at 5 degrees) for all 2 prong, total charge zero events with at least 1 photon and 1 lepton (with $E(\text{lepton})/E_{\text{beam}} < .77$) is shown in Figure 5.8a (b) for electron (muon) events. Note there is a small signal from converted photons which can be removed by requiring the coplanarity to be less than 175 degrees.

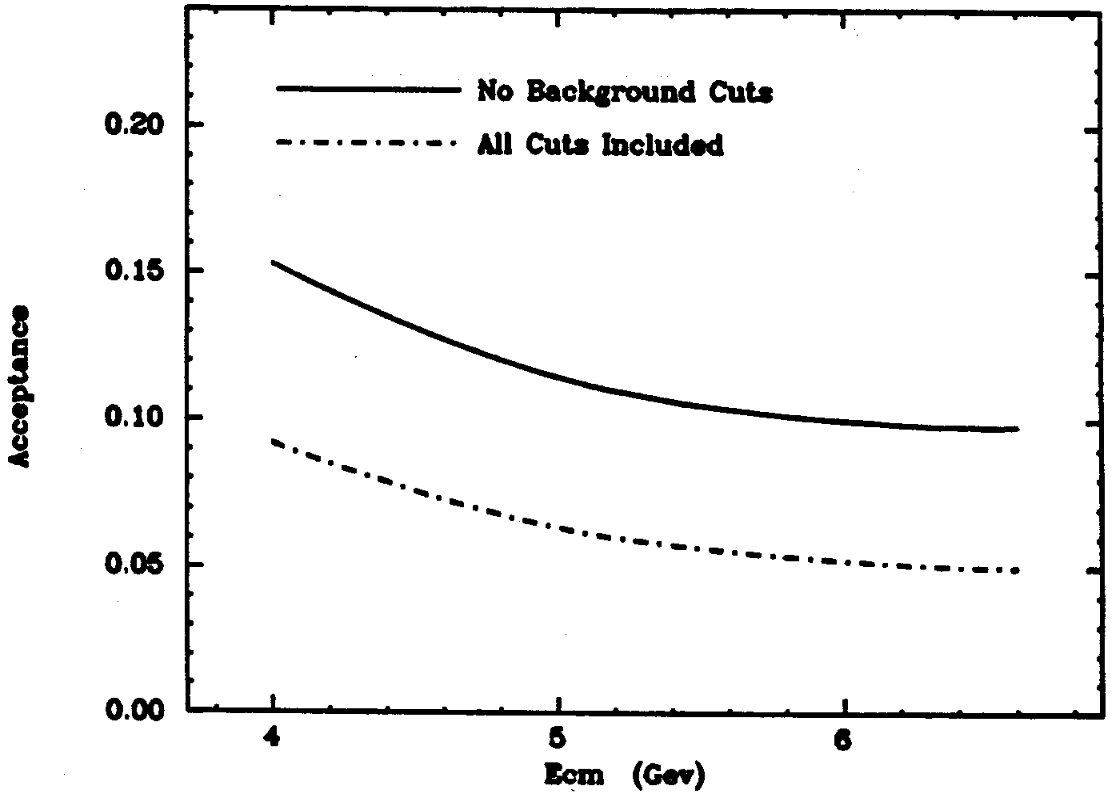

Figure 5.5. Υ -->$a\gamma$ acceptance as a function of center of mass energy. The acceptance is shown with and without the imposition of background cuts described in the text.

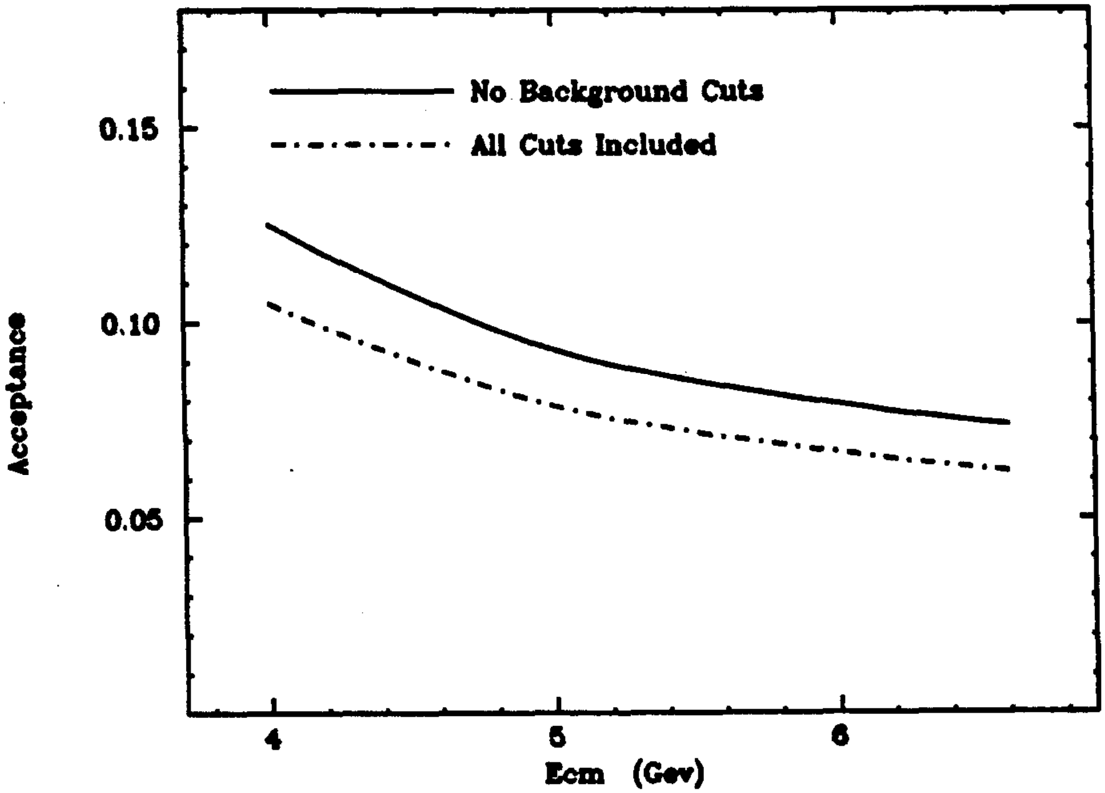

Figure 5.6. $\Upsilon \rightarrow \mu\gamma$ acceptance as a function of center of mass energy. The acceptance is shown with and without the imposition of background cuts described in the text.

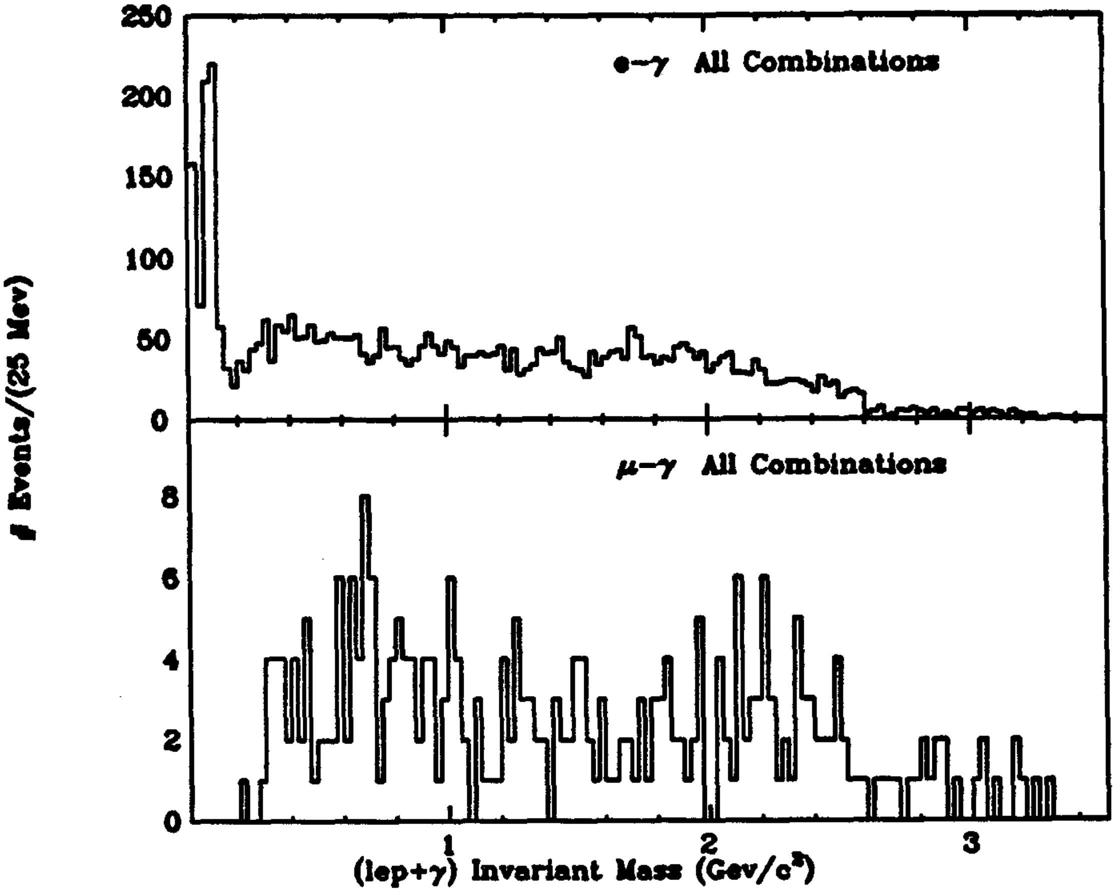

Figure 5.7. Measured lepton-photon beam constrained invariant mass with no background cuts applied.

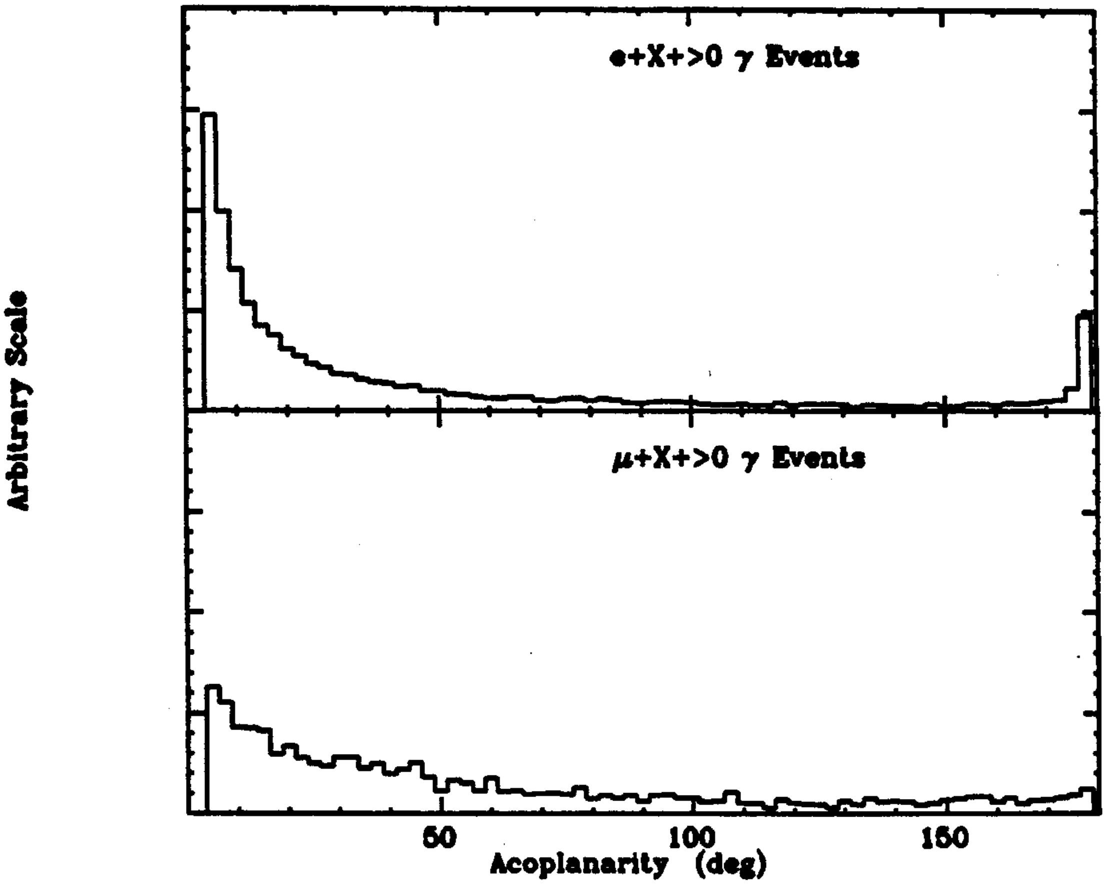

Figure 5.8. Charged track acoplanarity distribution for events with at least one lepton (E(lepton)/E(beam) < .77) and one photon.

Other cuts can be applied to reduce the background that arises from several known sources. As purely electromagnetic events form the largest contribution, we will first discuss a series of cuts designed to reduce this background.

Electron pair, photon pair, and muon pair events dominate electromagnetic processes at these energies. Processes which have 3 particles in the final state also have significant cross sections and provide a large background to our search for radiative tau decays. To define these events, the total 4 momenta of the two charged tracks and candidate photon is required to be consistent with the initial e+e- state. If this consistency condition is tested by simply adding the measured 4 momenta of the 3 particles, the poor photon energy resolution allows only a weak test to be performed. The optimal solution is to use a kinematic fitting program that takes all measurement errors into account (ie, SQUAW), to determine the probability that the constraints are satisfied, and then to make a decision based on this probability. This approach yields the best mass resolutions, but a simpler algorithm is used here.

The simple 4-momentum test can be rendered much more sensitive if the measured photon energy is not used (ie, one constraint is used to eliminate the photon energy). The following algorithm is based on this idea:

1.) Momentum conservation requires that the momentum vectors of the three final state particles lie in a plane. Therefore, if θ is the angle of the photon to the plane defined by the charged tracks, use only those photons with $\cos(\theta) > .98$.

2.) Using the measured charged track momenta and photon position, calculate the photon energy which minimizes the summed square error in the total energy and total momentum constraints:

$$E_p(\gamma) = .5(ECM - E_{charged} - \vec{P}_{charged} \cdot \hat{r}) \tag{9}$$

3.) Keep only those events whose measured photon energy is consistent with the predicted energy ($Z < .48$).

4.) Substituting the predicted for the measured photon energy, require the total energy of the three final state particles to be within 12% of the center of mass energy and the total momentum to be less than 400 Mev/c.

As an illustration of the nature of the events which pass this algorithm, in Figure 5.9 we show for all $\mu\mu\gamma$ candidates, the distribution of the measured total energy of the three final final particles relative to the center of mass energy.

Another source of background are lepton-lepton-gamma (l-l-γ) events where one of the initial electrons has radiated a hard photon so that the center of mass frame is no longer identical with the lab. We use the fact that the initial state radiation (ISR) is most often emitted along the beam direction to reduce this background. The algorithm is as follows:

1.) If the invariant mass recoiling against the two charged tracks and candidate photon is consistent with zero (|squared mass|<1.4 Gev^2/c^4), the event is considered a l-l-γ + ISR candidate.

2.) We then assume the recoiling mass is zero to calculate a predicted energy for the candidate photon and require the predicted and measured photon energy to be consistent ($Z < .48$).

3.) Substituting the predicted for the measured photon energy, calculate the momentum recoiling against the three particles. If it is larger than 300 Mev/c and if the cosine of its angle to the beam axis is greater than .95, then the event is called an ISR l-l-γ event and is discarded.

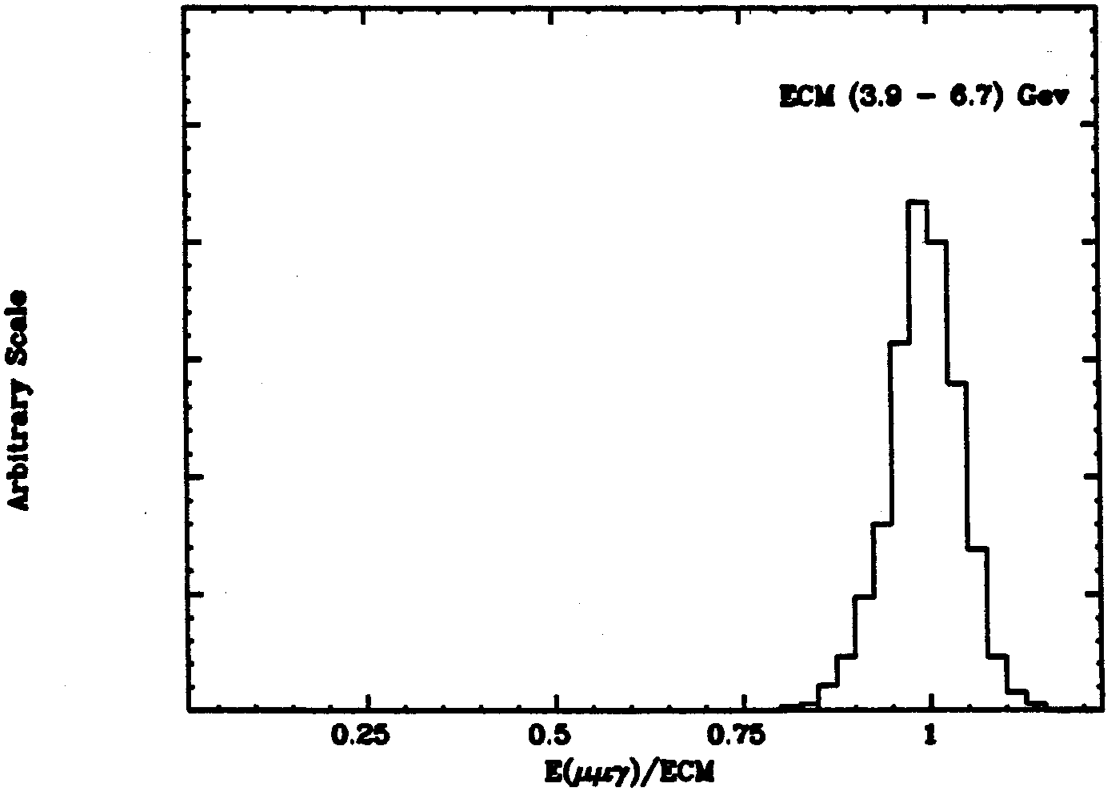

Figure 5.9. Measured $\mu\mu\gamma$ total energy divided by the center of mass energy for e+e- --> $\mu\mu\gamma$ events.

Figure 5.10 shows the distribution in the cosine of the angle of the recoiling momentum to the beam axis for events with at least one electron after the 300 Mev/c cut.

The two algorithms discussed above remove 65% of the μ-γ candidates and 45% of the e-γ combinations. However, there still remains an excess of events which have the charged tracks and photon in a plane. These events might be real events which failed the 1-1-γ algorithm for one of many reasons; for example, electron bremsstrahlung in the pipe count or excessive fluctuations in the photon's energy measurement (perhaps due to shower sharing, edge effect, or dead spaces in the module). Higher order electromagnetic processes where a photon is emitted along a direction near one of the charged tracks will result in planar events. In Figure 5.11a and 5.11b we plot the measured distribution in cos(θ) for those lepton-photon candidates which survive all the above cuts, and for comparison, Figure 5.11c shows Monte Carlo distribution for radiative tau decays at 5.2 Gev. We impose an additional cut that cos(θ) < .998 to eliminate the excess background with cos(θ) near 1.

Photons created when an electron radiates in the material preceeding the drift chamber cause another source of background which can be easily eliminated. Although the measured invariant mass of these combinations is near zero, higher mass backgrounds can be made from bremsstrahlung photons which combine with other leptons in multi-lepton events. The opening angle distibution between photons and leptons in our candidate sample is shown in Figure 5.12. There is a large bremsstrahlung signal which can be removed by discarding all photons for which the cosine of the opening angle between it and either charged

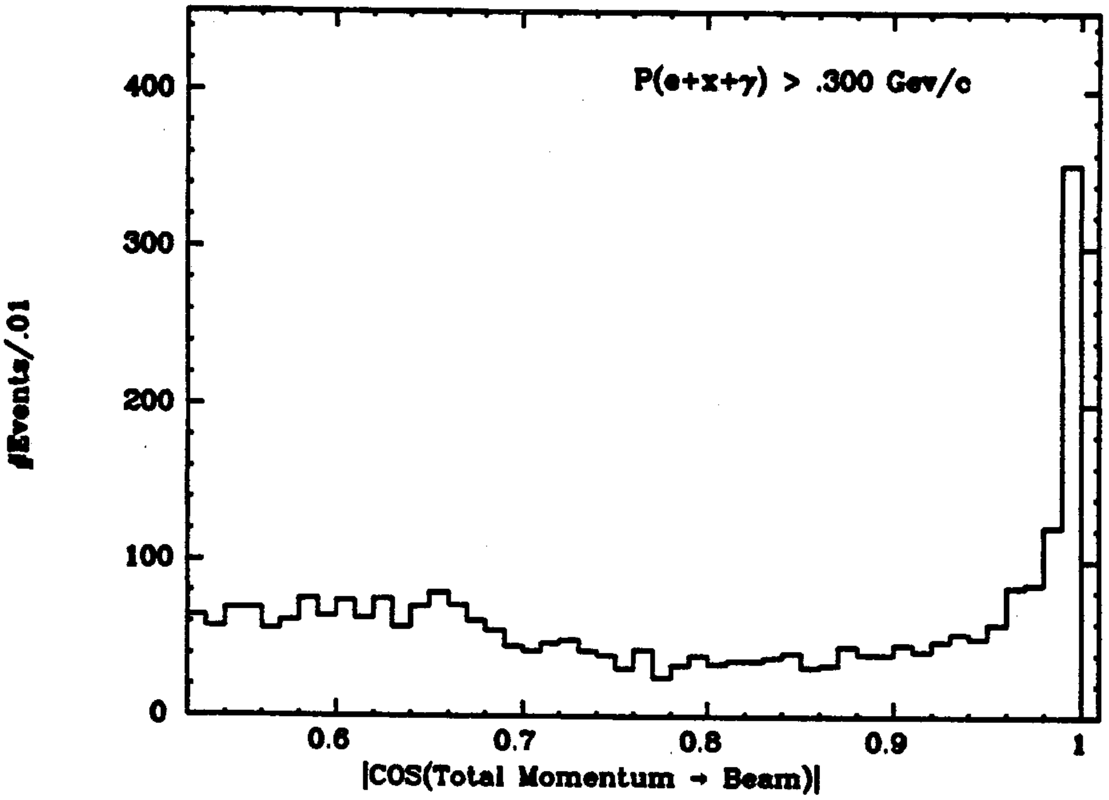

Figure 5.10. Cosine of the angle to the beam axis of the momentum recoiling against the charged tracks and photon in e+X+γ events.

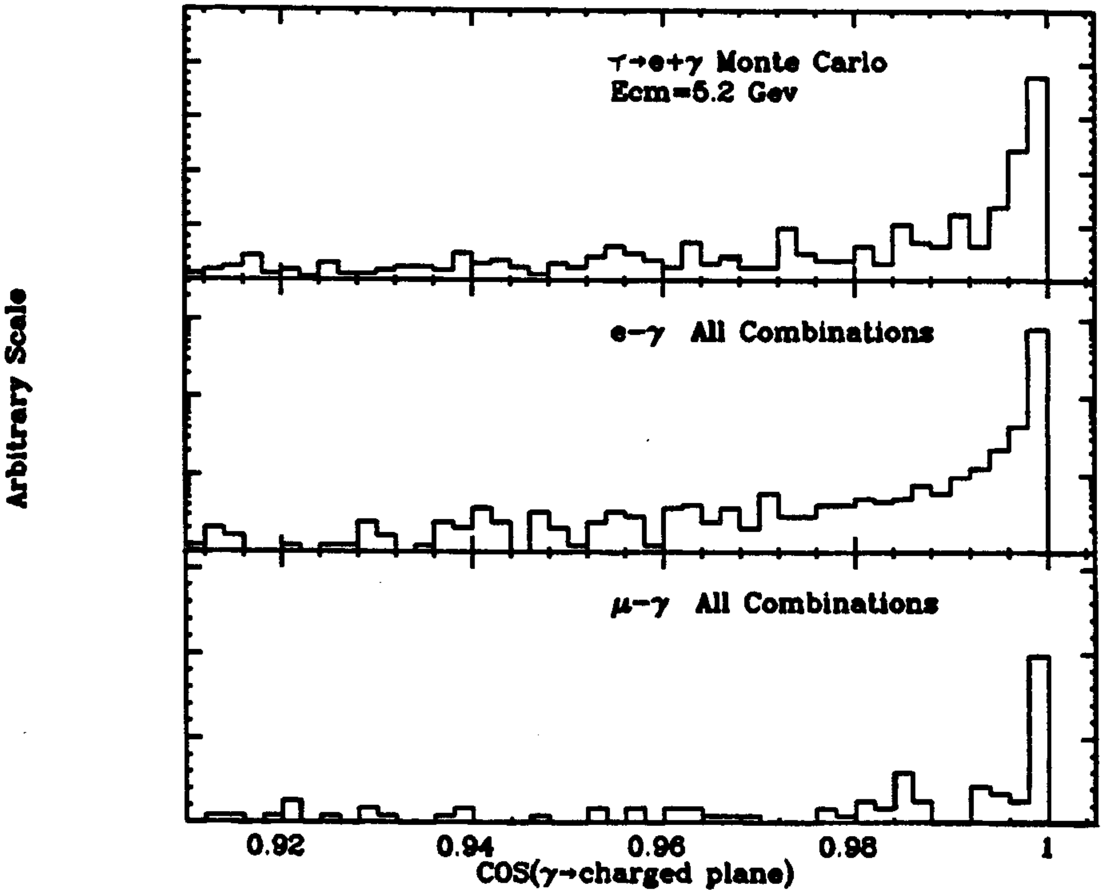

Figure 5.11. Cosine of the angle of the photon to the plane formed by the two charged track momentum vectors in lepton+ γ +X events. Note the logarithmic scale in the middle plot. A monte carlo calculation for the process ϒ+ϒ --> (eγ)+(X + neutrals) is also shown.

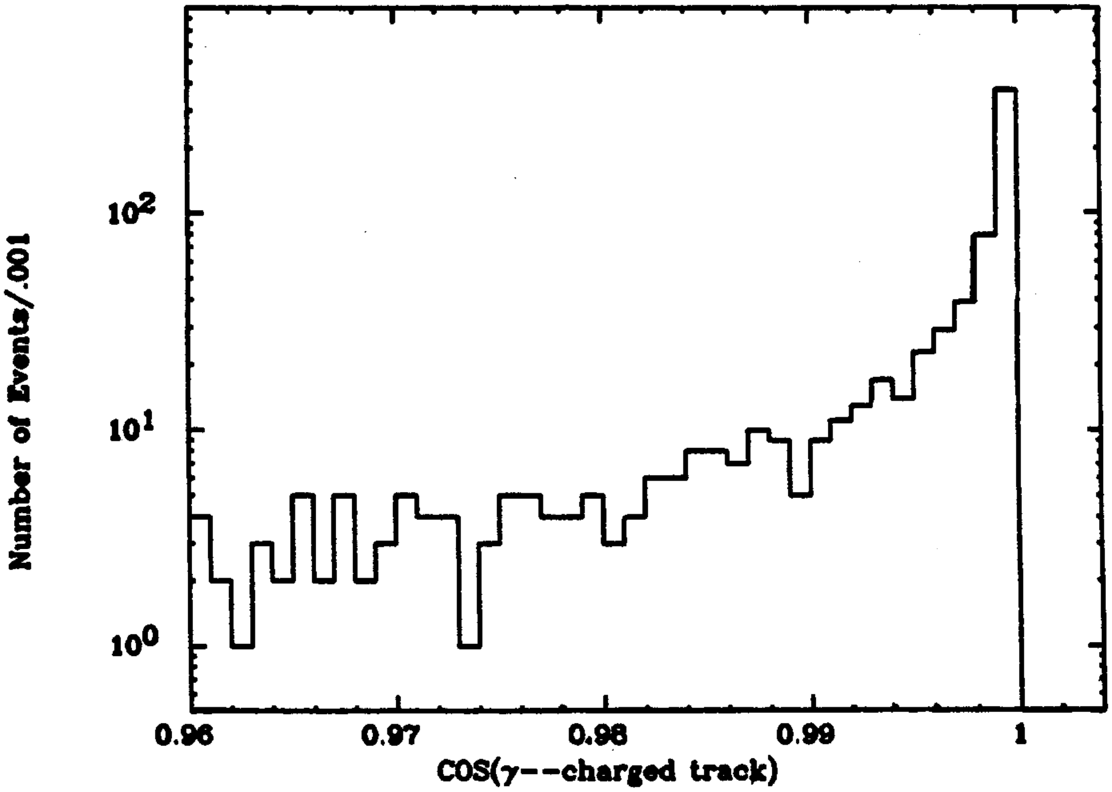

Figure 5.12. Cosine of the angle between the photon and the charged tracks in ϒ -->eγ decay candidate events.

track is larger than .986.

Conventional tau pair events provide another source of background. If one tau decays leptonically while the other decays via the rho-neutrino mode, the neutral pions from the decay of the rho produce photons that can combine with the lepton to mimic a lepton-gamma signal. Figure 5.13 gives an example of the μ-γ invariant mass spectrum resulting from this process at 5.2 Gev. Monte Carlo calculations indicate that 1% of the tau pairs which decay in this manner survive the analysis cuts. Roughly one-half of this background can be removed if photons which are used in reconstructed π^0s found by the program PIZERO (see section 7.4) are discarded. As can be seen in Figure 5.13, the background is concentrated in a several hundred Mev/c^2 wide region just below the beam energy. The data above 5.2 Gev does not contaminate the invariant mass spectrum in the region near the tau mass, but will provide a background for the general excited lepton search.

5.6 BRANCHING RATIO LIMIT FOR $\tau\rightarrow\mu+\gamma$:

With the addition of the cuts discussed above, we obtain the μ-γ invariant mass spectrum shown in Figure 5.14. The spectrum in the region near the tau mass is shown with an expanded scale in Figure 5.15 along with the resolution function obtained with the Monte Carlo. In Figure 5.5 we show as a function of the center of mass energy, the acceptance calculated with the Monte Carlo program with all background cuts included. The acceptance is defined to be the fraction of generated Monte Carlo events which survive the analysis cuts, and have a μ-γ invariant mass within 34 Mev/c^2 of the tau mass.

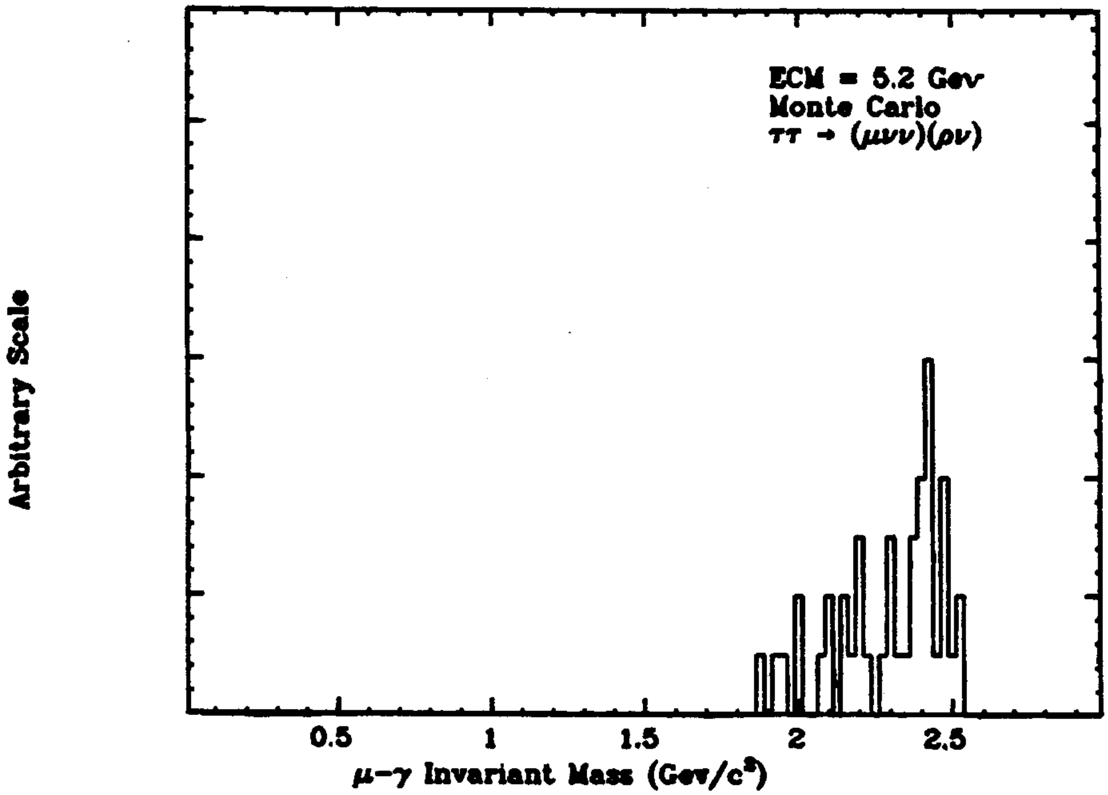

Figure 5.13. Monte Carlo calculation of beam constrained invariant mass distribution for the process $\tau + \tau \rightarrow (\mu\nu\nu) + (\rho\nu \rightarrow \pi\pi^0\nu \rightarrow \pi\gamma\gamma\nu)$ at 5.2 Gev.

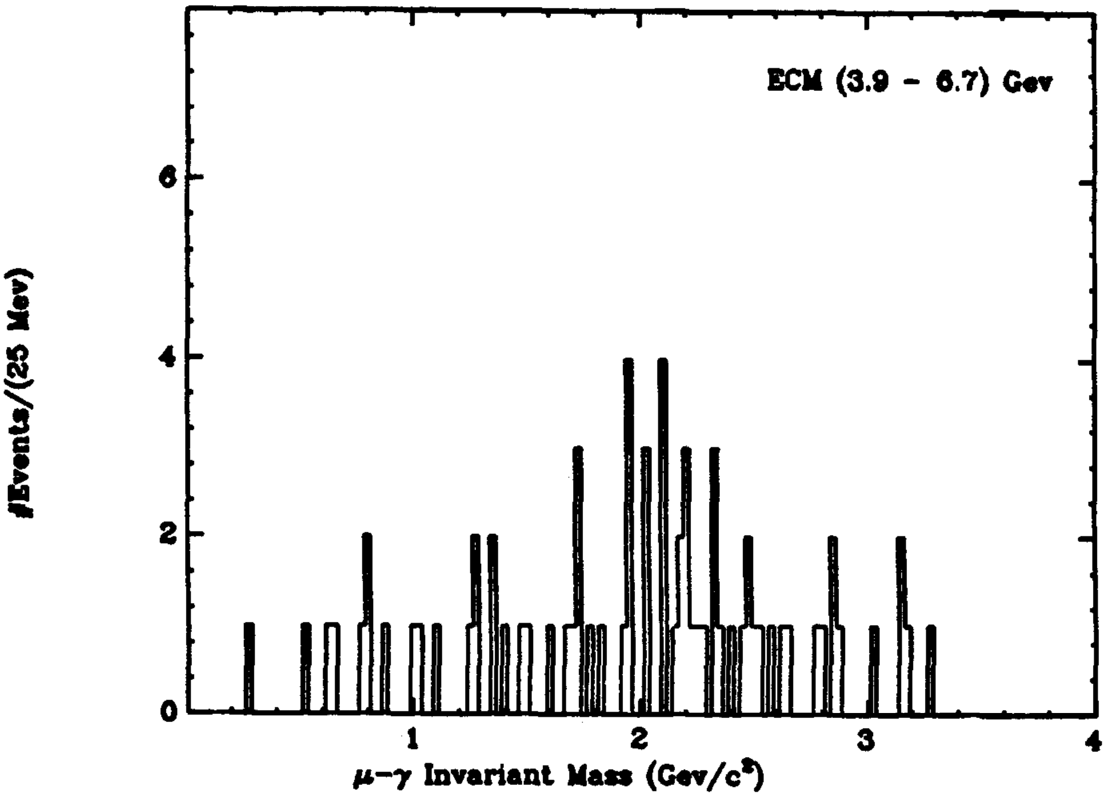

Figure 5.14. Measured $\mu\gamma$ beam constrained invariant mass distribution.

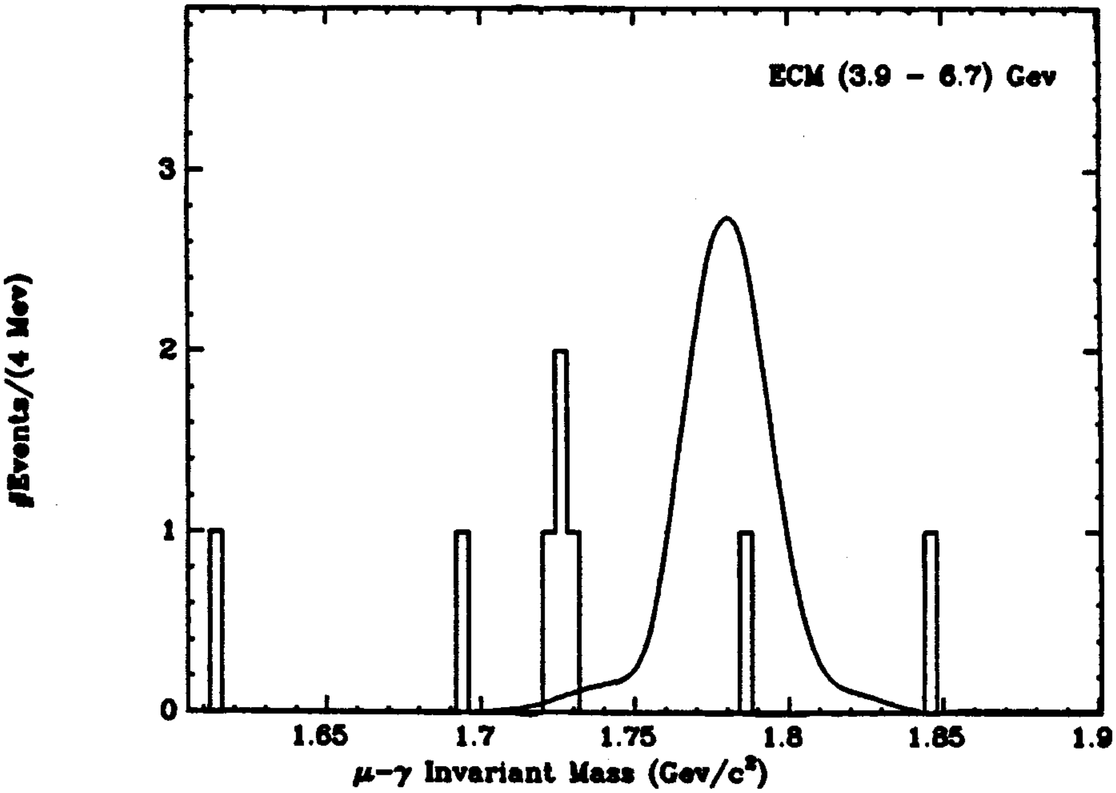

Figure 5.15. Measured $\mu\gamma$ beam constrained invariant mass distribution (Figure 5.14) with an expanded scale. The calculated resolution function is also shown.

There is no evidence for the μ-γ radiative decay of the tau. Using the measured luminosity and calculated acceptance, we can determine an upper limit to the branching fraction as indicated in equation (10)

$$BR \leq P(\#observed)/2\sum_{E}\sigma(E)L(E)A(E) \qquad 90\%\ C.L. \qquad (10)$$

where P(N) is the average for a Poisson distribution such that 90% of the probability is for values larger than N. The mean acceptance, averaged over the center of mass energy range with a weight function proportional to the number of produced tau pairs, is 7.3%. Given that the data sample contains 96,000 produced tau leptons, the single event which lies within the 68 Mev/c^2 wide region used to define the acceptance determines the 90% confidence level on the branching ratio of the radiative decay $\tau\rightarrow\mu+\gamma$ to be .055%.

There is no evidence in Figure 5.14 for any state that is produced with the beam energy and decays to a muon and photon. The distribution in the photon energy resolution for all events is shown in Figure 5.16 and is consistent with the background distribution observed in Figure 5.3. Assuming the "excited lepton" is pair produced with a cross section proportional to the point cross section (11),

$$\sigma = R_{\mu^*}\sigma_0 \qquad \sigma_0=43.3\beta(3-\beta^2)/S\ \text{nb} \qquad (11)$$

and has a unit branching fraction to the μ-γ final state, we can put an upper limit on the production cross section suppression factor R_{μ^*}. To do this, we must determine the detectors acceptance and resolution as a function of center mass energy over the excited lepton mass range of interest.

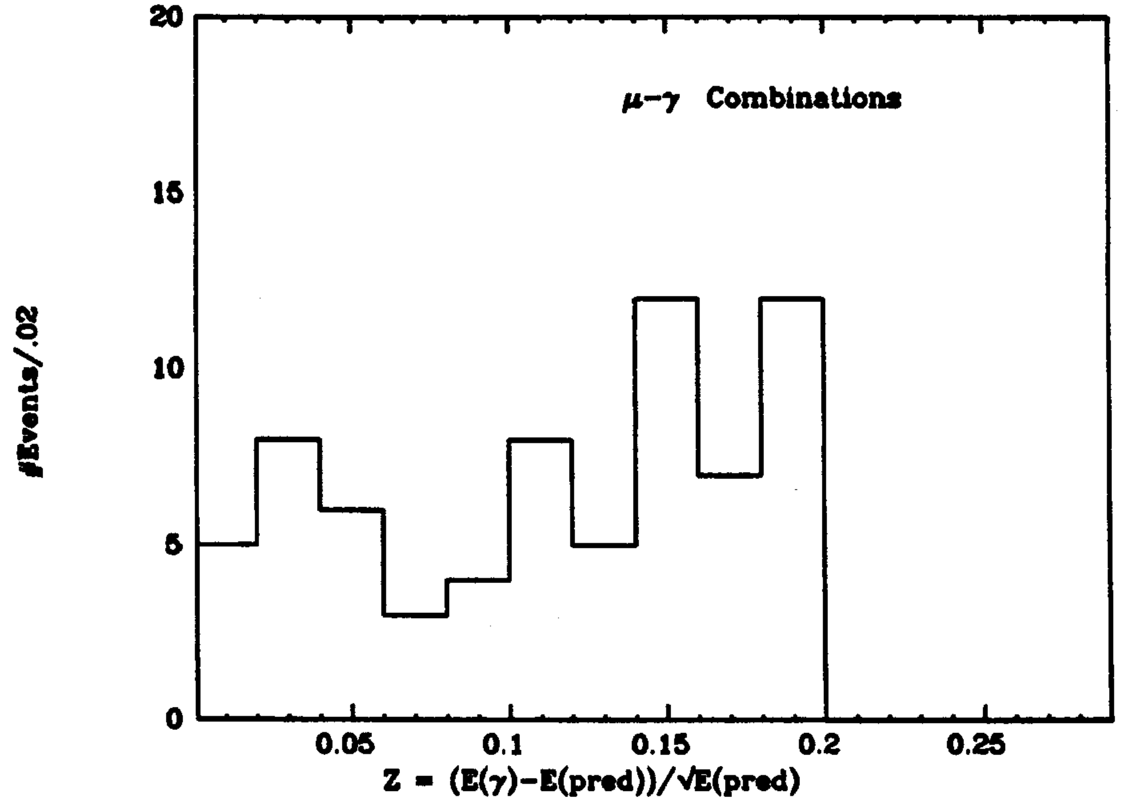

Figure 5.16. Photon Z distribution for passing $\mu\gamma$ events.

The invariant mass resolution varies according to mass and total energy as shown in Figure 5.17 where--due to the non-gaussian nature of the resolution function--we define the resolution as the limits around the central value which contain 80% of the detected events. The abscissa for the plot is the excited lepton mass divided by the beam energy ($m^*=m/E_{beam}$). For a given total energy, the resolution remains approximately constant until the lepton mass approaches the beam energy at which point it rapidly improves. For constant m^*, the resolution increases linearly with the total energy.

In Figure 5.18 we show the acceptance for detecting the decay products from one produced pair as a function of m^* and the total energy. As m^* approaches unity, the acceptance improves due to the back-to-back recoil of the secondary lepton and photon. As m^* approaches zero, the events tend to be colinear. Thus they fail both the acoplanarity cut and the requirement that the photon be out of the plane of the charged tracks. For constant m^*, the acceptance increases slightly with total energy due mostly to the decreased importance of the muon system momentum dependence.

In Figure 5.19 we show the number of produced lepton pairs as a function of lepton mass calculated using the point cross section and the luminosity distribution for the data. The expected number of detected lepton-gamma combinations can be determined by folding the acceptance into the calculation and is shown in Figure 5.20. For masses between .6 and 2.2 Gev/c^2 we would expect to detect approximately 8000 excited leptons if they were produced with the point cross section and decayed with with unit branching fraction to the μ-γ final state. For masses below .5 Gev/c^2, the decreasing acceptance limits this while

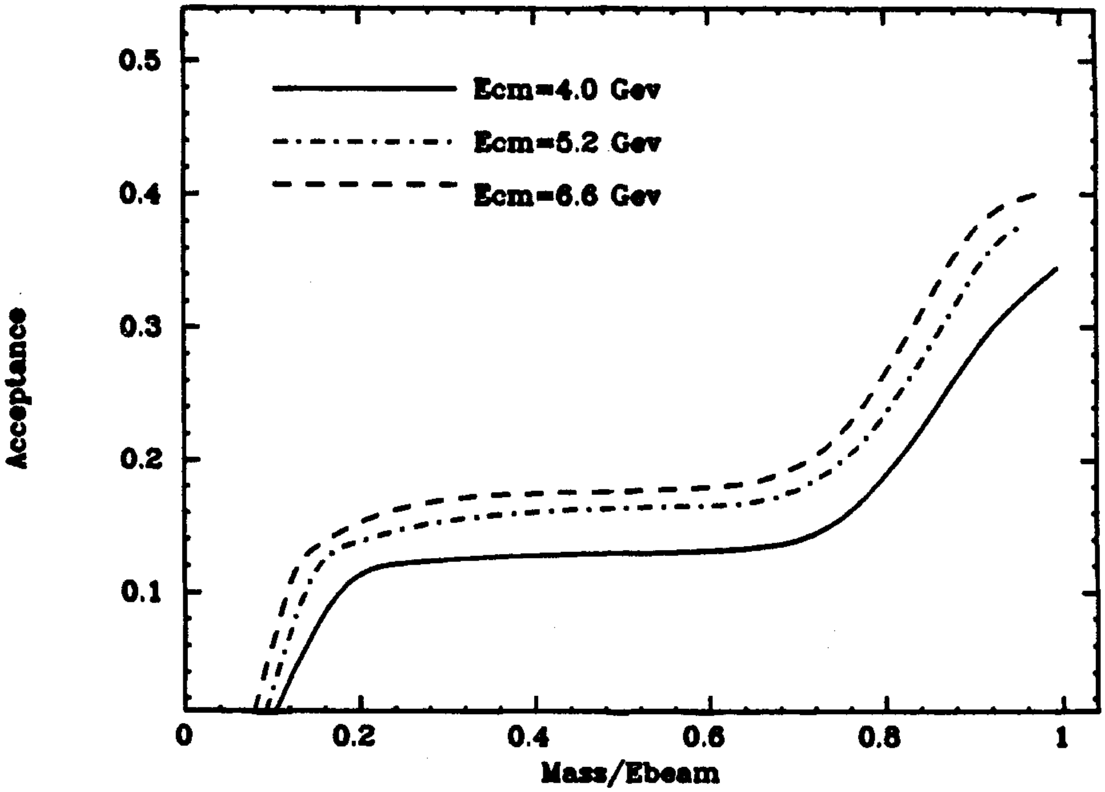

Figure 5.17. $\mu\gamma$ invariant mass resolution as a function of the excited lepton mass/beam energy for three center of mass energies.

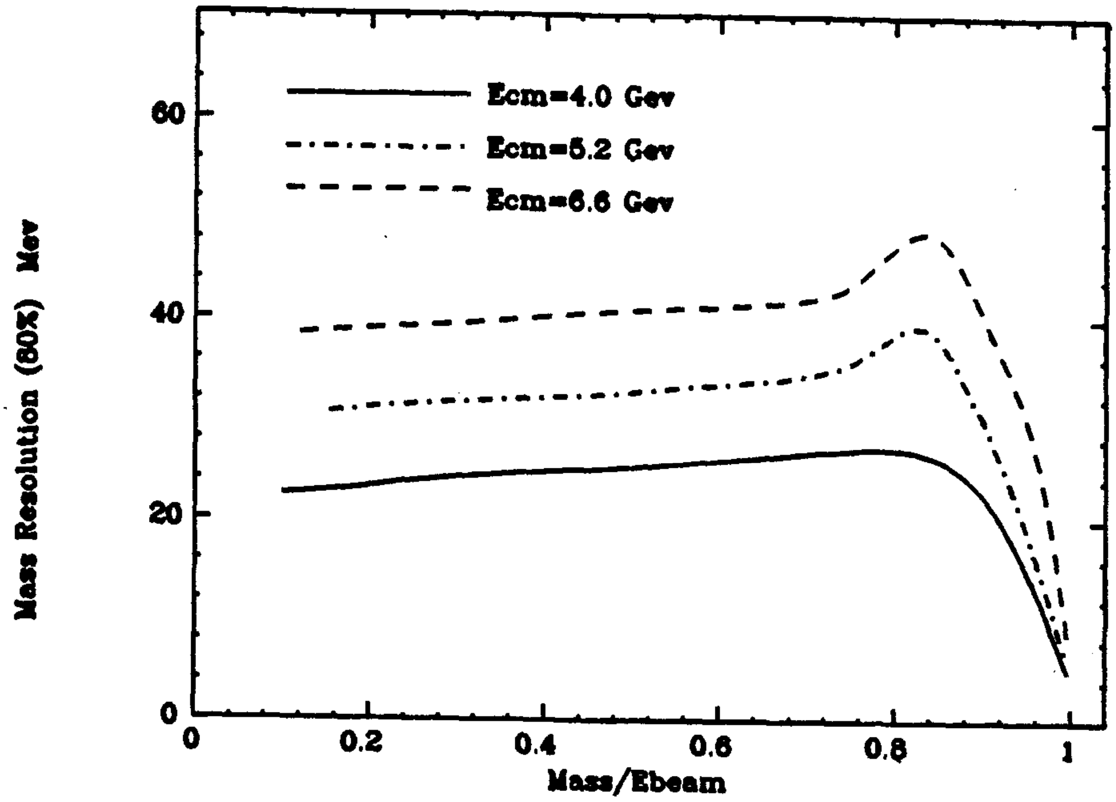

Figure 5.18. Acceptance for excited muon search as a function of the excited lepton mass/beam energy for three center of mass energies.

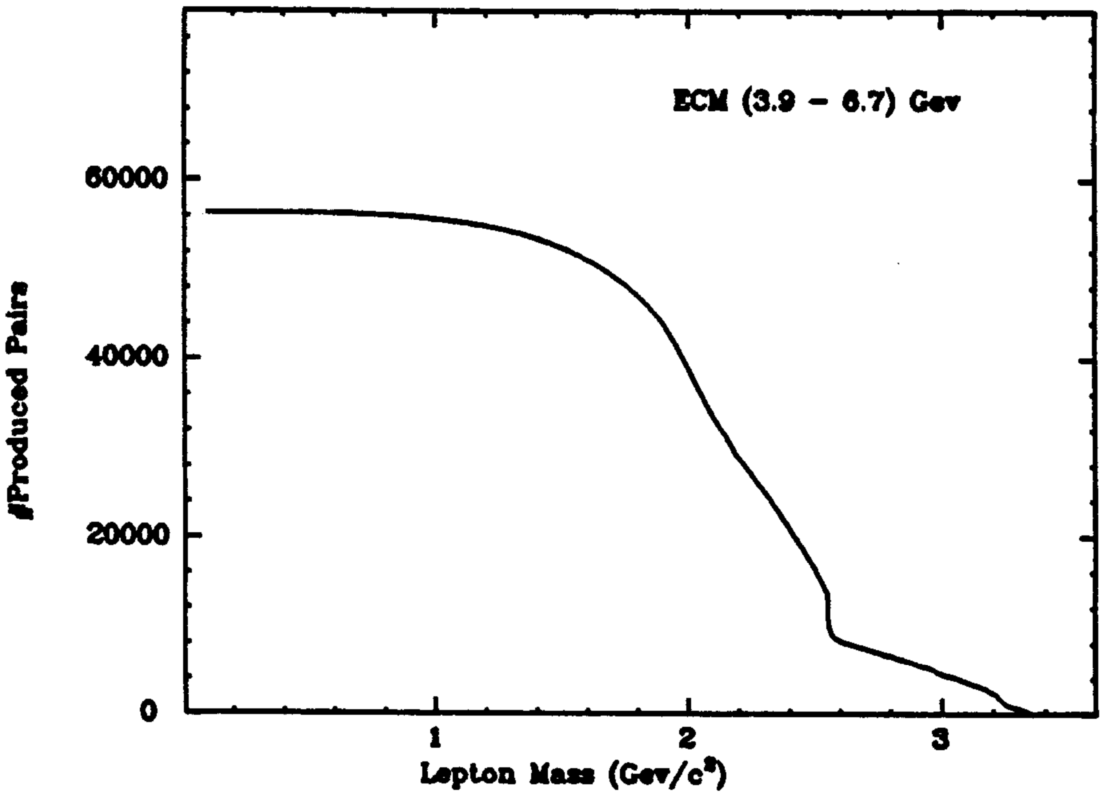

Figure 5.19. The number of produced lepton pairs assuming the spin 1/2 point cross section as a function of lepton mass.

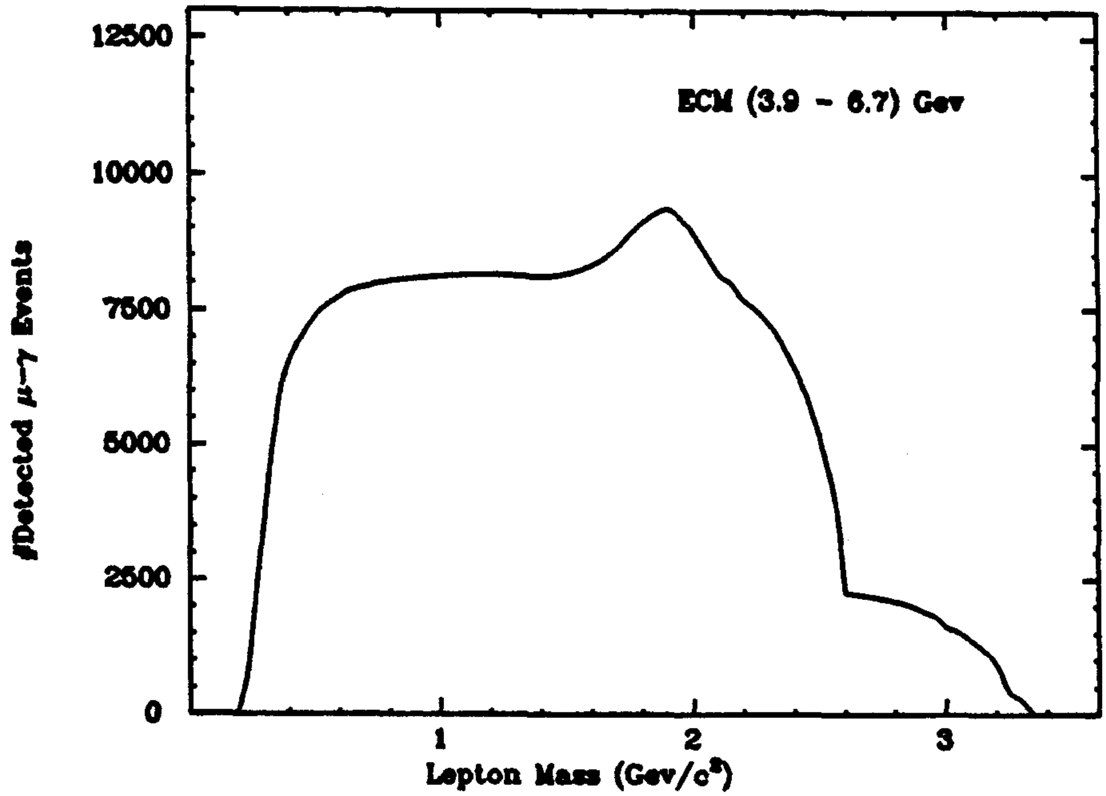

Figure 5.20. Expected number of detected M -->μ+ γ events as a function of excited muon mass.

above 2.6 Gev/c^2 only the high energy data contributes. The steep sholder between 2.2 and 2.6 Gev/c^2 is a reflection of the threshold function in the cross section and the large fraction of data with ECM=5.2 Gev.

As observed in Figure 5.17, the mass resolution varies with the total energy and excited lepton mass. When appropriately averaged over the energy distribution of the data sample, we obtain the 80% resolution shown in Figure 5.21 as a function of mass. The discontinuity near 2.5 Gev/c^2 is also a product of the 5.2 Gev data. The average resolution is always less than 45 Mev/c^2. Therefore, if we plot the measured invariant mass distribution in 25 Mev/c^2 wide bins, more than 80% of the events from an excited lepton's decay will lie within the three bins embracing the lepton's mass.

Using Figures 5.14 and 5.20, we can determine an upper limit for the cross section suppression factor $R_\mu{}^*$:

$$R_\mu{}^* \leq \frac{\text{P(\#observed)}}{\text{Expected \#detected events}} \tag{12}$$

In Table 5.1 we list, for various mass intervals, worst case values for the 90% upper limit on $R_\mu{}^*$ obtained by dividing the 90% Poisson probability for the largest sum of three adjacent bins within the mass interval by the minimum expected number of detected events.
Within these intervals there are certain regions where the limits are considerably better than the worst case values, but never better than .0004.

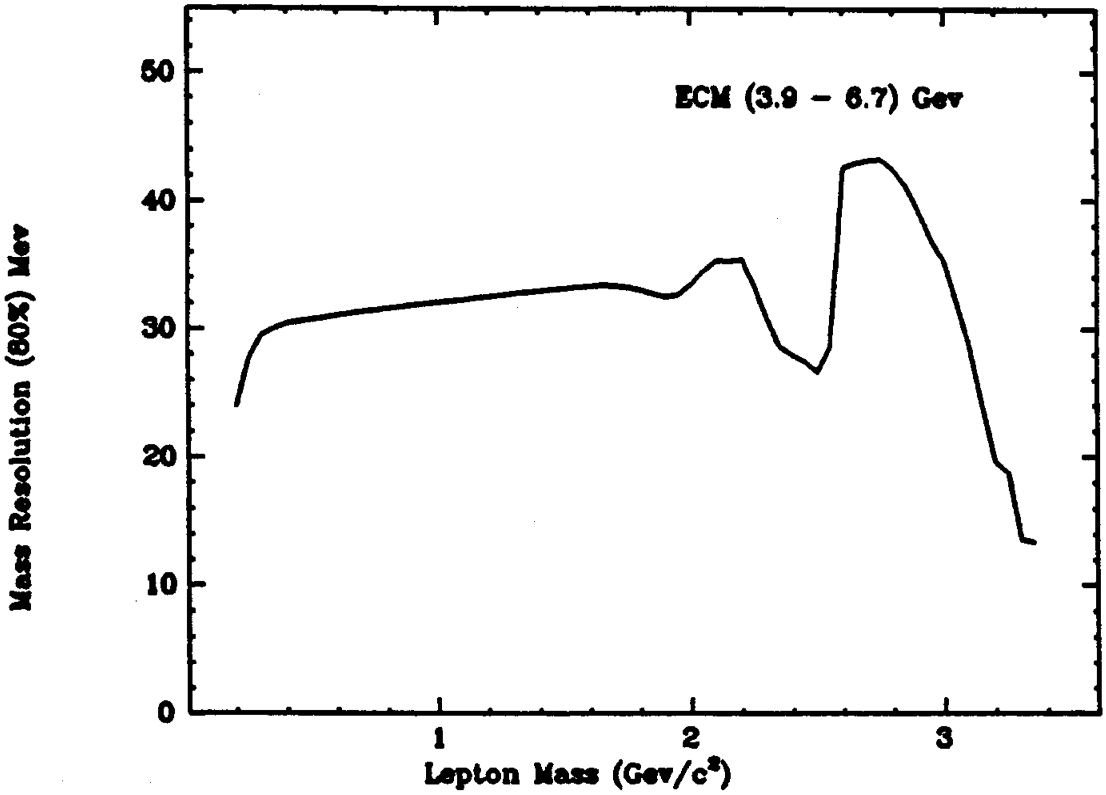

Figure 5.21. Average $\mu\gamma$ invariant mass resolution (80% width) as a function of the excited muon mass.

TABLE 5.1

Pair produced excited muon point cross section suppression for various lepton mass ranges.

Mass Interval (Gev/c^2)	Maximum Bin Sum	90% Confidence Level Upper Limit on R_μ^*
.6-1.6	3	.0010
1.6-2.1	5	.0014
2.1-2.5	6	.0025
2.5-2.9	3	.0043
2.9-3.2	3	.0090
3.2-3.3	1	.0193

5.7 BRANCHING RATIO LIMIT FOR $\tau \to e+\gamma$:

We now turn attention to the search for the electron-gamma decay of the tau. With the background cuts detailed in section 5.5 above, we obtain the invariant mass spectrum shown in Figure 5.22. The background is nearly an order of magnitude worse than what is observed in the muon-gamma decay, and consists mostly of purely electromagnetic processes with 2 electrons and 2 or more photons in the final state. We can impose additional cuts to reduce this background, but they are more expensive in terms of reduced acceptance than the cuts previously applied.

It was observed in Figure 5.8 that the charged track acoplanarity distribution in electron-gamma candidate events is sharply peaked towards small values. Figure 5.23 shows the acoplanarity distribution for all events used in Figure 5.22. By imposing a more stringent cut of 28 degrees on the acoplanarity, we can eliminate nearly 2/3 of the events.

For those events which remain where the oppositely charged track is unambiguous identified, more than 95% are identified as electrons.

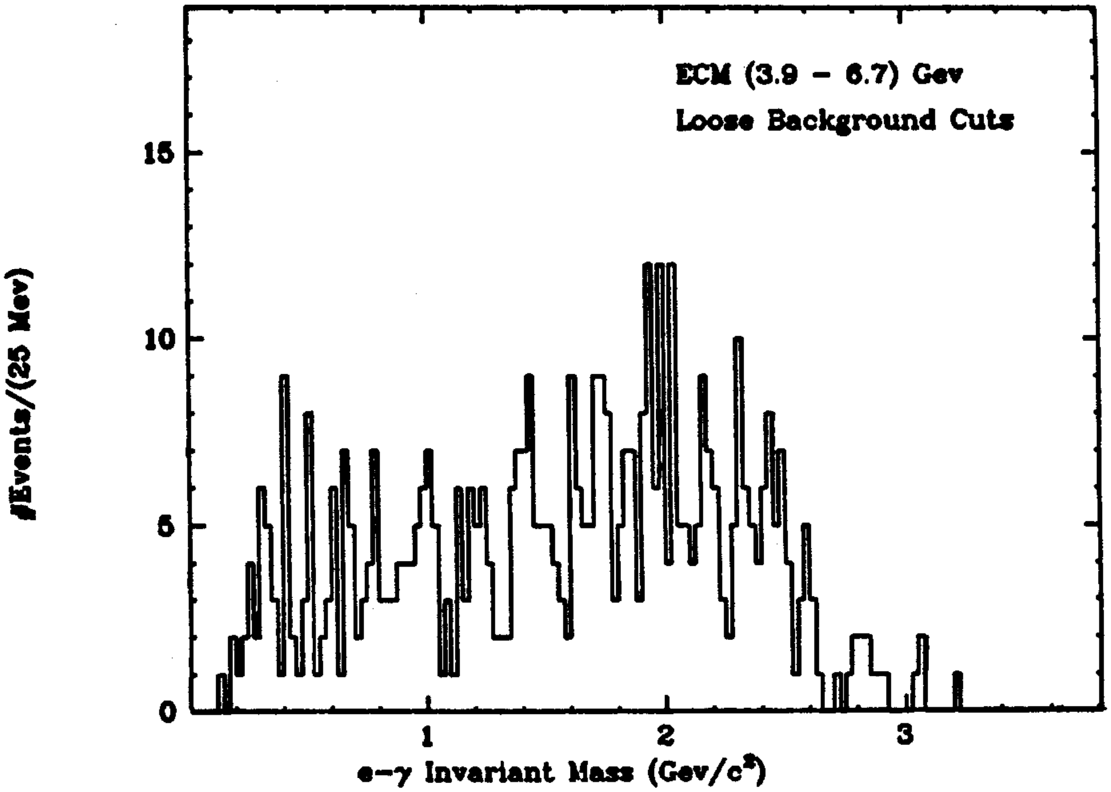

Figure 5.22. eγ beam constrained invariant mass distribution after applying only loose background cuts.

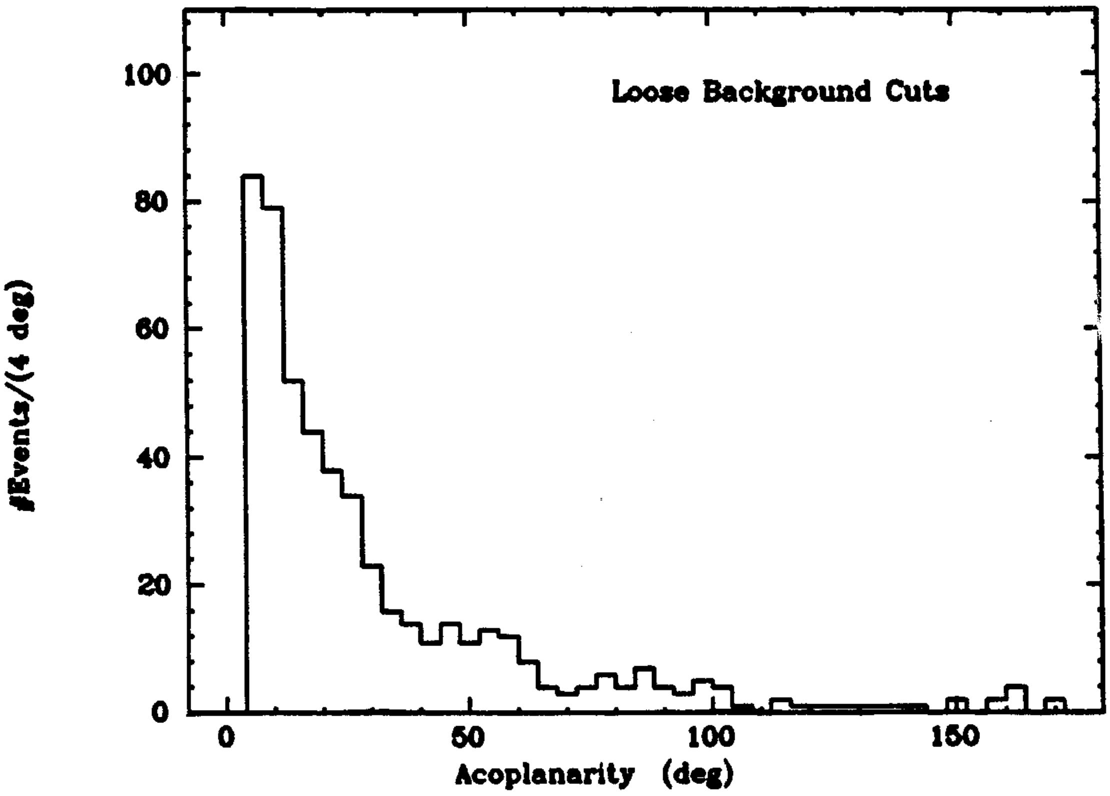

Figure 5.23. Charged track acoplanarity distribution for events with an electron+photon pair.

Therefore, requiring that the opposite track not be identified as an electron will remove an additional 60% of the background events.

With these two additional cuts, the e-γ mass spectrum shown in Figure 5.24 is obtained. The mass distribution near the tau mass is shown with an expanded scale in Figure 5.25 along with the resolution function calculated with the Monte Carlo. There is no evidence for the e-γ decay of the tau. The calculated acceptance (including all cuts) is shown in Figure 5.6 as a function of the center of mass energy. The mean acceptance, averaged over the total energy with a weight function proportional to the number of produced tau pairs, is 6.3%. Given the one event in Figure 5.25 within the 68 Mev/c^2 interval used to define the acceptance, the 90% confidence level upper limit on the branching fraction for the decay $\tau \rightarrow e + \gamma$ is .064%.

We can determine upper limits on the production cross section suppression factor $R_e{}^*$ for pair-produced excited electrons in exactly the same way that upper limits on $R_\mu{}^*$ were set in section 5.6. However, the requirement that the opposite track not be identified as an electron must be dropped. This leads to the e-γ mass distribution shown in Figure 5.26. The expected number of detected e-γ events (shown as a function of the excited lepton mass m^* in Figure 5.27) is less than the excited muon case due to the tighter acoplanarity cut. The average e-γ mass resolution is worse than the μ-γ mass resolution due to electron bremstrahlung. Therefore, we must increase the acceptance window from three to four 25 Mev/c^2 bins. Table 5.2 lists the resulting 90% confidence level upper limits on $R_e{}^*$ for various mass intervals.

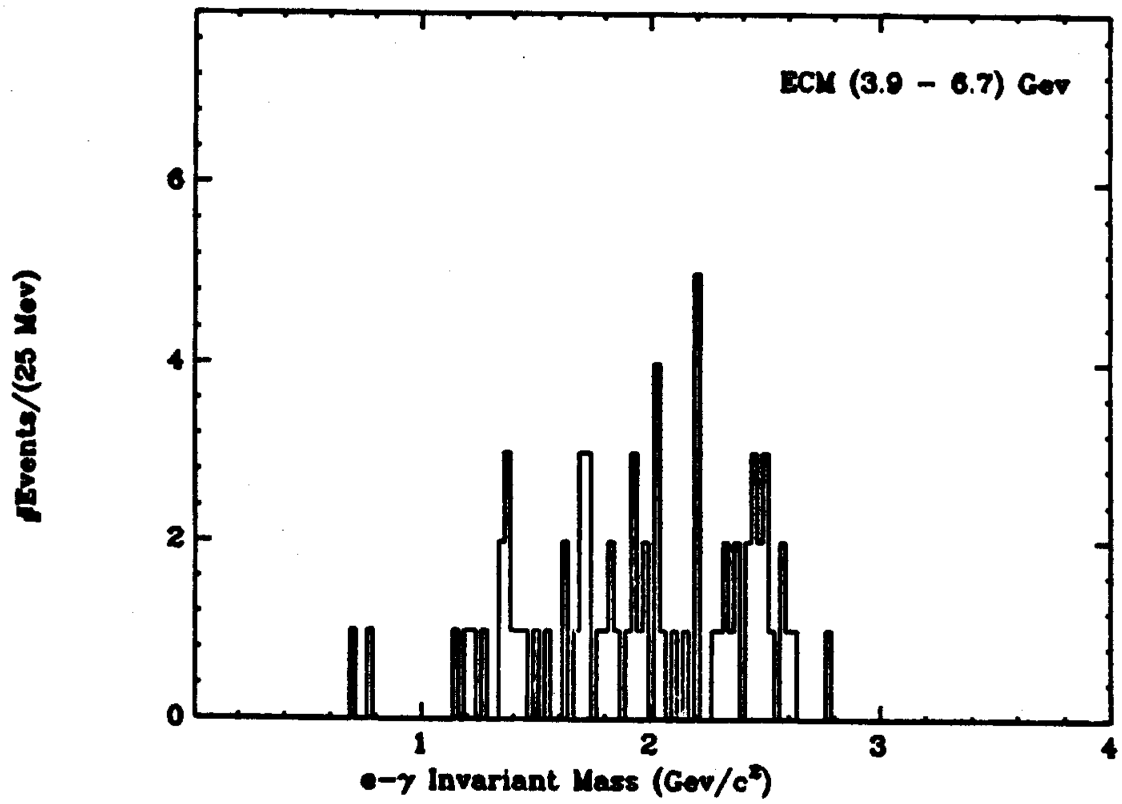

Figure 5.24. eγ beam constrained invariant mass distribution after applying tight background cuts.

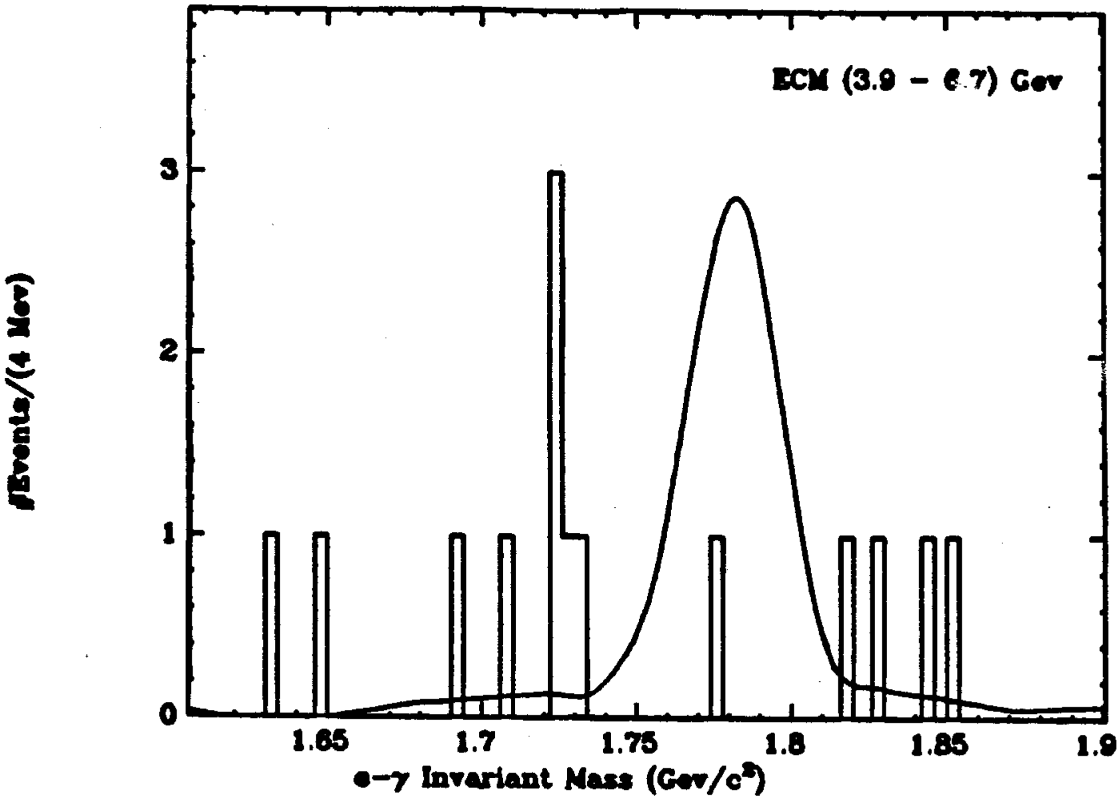

Figure 5.25 eγ beam constrained invariant mass distribution (Figure 5.24) shown with an expanded scale. The calculated resolution function is also shown.

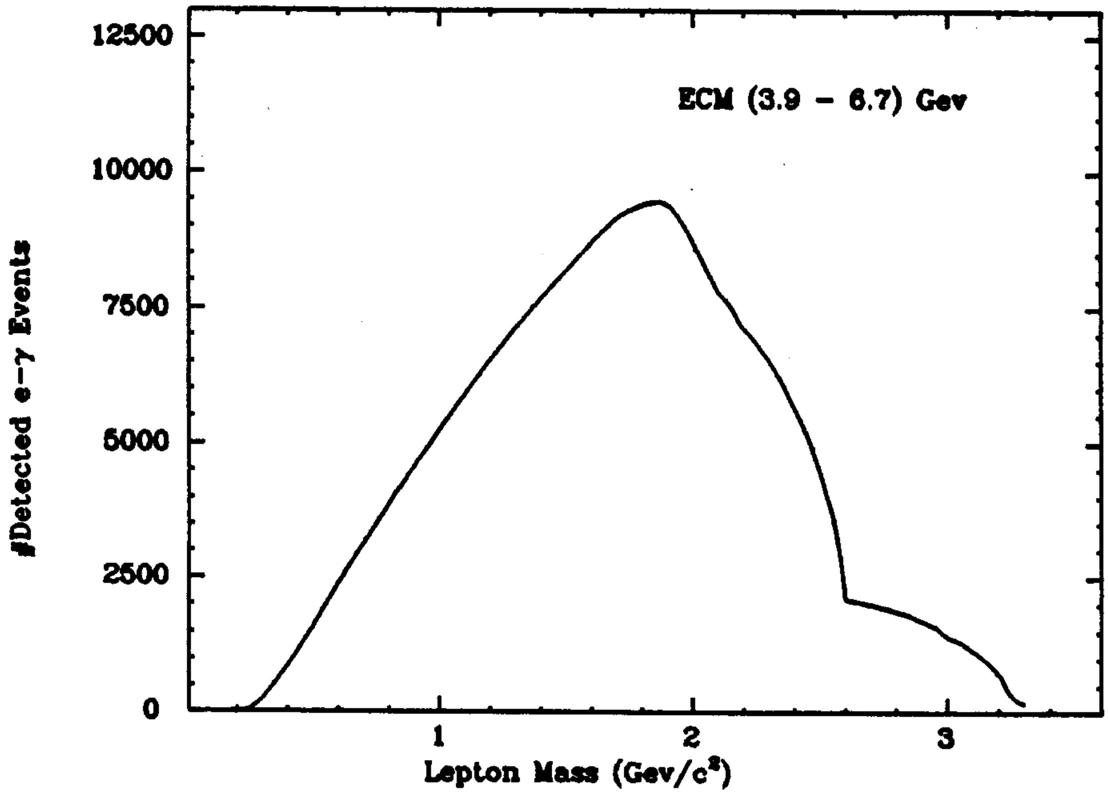

Figure 5.26. Expected number of detected E --> e^+ events as a function of the excited electron mass.

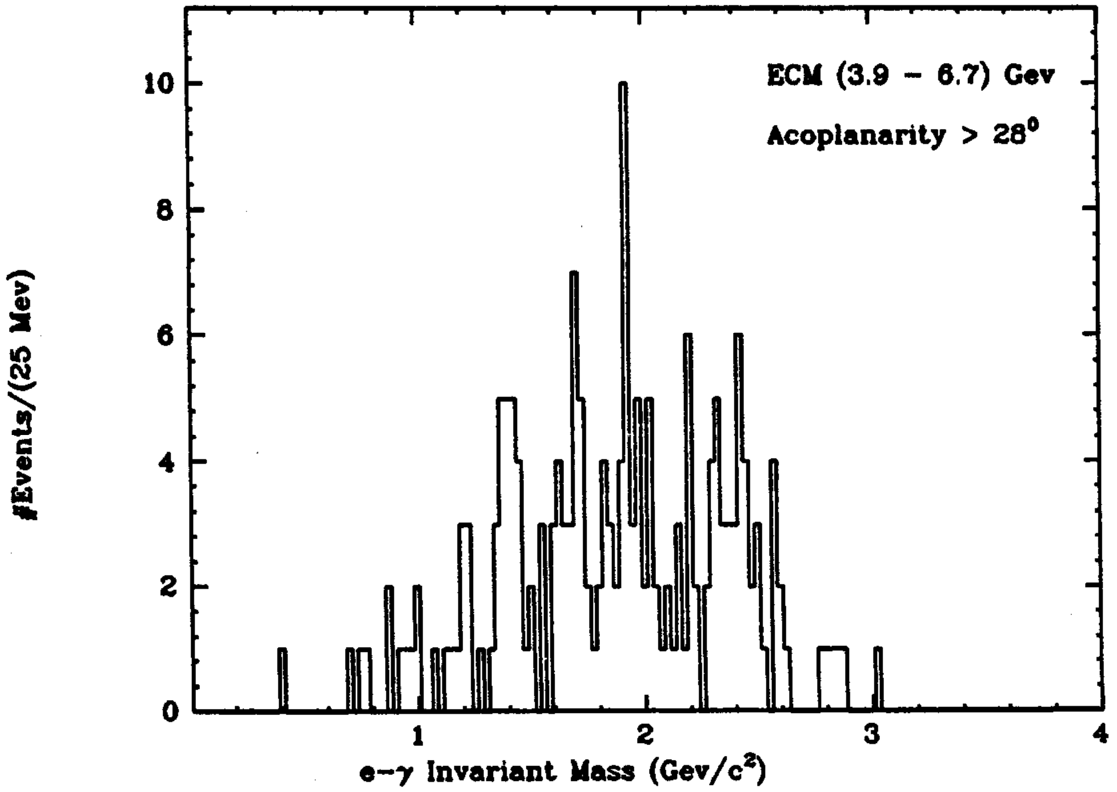

Figure 5.27. Measured e⁻ invariant mass distribution after applying an acoplanarity cut of 28 degrees. No cuts are imposed on the other charged track in the event.

TABLE 5.2

Pair produced excited electron point cross section suppression for various lepton mass ranges.

Mass Interval (Gev/c^2)	Maximum Bin Sum	90% Confidence Level Upper Limit on R_{e^*}
.5-.6	0	.0014
.6-.8	3	.0027
.8-1.0	5	.0023
1.0-1.3	8	.0025
1.3-2.0	22	.0041
2.0-2.3	15	.0030
2.3-2.5	16	.0051
2.5-3.0	10	.0096
3.0-3.2	1	.0039
3.2-3.3	0	.0110

References:

1.) J.D. Bowman et al., Phys. Rev. Lett. 42:556, (1979).

2.) C.A. Blocker, Ph.D. Thesis, LBL Report LBL-10801 (1980).

Chapter 6

A Search for the Decay Tau --> 3 charged leptons

6.1 INTRODUCTION:

Another test of the sequential lepton hypothesis is to search for the decays listed in (1) which violate lepton number conservation:

$$\tau\to ee^+e^-, \quad \tau\to\mu e^+e^-, \quad \tau\to e\mu^+\mu^-, \quad \tau\to\mu\mu^+\mu^- \qquad (1)$$

Analogous searches for the three electron decay of the muon have been conducted (2)

$$\mu\to ee^+e^- \qquad (2)$$

and have yielded an upper limit of $2\mathrm{x}10^{-9}$ on the branching fraction for this decay.[1] In this section we report on an analysis of a search for the three charged lepton decays of the tau. Previous experiments have determined an upper limit of .6% on the branching fraction for these decays[2], and given the improved lepton identification capabilities of the MARK II and our large data sample, these limits can be considerably strengthened.

Evidence for the decays will be found in the invariant mass distribution of all 3 charged lepton combinations in the data sample. Acceptance limitations, however, force us to also use combinations which have only 1 or 2 leptons identified. The data sample contains 48,000 produced tau pairs and is the same sample used in the search for radiative tau decays (see section 5.1).

6.2 EVENT TOPOLOGY:

Experimental studies have confirmed that over 70% of tau decays have one charged particle in the decay products. Therefore, in the search for the three charged lepton decays of the tau, we use all 3 and 4 charged prong events which have a total charge between -1 and 1, and which have one or more tracks identified as an electron or muon. No restrictions are placed on the number of neutral particles in the event. At least 3 of the charged tracks must form a vertex located within a cylinder 16 cm long and 8 cm in diameter centered about the interaction region. To insure a well-defined momentum cutoff, all tracks used in any invariant mass calculation must have a momentum larger than 100 Mev/c and must originate in the event vertex. Corrections are made to the measured track momenta to account for the energy lost in traversing the material in front of the drift chamber.

6.3 IDENTIFIED LEPTON REQUIREMENTS:

The MARK II's acceptance to detect and identify all 3 leptons from any of the four tau decays listed in (1), is small and decreases as the number of muons in the decay increases. Thus, we are forced to also consider 3 charged track combinations where only one or two tracks are identified as leptons. The background from random combinations increases with the number of unidentified tracks. Therefore, the contribution to each of the 4 decays from combinations where 1, 2, or 3 leptons are identified, are accumulated separately so that those with the worst background can be discarded. For example, contributions to the invariant mass distribution for the decay $\tau \rightarrow e\mu^{+}\mu^{-}$ can be from any of the following lepton combinations:

$$exx, \quad \mu xx, \quad e\mu x, \quad x\mu\mu, \quad e\mu\mu \tag{3}$$

where x represents a particle which was not identified as a lepton. Note that the electric charges of the particles are relevant. The combination exx can contribute to the decay only if x(1) and x(2) have opposite charges. If in the combination μxx, both x(1) and x(2) have the opposite charge from the muon, we will use only the combination which has the best chi-square for the beam constrained fit (see below).

6.4 MASS RESOLUTION AND THE BEAM CONSTRAINED FIT:

Given the measured 3 momentum and a mass hypothesis for each charged track, the invariant mass of the three charged track combination is calculated from equation (4).

$$m = [(\sum_{i} E_{i})^{2} - (\sum_{i} P_{i})^{2}]^{1/2} \tag{4}$$

The resolution in this measurment depends on the center of mass energy and the number of electrons in the decay. For the 3 muon decay, the resolution is typically 20 to 30 Mev/c^{2}, but it is several times worse for the eee decay. This can be improved by a factor of 2 to 3 if the fact that the tau is produced with the beam energy is used to correct the measured track momenta. If ΔE is the difference between the beam energy and the measured total energy of the 3 particles,

$$\Delta E = E_{beam} - \sum_{i} E_{i} \tag{5}$$

and dE_i is the expected measurement error in the energy of particle (i), then the energy of particle (k) is adjusted to satisfy

$$E_k' = E_k + \alpha E (dE_k')^2 / \sum_i (dE_i')^2 \qquad (6)$$

The chi-square of the fit is proportional to ΔE^2. Thus, requiring the fit have a good chi-square is equivalent to the requirement that ΔE be small. We implement this restriction by only considering those combinations where

$$A < Z \equiv \sum_i E_i / E_{beam} < 1.03 \qquad (7)$$

$$A(\mu\mu\mu) = .97, \quad A(e\mu\mu) = .96 = A(\mu ee) \quad A(eee) = .95$$

Figure 6.1 shows the measured Z distribution for all 3 muon candidates along with a Monte Carlo prediction for $\tau \to \mu\mu\mu$ at 5.2 Gev. In Figure 6.2 we plot the beam-constrained fit resolution function for both the 3 muon and 3 electron decays at 5.2 Gev.

6.5 BACKGROUNDS:

There are many different sources which contribute background to this search; for example, electromagnetic events, hadronic events where pions are misidentified or decay to muons, converted photons in hadronic events, semi-leptonic decays of charmed particles, and tau events. A few of these sources can be easily discriminated against, especially those which produce events with 3 or 4 detected leptons.

Listed in Table 6.1 are the number of 3 or 4 prong events in the data sample as a function of the number of identified muons or electrons in the event. There are no 4 muon or 3 muon events detected, but many events with 3 or 4 electrons are seen.

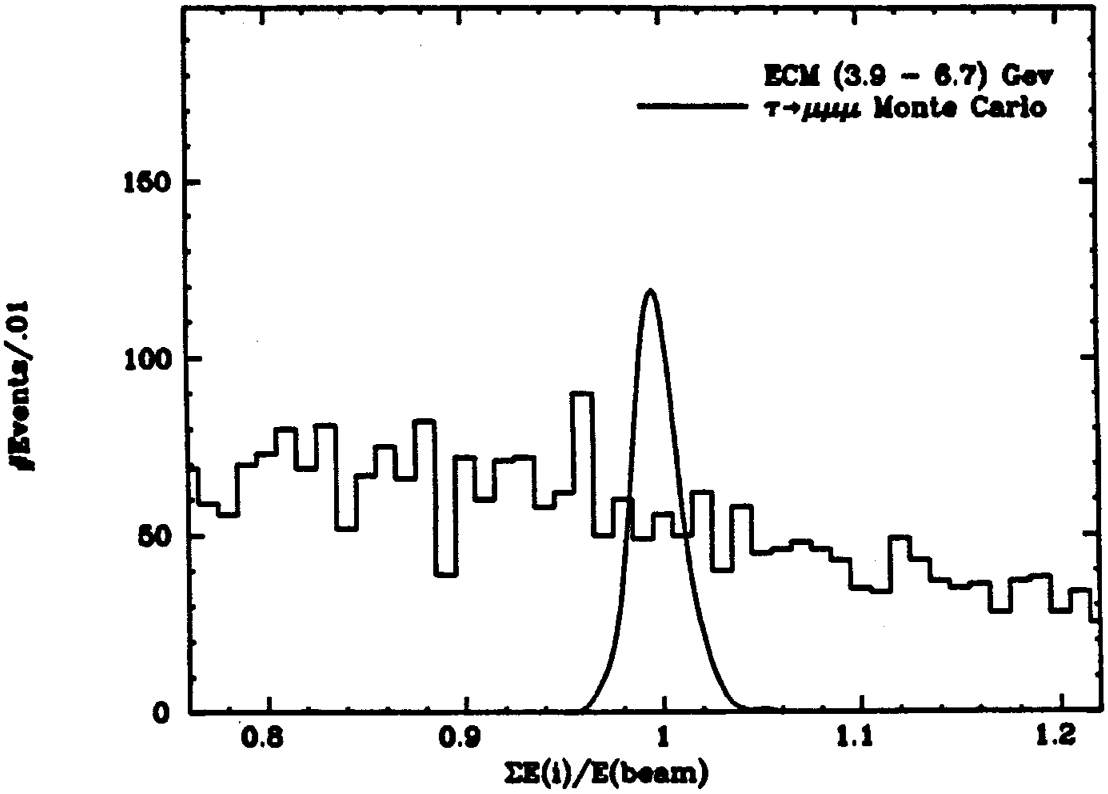

Figure 6.1. Total energy of the 3 muon candidates divided by the beam energy for the tau --> 3 muon decay search. The monte carlo calculation is also shown.

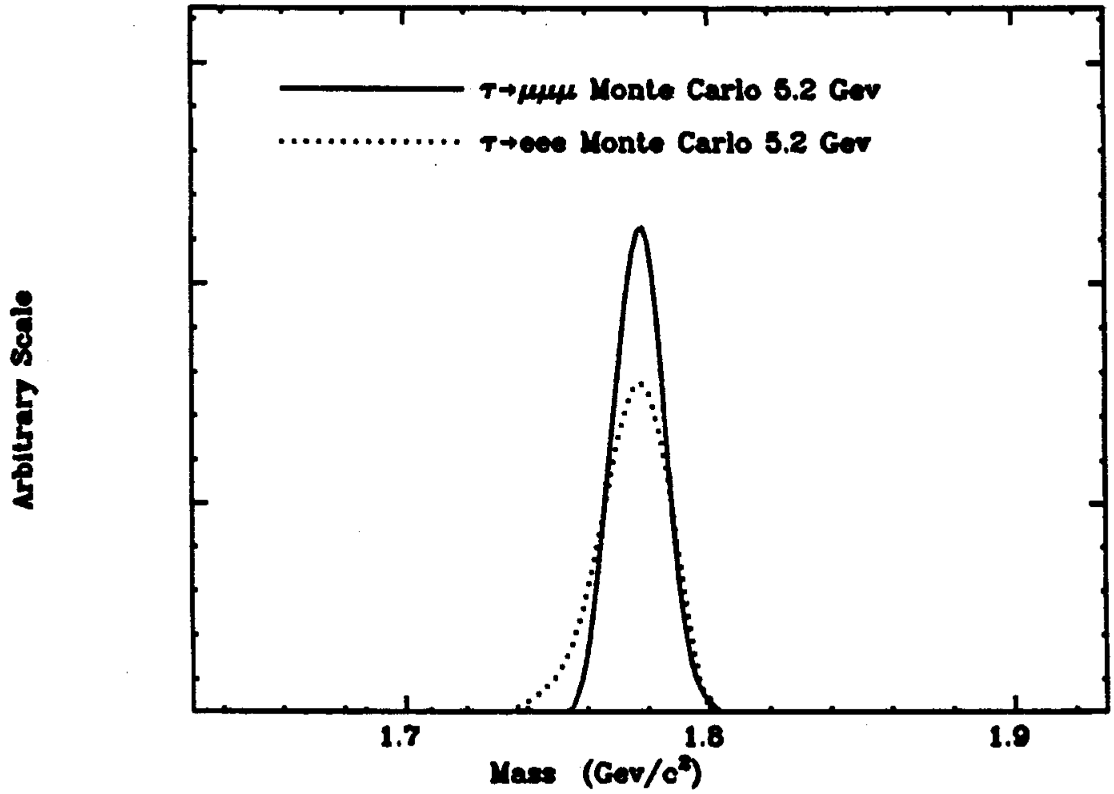

Figure 6.2. Monte carlo calculation of the 3 particle invariant mass resolution function for the 3 electron and 3 muon decays of the tau.

TABLE 6.1

The number of 3 or 4 prong events listed according to the number of detected muons and electrons.

#e	0	1	2	3	4
#μ					
0	--	9909	4059	1161	81
1	2477	392	27	1	
2	192	40	3		
3	0	0			
4	0				

Converted photons in both electromagnetic and hadronic events provide the largest single source of multi-lepton events. Therefore, we discard all events in which a converted photon is found. Table 6.2 shows the effect of including this cut.

TABLE 6.2

The number of 3 or 4 prong events listed according to the number of detected muons and electrons after removing converted photons.

#e	0	1	2	3	4
#μ					
0	--	8913	2729	574	8
1	2437	376	17	0	
2	175	37	1		
3	0	0			
4	0				

Most 4 electron events are either bhabha events, where one electron radiates a photon in the pipe material which then converts, or e-e-γ events (8) where the photon has

$$e^+e^-\to e^+e^-\gamma \qquad \gamma\to e^+e^- \tag{8}$$

converted. Most three electron events are this same type except one electron has not been identified or was not tracked. In converted bremsstrahlung Bhabha events, it is difficult for the tracking program to accurately track the 3 electrons that emerge in such a narrow cone particularly at high energies. The fact that all the tracks leave the origin nearly along a single axis provides a simple way to discriminate against these events. By considering only the projection of the tracks in the x-y plane, errors in the momentum reconstruction along the z axis can be ignored with the added benefit of also tagging those events where one of the incident electrons emits initial state radiation.

The following simple algorithm is effective in identifying these multiprong 'coplanar' events: if the average of the cosine of the coplanarity angle between one track and all other tracks in the event is less than -.970, discard the event (see Figure 6.3). The effects of this cut are illustrated in Table 6.3.

TABLE 6.3

The number of 3 or 4 prong events listed according to the number of detected muons and electrons after removing converted photons and coplanar events.

#e	0	1	2	3	4
#μ					
0	--	7714	881	129	3
1	2286	342	17	0	
2	86	27	1		
3	0	0			
4	0				

Several other observations can be made about Tables 6.1-6.3. Although the above cuts reduce the number of 3 and 4 electron events by a factor of 10 and the 2 electron events by a factor of 5, only 25% of the single electron events are removed. Thus, most electrons in events

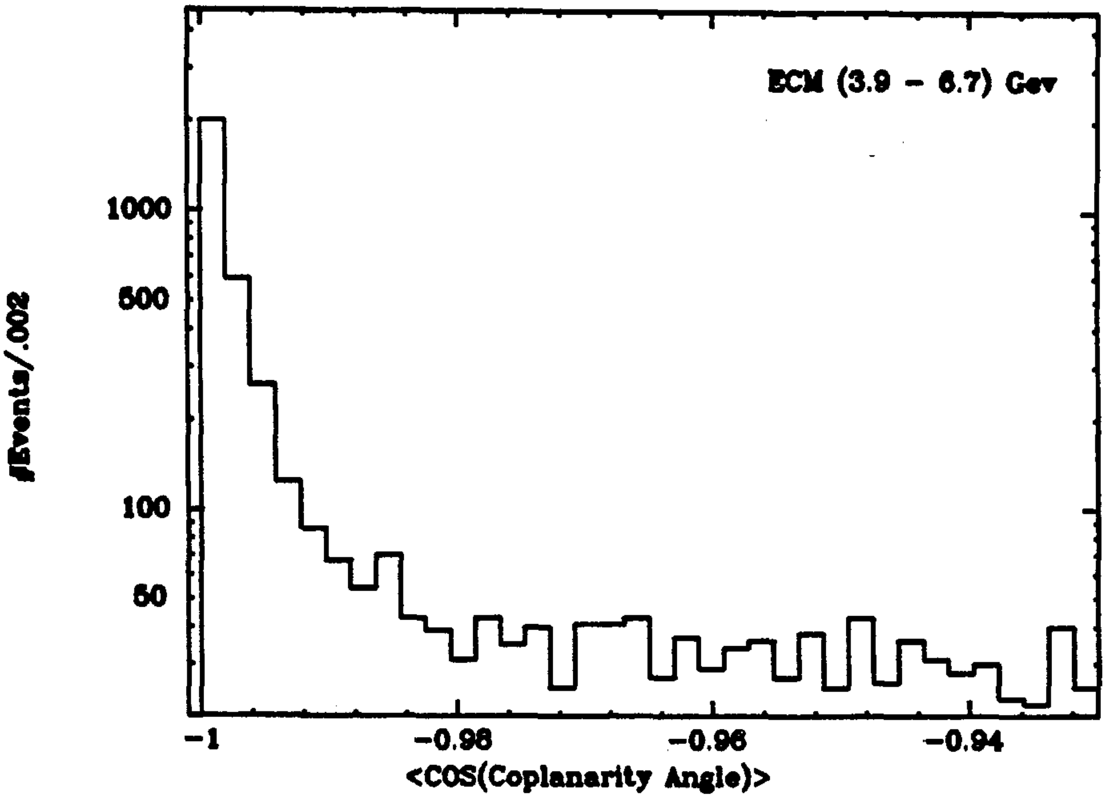

Figure 6.3. Measured 3 prong average coplanarity distribution.

with one identified electron do not come from converted gammas. The coplanarity algorithm removed roughly 1/2 of the 2 muon events and a considerable fraction of the two muon + one electron events. These events are usually muon pair or cosmic events with a knock-on electron as the third track. Most of the remaining μ-μ-e, μ-μ-e-e, and e-e-μ events are consistent with the electromagnetic process listed in (9).

$$e^+e^- \rightarrow e^+e^-\mu^+\mu^- \tag{9}$$

6.6 ACCEPTANCE:

We have calculated the detector's acceptance using the Monte Carlo program assuming two different models for the matrix element for the decay--invariant phase space, and a four fermion V-A type interaction. The two models yield very similar results with the V-A acceptance being slightly larger. In Figure 6.4 we show, for both models, the acceptance for the 3 muon decay as a function of center of mass energy. The acceptance to detect the three charged tracks from any of the decays in (1) is nearly the same, and is independent of the beam energy. However, the requirement that one or more of the tracks also be identified introduces a factor which depends on the beam energy. For example, with a beam energy of 2.0 Gev, it is nearly impossible to identify all 3 muons from the 3 muon decay due to the 700 Mev/c muon system momentum threshold. As the beam energy increases, the probability of detecting 2 or more muons is enhanced while the probability of detecting only one muon decreases.

In Figures 6.5-6.7, we plot the acceptance for the μee, $e\mu\mu$,

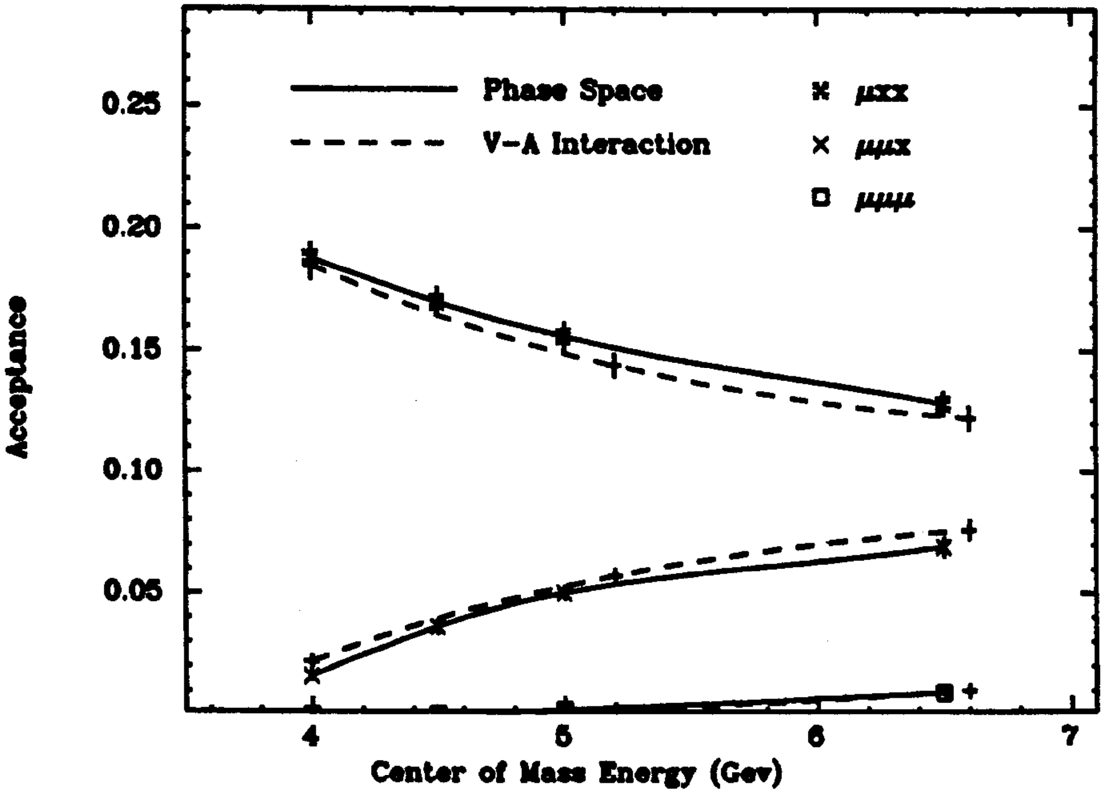

Figure 6.4. Detection efficiency for the tau-->$\mu\mu\mu$ decay as a function of the center of mass energy. Calculations for both invariant phase space and a V-A matrix element are shown for the different lepton identification catagories.

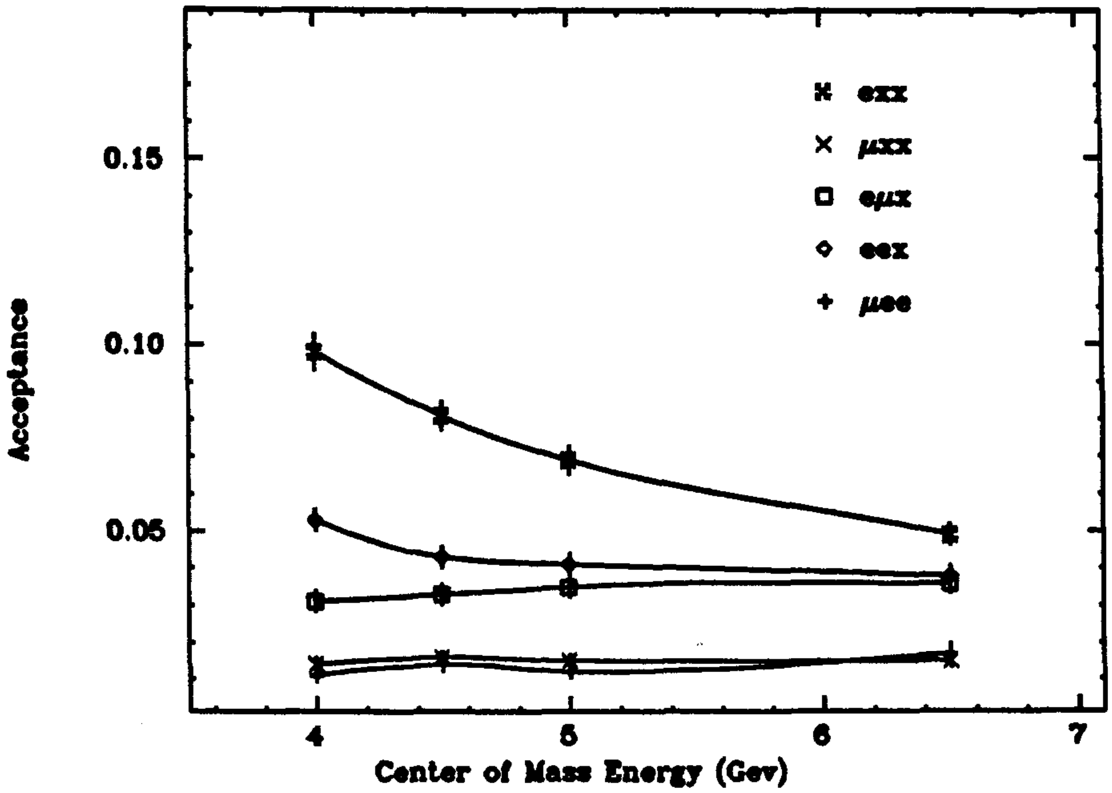

Figure 6.5. Detection efficiency for the tau-->μee decay as a function of the center of mass energy.

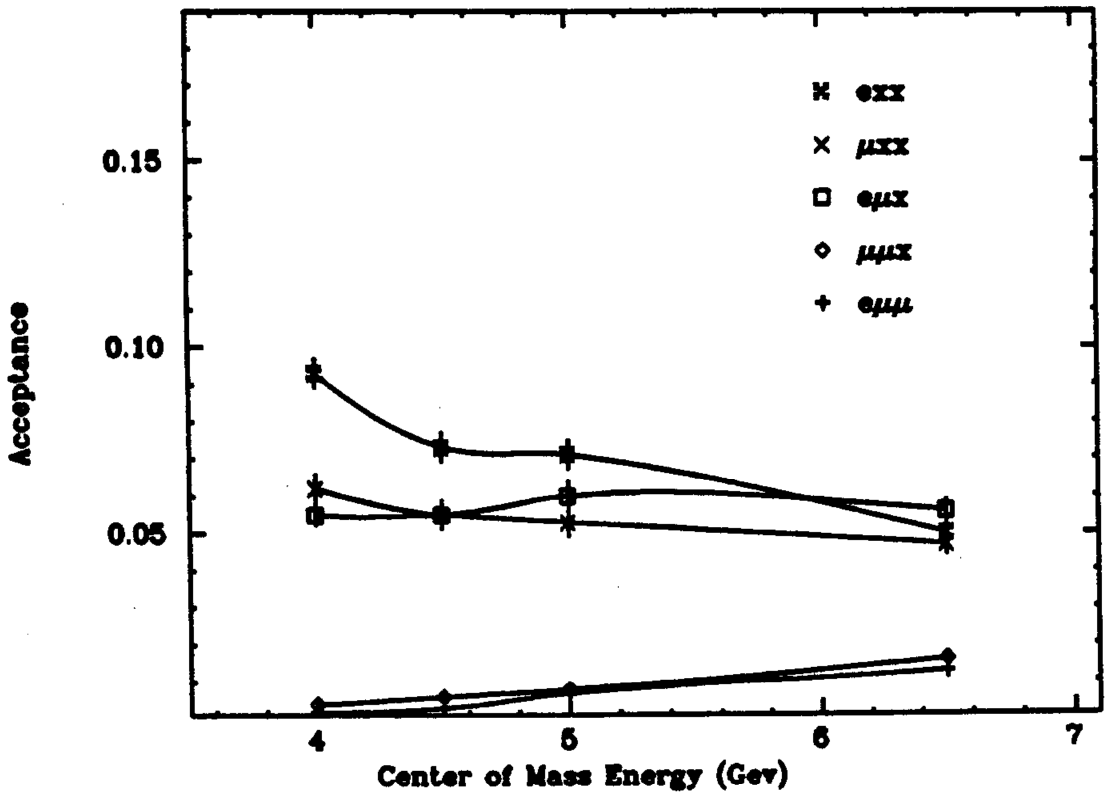

Figure 6.6. Detection efficiency for the tau-->eμμ decay as a function of the center of mass energy.

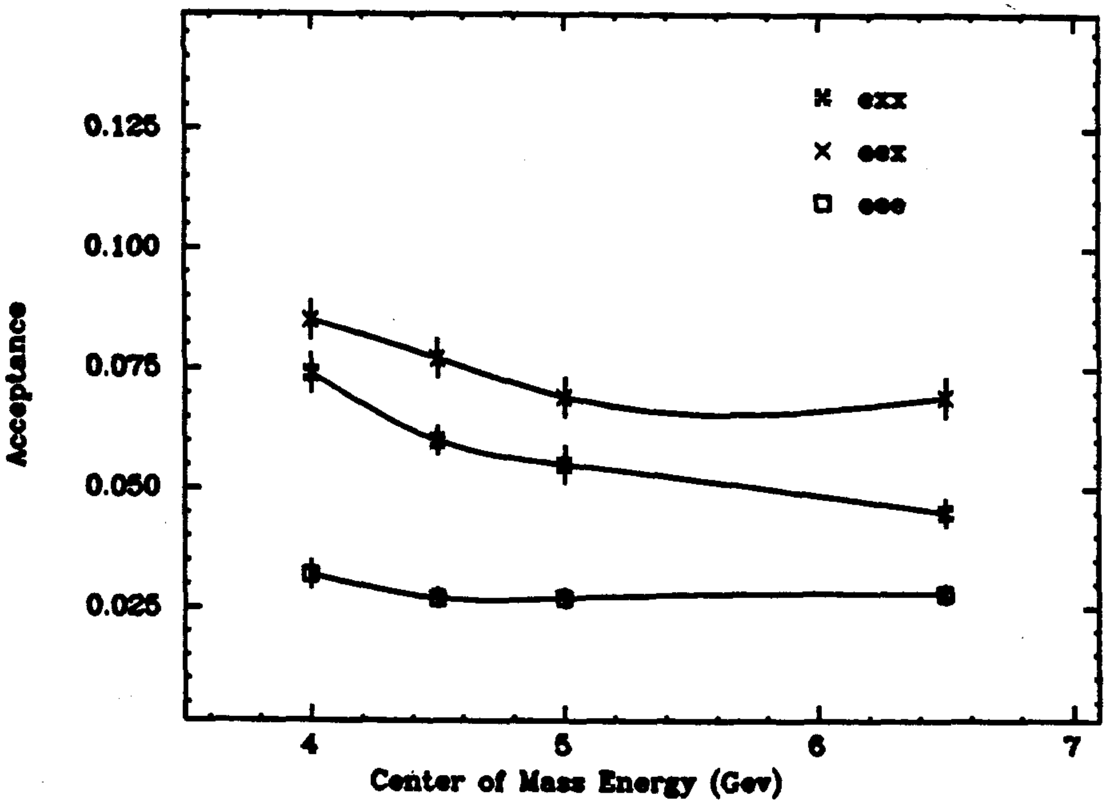

Figure 6.7. Detection efficiency for the tau-->eee decay as a function of the center of mass energy.

and eee tau decays calculated with the phase space Monte Carlo including all analysis cuts.

6.7 BRANCHING RATIO LIMITS:

The measured invariant mass distributions for 3 electron combinations with 1, 2, or 3 identified electrons is shown in Figure 6.8. There is no evidence in the plot for the decay $\tau \rightarrow eee$. Figures 6.9-6.11 show the equivalent plot for the other 3 decays: $\tau \rightarrow \mu ee$, $\tau \rightarrow e\mu\mu$, and $\tau \rightarrow \mu\mu\mu$. Again, no evidence can be seen for the decay of the tau to any three charged lepton combination.

Table 6.5 is a summary of the data for each of the 4 decays in the search. In this table we list, subdivided according to the catagory of identified leptons, the average acceptance for each decay, the number of detected events within the 40 Mev/c^2 region used to define the acceptance, and the 90% confidence level upper limit on the branching ratio. Within any single decay, the results from different sets of identified lepton catagories are statistically independent as different particle combinations contribute to each catagory. By adding the catagories with the least background together, the overall limit on the branching ratios can be improved. Table 6.6 summarizes the best limits obtainable in this way.

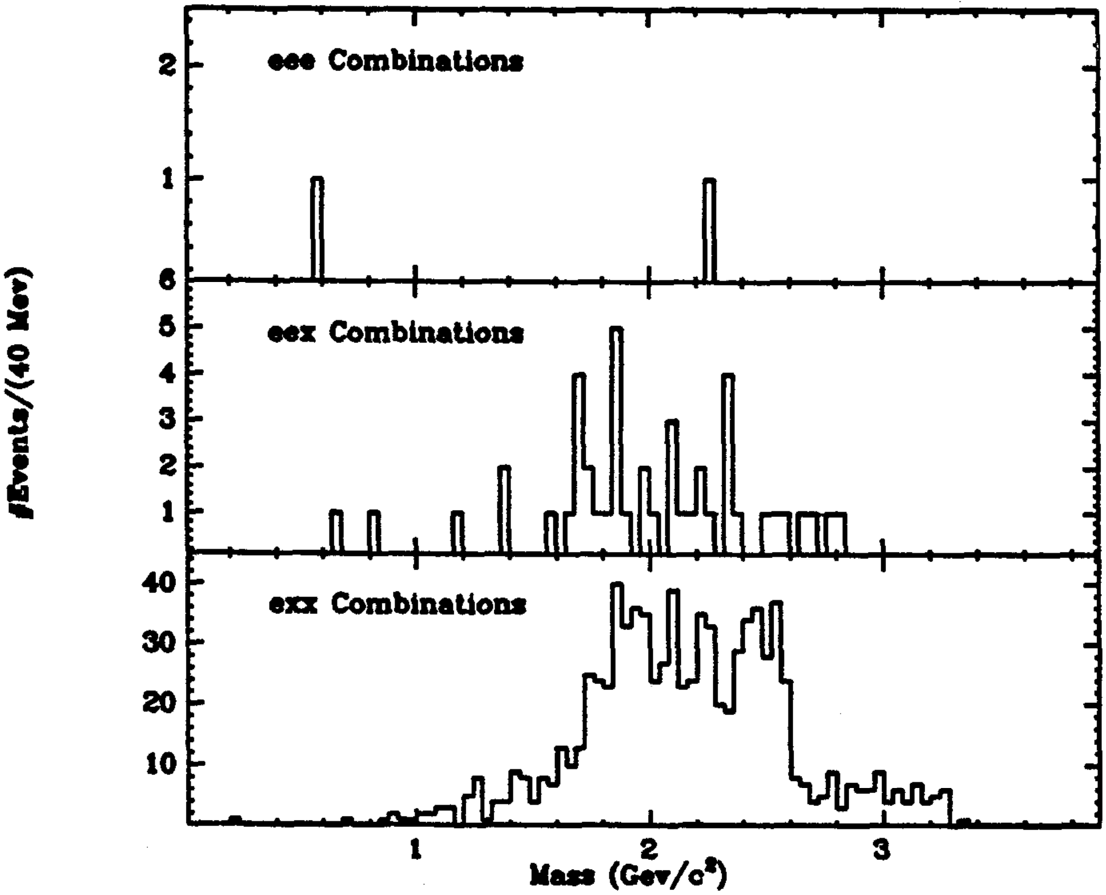

Figure 6.8. Tau-->eee search measured 3 particle beam constrained invariant mass distribution for different lepton identification catagories.

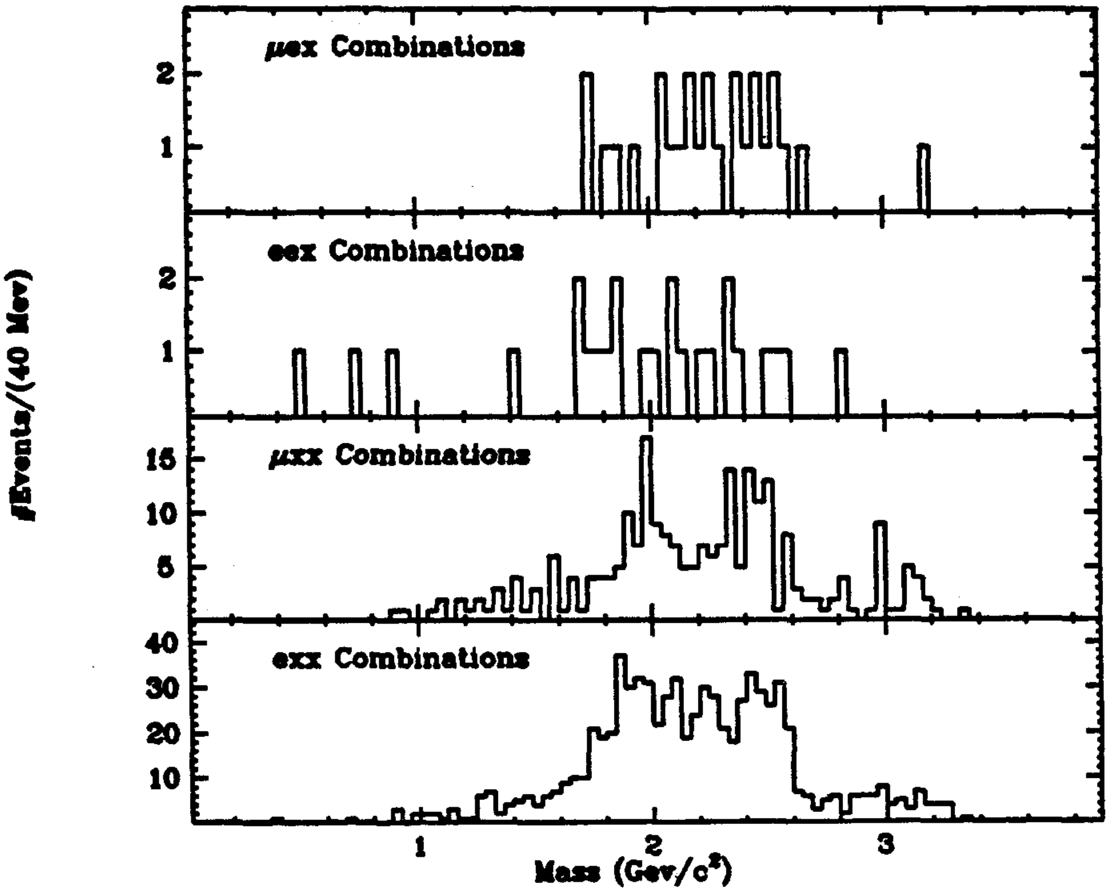

Figure 6.9. Tau-->e μμ search measured 3 particle beam constrained invariant mass distribution for different lepton identification catagories. The eμμ catagory had no events.

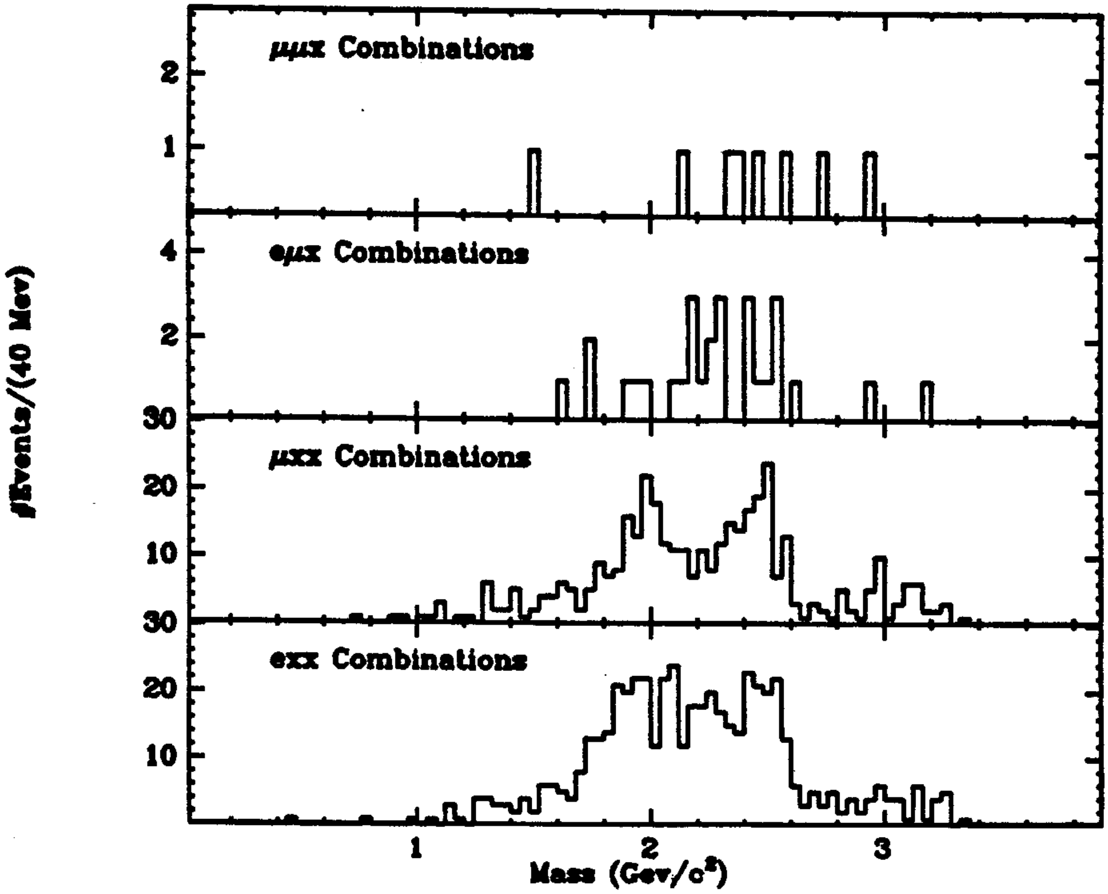

Figure 6.10. Tau-->μee search measured 3 particle beam constrained invariant mass distribution for different lepton identification catagories. The μee catagory had no events.

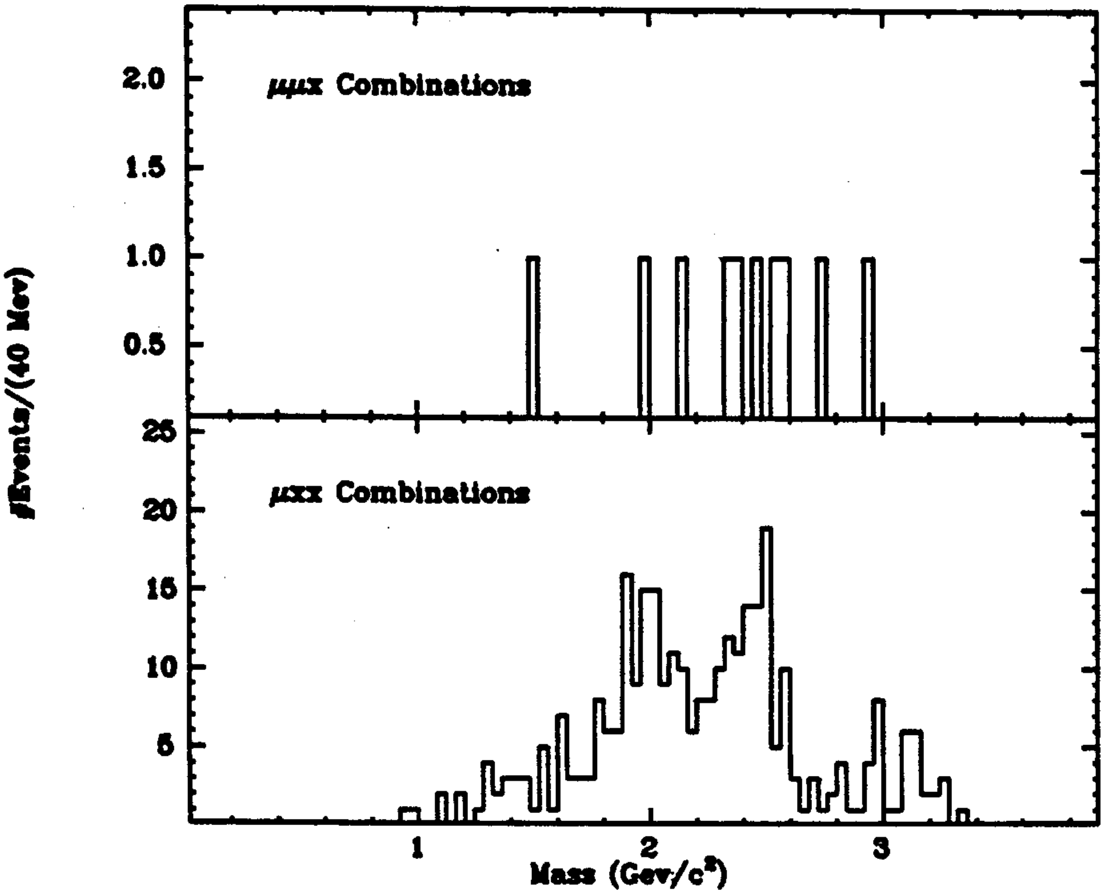

Figure 6.11. Tau-->$\mu\mu\mu$ search measured 3 particle beam constrained invariant mass distribution for different lepton identification catagories. The $\mu\mu\mu$ catagory had no events.

TABLE 6.5

90% confidence level upper limit on tau-> 3 charged lepton decays.

Decay	Lepton-ID	Average Acceptance(%)	#Detected Events	Branching Ratio Upper Limit(%)
μμμ	μxx	15.7	8	.086
	μμx	4.6	0	.052
	μμμ	.28	0	.86
eμμ	μxx	5.4	9	.28
	exx	7.1	13	.28
	μμx	.87	0	.28
	eμx	5.8	0	.042
	eμμ	.68	0	.35
μee	μxx	1.5	4	.56
	exx	7.1	13	.38
	μex	3.4	0	.070
	eex	4.2	1	.10
	μee	1.7	0	.14
eee	exx	5.8	24	.57
	eex	7.3	1	.056
	eee	2.8	0	.086

TABLE 6.6

90% confidence level upper limit on tau-> 3 charged lepton decay obtained by adding different lepton-id catagories.

Decay	Lepton-ID Used	Average Acceptance(%)	#Detected Events	Branching Ratio Upper Limit(%)
μμμ	μμx-μμμ	4.9	0	.049
eμμ	μμx-eμx-eμμ	7.3	0	.033
μee	eex-eμx-μee	9.3	1	.044
eee	eex-eee	10.1	1	.040

References and Notes:

1.) S.M. Korenchenko et al., Zh. Eksp. Teor. Fiz. 70:3, (1976) [Sov. Phys. JETP 43:1, (1976)].

2.) M.L. Perl, Proc. of 1977 Int. Symp. on Lepton and Photon Interactions at High Energies, Deutsches Elektronen-Synchrotron, Hamburg, Germany, (1977), p.145.

Chapter 7

A Search for Charged Lepton+Neutral Hadron Tau Decays

7.1 INTRODUCTION:

The unconventional tau decays discussed in chapters 5 and 6, i.e., the lepton-photon and 3 charged lepton decays, are analogs to the sequential lepton-number violating decays of the muon listed in (1).

$$\mu \rightarrow e\gamma \qquad \mu \rightarrow eee \qquad (1)$$

In fact, the non-observation of these muon decay modes played an important role in the development of the concept of electron and muon lepton-number conservation. As the muon is lighter than the lightest hadron, simple energy conservation rules out any muon decay modes containing a hadron, whether or not they violate lepton number conservation such as

$$\mu \dashrightarrow \pi^0+e \qquad (2)$$

But the large mass of the tau removes this restriction, and we can imagine many decay modes besides those discussed in chapters 5 and 6 which are forbidden by the sequential lepton model. In particular, a search for the electron(or muon)+neutral hadron decay of the tau can provide another test of the sequential lepton hypothesis.

In this chapter we report on a search for the lepton+ neutral hadron tau decays listed in (3).

$$\tau^{+(-)} \rightarrow l^{+(-)}+h^0 \qquad l=e,\ \mu \qquad h=\pi,\ K,\ \rho \qquad (3)$$

Although these are two body decays, the hadrons are short-lived and can be measured only by detecting their decay products. The rho is reconstructed using the charged pions from its $\pi^+\pi^-$ decay. As its large width allows only a loose mass cut to be made, the analysis is very similar to the 3 charged lepton decays discussed in chapter 6. The neutral kaon is reconstructed from the 2 charged pion decay of its short-lived component. The fact that the kzero can travel an appreciable distance from the interaction region before decaying, and the kinematic constraint provided by its narrow width requires a more detailed analysis to be made but results in an improved signal to background ratio relative to the rho-lepton decay. Photons detected in the liquid argon barrel modules are used to reconstruct neutral pions. The shower counter detection efficiency and limited solid angle restrict the acceptance, resulting in a reduced sensitivity for the charged lepton+pizero search.

The data sample, containing 48000 produced tau pairs, is the same used in the previous analyses (see Figure 5.1). The event topology used in the rho-lepton and kaon-lepton search is the same as that used in the three charged lepton decay search (except for one vertex cut in the kaon analysis), while the topology used in the pizero-lepton search is the same as that used in the lepton-photon search except that we require at least two photons to be detected in the event. Other similarities exist between this analysis and the previous ones, and we shall make many references to material previously presented.

The remainder of this chapter is divided into 3 sections. First we will discuss the search for the rho-lepton decay of the tau, followed by the kaon-lepton and pion-lepton searches.

7.2 SEARCH FOR THE DECAYS $\tau\rightarrow e+\rho$ AND $\tau\rightarrow\mu+\rho$:

The search for the rho+charged lepton decay of the tau is very similar to the 3 charged lepton analysis discussed in chapter 5 for the case of the µxx and exx lepton identification categories. The same event topology, background-removing cuts, and beam constraint technique are used. Only three differences exist:

1.) The two x tracks are assumed to be pions and must have opposite charge.

2.) To reduce the background a tighter cut is applied on the measured total energy of the three tracks ($Z=(E(\text{lepton})+E(\pi^+)+E(\pi^-))/E_{beam}$). In the previous analysis, a rather loose cut was used to maximize the acceptance, and it did not change with the center of mass energy. Because of the severe background (the µxx and exx events produced very poor limits which were easily superseded by the other lepton identification catagories), a tighter Z cut must be used. As the resolution in Z changes with the beam energy, the cut is now made to vary with the total energy as shown in Equation (4).

$$x=(ECM-4.0)\ \text{Gev}$$

$$\mu\text{-}\rho: \quad .975(1-.0038x) < Z < 1.025(1+.0038x) \qquad (4a)$$

$$e\text{-}\rho: \quad .975(1-.0038x) < Z < 1.020(1+.0038x) \qquad (4b)$$

The cuts were determined using the Monte-Carlo simulation program and are a compromise between maximizing the acceptance and limiting the background. The μ-ρ cuts (4a) were chosen so that a constant fraction (90%) of the signal events are accepted. Because the e-ρ

background is worse, a slightly tighter Z cut was chosen (4b) to improve the signal to background ratio. Figure 7.1 shows the measured Z distribution for the μ-$(\pi^+\pi^-)$ and e-$(\pi^+\pi$(a0) candidate events along with a Monte-Carlo prediction for tau decays at 5.2 Gev for comparison purposes.

3.) The invariant mass of the two pions must be consistent with the rho mass. In Figure 7.2 we plot the measured 2 pion invariant mass distribution for all μ-$(\pi^+\pi^-)$ candidate events passing the total energy (Z) cut along with the Bright-Wigner distribution expected for the rho (mass 785 Mev/c^2, width 110 Mev/c^2). A small rho signal is seen, and to maximize the signal to background ratio, the $\pi^+\pi^-$ invariant mass is required to be within 100 Mev/c^2 of the rho mass.

The beam-constrained rho-lepton invariant mass distributions obtained after applying the above cuts are shown in Figures 7.3a and b for the μ-ρ and e-ρ candidates. We see no evidence for the decays $\tau\to\mu+\rho$ or $\tau\to e+\rho$ nor do we observe any evidence for pair produced states decaying to a rho and charged lepton at any other mass. Figure 7.4 displays the invariant mass plots on a finer scale near the tau mass along with the expected resolution function for $\tau\to\rho$+charged lepton decays at 5.2 Gev.

The acceptance (using those events within 20 Mev/c^2 of the tau mass) has been calculated with the Monte Carlo simulation program and--averaged over the center of mass energy range represented by the data sample--is 5.5% for the $\tau\to\mu$-ρ decay and 6.5% for the $\tau\to e$-ρ decay. Given that no μ-ρ events are detected within the acceptance window, the 90% confidence level upper limit on the branching ratio for the decay $\tau\to\mu+\rho$ is

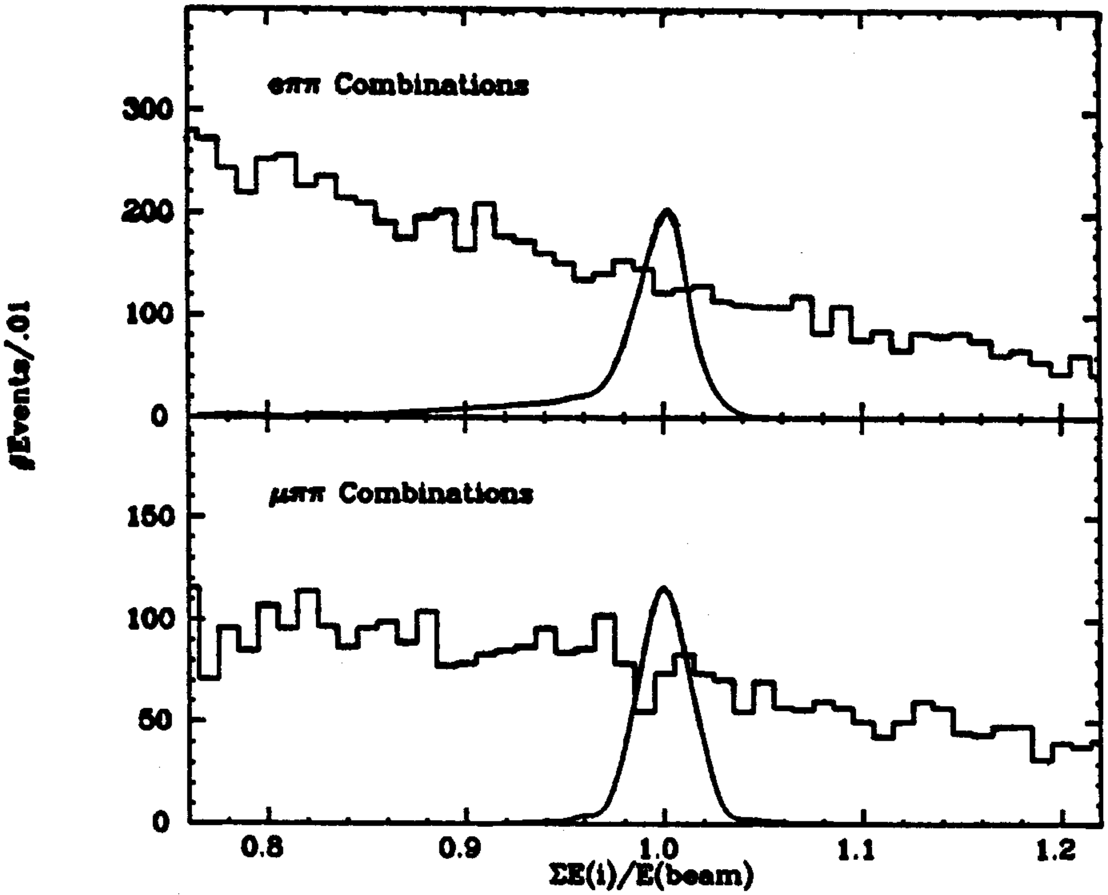

Figure 7.1. Measured sum of particle energies divided by the beam energy for μππ and eππ combinations. The curve shows a monte carlo calculation for ECM=5.2 Gev.

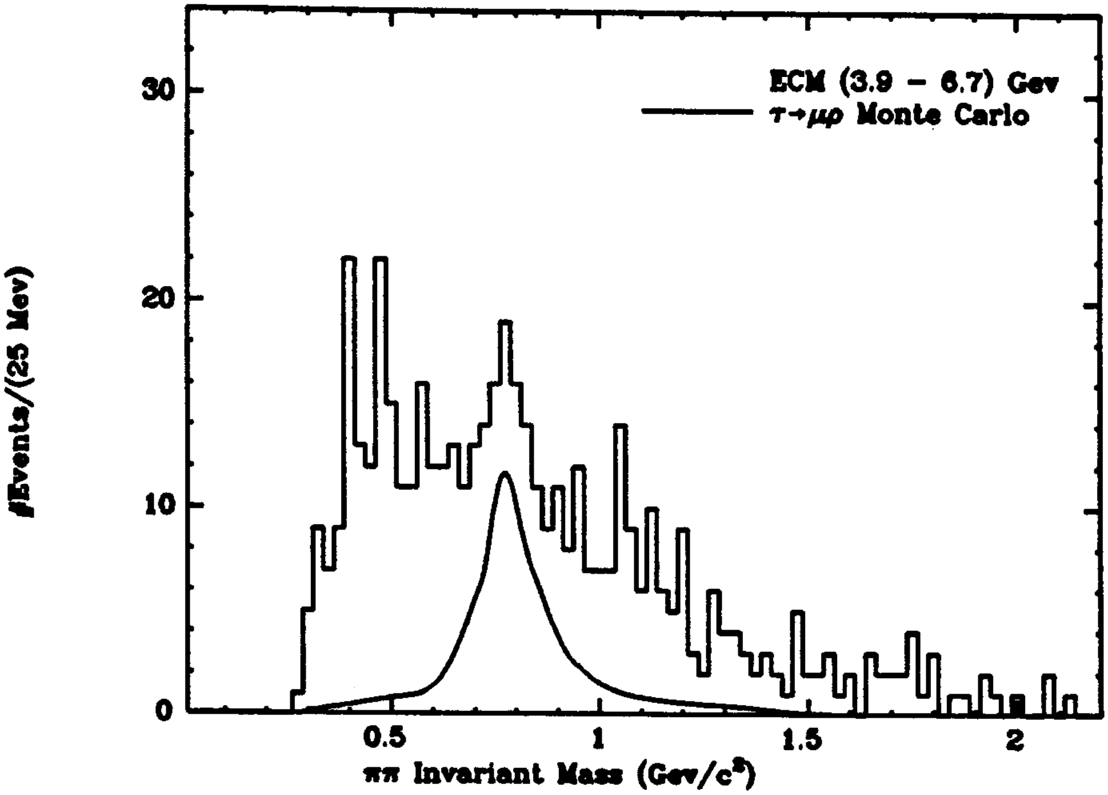

Figure 7.2. Dipion invariant mass distribution for candidates satisfying the Z cut. The curve shows the calculated distribution from the process $\Upsilon \dashrightarrow \mu\rho$.

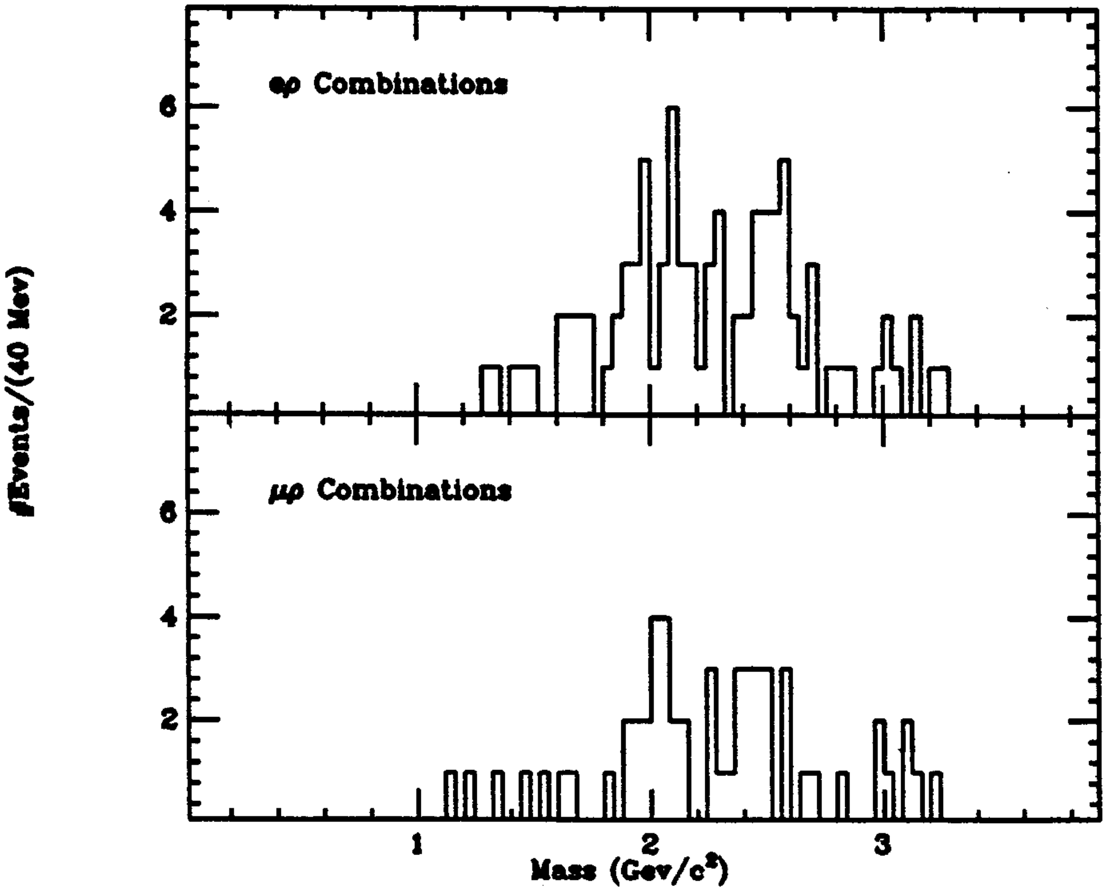

Figure 7.3. Measured rho-lepton constrained invariant mass distributions for tau-->$\mu\rho$ and tau-->$e\rho$ decay search candidates.

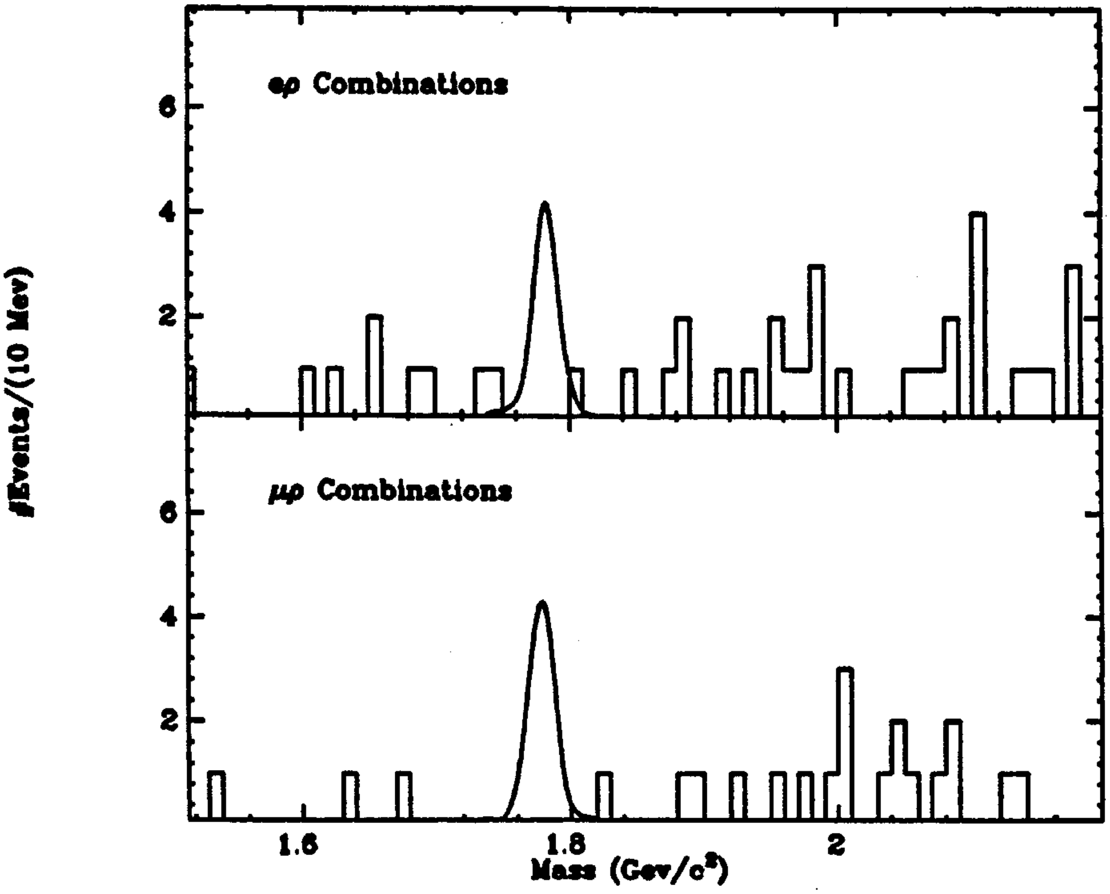

Figure 7.4. Rho-lepton constrained invariant mass distribution (Figure 7.3) shown with an expanded scale. The calculated resolution function is also shown.

$$BR \leq 2.3/(96000*.055) = .044\% \qquad (90\%\ CL) \qquad (5)$$

There are also no e-ρ events detected within the acceptance window. Thus the 90% C.L. upper limit on the branching fraction for the decay $\tau \to e+\rho$ is

$$BR \leq 2.3/(96000*.065) = .037\% \qquad (90\%\ CL) \qquad (6)$$

7.3 SEARCH FOR THE DECAYS $\tau \to e+K^0$ AND $\tau \to \mu+K^0$:

The search for the charged lepton + neutral kaon (kzero) decays of the tau is somewhat more involved than the rho+charged lepton search. When produced, the neutral kaon exists as an equal fraction of a short-lived (ct=2.7 cm) and a long-lived (ct=1554 cm) component. Although the long-lived component will escape the drift chamber before decaying, the short lived one can be detected via its $\pi^+\pi^-$ decay mode (branching fraction = 68%). Although the net acceptance for the kzero+charged lepton decay will be reduced over the rho case by a factor of .34, the fact that the kaon decay vertex is most often located away from the primary vertex can be used to significantly reduce the background. We can no longer, however, demand that the two pion tracks originate in the primary vertex. But all the other vertex, topological, and background removing cuts used in the 3 charged lepton tau decay search are retained.

The narrow width of the kaon allows an additional constraint to be applied to the measured pion track parameters, but we will see that this results in only a negligible improvement (3%) in the tau mass resolution. The algorithm which reconstructs neutral kaons from drift chamber tracks is discussed below.

7.3a) Neutral Kaon Reconstruction Algorithm:

The kzero reconstruction algorithm is straightfoward and yields a relatively clean kaon sample. We exploit the fact that in the uniform magnetic field of the Mark II, the charged particle trajectories projected in the X-Y plane are circles. The decay vertex is located at one of the two points where the circles intersect, and the invariant mass of the two tracks, calculated with the momenta measured at the decay vertex (not the point of closest approach to the interaction region) is--within errors--the kaon mass. Specifically, two tracks will be called a neutral kaon if they satisfy the following conditions:

1) The tracks must be oppositely charged, and must not be identified as electrons or muons.

2) The "overlap" of the two projected circles is defined as the distance between the two circle centers minus the two circle radii. If the overlap is negative, the two circles do not intersect so the vertex is taken to lie between the circles along the line joining their centers. Otherwise the circles intersect in two points (vertices). Ideally the overlap is non-negative, but measurement errors can result in negative values. Only track pairs with an overlap between -1.0 and 300 cm are considered.

3)The vertex (or vertices) must satisfy several conditions:

   a) The z coordinates of the two tracks at the vertex can be no further than 16.5 cm apart.

   b) The kaon half life and momentum spectrum imply a maximum useful distance of the vertex from the interaction region. Only vertices whose radial distance from the interaction region (R_{xy}) is less than 30cm are used.

c) As the kaon is assumed to come from the primary vertex, its line of flight should point back to the interaction region. Only those vertices are used for which the distance of closest approach between the radial line of flight (determined by the net momentum vector) and the interaction region is less than .60 cm. If R_{xy} is greater that 1.5 cm, the vertex must lie on the same side of the interaction region as the net momentum vector.

If both vertices pass the vertex cuts, it is ambigious which vertex is the real one. Since the reconstructed kaon 4-momentum is the same at each vertex, the main reason to determine the correct vertex (aside from dedx loss corrections) is that the vertex position provides a useful background cut. Since most of the background to the kaon signal comes from tracks which originate (and cross) in the interaction region, if both vertices pass the cuts, we choose the vertex closest to the interaction region so as not to diminish the effectiveness of the vertex position cut.

4) The tracks are corrected for dedx losses in the detector material depending on R_{xy}.

5) Figure 7.5a shows the dipion invariant mass distribution for a sample of candidate tracks. The kzero mass resolution (sigma) is roughly 6 Mev/c^2. Only those pairs with a mass within 18 Mev/c^2 of the kaon mass are retained.

6) At this point a large background from random track combinations with vertices near the interaction region remains. Figure 7.6 shows the

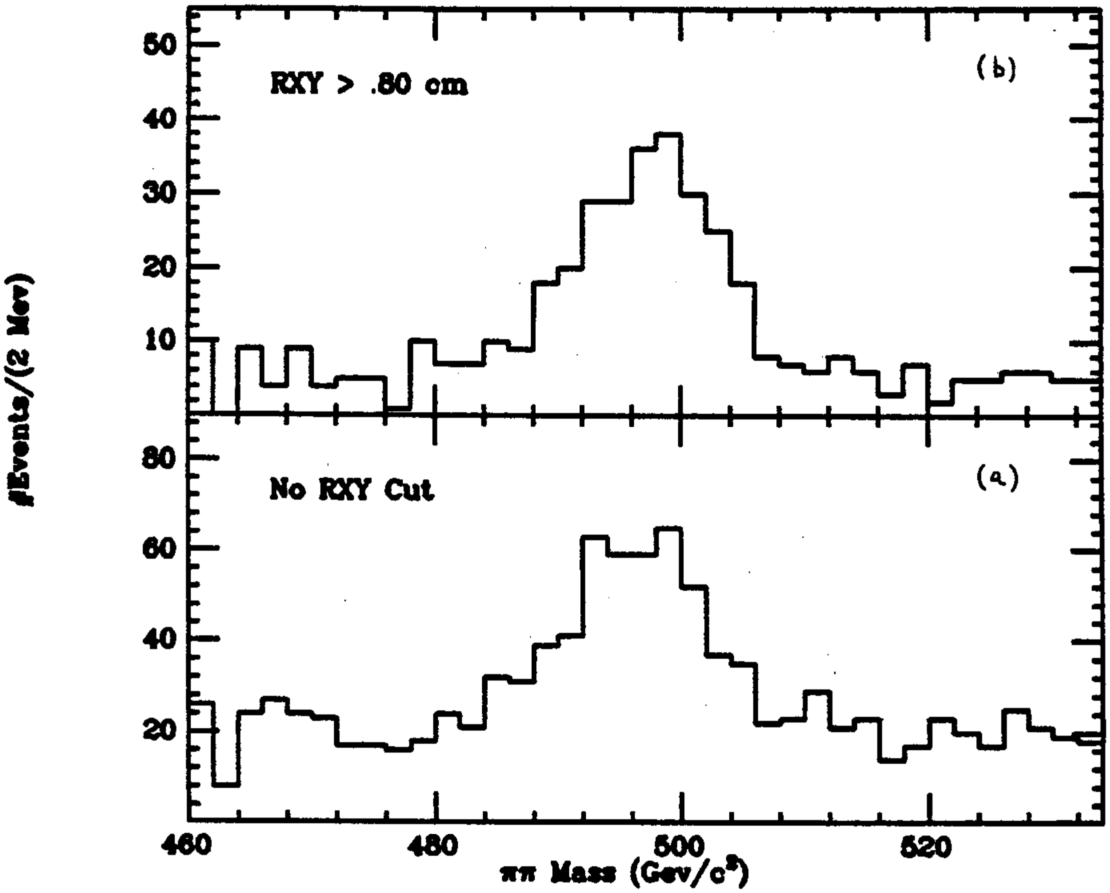

Figure 7.5. ππ invariant mass for pairs satisfying the neutral kaon reconstruction algorithm vertex cuts: (a) with no Rxy cut, (b) with Rxy > .8 cm.

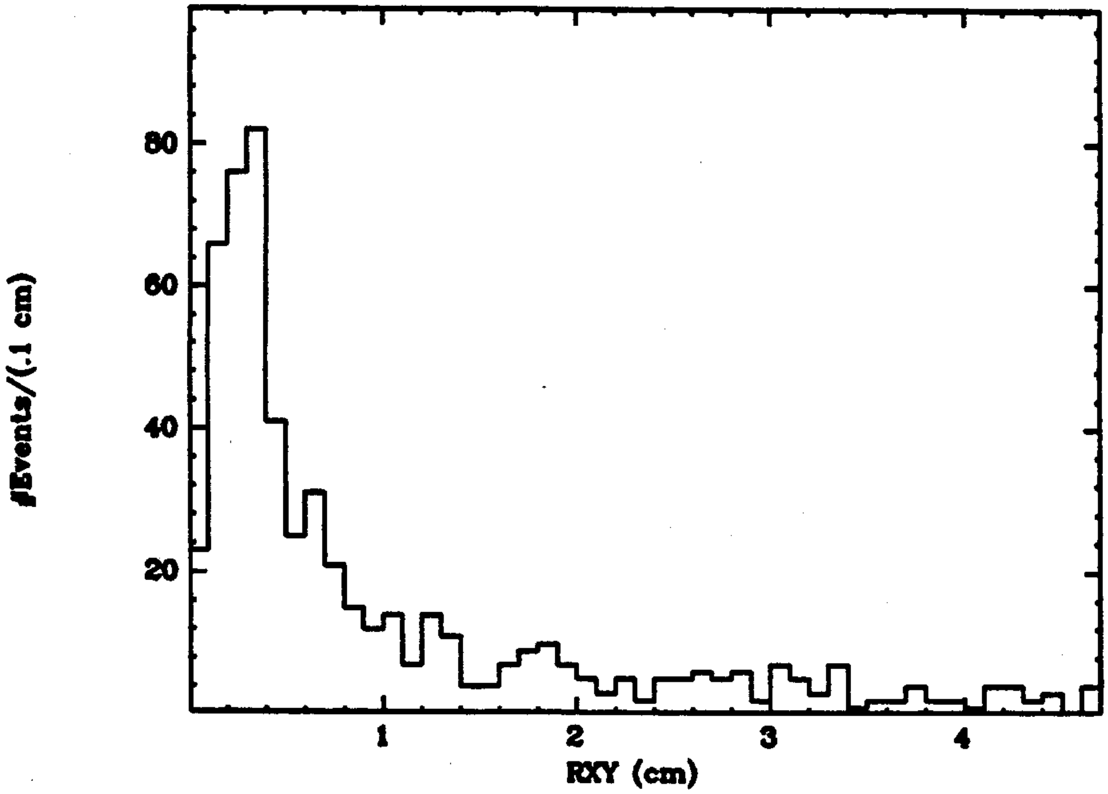

Figure 7.6. Rxy distribution for neutral kaon candidates.

R_{xy} distribution for the candidate sample. Much of the background can be eliminated by requiring R_{xy} to be greater than .8 cm. This results in an additional inefficiency (f) given approximately by Equation (7), which is largest for low momentum kaons but is

$$f=1-\exp(-R_{xy}\min(cm)/(4.6P(Gev/c)) \qquad (7)$$

unimportant here as the desired kaons arise from a two body decay of the tau. The loss induced by this cut ranges from 12% at 4.0 Gev to 9% at 6.6 Gev. Figure 7.5b displays the kzero mass distribution after applying this cut but prior to the kzero mass cut. The overall efficiency for this algorithm to call a pion pair (from a kzero+charged lepton tau decay) a neutral kaon is approximately 75% if both tracks are detected in the drift chamber.

7.3b) Kinematic Constraints and the Tau Mass Resolution.

We now address the question of the kinematic constraints which exist for the kzero+charged lepton tau decay and the effect on the tau mass resolution of fitting the events so as to satisfy these constraints. The beam energy constraint applies as before although the Z cut ($Z=E(total)/E_{beam}$) must be made looser because the momentum resolution is degraded for tracks which do not originate near the interaction region. In Figure 7.7 we show the Z distribution for all μ-K^0 and e-K^0 candidates. Only those candidates which survive the Z cut listed in Equation (8) are used.

$$x=(ECM-4.0)\ Gev$$

$$\mu\text{-}K^0: \quad .960(1-.0077x) < Z < 1.040(1+.0077x) \qquad (8a)$$

$$e\text{-}K^0: \quad .950(1-.0077x) < Z < 1.040(1+.0077x) \qquad (8b)$$

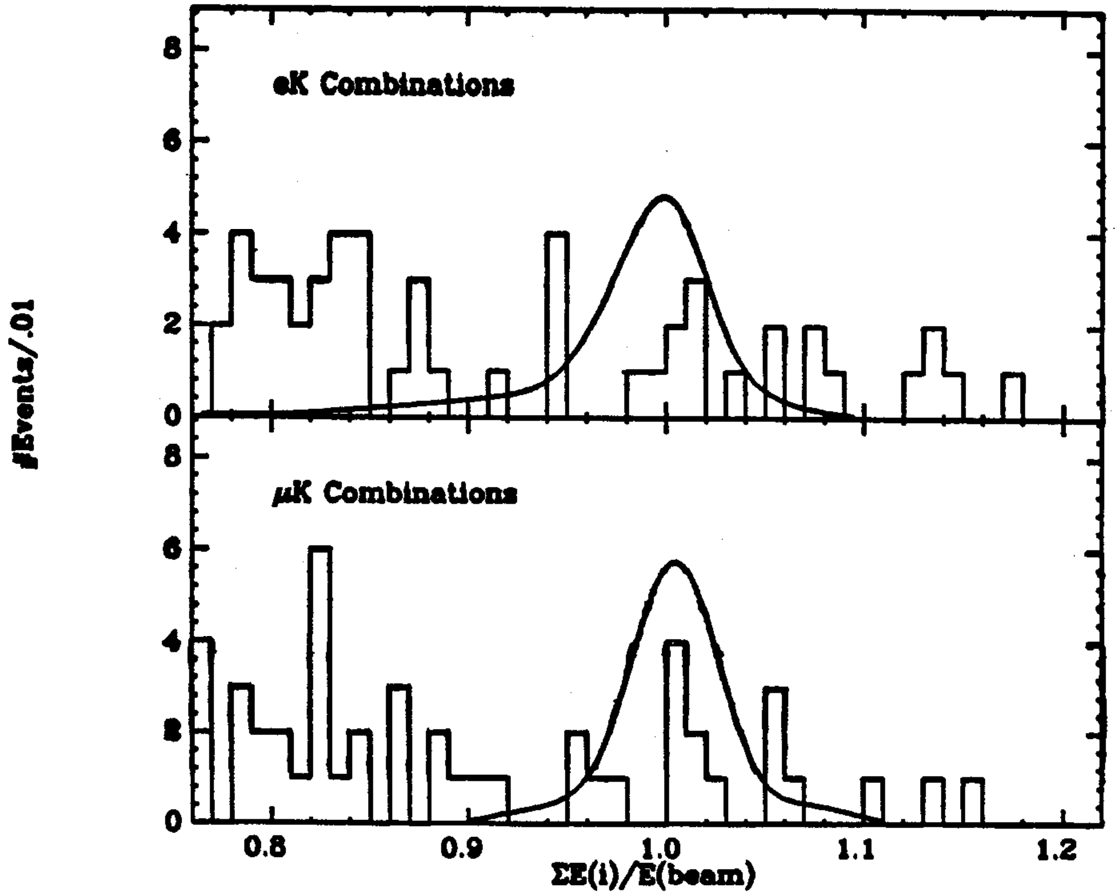

Figure 7.7. Measured sum of lepton and neutral kaon energies divided by the beam energy. A monte carlo calculation is also shown.

These cuts were determined using the Monte-Carlo simulation program and are looser than the rho-lepton decay cuts both because the resolution is poorer, and because the background is much reduced due to the kzero requirement.

For those candidates which pass the Z cut, we can apply the beam constraint technique to improve the lepton-kaon mass resolution as discussed in section 5.4. Figure 7.8 shows the resolution function for tau decays at 5.2 Gev measured with the Monte Carlo both before and after applying the beam constraint. The constraint improves the mass resolution (sigma) from 22 Mev/c^2 to 8.7 Mev/c^2.

The events can also be fit to force the two pions in the decay to have an invariant mass equal to the kaon mass. However, this improves the tau mass resolution only marginally as can be seen in Figure 7.8 where we have also plotted the resolution function after applying just the kaon mass constraint, and after applying both the beam-energy and kaon mass constraint in a 2-C fit. The addition of the kaon mass constraint improves the resolution by only 3%.

7.3c) Limits on $\tau\rightarrow\mu+K^0$ and $\tau\rightarrow e+K^0$ Decays:

The constrained K^0-μ and K^0-e invariant mass distributions are shown in Figure 7.9. The distributions contain no evidence for a charged lepton+kzero decay of the tau or of any other particle in the mass range accesible to this experiment. The acceptance for these decays has been calculated using the Monte Carlo simulation program, and averaged over the center of mass energy range represented by the data sample, is 2.4% for the $\mu+K^0$ decay and 3.1% for the e-K^0 decay of

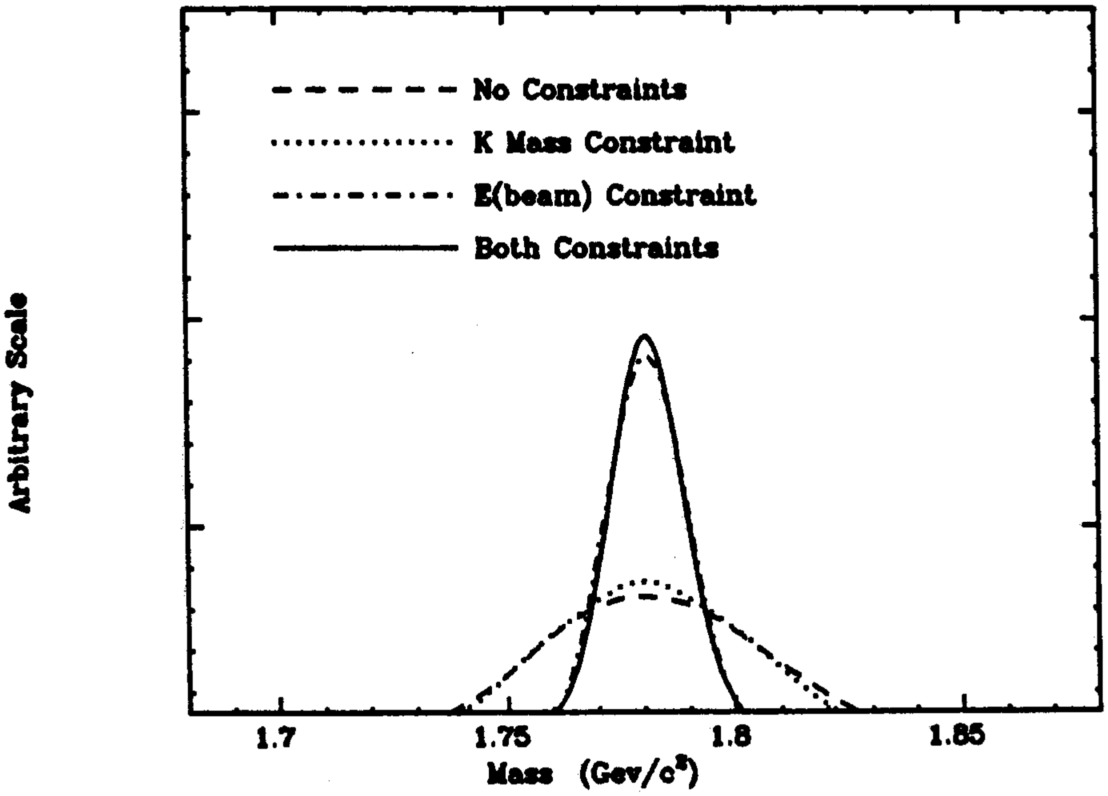

Figure 7.8. Monte carlo calculation of μ+K^0 invariant mass resolution function for different combinations of kaon mass and beam energy constraints.

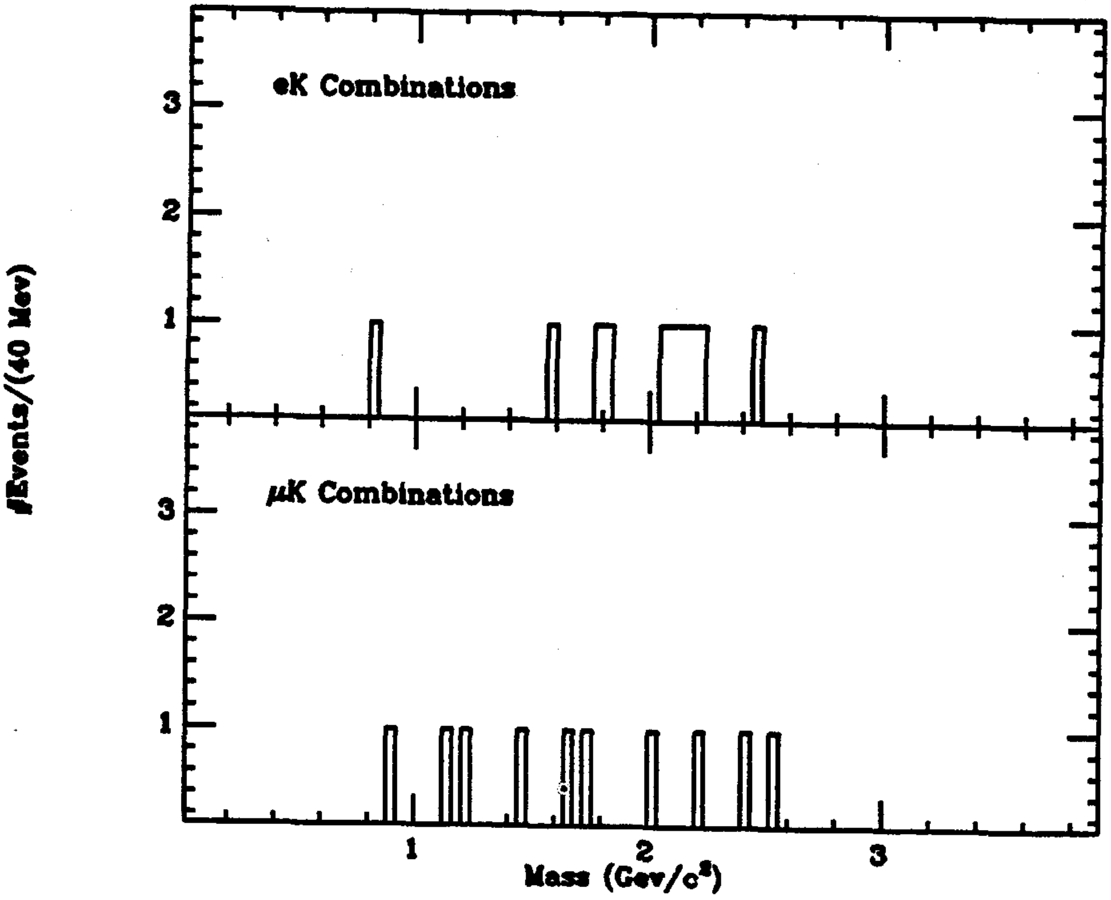

Figure 7.9. Measured K^o-lepton constrained mass distributions.

the tau. Given that no μ-K^0 events are observed which have an invariant mass within 20 Mev/c^2 of the tau mass, we can set a 90% confidence level upper limit on the branching fraction for the decay $\tau \rightarrow \mu + K^0$ of

$$BR \lesssim 2.3/(96000*.024) = .10\% \qquad (90\%\ CL) \qquad (9)$$

The single e-K^0 event observed in the 40 Mev/c^2 acceptance window determines the 90% C.L. upper limit on the branching fraction for the decay $\tau \rightarrow e + K^0$ of

$$BR \lesssim 3.9/(96000*.031) = .13\% \qquad (90\%\ CL) \qquad (10)$$

7.4 SEARCH FOR THE DECAYS $\tau \rightarrow \mu + \pi^0$ AND $\tau \rightarrow e + \pi^0$:

The final charged lepton+neutral hadron tau decays we shall discuss are the $\tau \rightarrow \mu + \pi^0$ and $\tau \rightarrow e + \pi^0$ decays. This analysis is in many ways similiar to that of the search for the charged lepton + photon decay discussed in Chapter 4. A subset of the events used in that analysis are used here-- 2 oppositely charged, acoplanar (>5 deg) tracks which originate in the interaction region, one or more of which is identified as a lepton, with 2 or more photons detected in the liquid argon barrel modules --and is therefore subject to the same sources of background. The algorithms discussed in section 5.5 to eliminate events of purely electromagnetic origin are also used in this analysis as they have a negligible effect on the acceptance (<2%) but reduce the background significantly. Because the lepton-pizero mass resolution is dominated by the photon energy resolution, the beam constraint technique yields nearly the same mass resolution as existed in the radiative decay search, and the inclusion of the pion mass constraint improves this somewhat. The acceptance is significantly smaller, however, as the two photons from the decay must be detected, and the sensitivity of this search is correspondingly reduced. We begin by discussing the algorithm used to reconstruct neutral pions from photons detected in the liquid argon barrel modules.

7.4a π^0 Reconstruction:

The K^0 reconstruction algorithm discussed in section 7.3 yielded a very clean sample of neutral kaons because it employed both the kzero mass constraint and vertex constraints to eliminate the background from random track pairs. In attempting to reconstruct π^0's using photons detected in the liquid argon shower counters, vertex constraints cannot be applied as the pizero lifetime is much too short and no directional information is obtained. Thus, only the pion mass constraint is available for use in identifying pizeros. Coupled with the low energy resolution of the shower counters, this fact results in a large background to the pizero signal especially for pions with low energy.

The reconstruction algorithm is extremely simple: all photon pairs whose invariant mass is consistent with the neutral pion mass are called pizeros. No attempt is made to resolve the ambiguity if a photon is used in more than one pizero.

The invariant mass is calculated from equation 11

$$m = [2E_1E_2(1-\cos\theta)]^{1/2} \qquad (11)$$

using the photons measured energy and position, and the assumption that they originate in the interaction region. Figure 7.10 shows the calculated invariant mass resolution (rmsd) for isotropically produced pizeros as a function of the produced pion energy. This Monte Carlo

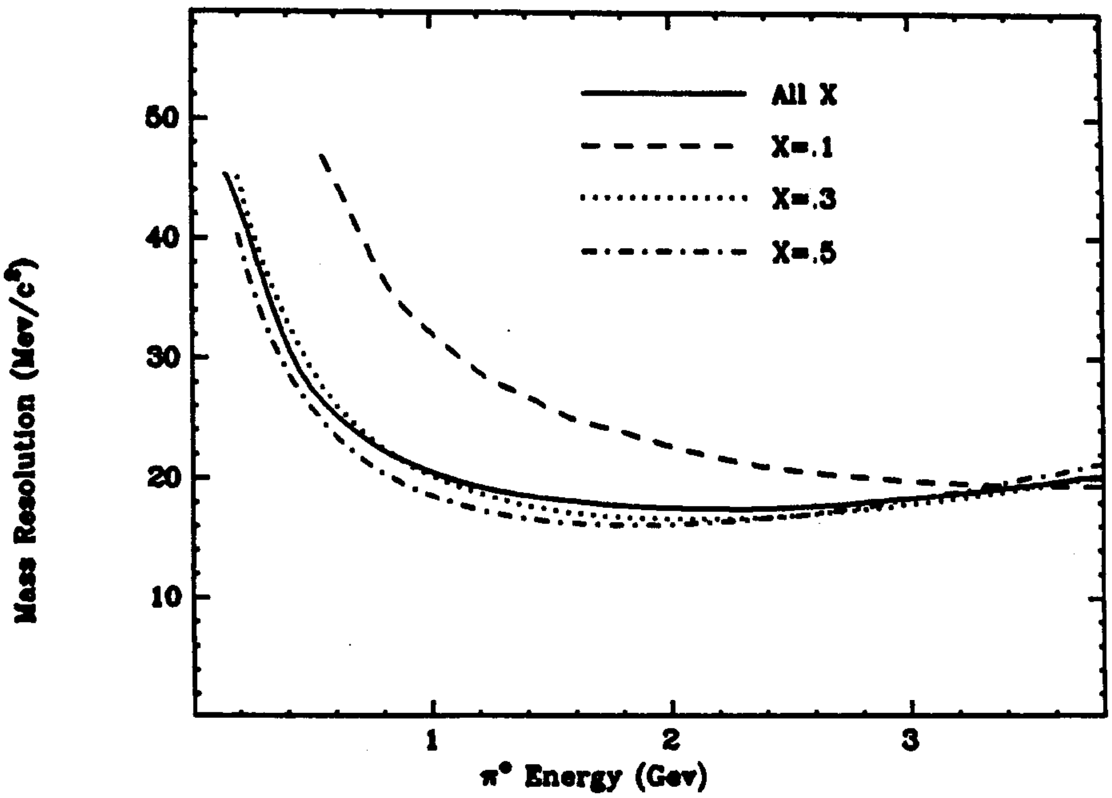

Figure 7.10. $\gamma\gamma$ invariant mass resolution for isotropically produced pizeros as a function of pion energy.

calculation takes into account the barrel solid angle coverage, the measured photon detection efficiency, and assigns gaussian errors for the energy and angular resolutions of the device:

$$\sigma(E)=.13\sqrt{E(Gev)} \qquad \sigma(\phi)=.008 \qquad \sigma(\theta)=.008*\sin^{2}(\theta) \tag{12}$$

The mass resolution has contributions from both the energy and angular resolutions; the angular resolution contribution increases linearly with the pion energy, while the contribution from the shower counter energy resolution decreases like the inverse square root of the pion energy. This is illustrated in Figure 7.11 which shows as a function of pion energy, the fraction of the mass resolution due to the photon angular resolution. For pions of fixed energy, the mass resolution varies with the asymmetry of the decay X

$$X = \mathrm{Minimum}(E1,E2)/(E1+E2) \tag{13}$$

as can also be seen in Figure 7.10 where we show the mass resolution for several X values. In the pion energy range where the photon energy resolution dominates (<2.5 Gev), the mass resolution worsens as the decay asymmetry increases ($X\rightarrow 0$). Thus, the signal to noise ratio will be poorest for pizeros with large asymmetry. This effect is particularly pronounced for high energy photon pairs as they tend to consist of one high energy and one low energy photon due to the nature of the inclusive photon spectrum.

The pizero detection efficiency is limited by the solid angle coverage of the shower counters and the photon detection efficiency. Figure 7.12 shows the pizero detection efficiency as a function of pizero energy for isotropically produced pizeros. The efficiency is a function of the pizero decay asymmetry and is also shown in Figure 7.12 for several values of produced X. Although pions decay uniformly in X

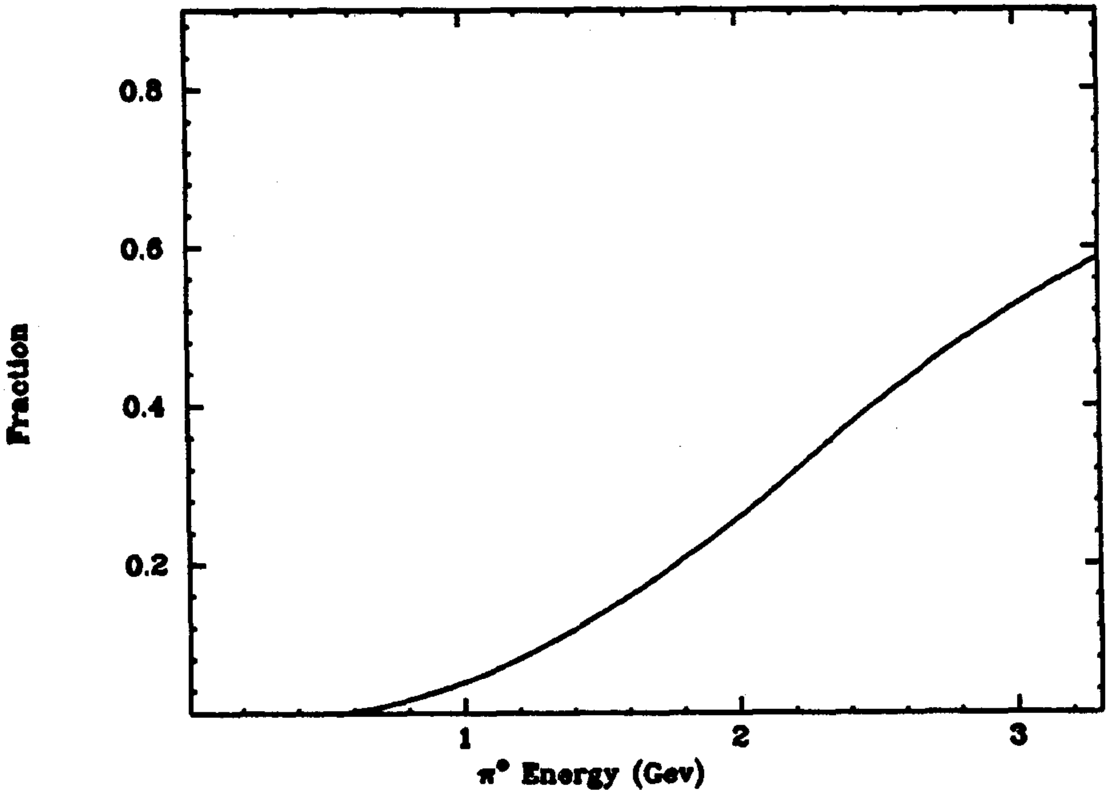

Figure 7.11. Fraction of pizero mass resolution due to shower counter angular resolution as a function of pion energy.

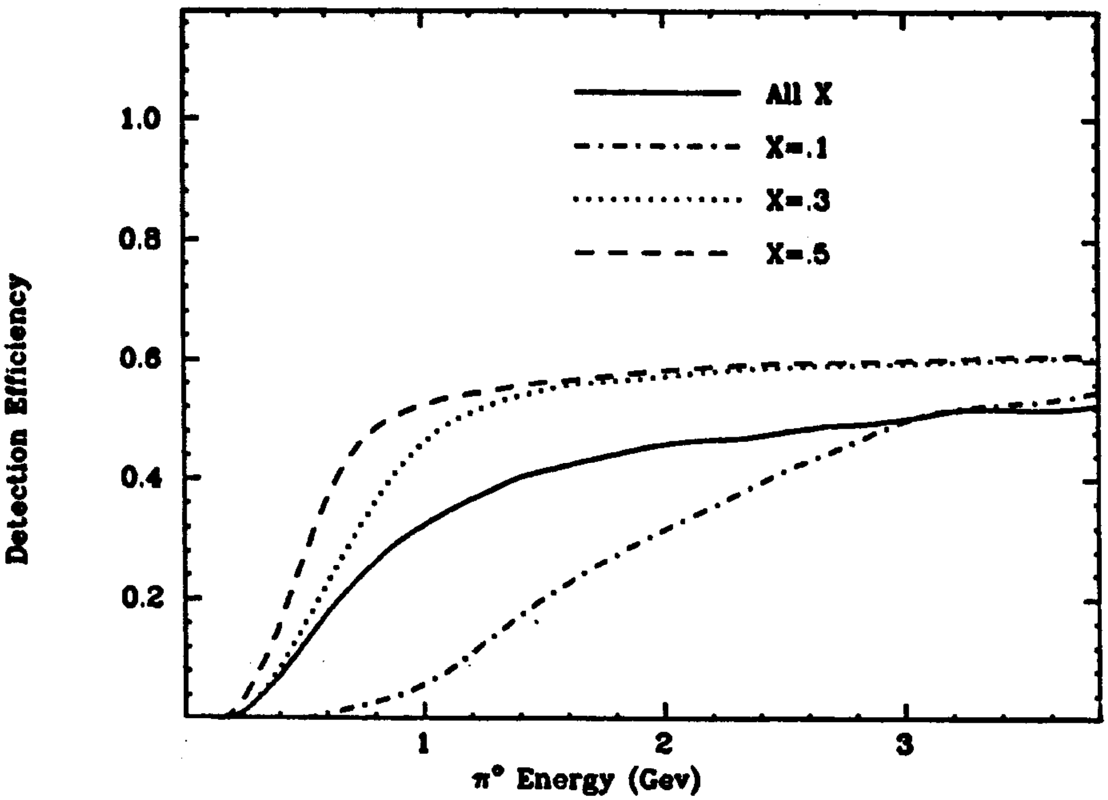

Figure 7.12. Pizero detection efficiency for isotropically produced pions as a function of pion energy for several different values of the pion decay asymetry (X).

within limits given by equation 14,

$$(1-\sqrt{1-(m\ /E)^2})/2 \ < X < .5 \qquad (14)$$

the threshold in the single photon detection efficiency causes a cut-off in the measured X distribution as X approaches zero. This is illustrated in Figure 7.13 which shows a monte carlo calculation of the measured X distribution as a function of produced pizero energy. The cut-off is exactly opposite to what will occur with background 'pizeros' from random photon combinations, and this can be exploited to improve the signal to noise ratio for high energy pizeros.

As an illustration of the above discussion, we plot in Figure 7.14 the 2-photon invariant mass spectrum from a sample of acoplanar 2 prong events. As an estimate of the background we use the mass spectrum measured with photons taken from adjacent events and normalized in the region above 300 Mev/c². A pizero signal is present which has a resolution consistent with the analysis discussed above. However, a large excess of low mass combinations is observed. Some of these come from real processes such as an electron radiating two or more photons during its flight from the interaction region to the shower counters. But most are the effects of fake photons found by the software. To create a photon in the barrel counters, the photon search algorithm requires a 'hit' in two orthogonal layers and the diagonal strip in the U layer which crosses over their interaction point. To discriminate against fake photons caused by fluctuations in the electronic noise, the individual layer energies and the sum of the three layer energies must exceed a threshold. In the presence of a real shower, the fake elimination power of these requirements is reduced, and artificial photons are sometimes generated which use the energy of the real shower

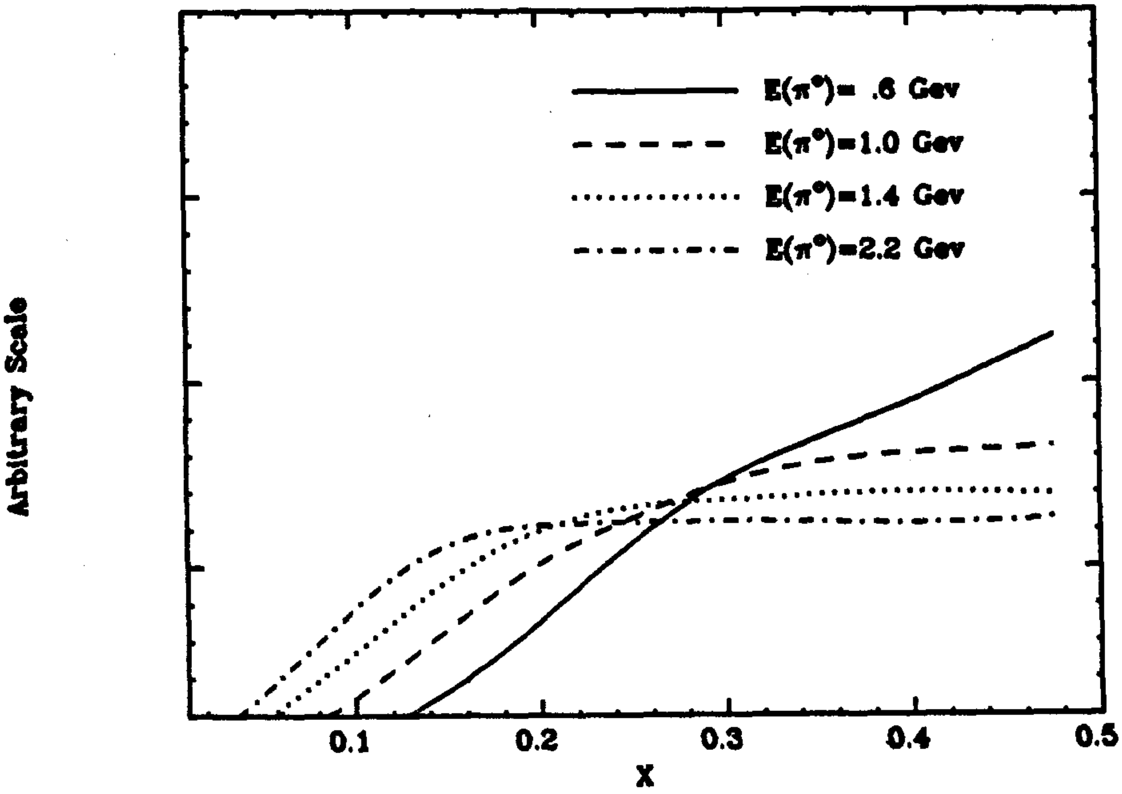

Figure 7.13. Monte carlo calculation of detected pizero asymmetry distribution for several energies. The low X cut-off is a result of the energy threshold in the photon detection efficiency.

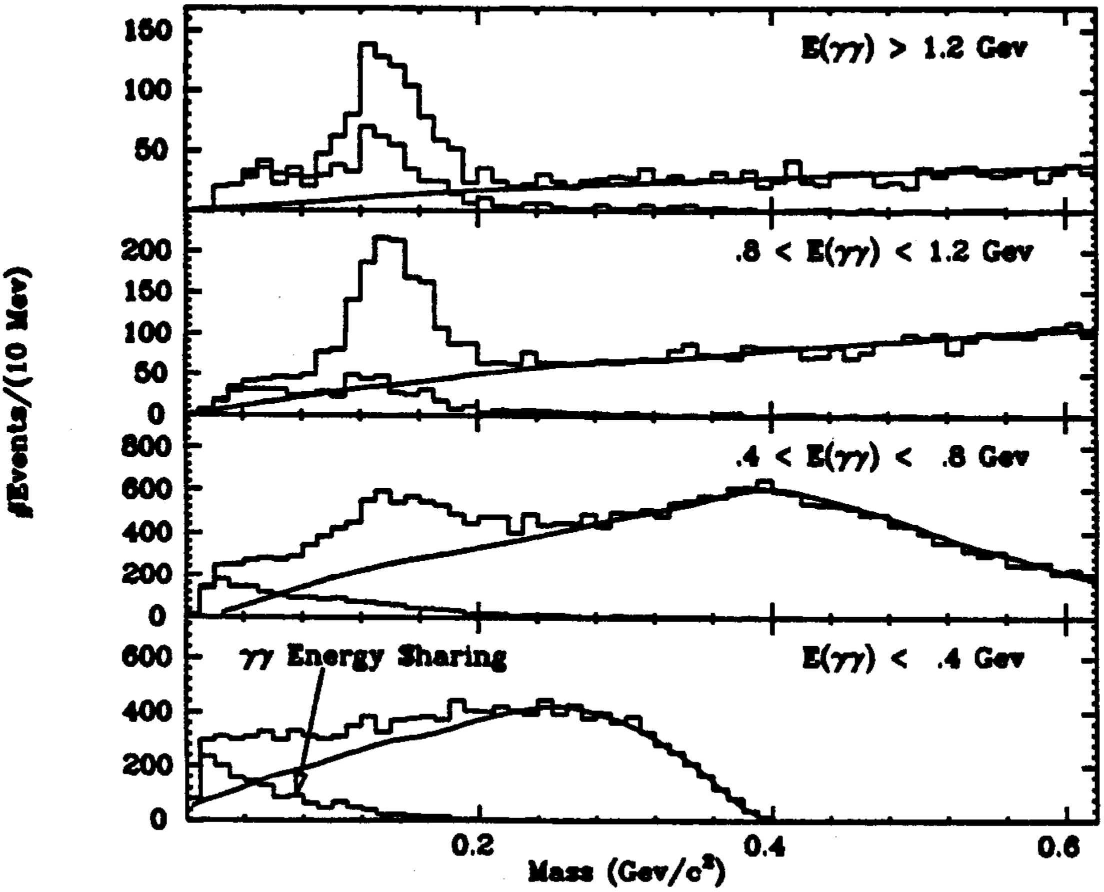

Figure 7.14. Measured $\gamma\gamma$ invariant mass distributions. The curve is a background extimate obtained by using photons from different events. The distributions for photon pairs which share energy in one or more shower counter layers is also shown.

in one or more layers (called sharing). This produces photon pairs with low invariant mass. A large fluctuation in the electronic noise on one strip can partially mimic this situation resulting in two low energy photons which share energy. The invariant mass distribution for those pairs which share energy is also shown in Figure 7.14. It is clear that most of the low mass enhancement arises from these pairs. Note that a large fraction of the high energy pizeros use energy sharing photon pairs. This is to be expected given that as the energy of the and pizero increases, the average photon opening angle decreases, the showers tend to overlap in one or more layers. This will cause the mass resolution to deteriorate faster than expected simply from the angular and energy resolutions for independent photons, and will eventually result in the inability to separate pizeros from single photons. Figure 7.15 plots, as a function of their energy, the measured fraction of identified pizeros (see below) which use photons that share energy. From Figure 7.14 we know that the plot is contaminated with a large amount of background, but this contamination is less significant for the high energy points. The sharing problem is important, but as the majority of pizeros of interest in this analysis are below 2.5 Gev in energy, it is not of fundamental concern here.

Two cuts are used to decide whether a given photon pair is to be called a pizero. The pair is required to have an invariant mass between 50 and 250 Mev/c^2. Pairs which survive this cut are subject to a 1-C fit to the pizero mass in which all the photon parameters are varied, and those which have a chi-square less than 5 are called pizeros. These cuts are loose and maximize the pizero detection efficiency at the expense of a large background.

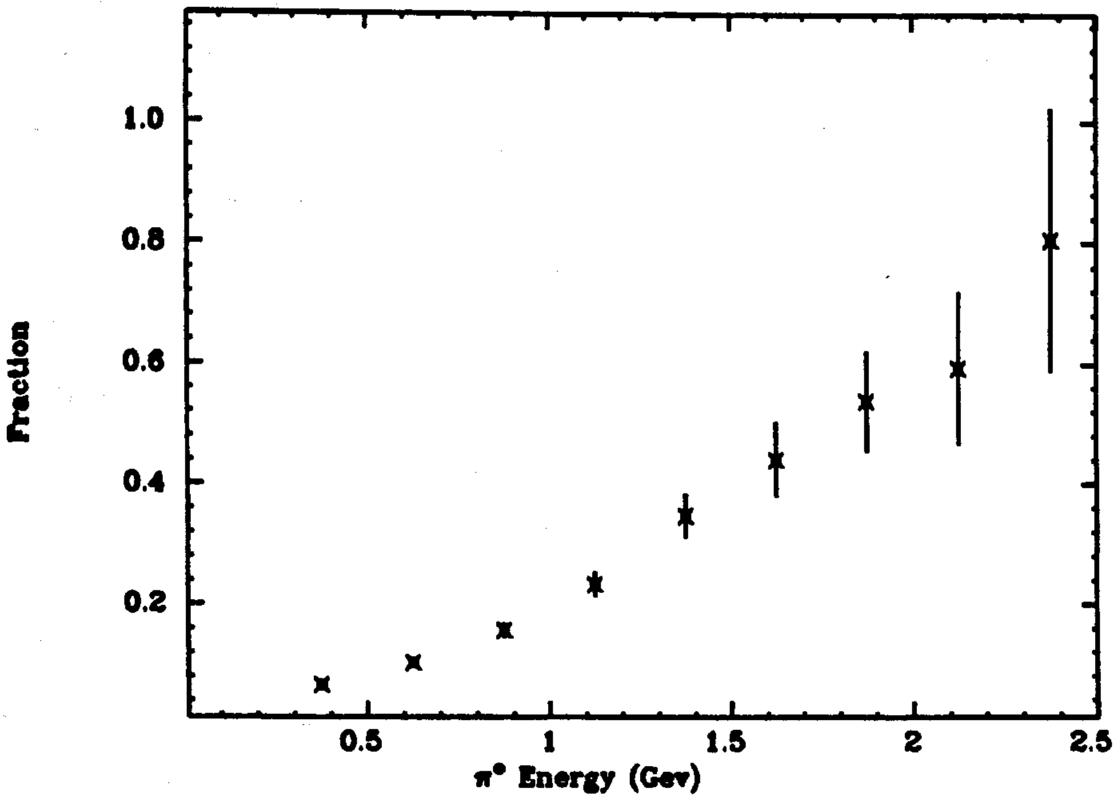

Figure 7.15. Fraction of reconstructed pizeros which use photon pairs that share energy as a function of pion energy.

Photons from which random background pizeros are made come from three sources: real photons from the particle decays (pizeros, etas, etc.), real photons from other processes (bremstrahlung radiation, final state particles in purely electromagnetic events, etc.), or fake photons. Photons from the second catagory are often relatively easy to identify. For example, see the discussion on backgrounds in section 5.5. Fake photons are typically of low energy and can be discriminated against by applying a minimum energy cut. Figure 7.16 shows the photon energy distribution for all events satisfying the topology cuts for the $\tau \rightarrow e + \pi^0$ decay search listed above. To determine the contribution from fake photons, the photon energy distribution from muon-pair events in the same data sample was measured, and is shown in Figure 7.16 normalized to the number of events in the electron sample. Fakes contribute an average of .16 photons/event with 90% having an energy below 250 Mev. However, a substantial number of real photons are present in this energy range, and the pizero efficiency will suffer--particularly for pizeros below 1 Gev in energy--if a minimum photon energy cut is applied to remove this background.

Another way to improve the signal to background ratio exploits the difference in the decay asymmetry (X) distributions for real and background 'pizeros' as discussed above. The measured X distribution for all identified pizeros in the electron sample is shown in Figure 7.17. By accepting only those pairs with X larger than .15, much of the background in the high energy pizeros can be removed. This will reduce the acceptance by no more than 14% for pizeros between 1.5 and 2.5 Gev, but will remove the majority of the background.

The signal to background ratio in the identified pizero sample can

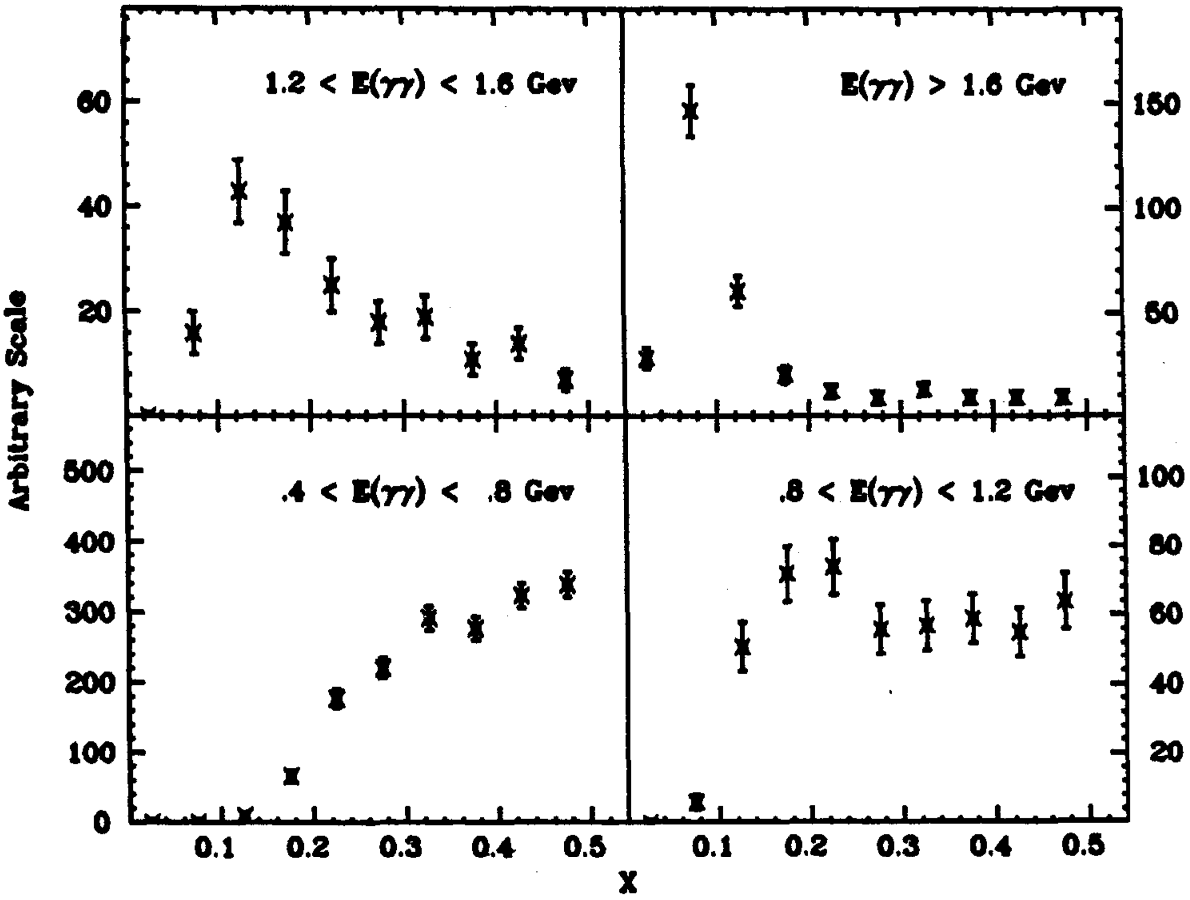

Figure 7.17. Measured pizero decay asymetry (X) for pions in four energy intervals.

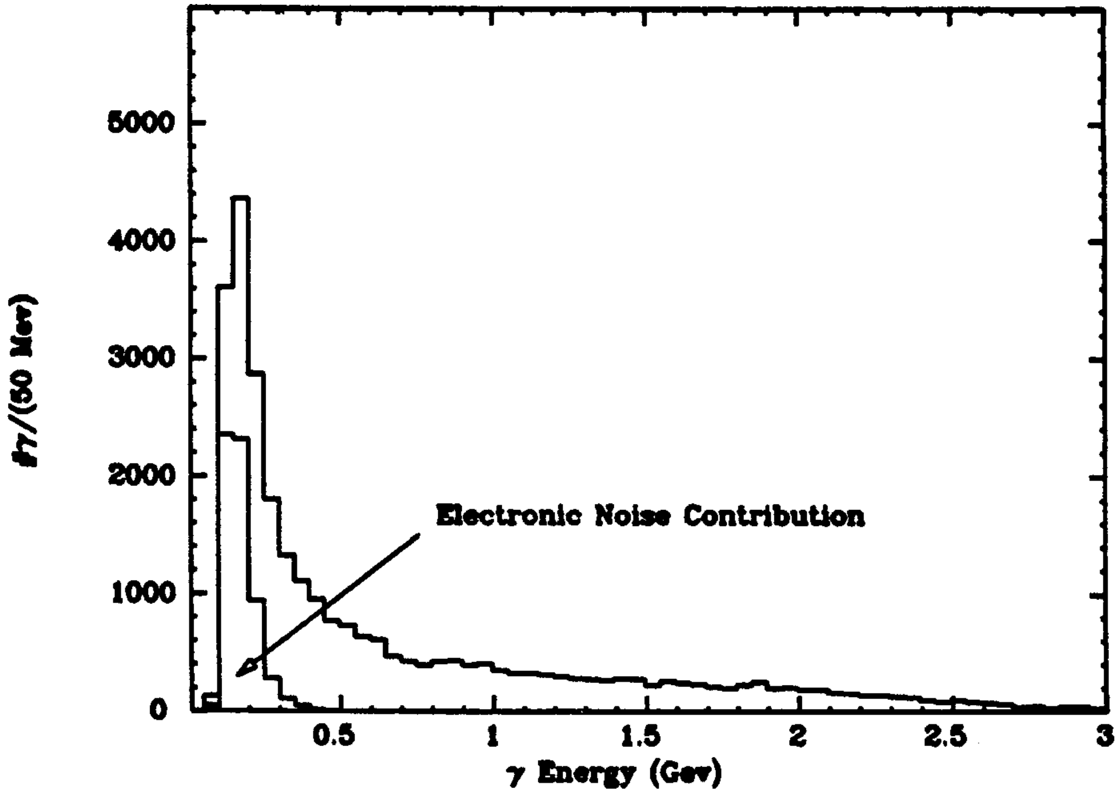

Figure 7.16. Photon energy distribution from pizeros which satisfy the topology cuts for the $\Upsilon \rightarrow e+\pi^0$ decay search. The contribution from fake photons generated by fluctuations in the amplifier noise is also shown.

be estimated from the photon-pair invariant mass distribution. Given the mass and chi-square cuts listed above, the signal to signal+background ratio shown in Figure 7.18 is obtained for the e-π^0 sample. The contamination is large especially for the low and high energy pizeros. However, low energy pizeros are not needed for this analysis while the high energy sample can be improved by implementing the asymmetry cut. A small additional improvement can be obtained by tightening the mass and chi-square cuts but only with a significant reduction in pizero efficiency.

7.4b Decay Constraints and the Tau Mass Resolution:

Having reconstructed the neutral pions, the invariant mass is calculated for all lepton-pizero combinations which have a total energy consistent with the beam energy. As the resolution in ETOT=E(π)+E(lepton) varies with the lepton and pion energy, a cut is applied to the normalized variable Y:

$$Y=(ETOT-E_{beam})/\sigma(ETOT) \tag{15a}$$

$$\sigma(ETOT)=[\sigma(E(lep))^2+\sigma(E(\pi))^2]^{1/2} \tag{15b}$$

$$\sigma(E(\pi))=.13\sqrt{E(\pi)(Gev)} \tag{15c}$$

$$\sigma(E(lep))=.01P\sqrt{P^2+2.25}dE/dP \tag{15d}$$

The square of Y is equal to the chi-square for the 1-C fit constraining ETOT to the beam energy. Figure 7.19 shows the measured Y distribution for both the e-π^0 and μ-π^0 candidates along with the expected distributions for lepton-pizero tau decays calculated with the Monte Carlo simulation program. All combinations for which the magnitude of Y

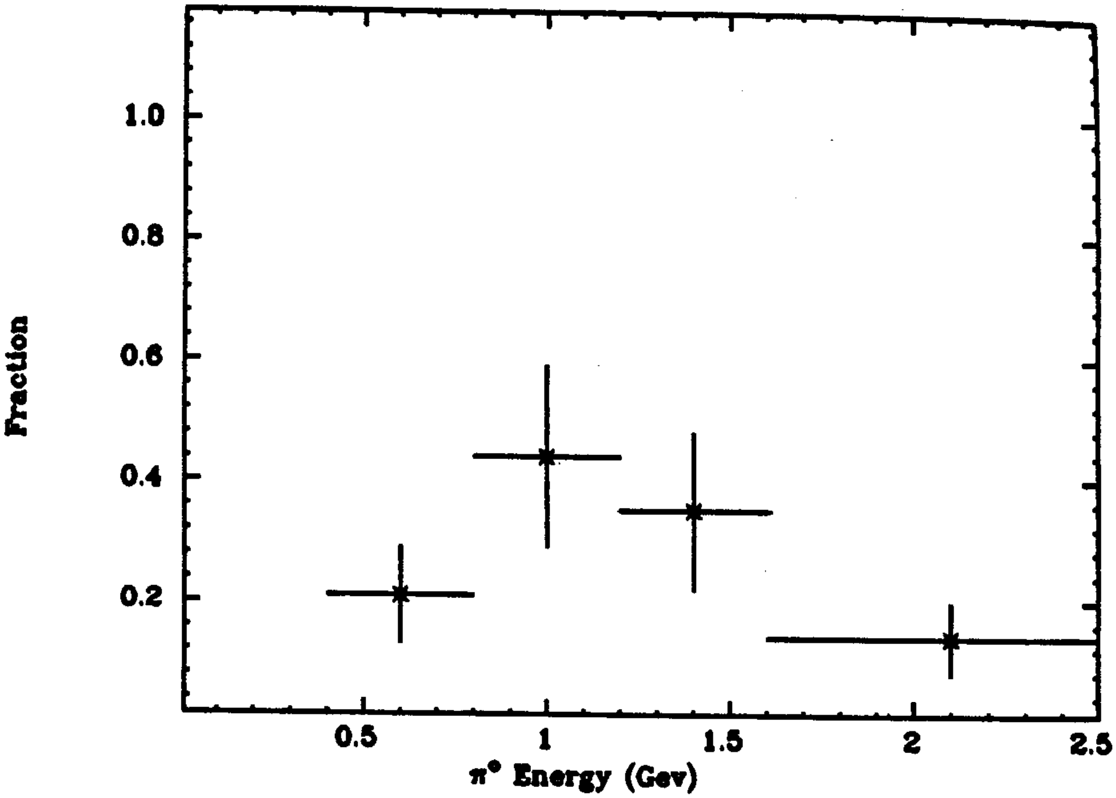

Figure 7.18. Signal/(signal+background) ratio for pizeros in the electron+pizero tau decay search sample.

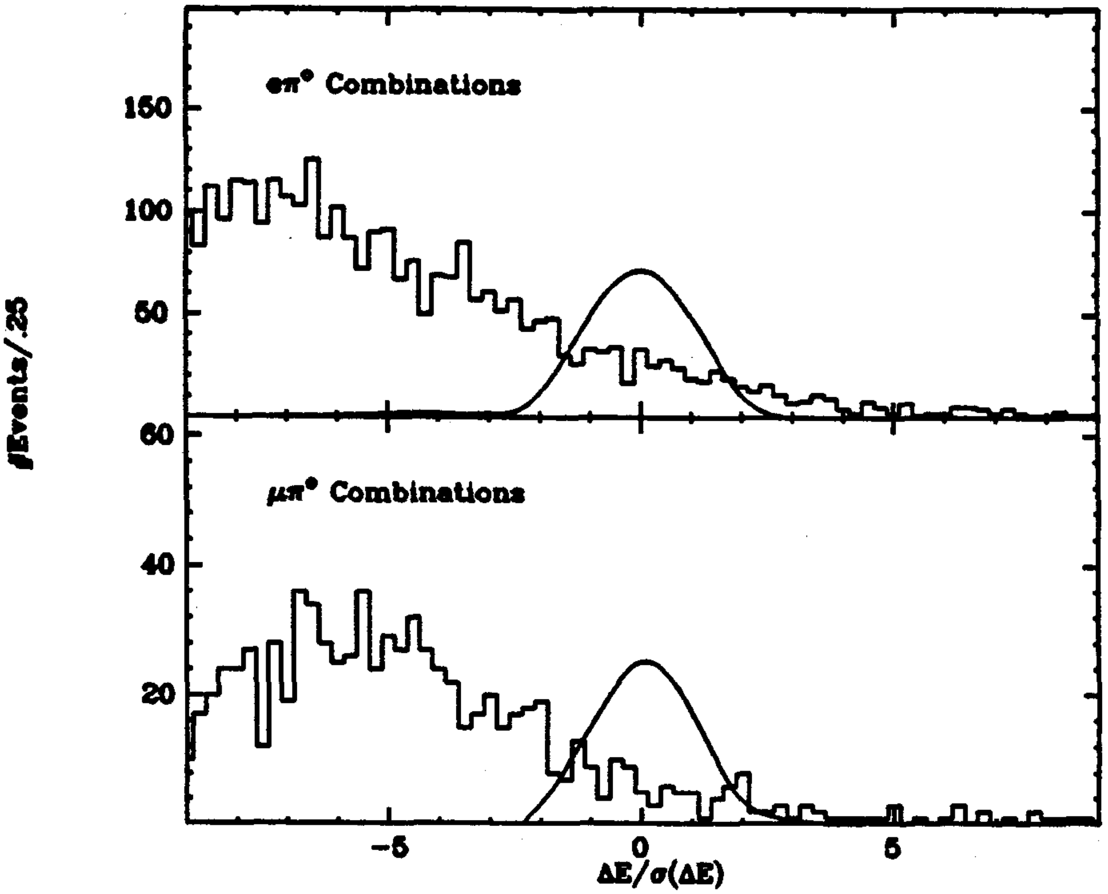

Figure 7.19. Y distribution for lepton + pizero combinations. Monte carlo calculations for the decays tau-->lepton+π^0 are also shown.

is greater than 2.0 are rejected.

The lepton-pion invariant mass resolution using the measured lepton and pion track parameters is approximately 100 Mev/c^2 (sigma). Using the parameters from the 1-C fit to the pizero mass reduces this to 80 Mev/c^2, while employing the beam constraint improves the resolution to 16 Mev/c^2. Performing a simultaneous fit to the mass and beam constraints gives an additional 10% improvement as is illustrated in Figure 7.20. The 2-C fit, however, has the added advantage that the chi-square for the fit is a better test of the decay constraints than the pizero mass and beam energy constraints taken separately. Figure 7.21 shows the measured 2-C chi-square distribution for the μ-π^0 candidates along with the distribution calculated with the Monte Carlo. Candidates with a chi-sqauare larger than 7 are rejected.

The lepton-pizero mass resolution varies with the asymmetry of the decay, and deteriorates rapidly as the lepton energy approaches the beam energy. As the pizero energy resolution is identical to the single photon energy resolution (equation 15c), the mass resolution varies with $X=E(\text{lepton})/E_{\text{beam}}$ in the same way discussed for the lepton-photon decay in section 5.3. To eliminate the X region with poorest resolution, only events with X less than .8 are used.

7.4c Backgrounds

Figure 7.22 plots the constrained lepton-pizero mass for all candidates passing the decay constraints. A large background is present which originates from several sources, and further cuts can be applied to suppress it. As was demonstrated in Figure 7.18, the signal to background ratio in the pizero sample is poor. We first discuss several

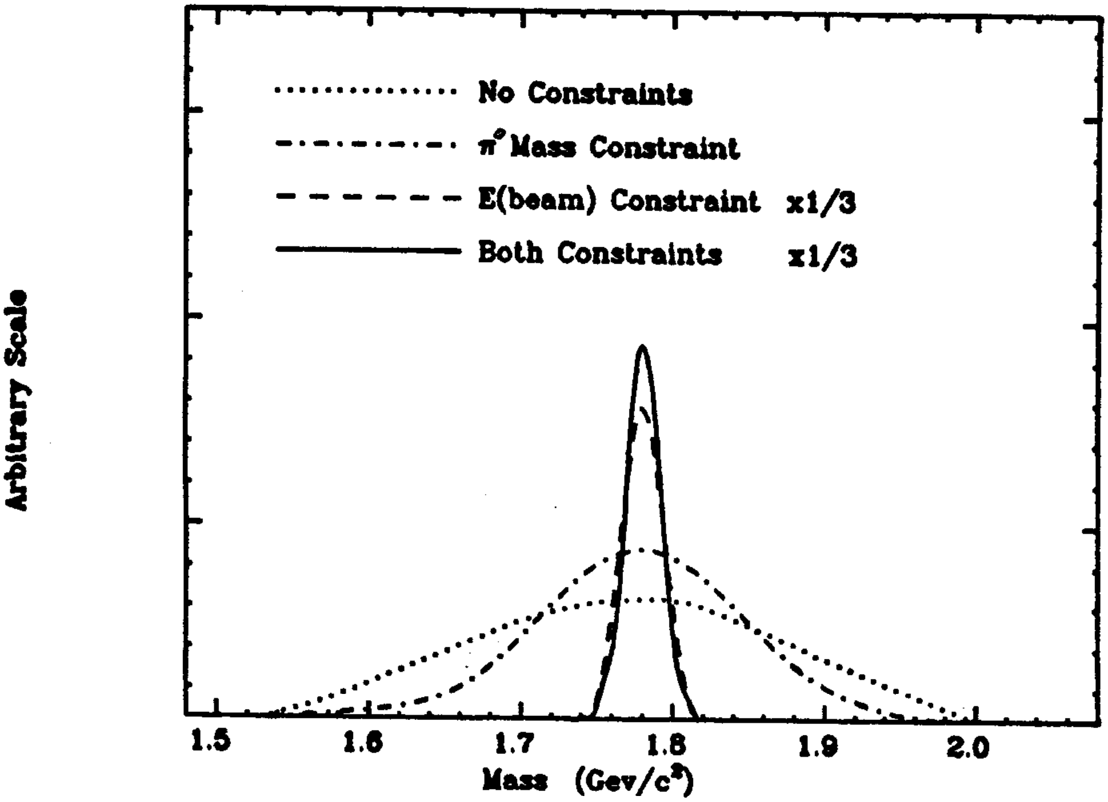

Figure 7.20. Calculated $\mu\pi^0$ invariant mass resolution function for different combinations of pion mass and beam energy constraints.

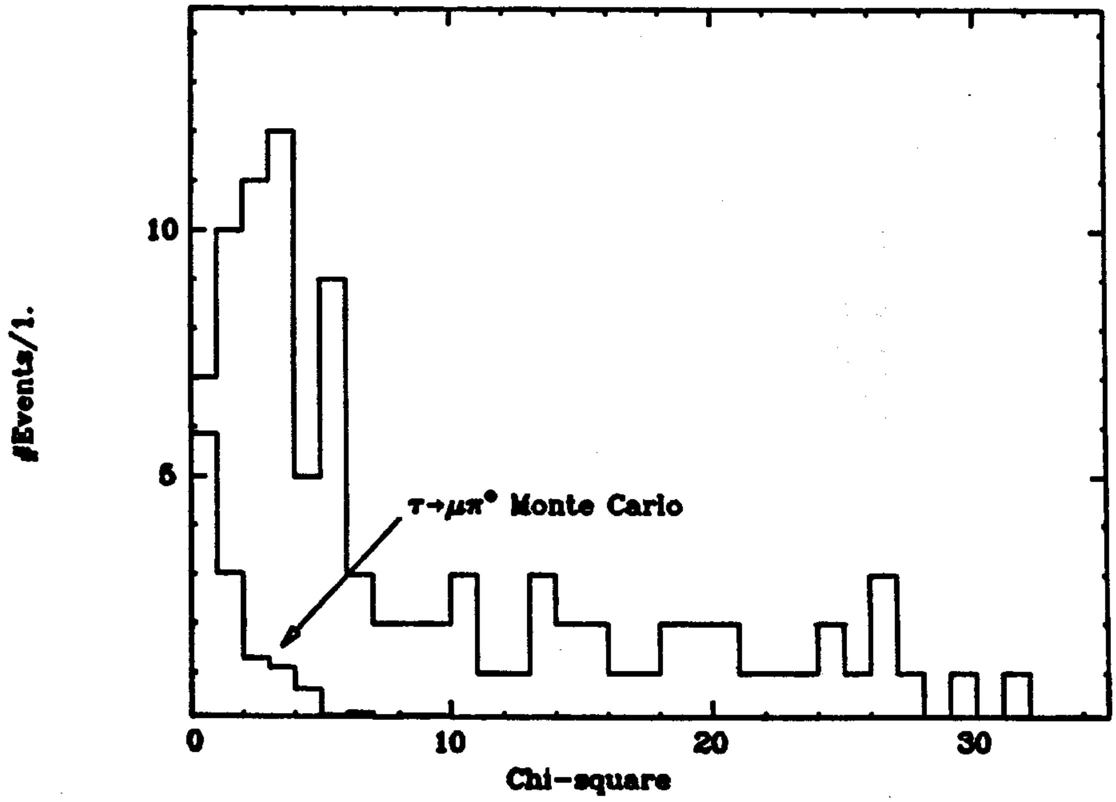

Figure 7.21. Measured chi-square distribution from the 2-C fit for tau-->$\mu+\pi^0$ decay candidates. The monte carlo prediction is also shown.

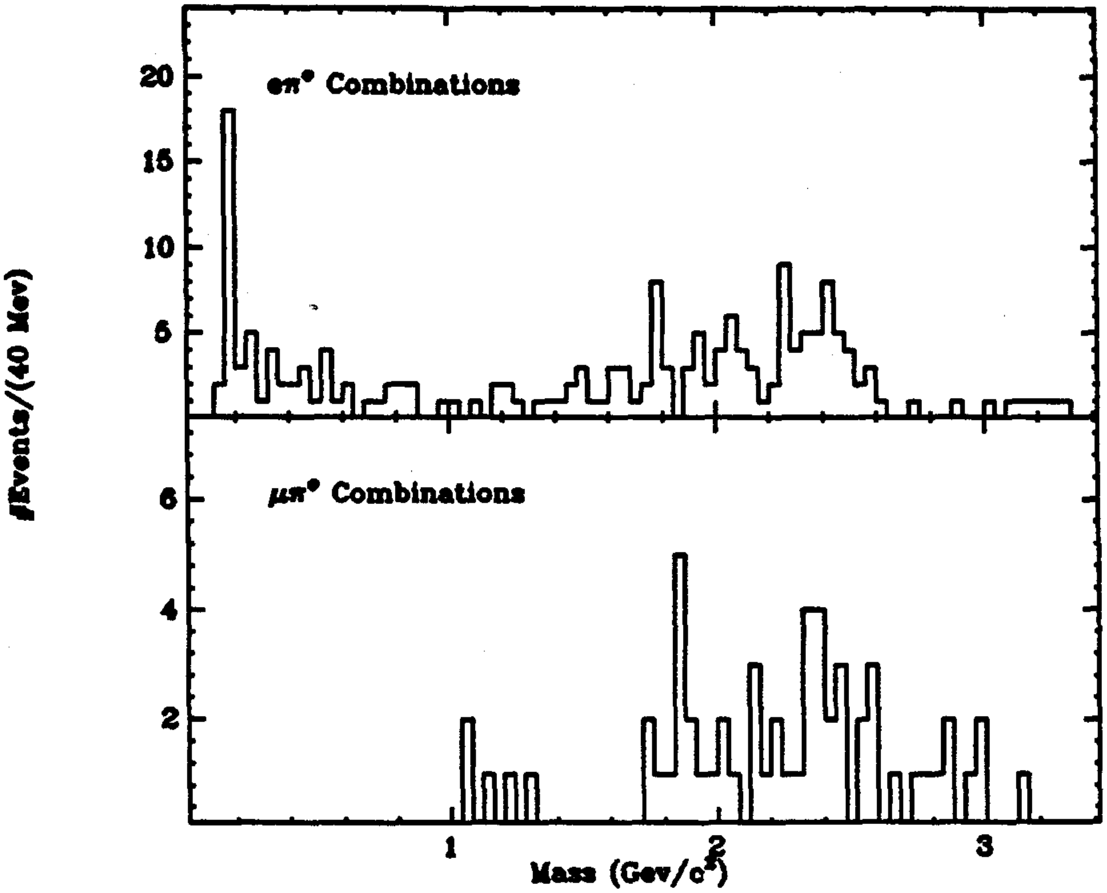

Figure 7.22. Measured lepton-π° invariant mass distribution for all events satisfying the decay constraints.

cuts designed to reduce the pizero background.

Any cuts which discriminate against photons from sources other than pizeros will reduce the contamination in the pizero sample. Photons arising from electron bremstrahlung in the detector material can easily be identified. Thus, we reject any pizero which uses a photon that is labeled as bremstrahlung radiation using the cut described in section 5.5. This cut reduces the acceptance by no more than 2% but succeeds in reducing the number of e-π^0 candidates by 30%.

As discussed in section 7.4a, the large number of high energy background pizeros with a low value of the asymmetry parameter X can easily be eliminated: only pizeros which have X larger than .15 are retained. Although this cut removes 27% of the e-π^0 candidates, the acceptance is reduced by an amount ranging from 7% at 4 Gev to 13% at 6.6 Gev. The e-π^0 invariant mass distribution after the imposition of these cuts is shown in Figure 7.23.

The background due to fake photons can be suppressed by imposing a minimum photon energy cut. Therefore we reject any pizeros which use a photon with energy less than 200 Mev/c^2. This cut reduces the acceptance by a fraction which varies from 14% at 4 Gev to only 4% at 6 Gev, while it reduces the total number of e-π^0 candidates by 33% and μ-π^0 candidates by 25%.

As was discussed in section 5.5, purely electromagnetic processes tend towards small values of the charged track acoplanarity angle. We can remove any remaining contamination from this source by applying a tighter cut on the acoplanarity angle. Figure 7.24 plots the measured acoplanarity distribution for the lepton-pizero candidates. The cluster of event in the e-π^0 sample with small acoplanarity can be removed

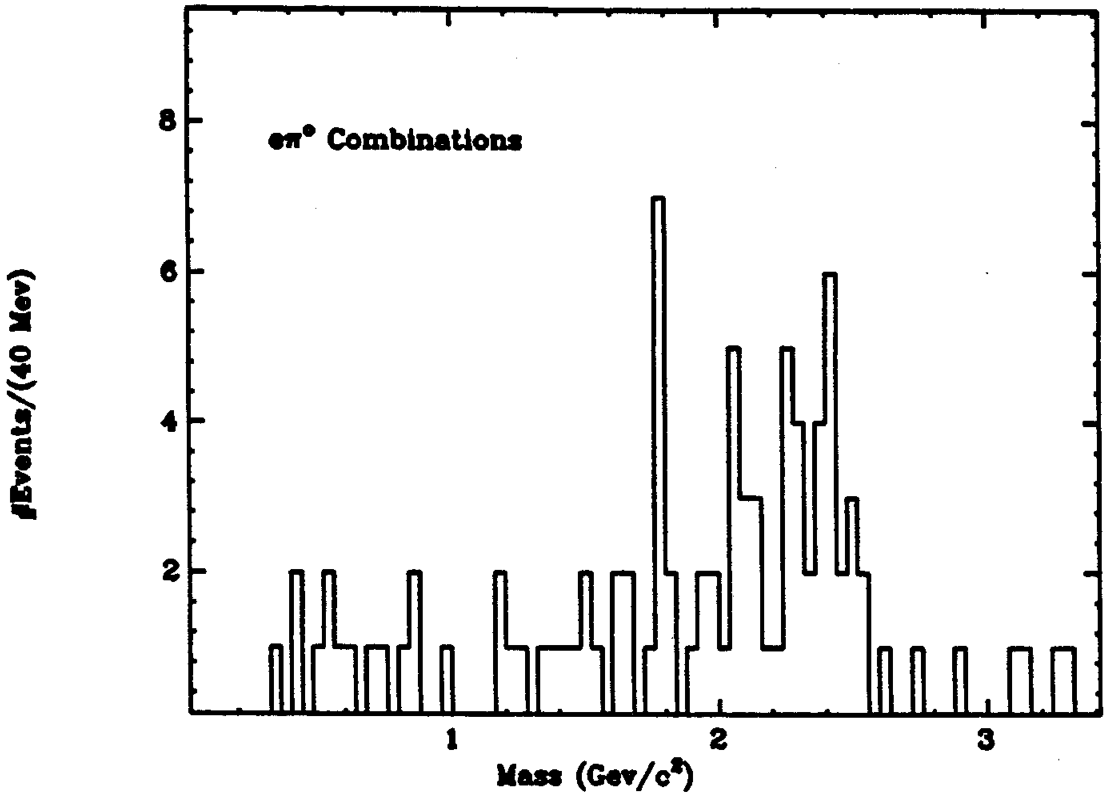

Figure 7.23. Electron-π^0 invariant mass distribution after the bremstrahlung photon and pizero asymmetry cuts.

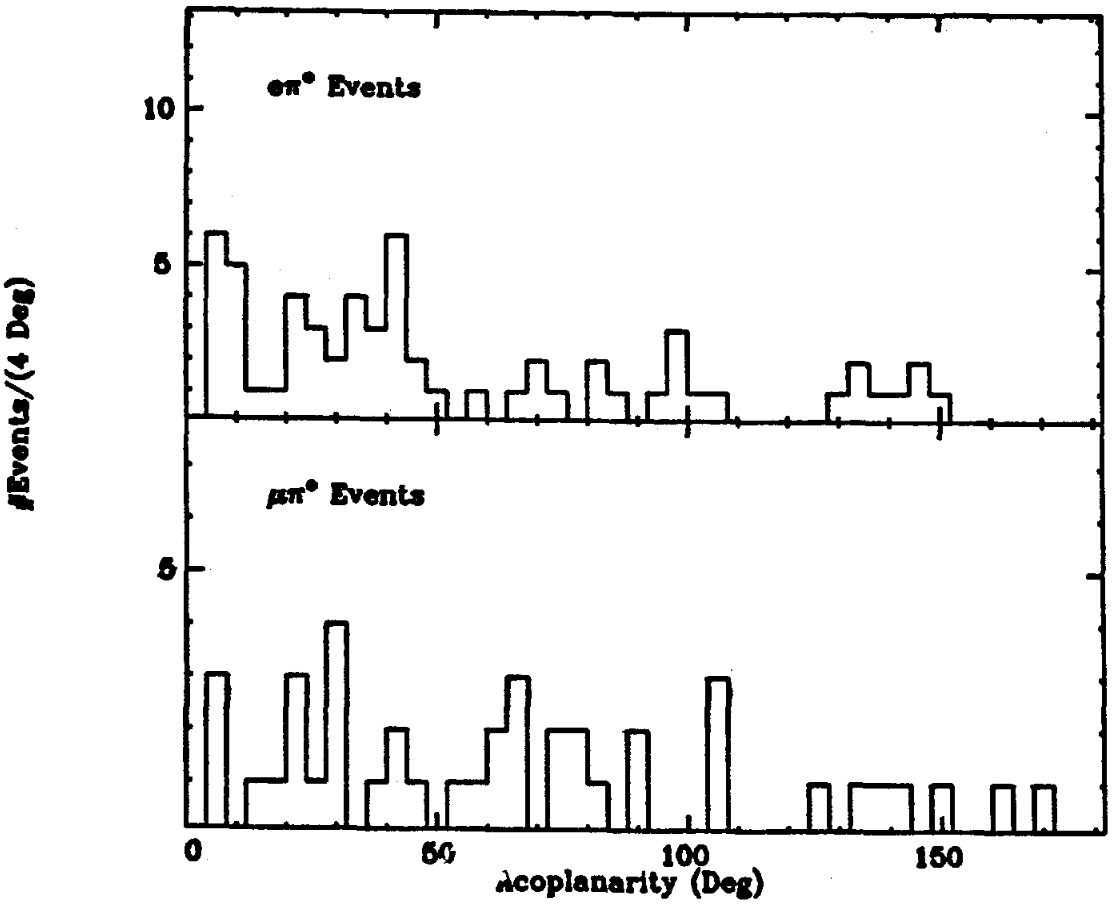

Figure 7.24. Charged track acoplanarity for tau-->lepton+π^0 decay candidates.

by demanding the acoplanarity be larger than 12 degrees. The reduction in the acceptance caused by this cut ranges from 3.4% at 4.0 Gev to 9.5% at 6.6 Gev.

The lepton-pizero invariant mass distribution for those events which survive the background cuts is shown in Figure 7.25. Although no evidence for the μ-π^0 decay of the tau is seen, 6 e-π^0 decay candidates remain in the 40 Mev/c^2 wide bin centered near the tau mass. The e-π^0 mass plot is shown on an expanded scale in Figure 7.26 along with the Monte Carlo resolution function measured at 5.2 Gev.

One significant source of background remains which populates this mass plot in a manner that is strongly dependent on the center of mass energy. This background comes from standard decays of the tau.

The branching ratio for the decay $\tau \to \rho + \nu$ has been measured to be 21%. If one member of a produced tau pair decays in this manner while the other decays leptonically to an electron or muon (18% branching ratio for each mode), the charged lepton from one decay can combine with the pizero from the other and mimic the process for which we are searching. Since the taus are produced back to back in the detector, the pizero and lepton tend to recoil in opposite directions resulting in large values for their invariant mass. Figure 7.27 plots constrained mass distributions for this process calculated with the Monte Carlo at three center of mass energies. This background peaks near the beam energy and does not contribute in the region of the tau mass for center of mass energies larger than 5.2 Gev. The fraction of produced tau pairs decaying in this manner which survive all the analysis cuts and constraints is .8% at 5.2 Gev and grows slowly with the center of mass energy. Given that our data sample contains 48000

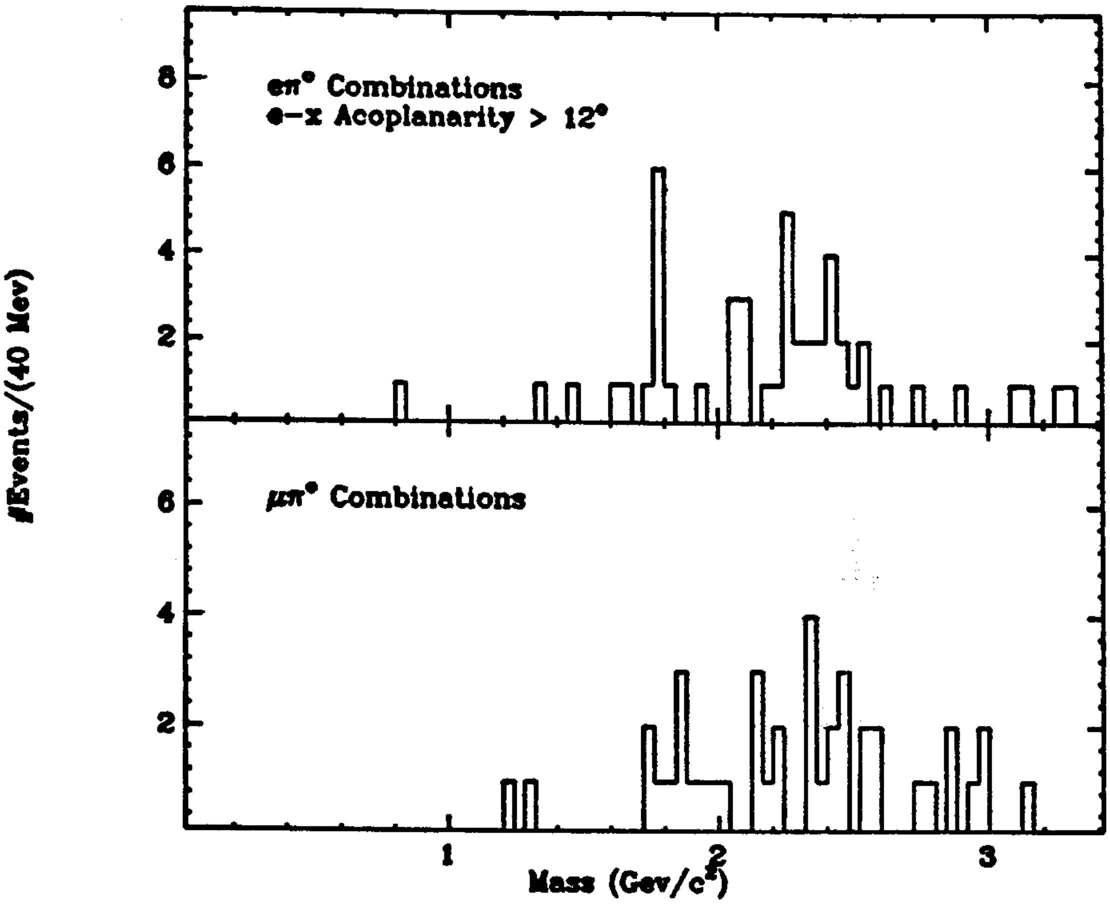

Figure 7.25. Lepton-π^0 invariant mass distribution after the minimum photon energy, bremstrahlung photon, and pizero decay asymmetry cuts.

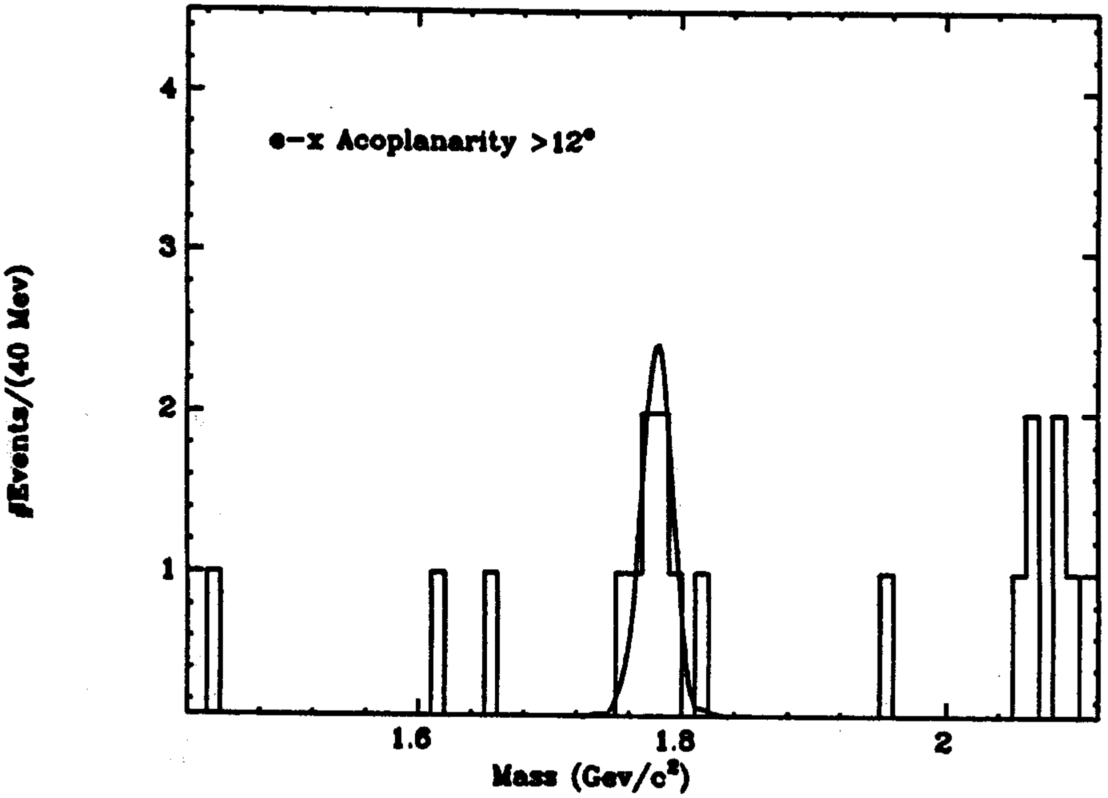

Figure 7.26. Electron-π^0 invariant mass distribution (from Figure 7.25) with an expanded scale. The expected resolution function for the decay tau--> e+π^0 is also shown.

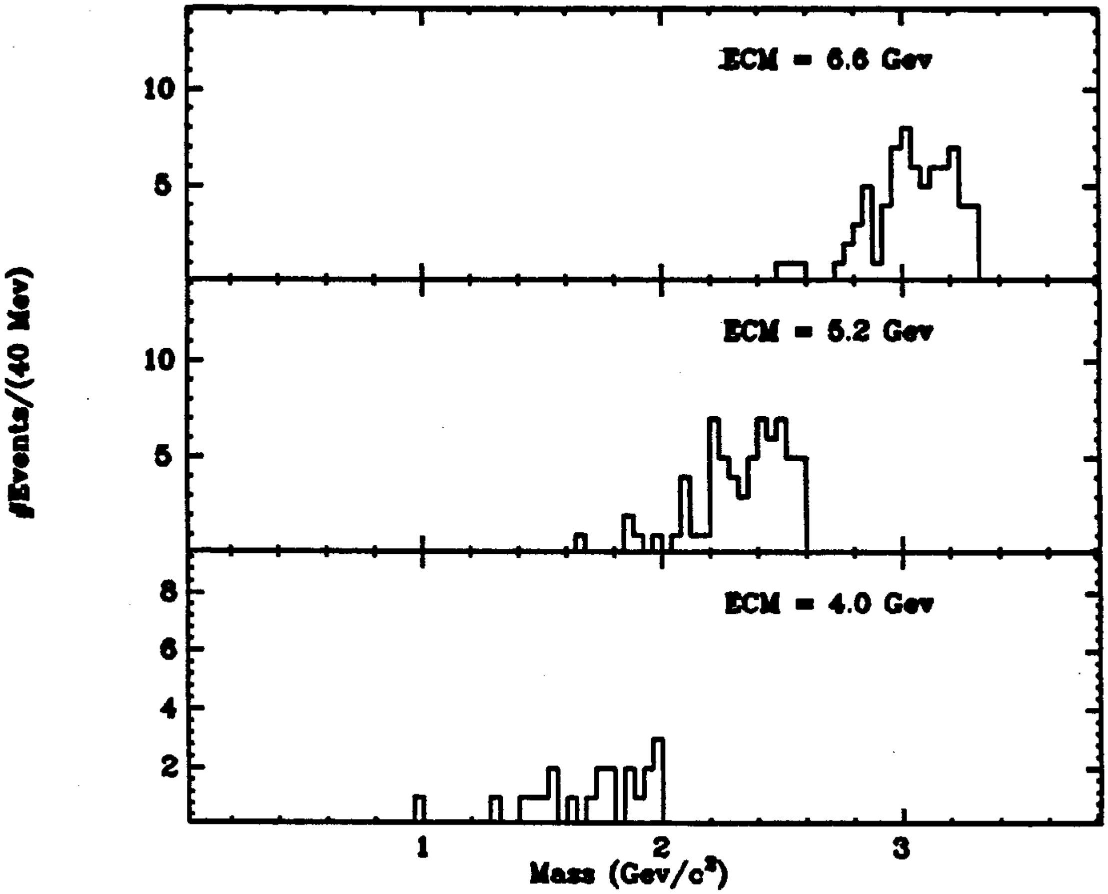

Figure 7.27. Monte carlo calcualation of μ-π^o constrained invariant mass distribution for the process $\tau\tau$--> $(\mu\nu\nu)$ $(\rho\nu$-->$\pi\pi^0\nu)$.

produced tau pairs, we expect approximately 33 events in the mass plots to be from this source.

The fact that the pizero is a decay product of the rho provides a way to discriminate against this background: the invariant mass of the other charged track in the event and the pizero will be consistent with the rho mass. Figure 7.28 shows this mass distribution for the remaining pizero-lepton candidate events. A very clear rho signal is present. Monte Carlo calculations for this distribution under the hypothesis that the pizero came from a tau→lepton+pizero decay and the charged track came from any of the standard tau decays, are shown in Figure 7.29 for three center of mass energies. Demanding that the invariant mass of the pizero and opposite track be outside of the region from 650 to 950 Mev/c^2 reduces the acceptance for the charged lepton+pizero decay by roughly 20% at 4 Gev and only 6% at 6.6 Gev. Applying this cut to the data removes 33 events from the e-π^0 distribution (66%), and 22 events from the μ-π^0 distribution (54%). The lepton-pizero mass distributions remaining after this cut are shown in Figure 7.30.

7.4d Branching Ratio Limits

No evidence is seen in Figure 7.30 for the $\mu+\pi^0$ decay of the tau. The acceptance has been calculated with the Monte Carlo simulation program, and is 2.9% when averaged over the center of mass energy region spanned by the data sample. No events are detected within the 40 Mev/c^2 region which defines the acceptance. This determines the 90% confidence level upper limit to the branching fraction for the decay $\tau\to\mu+\pi^0$ to be .082%.

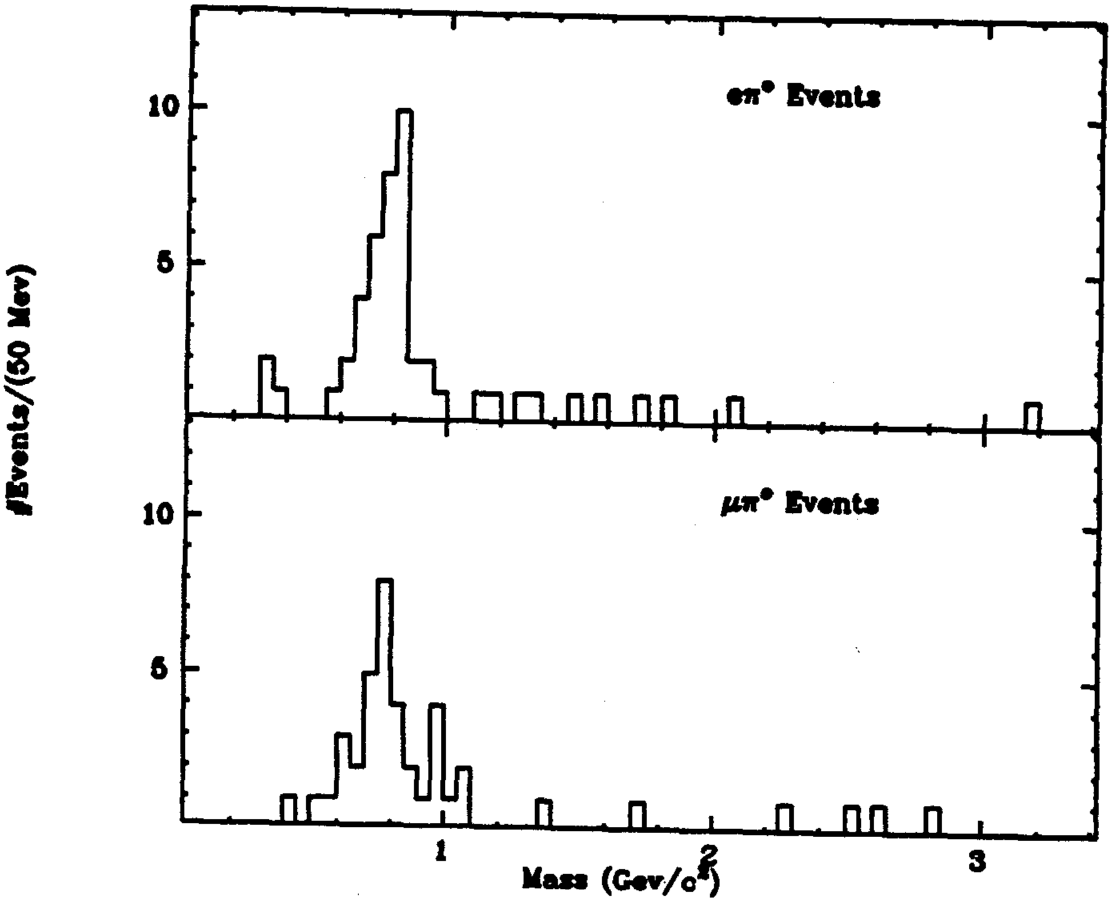

Figure 7.28. π^0-X invariant mass (X is the other charged track in the event) for tau-->lepton+π^0 candidate events.

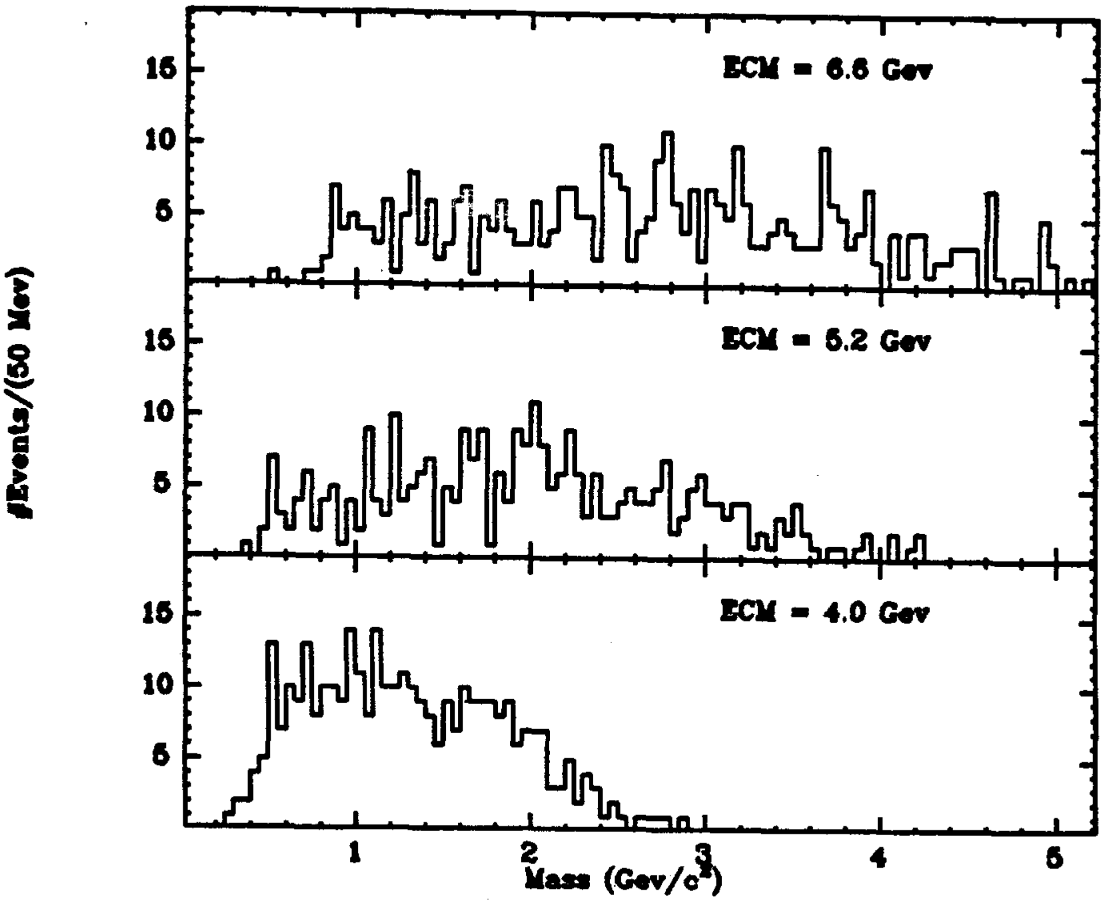

Figure 7.29. Monte carlo calculation of π^0-X constrained invariant mass for the process $\Upsilon\Upsilon \dashrightarrow (\psi\pi^0)$ (X + neutrals).

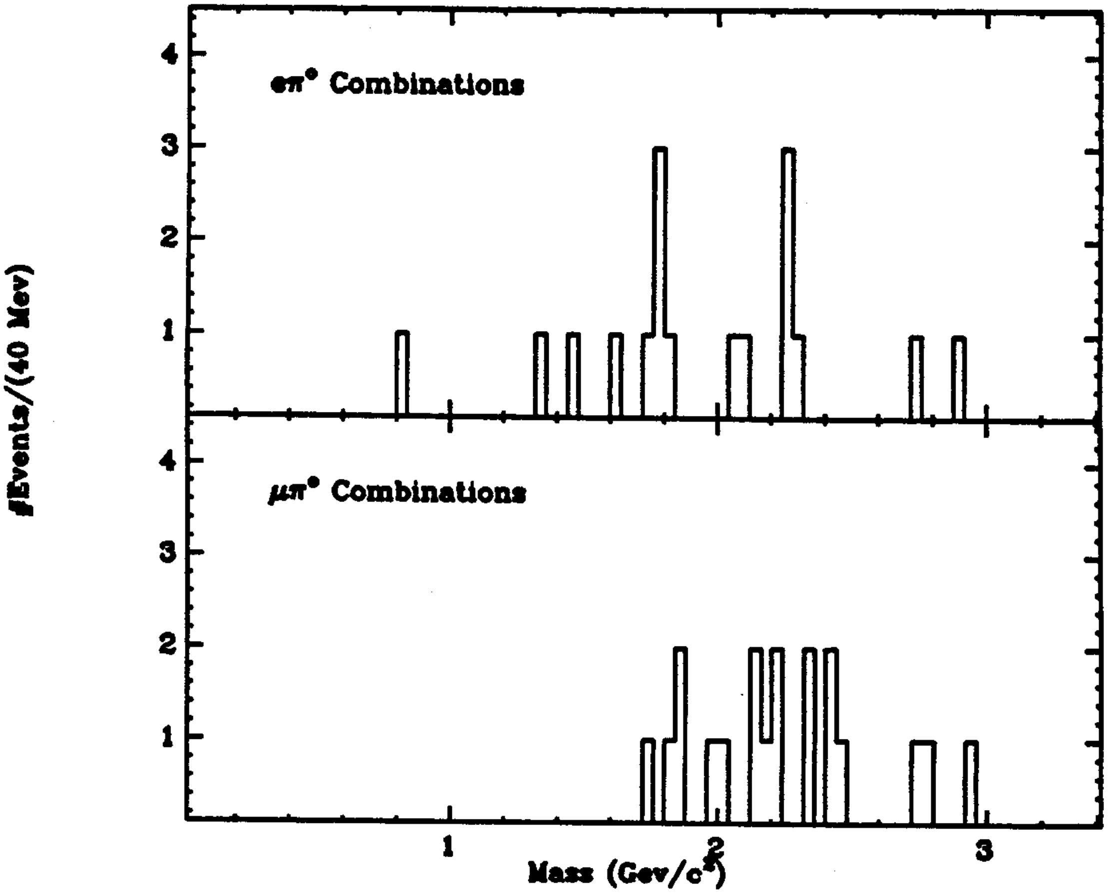

Figure 7.30. Lepton-π^0 constrained invariant mass distribution for candidates which survive all background cuts.

$$BR \leq 2.3/(96000*.029) = .082\% \qquad 90\% \text{ C.L.} \qquad (16)$$

After application of all the background cuts discussed above, three events remain in the 40 Mev/c^2 wide bin encompassing the tau mass. The acceptance, calculated with the Monte Carlo and averaged over the center of mass energy region, is 3.5%. Thus, the 90% confidence level upper limit on the branching fraction for the decay $\tau \rightarrow e + \pi^0$ is:

$$BR \leq 6.7/(96000*.035) = .21\% \qquad 90\% \text{ C.L.} \qquad (17)$$

CHAPTER 8

Summary

In this thesis we studied two properties of te tau lepton--its production cross section in e+e- annihilation, and the conservation of lepton number in tau decays.

The tau production cross section was found to be consistent with the spin 1/2, point particle cross section in the center of mass energy region between 3.85 and 6.85 Gev. The branching ratio product for the electron and muon leptonic decay modes was measured to be .032±.002±.004.

No evidence was seen for any of the 12 lepton number violating decays of the tau listed in Table 8.1. Upper limits (90% C.L.) on each of the 12 modes were determined. The observed lack of these decays provides further support for the sequential lepton nature of the tau.

TABLE 8.1

90% confidence level upper limits on the branching ratio for 12 decay modes of the tau lepton.

Mode	Upper Limit (%)
$\tau \to e\gamma$	.064
$\tau \to \mu\gamma$	.055
$\tau \to eee$	.040
$\tau \to e\mu\mu$	.033
$\tau \to \mu ee$	.044
$\tau \to \mu\mu\mu$	.049
$\tau \to e\rho$	.037
$\tau \to \mu\rho$	.044
$\tau \to eK^0$	.13
$\tau \to \mu K^0$	.10
$\tau \to e\pi^0$	.21
$\tau \to \mu\pi^0$	.082

Appendix A

Electromagnetic Interaction of Heavy Charged Particles with Matter

In this appendix, we briefly review the electromagnetic interactions of heavy charged particles in matter. These interactions are important in understanding the properties of the MARK II liquid argon shower counters and the muon range counters.

When a charged particle traverses matter, it loses energy by atomic excitation and ionization. In the classical interpretation, the incident particle suffers elastic collisions with the charged particles of the media thereby losing kinetic energy. Very little energy is transferred to atomic nuclei due to their large mass. A proper treatment takes into account the fact that electrons are bound in atoms which obey the laws of quantum mechanics, and yields the result for the mean ionization loss[1]

$$-\frac{dE}{dx} = \frac{2\pi N e^4}{m_e c^2 \beta^2}\left[\ln\left(\frac{2m_e c^2\beta^2 \mathrm{wmax}}{I^2(1-\beta^2)}\right) - 2\beta^2 - U - D\right](1+\nu) \qquad (1)$$

where N is the electron density, WMAX is the maximum amount of energy which can be transferred to an electron in a single collision, and U, I, V, and D are phenomenological functions. U represents atomic structure corrections for very slow particles; V accounts for higher order electrodynamic corrections important for slow or highly charged particles. The parameter I represents the average effect of the excitation and ionization potentials of the atom. The polarization of the medium reduces the effect of the incident particles' electric field at large distances and is represented by the function D. At low incident energies, D is defined to be zero, and any polarization effects are included in the parameter I. At high energies, D takes the value

$$C + 2\ln\beta\gamma \tag{2}$$

so as to cancel the logarithmic rise with momentum in the ionization loss due to distant collisions. Thus the mean ionization loss increases at large energies due only to the increase in WMAX. Detectors which measure the ionization loss usually have a limited response for knock-on electrons with energy greater than some value. In this case, the energy loss recorded by the detector approaches a constant at high energies known as the Fermi plateau.

Except for the insignificant mass dependence in WMAX, the ionization loss is dependent only on the velocity of the incident particle. Figure A.1 shows the dE/dx losses for various particles in aluminum as a function of momentum. Different materials have different values of N and I, and Figure A.2 plots the dE/dx losses for muons in 4 materials used in the MARK II.

The density effect function D has been parameterized by Sternheimer as[2]

$$\begin{aligned} &D=0 && X < X_0 \\ &D=4.606X+C+a(X_1-X)^m && X_0 < X < X_1 \\ &D=4.606X+C && X > X_1 \end{aligned} \tag{3}$$

where $x=\log_{10}(P/m_e c)$. The constant values determined for liquid

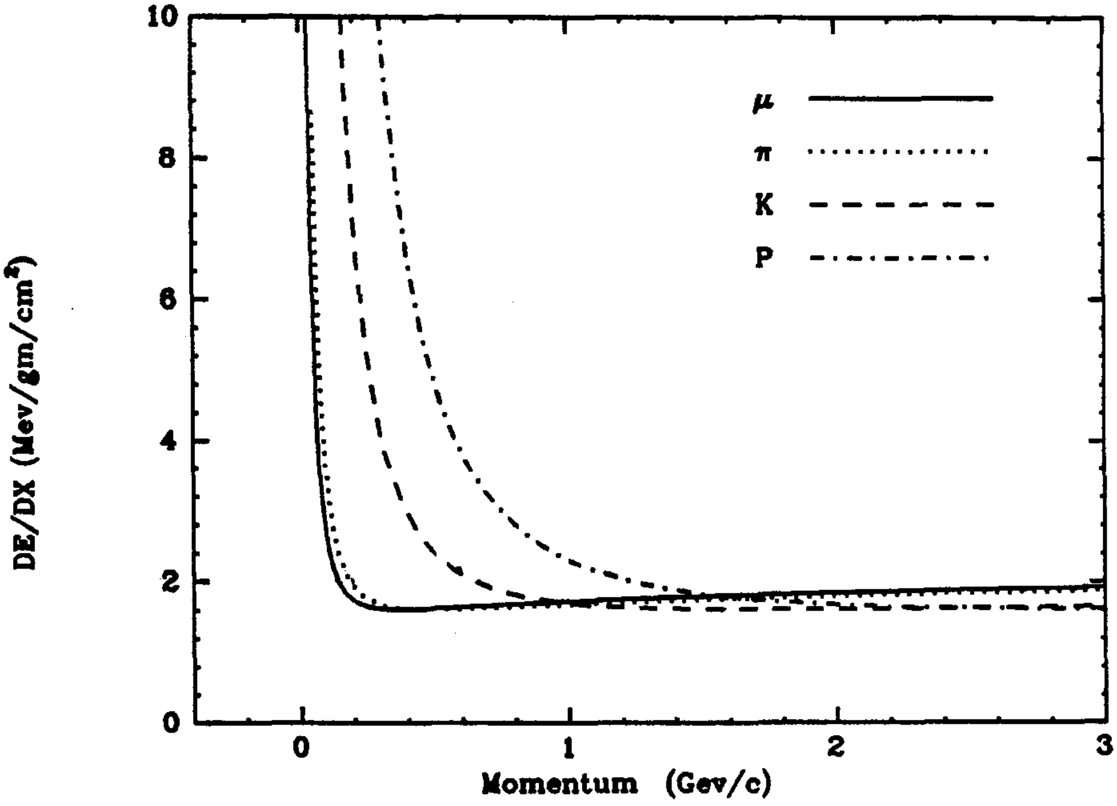

Figure A.1. Energy loss for several particles in aluminum as a function of particle momentum.

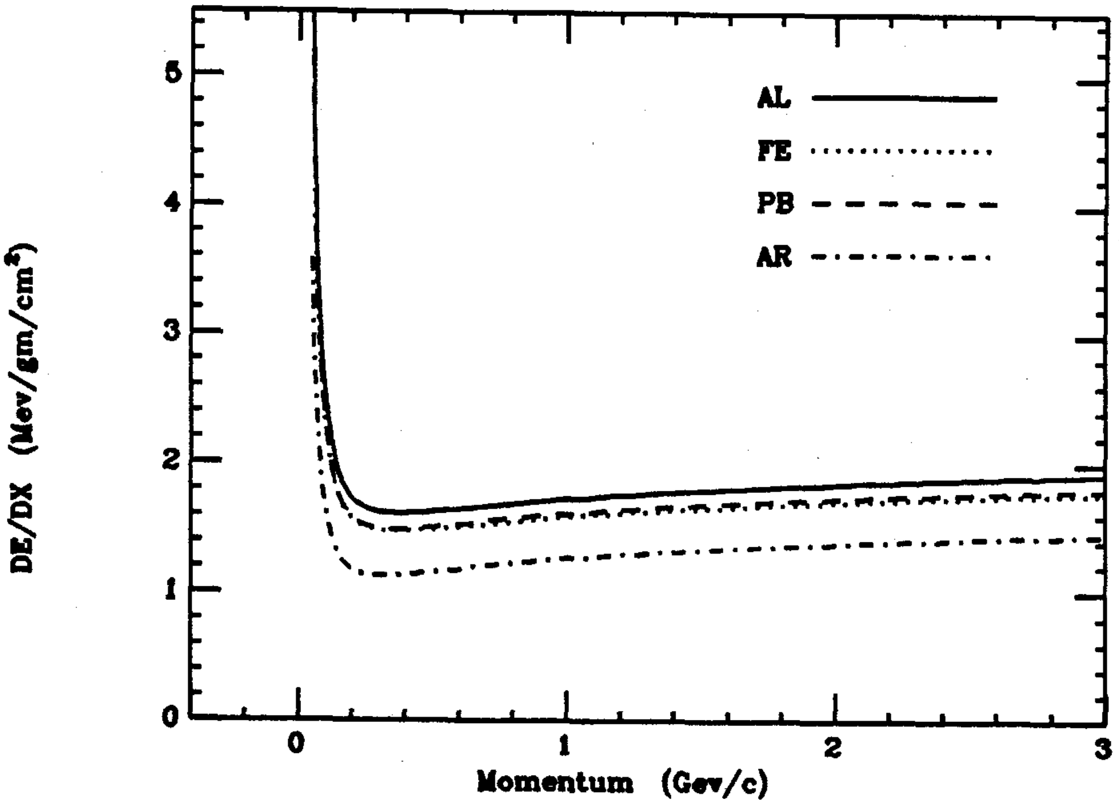

Figure A.2. Energy loss for muons in several materials as a function of momentum.

argon are listed below[2].

$C=-5.43 \quad X_0=.270 \quad X_1=3.0 \quad A=.2058 \quad m=3.0$

Because the ionization loss is a statistical process, individual particles experience fluctuations. Collisions which occur most infrequently are those which cause the greatest energy loss. Therefore, situations exist where the distribution of energy losses is not gaussian. To be more precise, if the probable number of collisions in each energy loss interval is large, then the energy loss distribution will be gaussian. In a thin absorber (one in which the average energy loss is much smaller than the total energy) this condition will occur if K=F/WMAX is much greater than 1. If K is much less than 1, large fluctuations are likely and lead to a distribution with a long tail towards large energy losses[3] The case for arbitrary values of K has been treated by Vavilov[4].

The statistical fluctuations in energy loss lead to a fluctuation in range. Sternheimer has made numerical calculations[5] for the rms deviation in the range of muons in various materials. Figure A.3 plots the relative range straggling for muons in 3 materials as a function of momentum. The Z dependence is very slight.

Although electromagnetic interactions with nuclei do not lead to energy loss, they can deflect the incident particle. Usually the individual deflections are small and lead to a gaussian distribution for the multiple scattering. However, large individual scattering can occur and leads to long non-gaussian tails. A useful formula due to Rossi and Greisen for the mean square scattering angle is[6]

$$\langle\theta\rangle^2=t(E_0/\beta P)^2 \qquad E_0\simeq 21 \text{ Mev} \qquad t=X/RL \tag{4}$$

where RL is the radiation length of the absorber, t the absorber

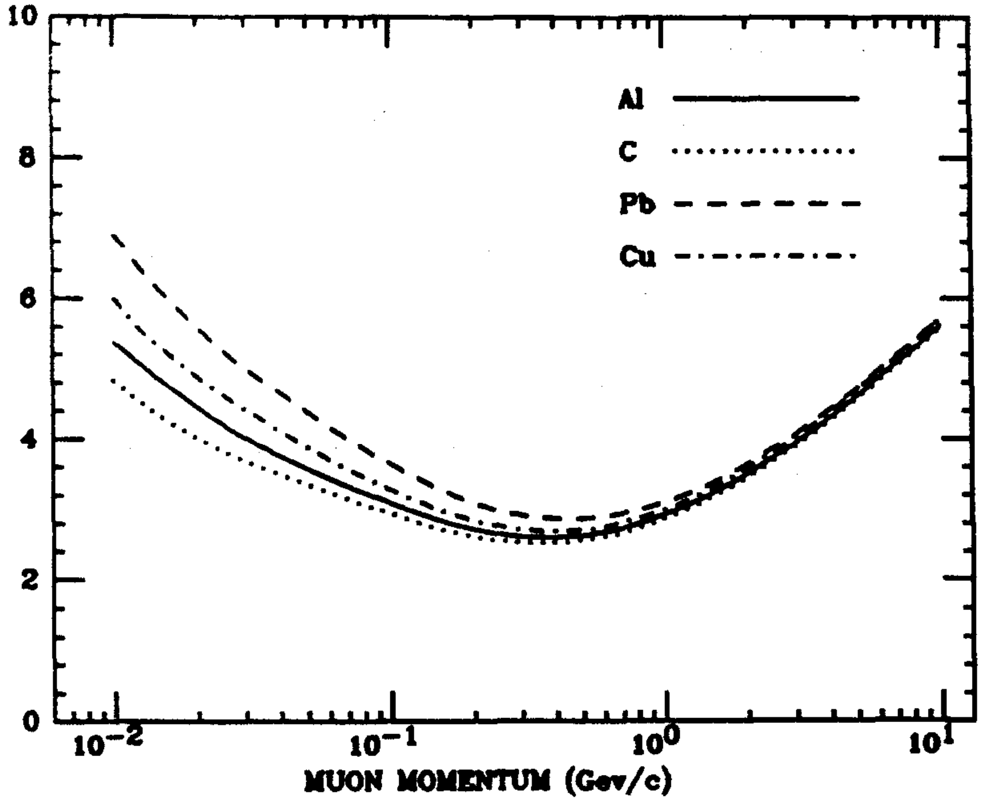

Figure A.3. Relative range straggling for muons in several materials as a function of momentum.

thickness. We shall use this formula as a good estimate for the multiple scattering.

Notes and References:

1.) R.M. Sternheimer, Phys. Rev. 103:511 (1956).

2.) R.M. Sternheimer and R.F. Peierls, Phys. Rev. B3:3681 (1971).

3.) L.Landau, J. Exp. Physics (USSR) 8:201 (1944).

4.) P.V.Vavilov, JETP 5:749 (1957).

5.) R.M. Sternheimer, Phys. Rev. 117:485 (1960).

6.) B. Rossi and K. Greisen, Rev. Mod. Phy. 13:240 (1941).
See Also V.L. Highland, NIM 129:497 (1975).

Appendix B

Liquid Argon Shower Counter System

B.1 INTRODUCTION:

The Mark II shower detectors have the dual function of photon detection and separation of electrons from hadrons. Photon detection requires that the counter be many radiation lengths deep so that the photon energy resolution is not dominated by shower leakage through the rear of the module. To accomplish the second function, the detector must exploit the difference between hadronic and electromagnetic showers. The most fundamental difference is the length scale which parameterizes the shower development. Electromagnetic cascade shower development is primarily governed by the related processes of bremsstrahlung emission and photon pair production[1]. The natural length scale for these processes is the radiation length for the medium in which the shower occurs. Hadronic cascades are of a different character[2]. A hadron, in traversing a material, will typically travel one absorption length before it interacts. The secondary hadrons leaving the interaction will then travel another absorption length before interacting. Thus, the natural length scale for hadronic cascades is the material's absorption length. To lowest order, the radiation length[3] of a material is proportional to $1/Z^2$ while the absorption length varies as $1/A$. Therefore, to accentuate the difference between hadronic and electromagnetic showers, an absorber with a large atomic number should be used.

A practical shower detector must not only generate and contain the shower, it also must provide a way to extract information about it. If the absorber is a scintillator and does not absorb the fluorescent radiation, the emitted light can be used to measure shower characteristics; such is the case with thallium activated sodium iodide[4]. Another type of shower measurement is detection of the ionization generated in the absorber by the passage of electrically charged shower particles. Unfortunately, good absorbers usually do not make good ionization detectors. To circumvent this problem, shower counters often consist of alternating layers of radiator (to generate the shower) and any of several charged particle detectors. Such a detector is known as a 'sampling' shower detector.

In principle, an electromagnetic shower counter which detects ionization can have very good resolution since nearly all the original shower energy is eventually spent in ionization. In practice, the resolution would be limited by the escape of low energy photons through the back of the detector. Other less fundamental effects such as amplifier noise and nonlinearity, or detector inhomogeneity can worsen the resolution. In a sampling detector, however, because only a fraction of the incident energy is measured, event by event fluctuations in the measured fraction will be the limiting factor determining the resolution. The resolution will improve as the thickness of the radiator plates is reduced.

The Mark II shower counters are sampling detectors. They consist of a stack of lead sheets (2mm thick with 3mm gaps) immersed in a tank of liquid argon kept at 86-89 (deg K). The detectors are actually large parallel plate ionization counters in which the lead sheets generate the shower and provide the collecting surfaces for the ionization counters.

Liquid argon shower counters (LASC's) have several advantages over other sampling detectors. The absorber plates can be made very thin, thus reducing the sampling fluctuations. The plates are easily subdivided thereby allowing spatial information on the shower to be extracted. The mechanical portion of the detector can be made quite homogeneous, and local variations in the sheet location do not change the total liquid argon gap. Since the created ionization is not multiplied, calibration is simple and with care will be very stable for long periods of time. The device is not subject to radiation damage, and with appropriate design can handle high rates.

Liquid argon shower counters are not without their drawbacks, however. The cryrogenic requirements of liquid argon demand much work during the design, construction, and day to day operation of the system. Secondly, the signal magnitude is small. A typical value for the collected charge is 1 picocoulomb per Gev of incident energy, so care must be given to the design and shielding of the electronic circuitry.

Pioneering work on liquid argon shower counters was done in the first half of the 1970's[5]. The Mark II LASC system is a product of the early work but represents several extensions: 1)The system was designed to function in the unique environment provided by e+e- storage rings. 2)Electrons and photons are detected over a wide momentum range extending from 100 Mev to many Gev. 3)The modules cover a large fraction of the total solid angle which requires accepting particles at large incidence angles. The rest of this appendix will describe two aspects of the performance of the Mark II shower detectors. We will briefly discuss the physical construction of the modules, review the long term stability during the one and one-half year run of SP-29, and describe their response to minimum ionizing particles. We also report on a monte carlo study of the response of liquid argon counters to electromagnetic showers.

B.2 PHYSICAL CONSTRUCTION[6]:

The LASC system is composed of 8 modules providing detection capabilities over 60% of 4π (see Figure 2.1). Each module covers 1/8 of the azimuthal coordinate and extends 1.9 meters along the beam axis either side of the interaction region. A module consists of a stack of 37 rectangular lead plates (2mm thick), separated by 3mm gaps filled with liquid argon. The structure can be conceptually divided into 18 'cells' each consisting of 2 lead sheets and 2 gaps. The 37th sheet serves as a ground plane for the last cell. The first sheet of each cell is solid and is held at ground potential. The second is cut into strips along lines that are parallel to one of 3 directions. The strips which are oriented so as to measure the spherical angles theta or phi are labeled 'F' or 'T' respectively. The third set, aligned along a 45 degree angle relative to the F and T strips, are called 'U' strips.

To save on the number of electronic channels, the 18 cells are ganged together to form 6 'layers' as indicated in Figure B.1, resulting in three F, one U, and two T layers. The strips in all but the U layers are 3.49 cm wide separated by spaces of .31 mm. Strips in layer U are $\sqrt{2}$ wider. Except for the two strips on either end, adjacent pairs in

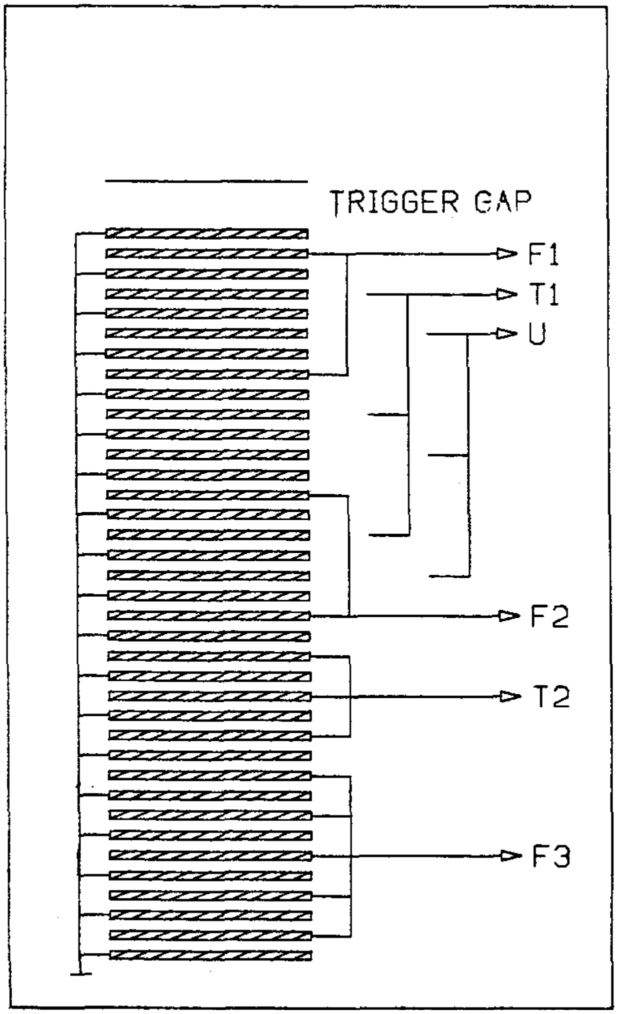

Figure B.1. Diagram of the electrical connections of the lead plates in the shower counter stack.

layer T2 are wired together, resulting in double width strips. The end strips in layer U are quadruple width and the four preceding ones on either end are double width.

The modules are mounted behind the solenoid coil and other material totaling 1.34 radiation lengths. Electromagnetic showers will begin their development in this material and since we do not sample the energy deposited there, fluctuations in that quantity adversely affects the energy resolution of the stack, especially for low energy particles. One way to correct for this effect is to measure the state of shower development at the front of the stack, then correct the energy measured in the stack using the known correlation between the state of shower development at the stack entrance, the energy deposited in the stack, and the energy lost in the coil. To implement this correction, a special low noise cell consisting of two 6 mm gaps, two 1.6 mm aluminum ground planes, and 1.6 mm aluminum signal electrodes is mounted on the upstream face of the stack. The signal plane is divided into strips which have the same length, orientation, and width as the F layers. For historical reasons, this cell is called the 'trigger gap' layer. The front section of the modules are tapered so that they can be closely packed. This was done by leaving out the strip on either end of layer F1, and the last two strips on either end in the trigger gaps.

B.3 ELECTRONICS AND CALIBRATION:

Electromagnetic shower development occurs in a module on the time scale of a few nanoseconds. The electrons created in the argon drift in the applied electric field with a velocity of 180 ns/mm[7] until they reach the collection electrode. The charge collected by a single cell as a function of time is shown in Figure B.2. Ignoring the charge lost to recombination or electro-negative impurities, the signal electrode collects all the produced electrons but for a uniformly ionizing track only half of the charge is useable since the positive ions (immobile on this time scale) induce a charge on the plates[8]. Using the fact that the average energy needed to create an ion pion in liquid argon is 24.6 eV[9], we can calculate the total charge collected from a minimum ionizing track in a cell to be

$$Q=(e/2)(dE\ \mathrm{minion})/(24.6\ \mathrm{eV})=(.6\mathrm{mm})(4000\ e/\mathrm{mm})=2.4\mathrm{x}10^4 \qquad (1)$$

which is .0038 picocoulomb. This amount of charge would be induced by two millivolts of noise through 2 picofarads of stray capacitance!

The 8 module system has 2944 electronic channels. All channels connected to the stack are treated in identical fashion, but the trigger gap signals require slightly different processing due to the longer drift time in the double width gap, and the better signal to noise ratio required by the trigger gaps' special function. A fraction of the collected charge is coupled through a high voltage blocking capacitor and impedance matching transformer into a charge-sensitive amplifier. The amplified signal is shaped and sent via bipolar drivers to the electronics trailer where it is sampled and saved until the trigger decision is made. If the event is accepted, a microprocessor controlled acquisition system digitizes the signal, reduces it, and stores the result in memory. The data reduction process consists of a minimum pulse height cut (1 sigma of the channel's measured electronic noise), a pedestal subtraction, a quadratic correction, and a scale conversion to units of energy deposited in the liquid argon. The 4 constants used in

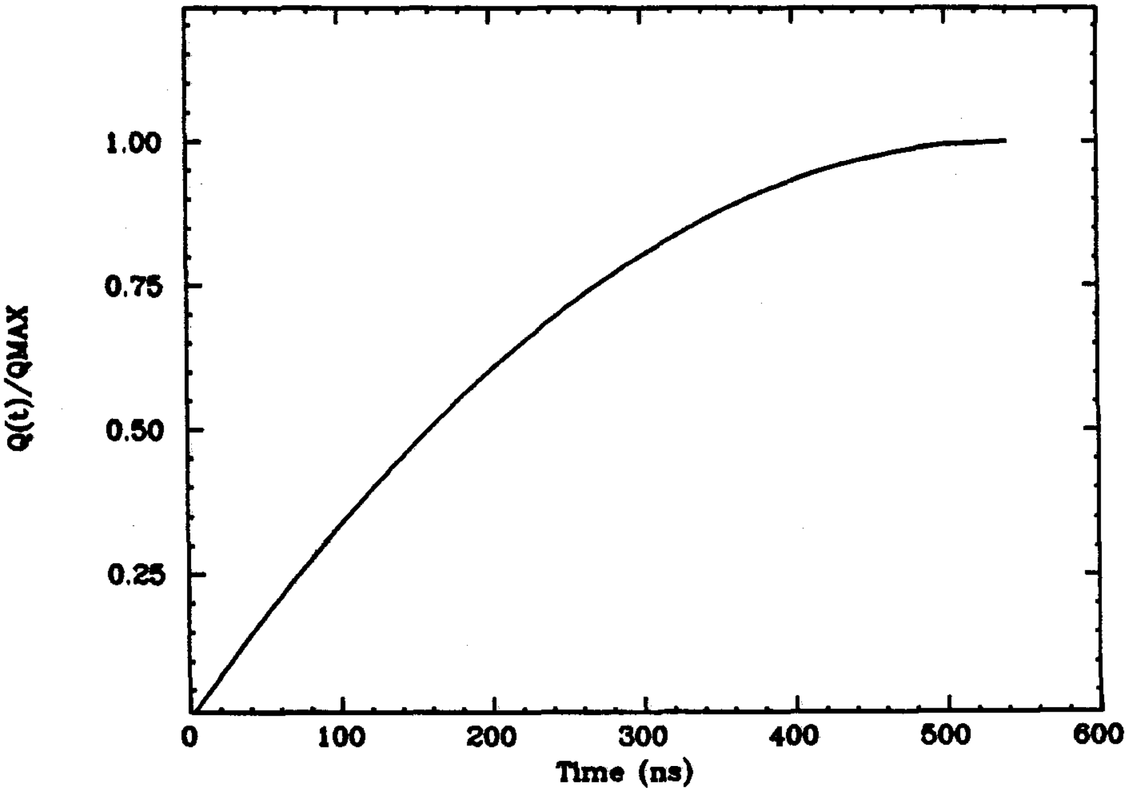

Figure B.2. Collected charge as a function of time in the standard stack cell.

the reduction sequence are measured simultaneously for all 2944 channels during a calibration run and are stored in the microprocessor memory.

Each channel has a 10pf calibration capacitor connected to the low voltage side of the blocking capacitor. A calibration consists of injecting a known amount of charge through the calibration capacitor (by applying a fixed voltage), and measuring the channel's response. This is done 20 times for each of five different voltages and once with no charge injection in order to measure the pedestal. A quadratic fit is made to the measured response, yielding the gain and quadratic correction factor. A correction is required to account for the fact that the charge is not directly injected onto the strip, and this was measured for each channel during module construction. The rms deviation of the channel response for a fixed input defines the electronic noise. This quantity is measured during the calibration and is combined with the pedestal to form the minimum pulse height cut used in the data reduction process. After the calibration is finished, any channel which has constants that significantly differ from nominal values is turned off by setting the minimum pulse height cut beyond the range of the ADC.

The small amplitude of the signals produced in the detector dictates that care be taken to minimize electronic noise. The noise level determines the lowest energy at which photons can be detected. They must be sufficiently above the noise so that random noise fluctuations are not called photons by the photon finding algorithm. Also, the separation of electrons from hadrons is enhanced for low momentum tracks if the minimum ionizing signal is clearly separable from the noise.

The occupancy of a channel is defined as the fraction of samples for which the channel's pulse height is above its one-sigma cut. The occupancy is very sensitive to changes in the pedestal or the background noise, and makes a useful indicator of failing electronic channels. Assuming the pulse height cut is nominally set at one sigma, for gaussian noise the occupancy will be 16%. (As can be seen from Figure B.9, the noise is approximately gaussian.) The fractional change in the occupancy for a small change in the electronic noise is then given by

$$d(occ)/occ = 1.5\ d\sigma/\sigma. \qquad (2)$$

There are contributions to the noise from both the amplifier thermal noise and external noise sources. During the run at SPEAR, the measured noise was found to vary with beam current. The average system occupancy as a function of beam current is plotted in Figure B.3 at several energies, where the data for each spans only one calibration. The noise increases with current at all energies but the largest increase occurs at the highest energy. Adding the noise sources in quadrature, the change in occupancy between the start and end of the fill implies the external noise at the maximum beam current can be as large as half the thermal noise.

The occupancy frequency distribution for T1 strips is shown for a typical run in Figure B.4. Although the average occupancy is near 16%, the deviation is large. The minimum pulse height cut is at best accurate to one ADC count, so part of this deviation is caused by the limited resolution of the ADC for signals of this level. Demanding that the resolution for minimum ionizing signals not be limited by ADC resolution, and that large signals from multi-Gev showers be analyzed, requires a high resolution ADC and electronic channels with a large

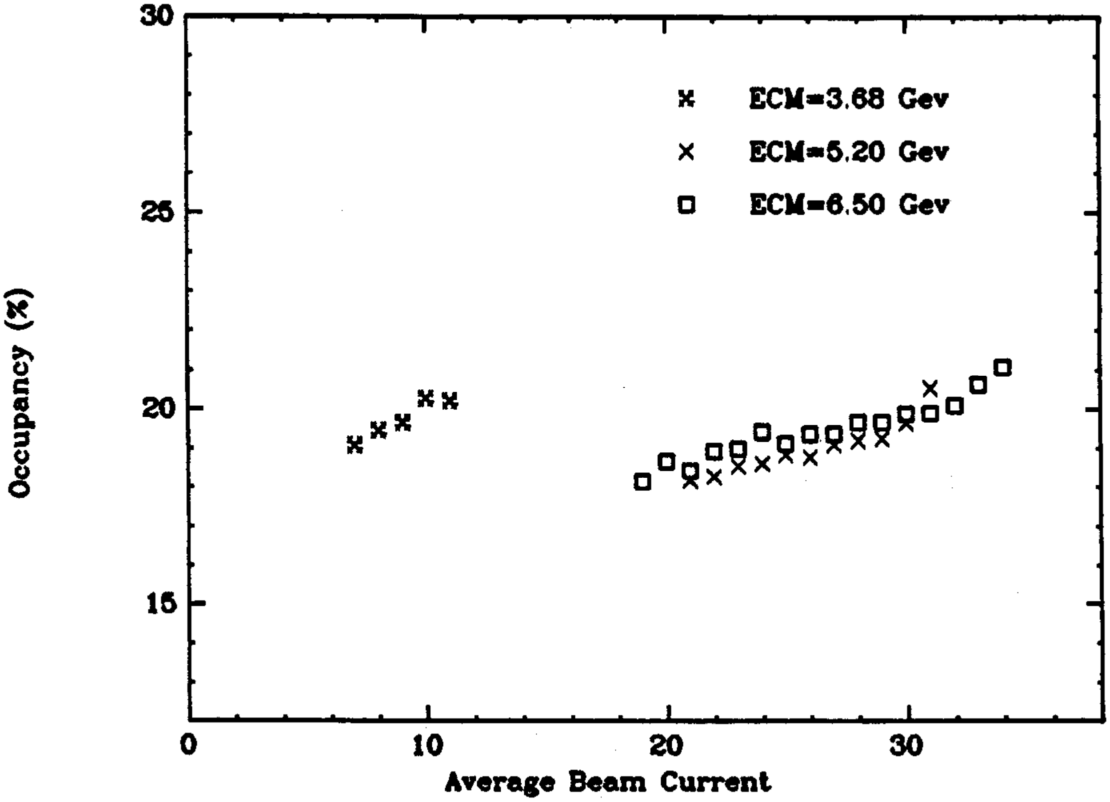

Figure B.3. Shower detector average system occupancy as a function of beam current for 3 center-of-mass energies. The data for each energy span only one calibration.

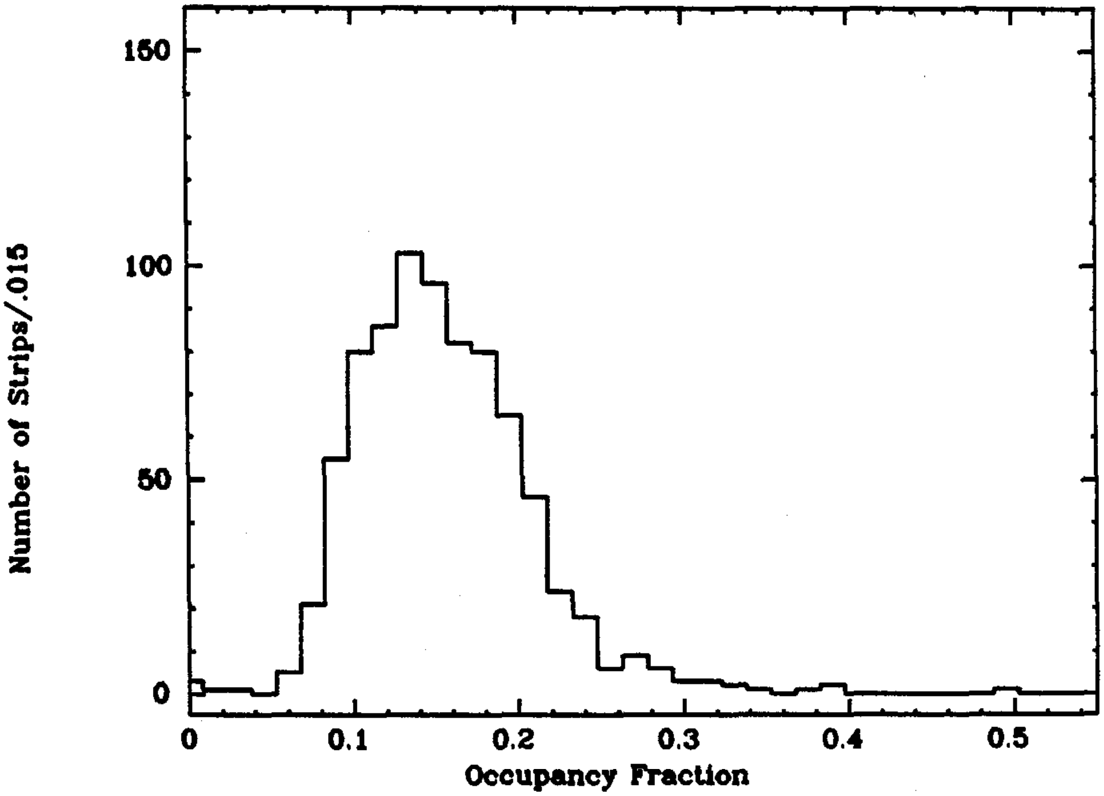

Figure B.4. Occupancy frequency distribution in a typical run for all strips in layer T1.

dynamic range.

Since the amplifier noise depends on strip capacitance, the ganged layers have different noise levels. Table B.1 lists the average rms noise for each layer.

TABLE B.1

Average rms noise for each layer.

	Trg	F1	F2	F3	U	T1	T2
Noise (Mev)	.59	.95	.95	2.0	.93	.64	1.0

In layer U, the noise varies with strip dimensions as is shown in Figure B.5. Individual variations in channel noise are expected, but high gain amplifiers are subject to oscillation; and poor connections, supply variations, or environmental changes can trigger them. In a system with thousands of channels, at any time a few may be on or over the edge of stability. When the data is analyzed, the photon finding algorithm meticulously searches for signals which exceed the expected background level. Oscillating, or otherwise noisy channels, represent just such a signal. It is imperative that the data be monitored so any 'beacons' can be found and silenced.

B.4 LONG TERM STABILITY:

The stability of the LASC performance from October of 1978 through June of 1979 is indicated in Figure B.6. This figure shows the average minimum ionization pulse height in module 1 from muon-pair events as a function of run number. Also shown is the average noise performance obtained by tracking 'imaginary' particles in the same events. A signal

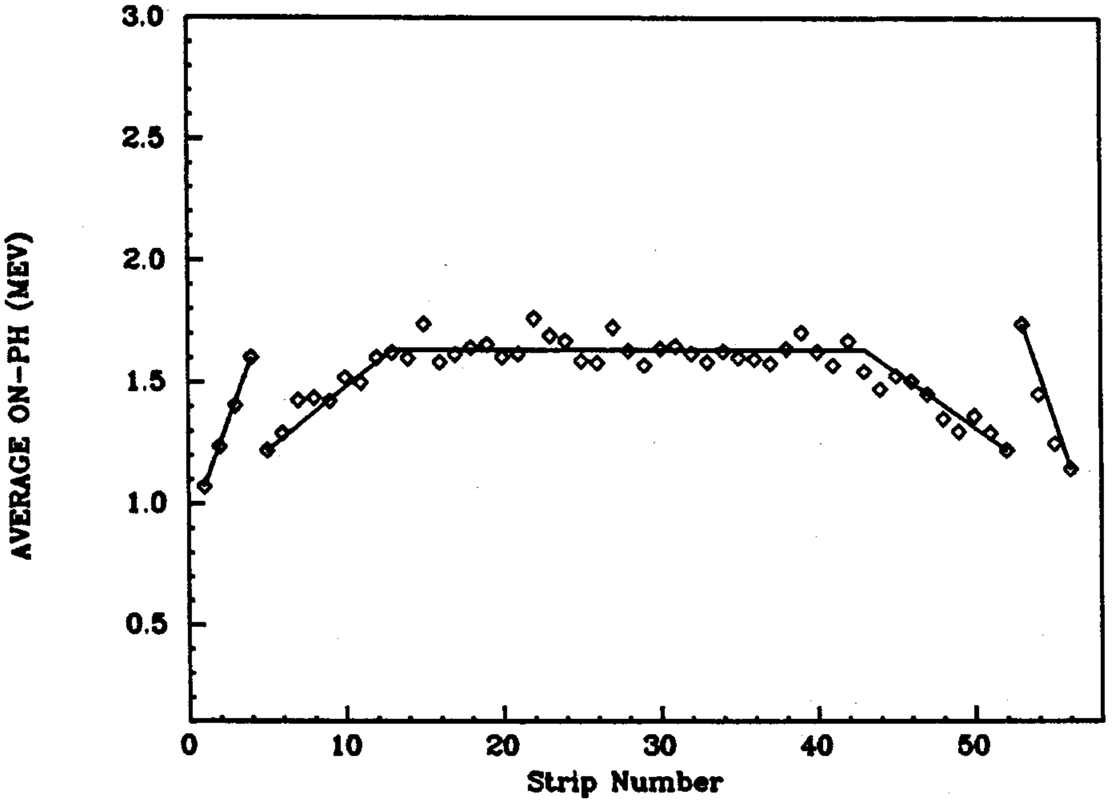

Figure B.5. Average-on noise pulse height for strips in layer U as a function of strip number. The effect of different strip dimensions is clearly seen.

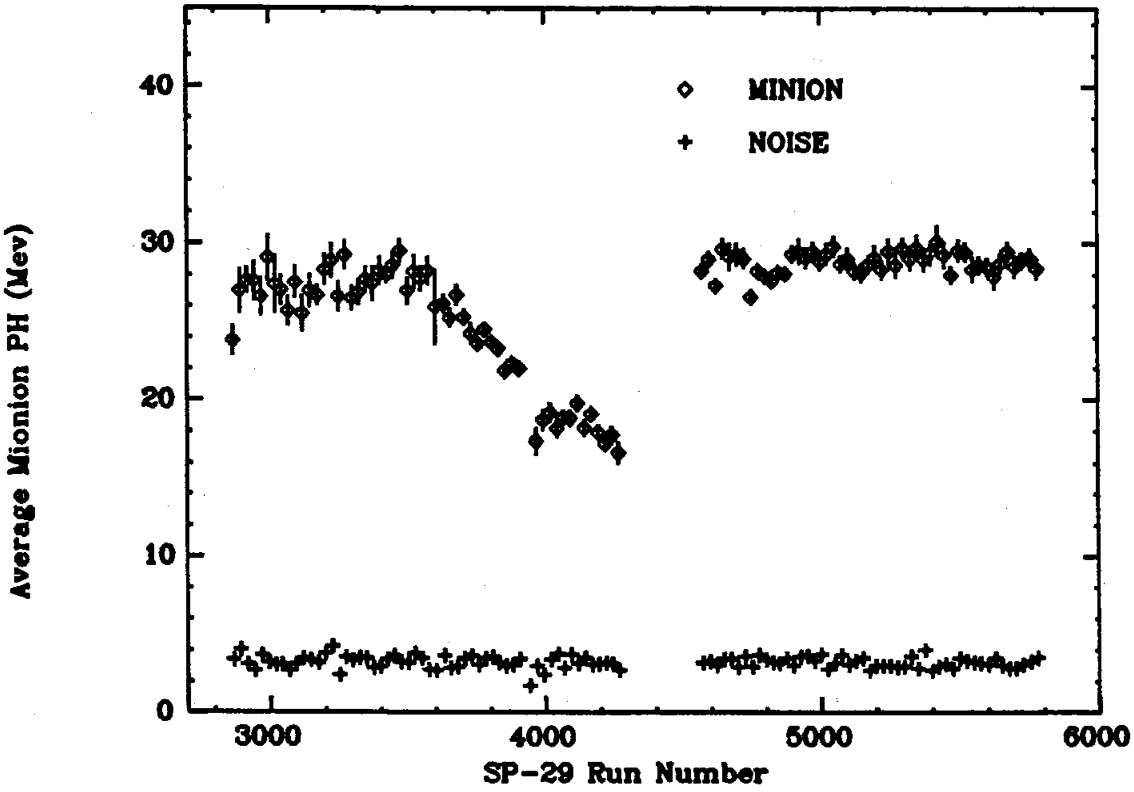

Figure B.6. Average pulse height for minimum ionizing tracks in module 1 as a function of run number. The decrease in pulse height is caused by nitrogen contamination in the argon.

loss occured near run 3600 when the argon became contaminated with nitrogen from an undetected leak in the argon storage dewar's liquid nitrogen cooled heat exchanger. Different modules experienced different amounts of contamination which increased linearly until the end of the fall cycle. During the Christmas break, the argon was transferred to the dewar thereby suffering further contamination. When the modules were refilled, there was a 35% reduction in the minimum ionization signal in all 8 modules. The argon was exchanged near run 4300 with argon contaminated with an as yet unknown substance. This contaminated argon was replaced with pure argon near run 4560 which remained pure for the duration of the experiment. The new argon increased the minimum ionization signal by 7% above its value at the start of the fall cycle.

B.5 MINIMUM IONIZING PARTICLES:

Although the main functions of the liquid argon shower counters are to separate electrons from hadrons and detect photons, they can also be used to help identify muons. A small probability exists that the muon system will identify an electron as a muon, due to either background signals (electronic noise, cosmics, etc.) or conversion in a muon chamber of low energy photons from the electrons's shower. By requiring that any track identified as a muon by the muon system also have a muon-like signal in the LASC, we can reduce the misidentification probability for electrons to be called muons nearly to zero. Muons also provide a clean minimum ionizing signal useful for studying the barrel's response and therefore provide a good starting point for the examination of the liquid argon system.

The philosophy for identifying minimum ionizing tracks in the liquid argon is simple: use the drift chamber information to select the appropriate strips to be examined in each layer, and compare the measured pulse height from these strips against that expected for a minimum ionizing particle. To carry out this program, one must determine the optimal search region for each layer, then use a known source of muons to determine the liquid argon minimum ionization response. Because the signal to noise ratio is low (it varies within the layer for the 3 non-F layers), it is important to make the search region as narrow as possible. There are several factors which need to be considered: 1.) the size of the region in which the ionization is created, 2.) the drift chamber resolution and multiple scattering in the coil and stack, 3.) the angle of incidence and the ganging of the different physical layers.

For muons, the width of the ionization region is negligible. A more important effect is the uncertainty in the tracks' predicted position due to the finite resolution of the drift chamber. For the 4 layers which measure phi, the drift chamber resolution is excellent and causes a negligible uncertainty in the predicted position. The 4 mrad resolution in theta corresponds to a one-sigma uncertainty in position of .7cm/$\sin^2(\Theta)$ for the T layers. The barrels cover the region up to $\sin^2(\Theta)=.5$ resulting in a maximal one-sigma uncertainty in the predicted track position of .4 strip widths in layer T1. Because the strips in layer T2 are twice as wide (except for the two single width strips on either end) the position uncertainty in T2 is reduced to at most .2 strip widths. The 45 degree orientation of layer U and the fact that the strips are 40% wider than the standard 3.8 cm width, reduces the predicted uncertainty in position to at most 1/5 of a strip.

Multiple scattering is an important contribution to the tracking uncertainty for low momentum tracks. The rms multiple scattering of normally incident muons as a function of depth in the stack is shown in Figure B.7 for several different muon momenta. The coil (and related materials) represent the dominant contribution to the scattering in the first third of the stack after which point the scattering in the stack itself becomes more important. To determine the net position resolution, add the multiple scattering in quadrature with the drift chamber resolution. Note that the multiple scattering is the main contribution to the resolution below an incident momentum in the range of .5 to .6 Gev/c.

Another important effect to consider when determining the search region is the ganging of several physical layers to produce the signals which constitute the data. Tracks which enter the barrels at non-normal angles will intersect the physical layers at different places thus making the measured width appear larger than the true one. In fact, for tracks which have a large enough angle of incidence, the situation can occur where ionization created in the first ganged layer is collected by a strip which is not adjacent to the one which collects the ionization in the deepest ganged layer. However, for tracks which originate near the interaction region, this situation can never occur. If D is the separation between the first and last physical layer in a ganged layer, and A is the angle of the track relative to the normal to the stack in the plane which contains the coordinate axis and the normal, the measured width will be

$$W(\text{measured})=D*\tan(A)+W(\text{ionization})/\cos(A). \qquad (3)$$

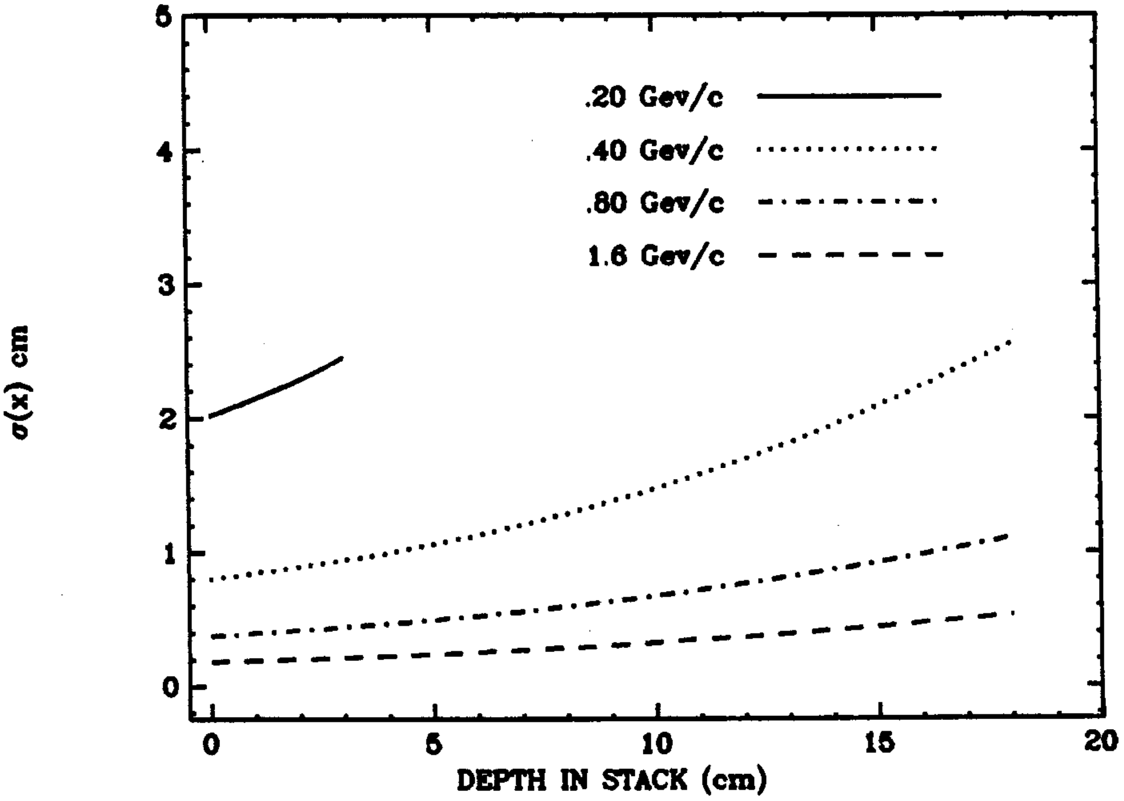

Figure B.7. Average projected multiple scattering for muons in the lead stack as a function of depth. Scattering in the solenoid coil is included.

The value of D for each of the 7 layers is listed in Table B.2. The angle where each term contributes equally to the measured width is also listed in Table B.2 for a typical ionization width of 2 centimeters.

TABLE B.2

Separation (D) between first and last physical layers, and angle (A) where ionization width and ganging width are equal.

	Trg	F1	F2	F3	U	T1	T2
D(cm)	---	3.8	3.8	4.8	6.8	6.8	2.8
A(deg)	---	30	30	25	17	17	46

For tracks which originate in the interaction region, the maximum value of A is less than 25 degrees for the F layers, but can be as large as 45 degrees in the T layers and 38 degrees in layer U. Thus we see the angular region in which the ganging does not confuse the width information is limited in layers T1 and U. This effect is partially compensated by the one-sigma pulse height cut in the raw data. Because the signal to noise ratio is low for minimum ionizing tracks, if only a fraction of the ganged physical layers receive ionization for any given strip, the signal will be proportionately less than the full minimum ionizing signal and therefore less likely to pass the pulse height cut. This lessens the effective signal widening due to ganging but also causes a net signal loss! The ganging problem could be nearly eliminated if the widths of the ganged strips in the deeper physical layers were made larger in proportion to their distance from the interaction region so that the edges of the ganged strips lie in a plane which contains the interaction region.

A very direct way to visualize the liquid argon response to minimum ionizing particles is to plot the average pulse height measured by a particular strip as a function of z where z is defined to be the difference between the predicted coordinate of a track at the average depth of the ganged layer and the coordinate of the center of the strip. Figure B.8a shows a plot of the average pulse height vs. z for trigger gap strip #18 (near the module center) made using muons from muon-pair events and averaged over all 8 modules. The very sharp cutoff at the edges of the strip reflects the quality of the drift chamber resolution in phi, while the typical average noise pulse height is reflected in the tails of the plot. The ratio of the signal at the peak to the average noise is nearly 18. Figure B.8b is a plot of the occupancy as a function of z where, as before, the occupancy is defined as the fraction of time when the pulse height is above the one-sigma cut. The average efficiency at the peak is 98%. Figure B.8c is a plot of the average pulse height for only those cases when the pulse height is above the cut. This signal to noise ratio is now only 4 and is more representative of the true signal to noise. We define the ′best physical signal to noise′ ratio as this ratio measured with minimum ionizing tracks at normal incidence. Figure B.8d is the same as Figure B.8c except it is for a strip in layer F1. The signal to noise ratio is worse for this layer than for the trigger gaps. Given that the pulse height exceeds the cut, it is difficult to separate a minimum ionizing signal from the noise. This makes it clear why it is important to use the narrowest search region possible when tracking minimum ionizing particles. Table B.3 gives the best physical signal to noise ratio (as defined above) for each layer.

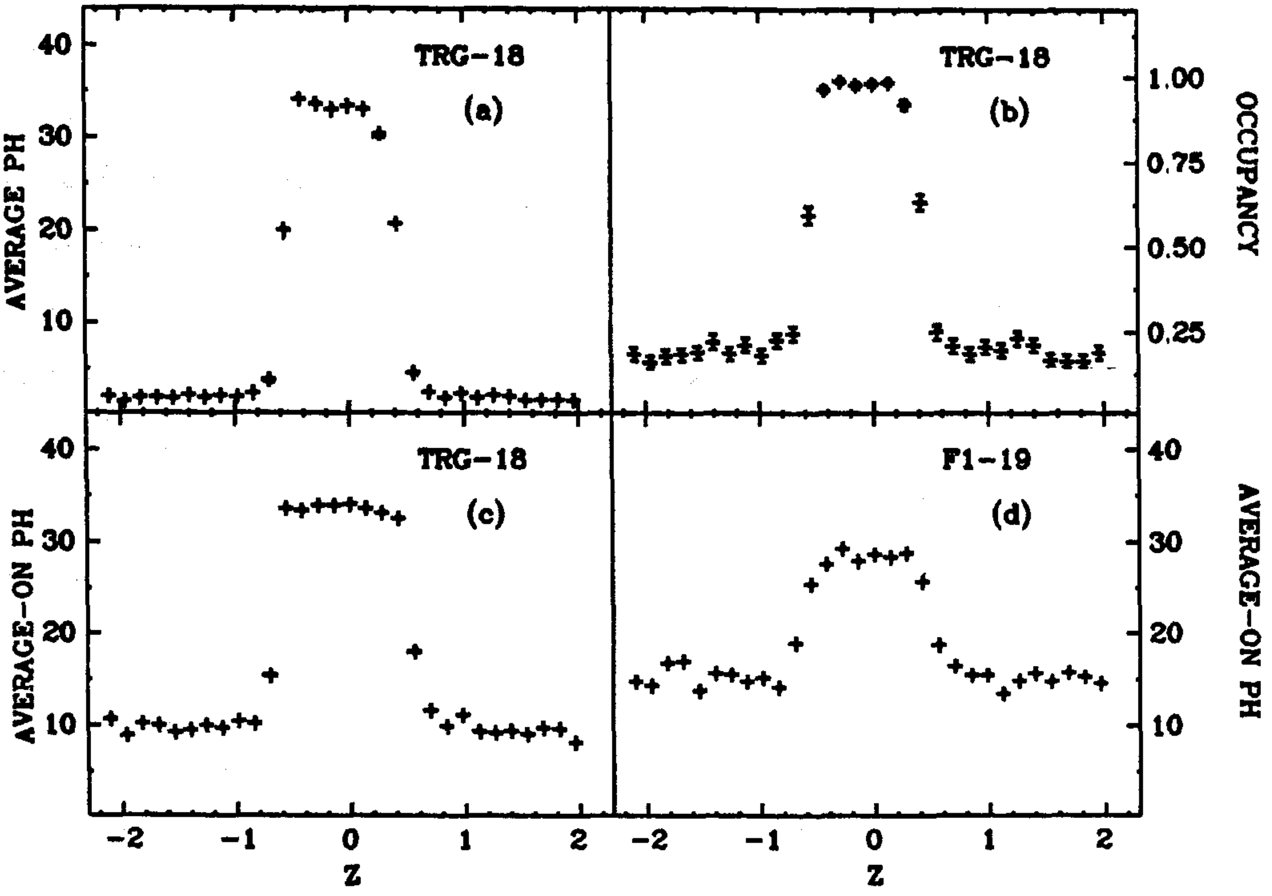

Figure B.8. Single strip response to minimum ionizing particles as a function of Z where Z is defined to be the difference between the predicted coordinate of the track at the average depth of the ganged layer and the coordinate of the center of the strip. For trigger gap strip 18 we show the (a) average pulse height; (b) occupancy, and (c) the average-on pulse height. For comparison, (d) shows the average-on pulse height for strip 19 in layer F1.

TABLE B.3

Best physical signal to noise ratio for each layer.

	TRG	F1	F2	F3	U	T1	T2
Best S/N	3.5	1.9	1.9	2.0	2.4	3.1	2.2

For the 4 F layers, the best physical signal to noise ratio is constant throughout each, but it varies in the other layers. Because the path length in an argon gap increases as the inverse cosine of the incident angle, the ionization increases and the signal to noise ratio should grow. This is what happens in layer T2. But in layer T1, as was mentioned before, as the angle of incidence increases there comes a point where the particle traverses at most only 2 of the 3 ganged physical layers for any given strip, thus reducing the signal by one third. As the incidence angle is further increased, eventually only one physical layer is traversed and the signal becomes lost in the noise.

The pulse height distribution for muon tracks which go through the central region of trigger strip 18 in module 1 is shown in Figure B.9. Also shown is the pulse height distribution expected from the Landau theory[10], and from the Landau theory folded with a Gaussian resolution function. This data was collected over several months, so the resolution has contributions both from the electronic noise and the intrinsic resolution of the calibration system for this channel. What does not contribute to this resolution but will contribute to the overall system resolution are any channel to channel differences, incidence angle effects, or tracking peculiarities such as edge effects or noise from other strips in the search region.

Because the average pulse height versus z function is very

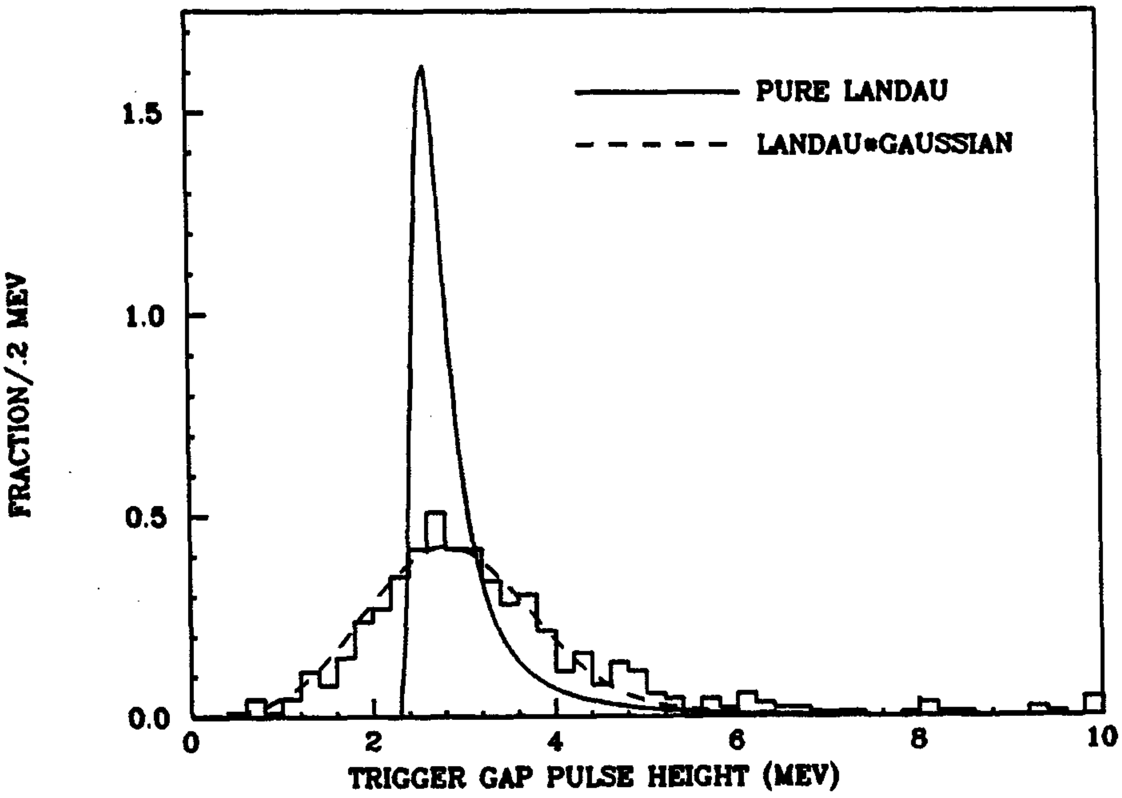

Figure B.9. Response of the trigger gap to minimum ionizing particles. The Landau distribution is shown along with the expected distribution after folding in the electronic noise.

distinct, we can use it to measure individual strip positions relative to the drift chamber prediction. In particular, this method was used to verify the correctness of the strip wiring. About 1% of the strips were found to be miswired, although most cases were relatively minor interchanges of adjacent strips. A small misalignment of the drift chamber was discovered which resulted in errors for modules 5 through 8 in the z coordinate predictions for which corrections are made. The points where the z response function drops below 150% of the average noise is plotted for layer T1 in Figure B.10. The increase in the width of the z function near the module ends has contributions both from the ganging and the worsening of the tracking resolution as the polar angle theta moves away from 90 degrees. The search region algorithm for minimum ionizing tracks uses the width measured in this manner for each layer and includes the contribution expected from multiple scattering for lower momentum tracks.

We will now discuss the muon response of the liquid argon counters as defined by the search algorithm mentioned above. Muons from muon-pair events and from cosmic ray events are used as muon samples. Cosmic events are required to be no more than 20 cm from the interaction region along the z axis, and only the outgoing track is used. Except for layer T1, the minimum ionization pulse heights have the expected 1/cos dependence on the incident angle and unless otherwise stated, all minimum ionization pulse heights will have this factor removed.

The material preceding the trigger gaps represents 30 g/cm^2 dE/dx equivalent of aluminum. Normally incident muons with momentum less than 180 Mev/c will range out in this material. The additional 85 gm/cm^2 of lead and 17 gm/cm^2 of argon in the stack will stop muons with

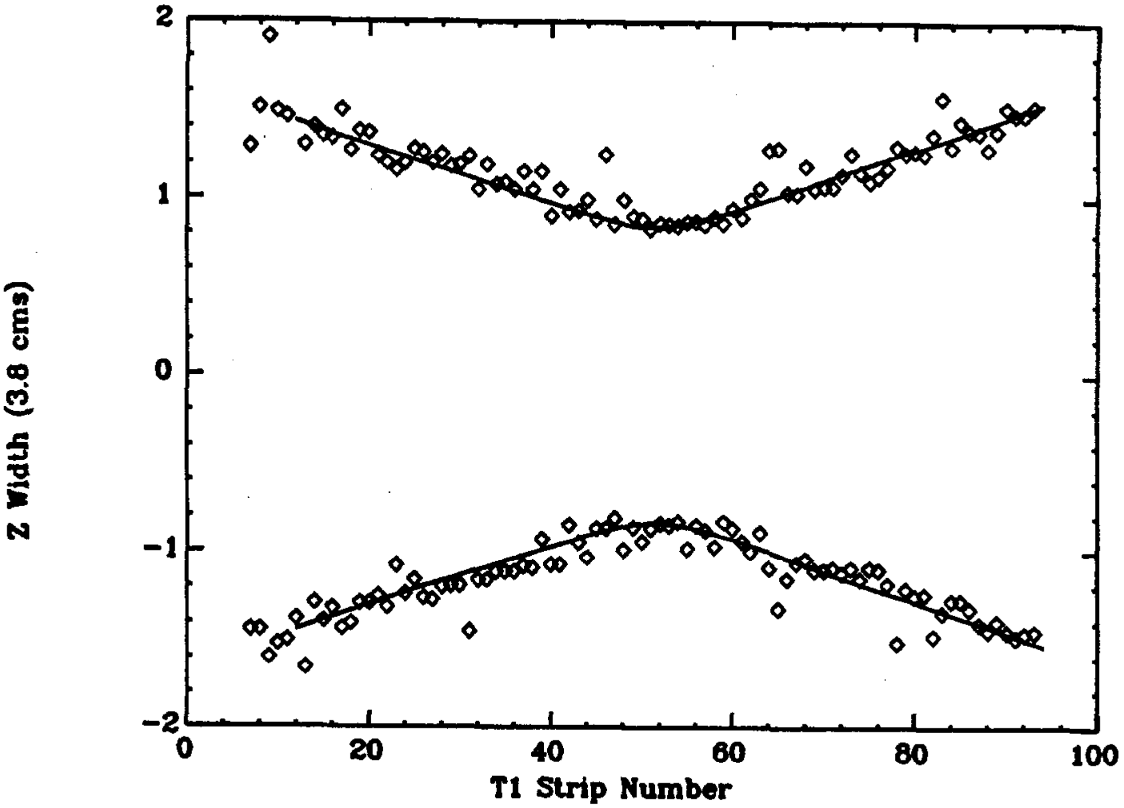

Figure B.10. Width of the Z response function for minimum ionizing particles as a function of strip number in layer T1.

momentum less than 320 Mev/c. Figure B.11 is a plot of the range in the stack for muons at normal incidence and at an incidence angle of 45 degrees. The layers' response to stopping tracks is complicated by the fact that they are either thick (F3) or effectively thick due to ganging. Figure B.12 plots the average layer pulse height for muons as a function of the range in the stack for the trigger gaps and the two T layers. Because its cells are adjacent, the response in layer T2 experiences a sharp rise, peaks, and then levels off as the particle range increases. The response for layer T1 is more gradual because its cells are not contiguous. The layer efficiency for detecting minimum ionizing tracks peaks, as expected, where the minimum ionization pulse height peaks. The average minimum ionization total pulse height is plotted as a function of muon momentum in Figure B.13. The average energy loss, which quickly approaches the Fermi plateau, is compared to the theoretical expectations shown with or without the density effect contribution (see Appendix A).

The frequency distribution for the total pulse height is shown in Figure B.14 along with the response from 'imaginary' tracks obtained by tracking muons in the wrong module. The minimum ionizing signal is easily separable from the noise. For comparison, Figure B.15 shows the pulse height distributions for the trigger gaps and layer F1. For the sake of clarity, the point at zero response is not shown. Table B.4 lists, for both real and 'imaginary' tracks, the fraction of time the layer had no signal. Also listed is the most probable signal for real tracks, and for the imaginary tracks, the one sigma noise level. We can see here the effects of dead or inefficient channels (i.e., the minimum ionizing particle efficiency for a good trigger strip is above 98%).

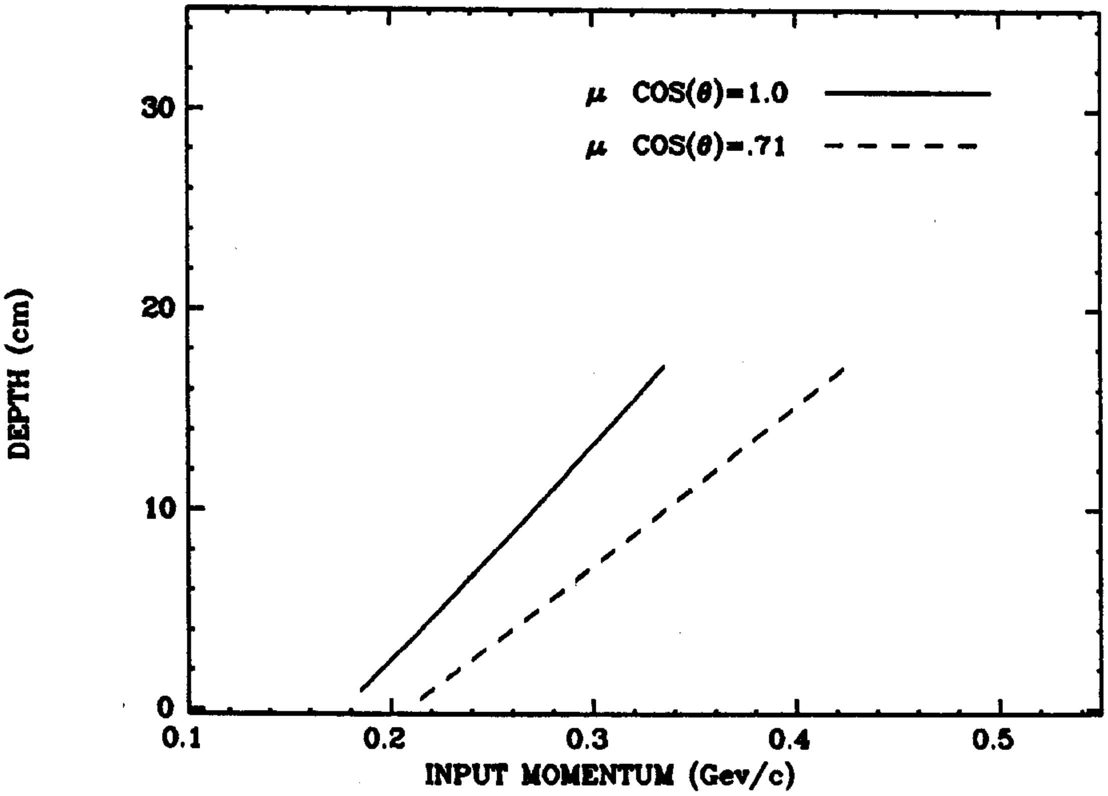

Figure B.11. Muon range in the lead stack as a function or momentum. Energy losses in the upstream material have been included.

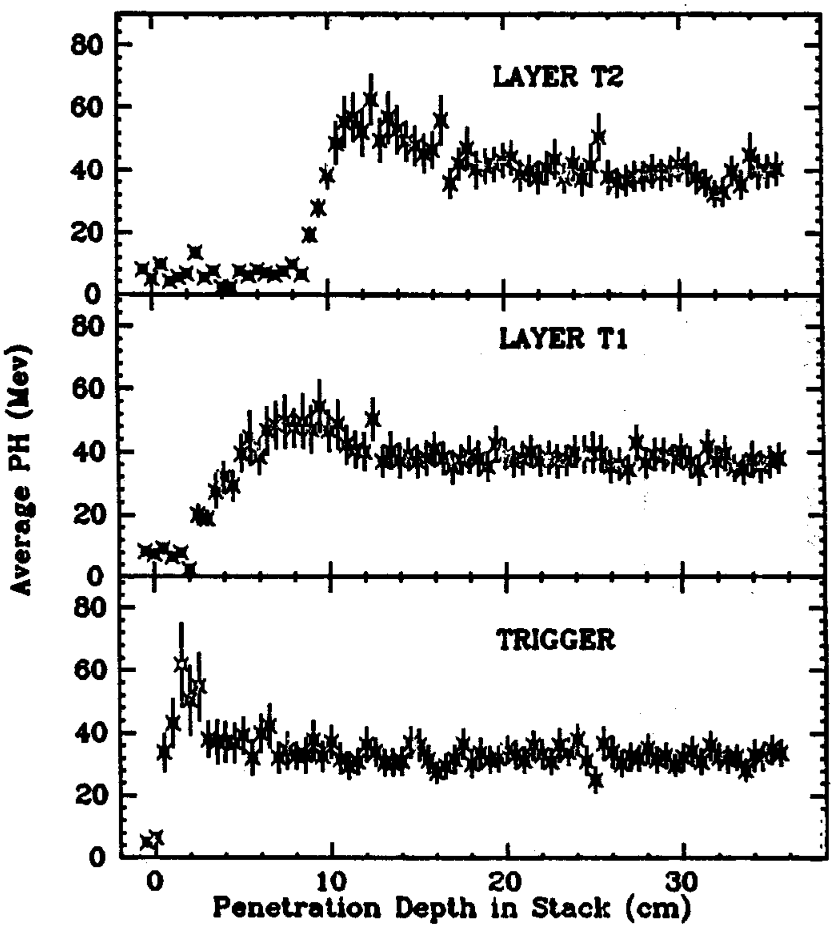

Figure B.12. Average pulse height for minimum ionizing particles as a function of range in the stack for layers T1 and T2, and the trigger gaps.

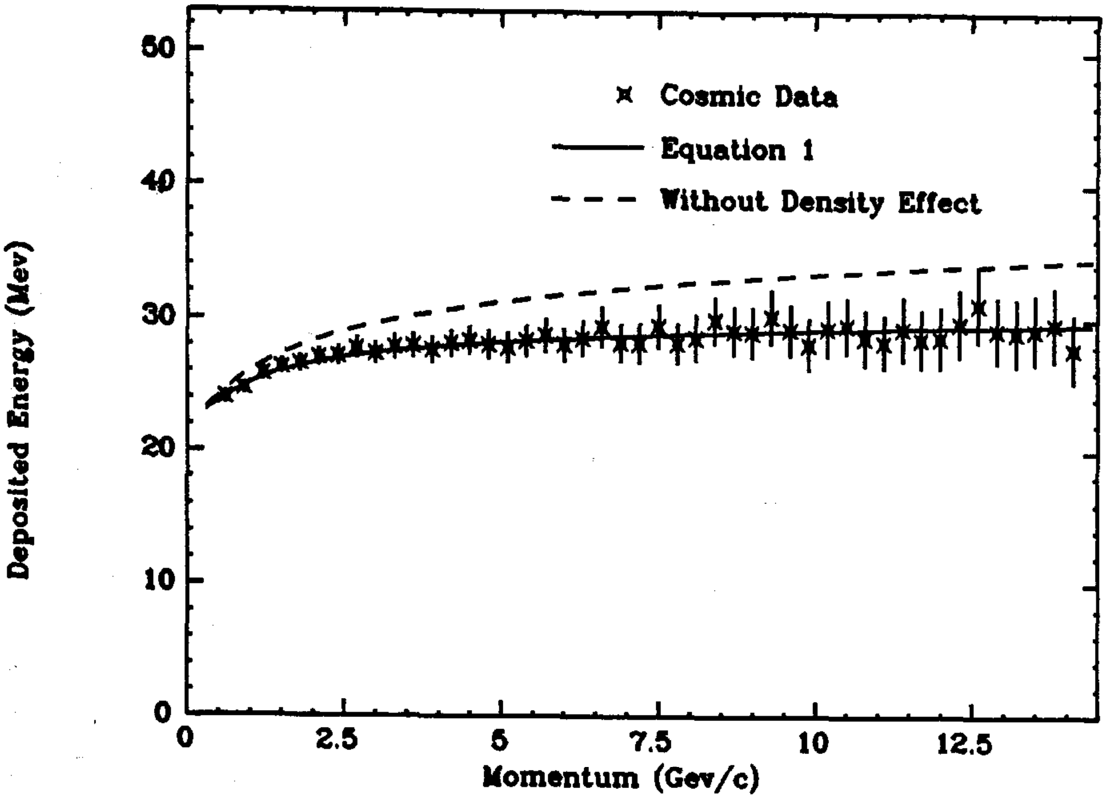

Figure B.13. Average total pulse height for muons as a function of momentum. The theoretical predictions with and without the density effect correction are shown.

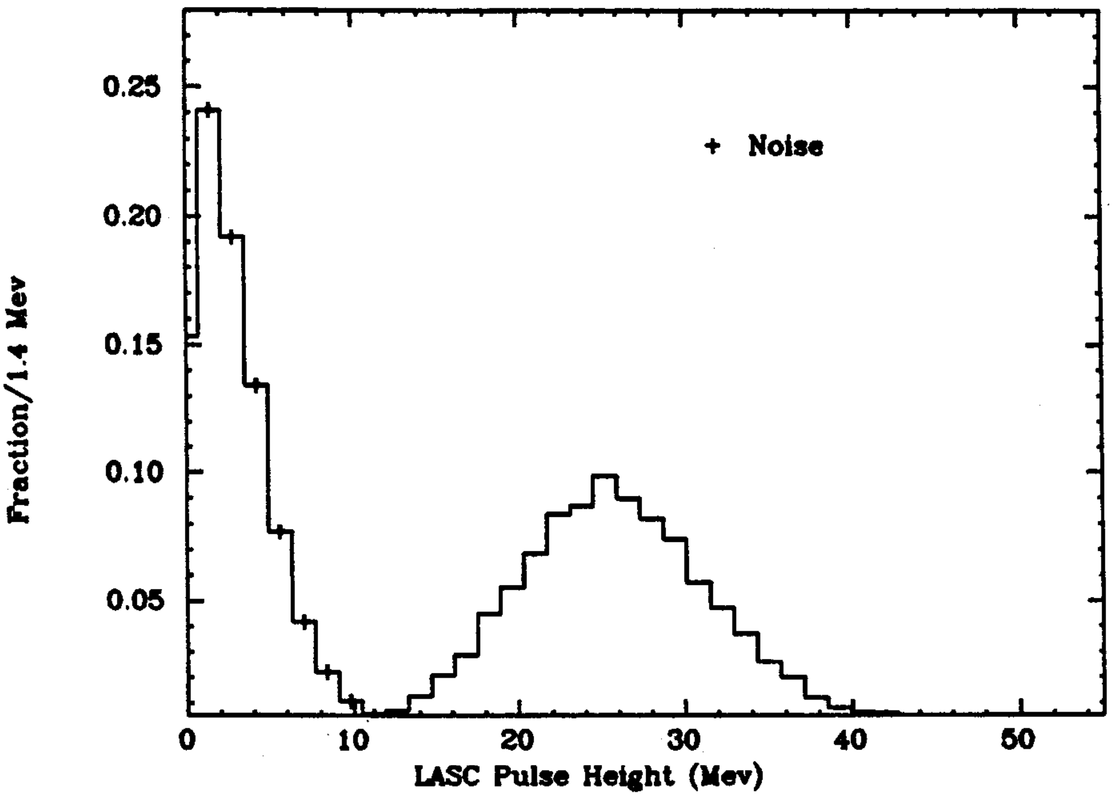

Figure B.14. Distribution in total pulse height for minimum ionizing tracks in the shower counter. The noise response is also shown.

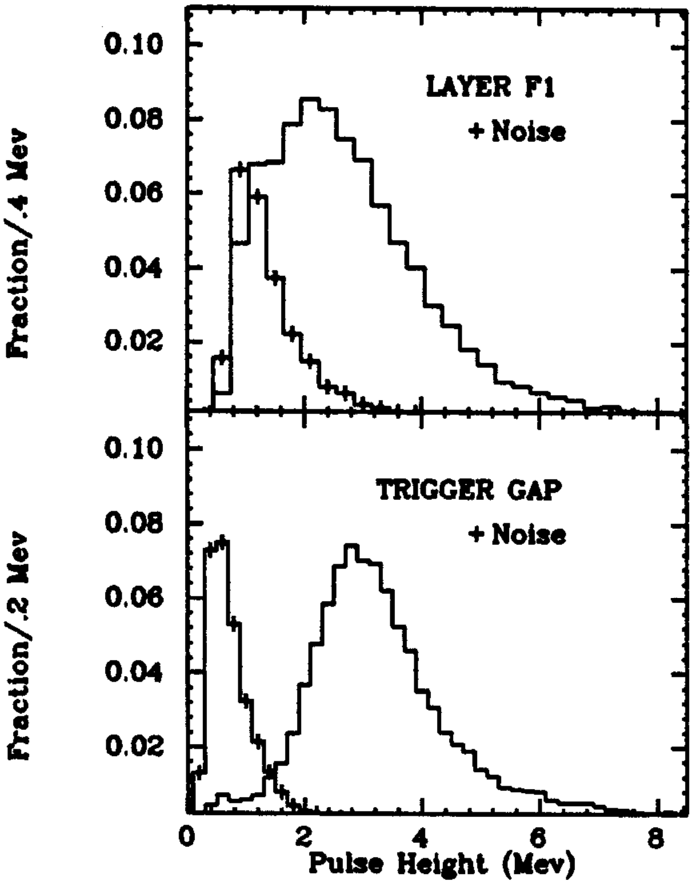

Figure B.15. The pulse height distribution for minimum ionizing tracks in the trigger gap and layer F1. The noise response is also shown. The point at zero response is not plotted.

Note also the noise occupancy is larger than the 16% expected from individual strips due to the search region requirements.

TABLE B.4

Shower counter inefficiency and most probable pulse height for minimum ionizing tracks. The occupancy and average pulse height due to noise are also listed.

	Trg	F1	F2	F3	U	T1	T2
Zero response fraction(%)	8.7	14.	14.	12.	5.0	2.4	6.8
Noise occupancy(%)	30	24	23	27	27	34	25
Most probable pulse height (Mev)	2.9	2.3	2.4	6.3	3.6	3.4	3.6
Noise (Mev)	.77	1.2	1.2	2.8	1.4	1.1	1.4

B.6 ELECTROMAGNETIC CASCADE SHOWERS:

Next we discuss the basic processes which govern electromagnetic shower development[11]. For electrons, bremsstrahlung is the dominant energy loss mechanism until the energy falls below the critical energy[12] of the shower material. At that point ionization losses become more important.

Pair production is the most significant photon interaction for photon energies above a few Mev. The cross section rises with photon energy until a plateau is reached when the photon wavelength is on the order of a nuclear diameter (~200 Mev). Low energy photons lose energy primarily by Compton scattering (4)

$$\gamma+e^- \rightarrow \gamma+e^- \tag{4}$$

which has a cross section that goes inversely as the photon energy[13]. Thus the total photon cross section has a minimum near an energy of a few Mev, and photons of this energy will be the end products of electromagnetic showers. As they are absorbed comparatively weakly, a certain fraction of the shower energy will escape through the back of the shower counter. Other interactions, such as the photoelectric effect, positron annihilation, and photo-meson production make less important contributions to the shower development[14].

The transverse momentum transfer in the electromagnetic processes mentioned above is typically no greater than m_e*c so that the emission angle between the photon and electron in bremsstrahlung is small as is the angle between either electron and the primary photon in pair production. These processes cause very little transverse spreading in the shower. Multiple coulomb scattering produces much larger transverse deflections of the charged shower particles and therefore dominates the transverse shower development.

Simple arguments like those above can be used to qualitatively understand electromagnetic cascade showers. However, a shower is a complicated stochastic process and detailed description using analytic methods is difficult. Monte carlo simulation of the shower provides an alternate method and allows shower development in complicated geometries to be explored. The EGS[15] shower simulation program available at SLAC has been used to study shower development in the liquid argon shower counters. Some results of this study are presented below.

B.7 MONTE CARLO SIMULATION OF ELECTROMAGNETIC SHOWERS:

Interpretation of the shower development in the modules is complicated by the electrical ganging of the physical cells, electronic noise, and the large width of the strips. Therefore, we will begin by discussing shower simulation in a module without electronic noise or ganging, and with strips narrow enough to provide a clear measurement of the transverse shower development. The material upstream of the trigger gap layer totals 1.34 radiation lengths and is included in the shower simulation. Average shower properties will first be discussed.

The average longitudinal shower development as measured by the energy deposited in the liquid argon gaps is shown in Figure B.16 for electrons of several different momenta. The position of shower maximum increases like the logarithm of the initial energy, and the shower has an exponentially decaying tail. The fraction of the total energy which leaks out the back grows logarithmically with the energy and varies exponentially as the effective stack thickness for different incident angles.

In Figure B.17 we have plotted normalized average transverse energy distributions for 750 Mev electron showers as seen by cells at several depths. The distributions have larger tails than gaussians, especially for the trigger gap layer due to the large distance between it and the coil. A measure of the width of the distribution is its root mean square deviation σ_w. We show σ_w in Figure B.18 as a function of cell depth for several incident energies. As the energy increases, σ_w narrows as expected from multiple coulomb scattering. If there was no material upstream of the stack, σ_w would grow with increasing depth. But the coil material, located roughly 20 cm upstream, broadens the shower in the first part of the module.

Another, perhaps more useful, measure of the transverse width is

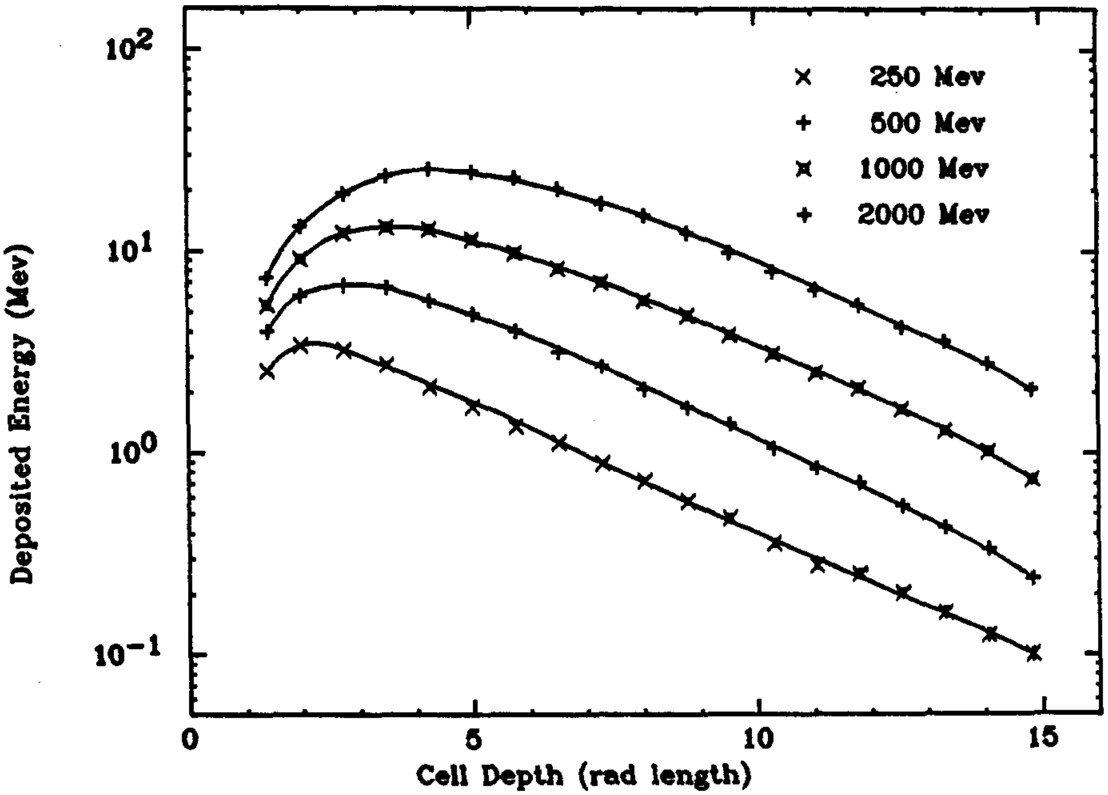

Figure B.16. Monte Carlo calculation of the average lognitudinal shower development as measured by the energy deposited in the liquid argon gaps.

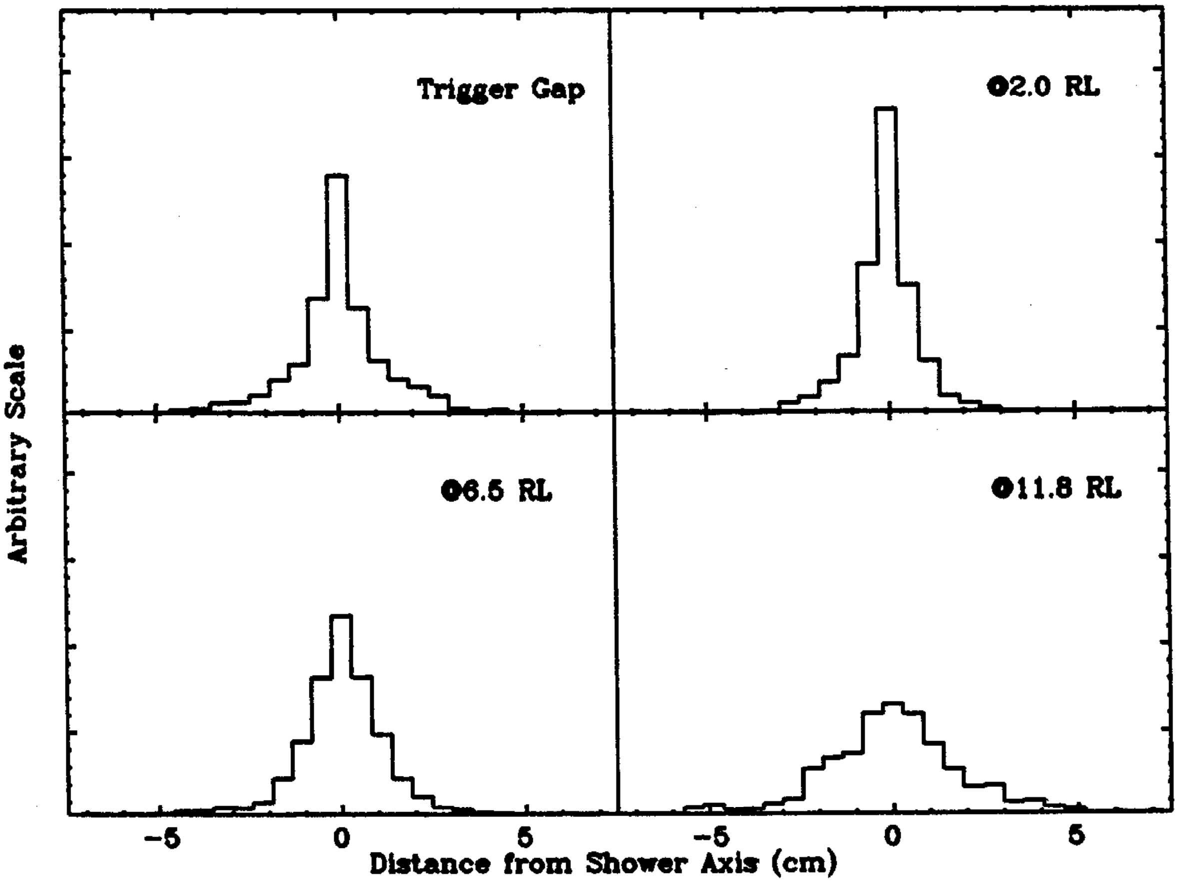

Figure B.17. Monte Carlo calculation of the average transverse shower distribution in the trigger gaps and at three depths in the stack. The effects of the material upstream of the counter are included.

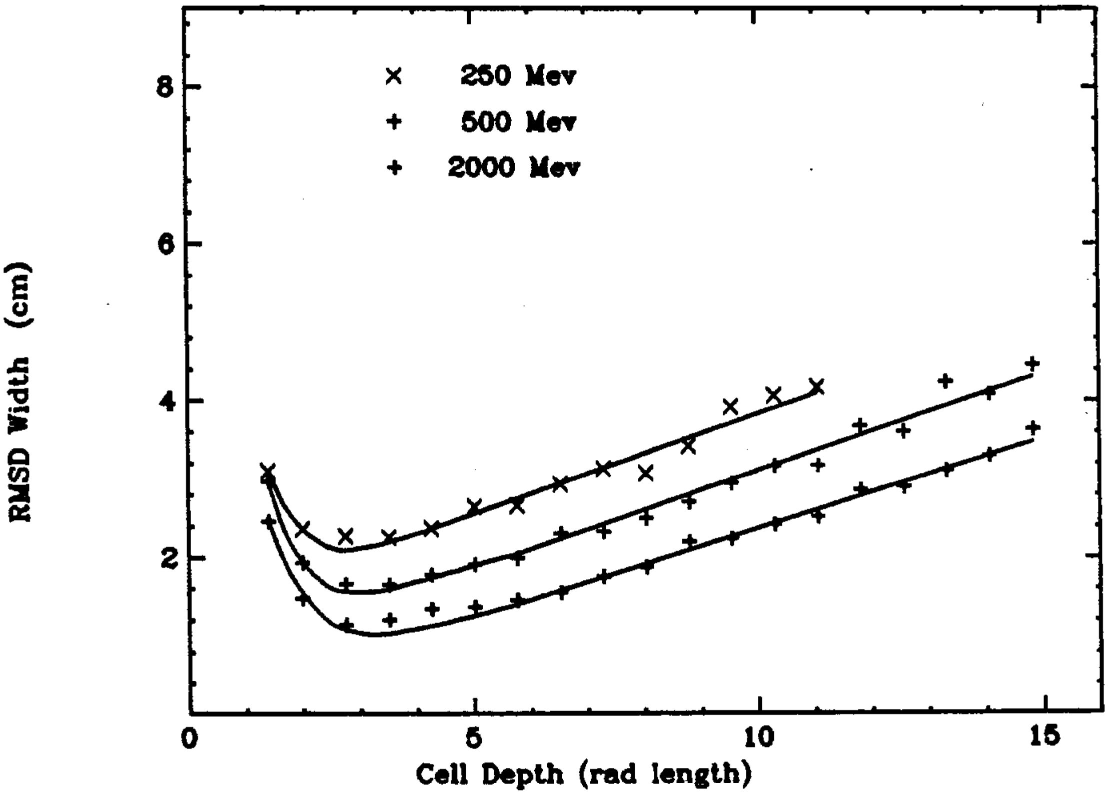

Figure B.18. RMSD width of the average shower transverse energy distribution as a function of depth in the stack.

the energy fraction width σ_{ew} defined as the distance between the two points where the energy in the tails of the distribution is a certain fraction of the total energy (e.g., for $\sigma_{ew}(90\%)$, each tail contains 5% of the total energy). This quantity is less sensitive to the long tails found in the transverse distribution, and is useful in determining tracking regions. Figure B.19 plots $\sigma_{ew}(90\%)$ as a function of cell depth for several incident energies. The ratio of σ_{ew} to σ_{w} depends, of course, on the shape of the transverse distribution, but it is found to vary from its average value by no more than 30% for different depths or incident energies. In Figure B.20 we have plotted the ratio, $\sigma_{ew}(P)/\sigma_{w}$ averaged over all cells, as a function of P for 750 Mev showers. The ratio quickly rises as P exceeds 90%. As concerns the particle identification function of the shower counter, it is desireable to limit the search region in the tracking algorithm at the expense of a small loss in the measured shower energy.

As an illustration of the effects of the coil material, Figure B.21 plots $\sigma_{ew}(90\%)$ for 750 Mev showers as a function of cell depth with and without the upstream material. The coil material dominates the transverse development up to the region near shower maximum.

The main effect governing the change in the longitudinal shower development as the angle of incidence changes, is the apparent scale change in the longitudinal construction of the shower counters. Beyond the first few radiation lengths, the average longitudinal energy distribution can be calculated from that at normal incidence by scaling a cell's pulse height and depth by the inverse cosine of the normal angle. Shower development in the first few radiation lengths depends

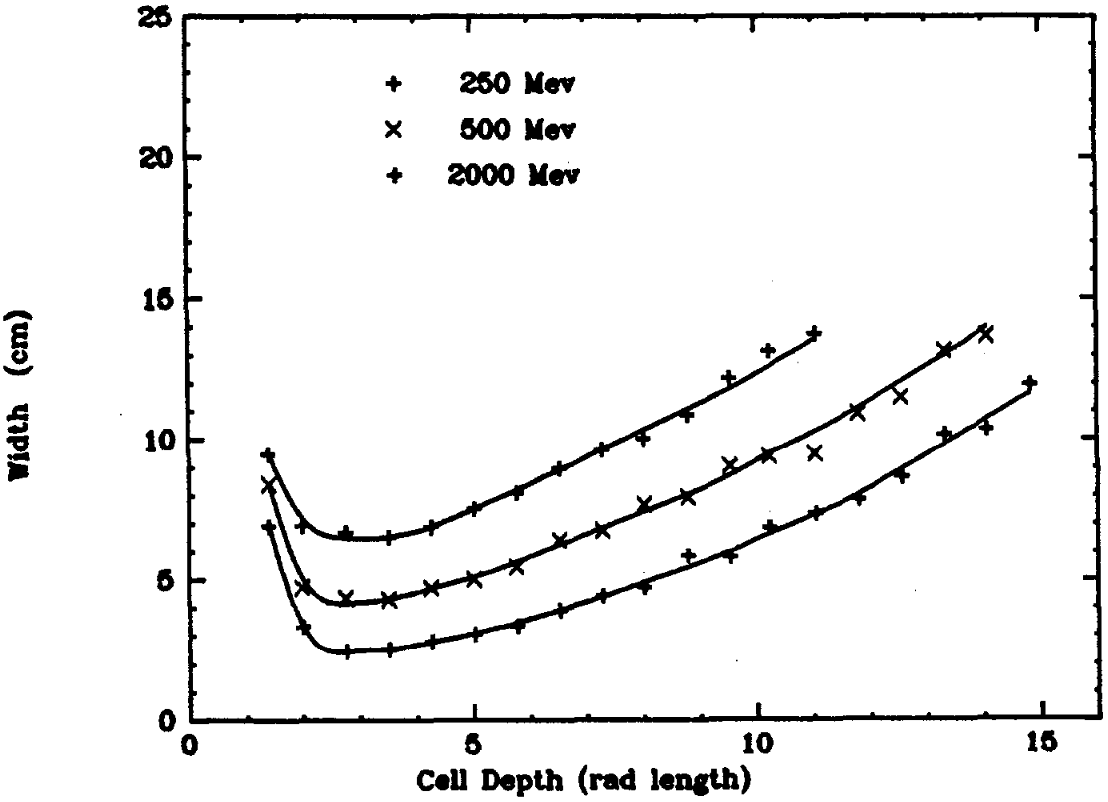

Figure B.19. 90% energy fraction width of the average shower transverse distribution as a function of depth in the stack.

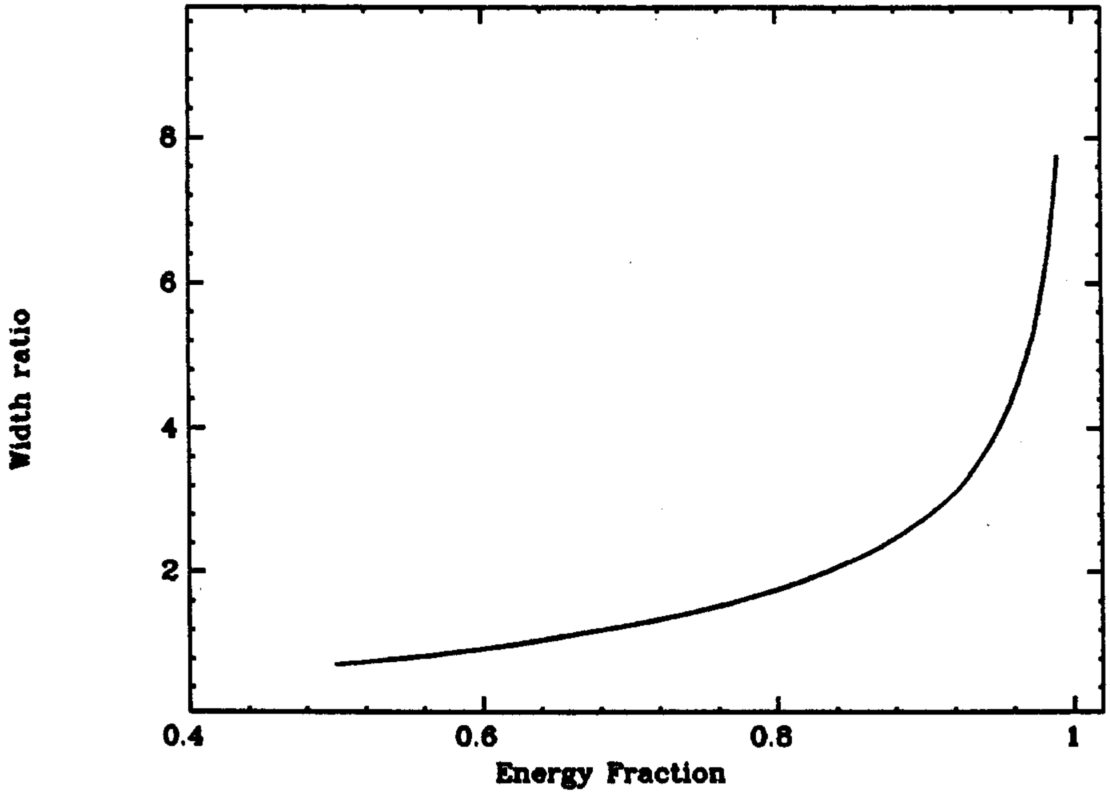

Figure B.20. Ratio of the energy fraction width to the RMSD width of the average shower transverse distribution as a function of the energy fraction for 750 MeV electrons.

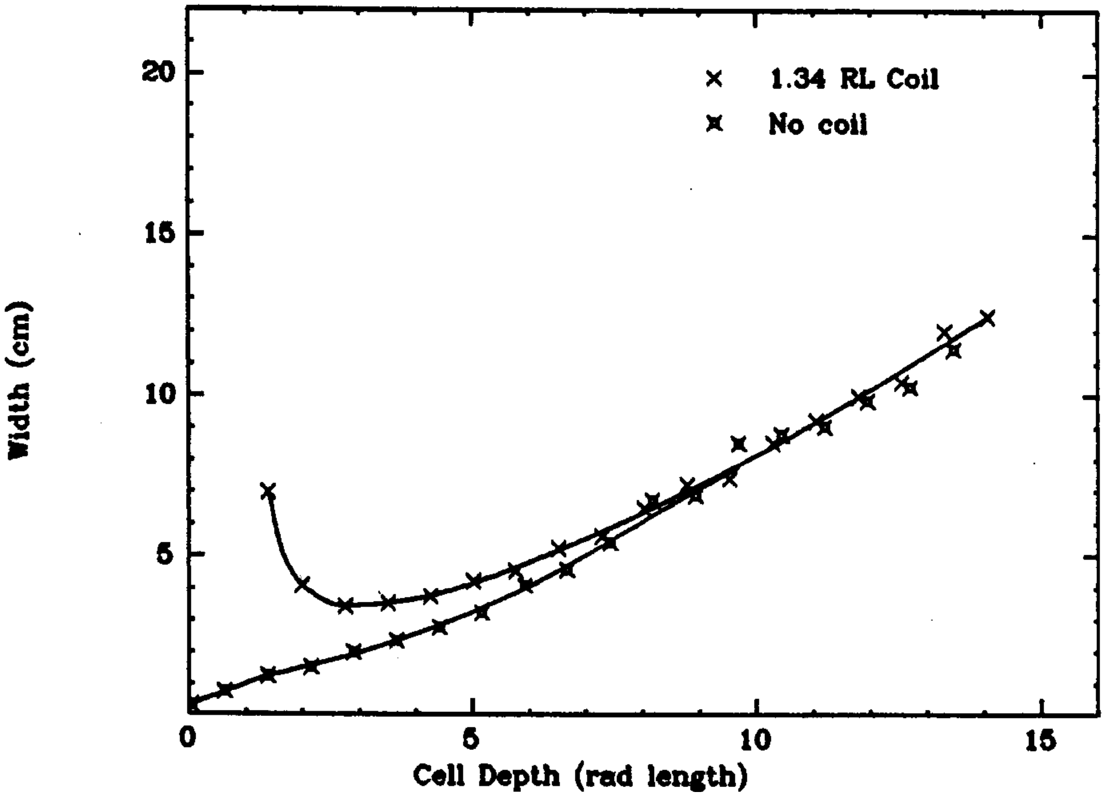

Figure B.21. 90% energy fraction width for 750 MeV showers as a function of depth in the stack with and without the material upstream of the counter.

more strongly on the thickness of the lead absorber plates and the simple scaling arguments seem to slightly overestimate the measured values. This is illustrated in Figure B.22 which shows the average longitudinal energy distribution for 500 and 2000 Mev showers incident at 45 degrees, along with that expected from simple scaling.

Several effects are important in determining the average transverse shower development as the incidence angle changes. The centroid, as measured by the energy deposited in the liquid argon gaps, deviates from that predicted from the initial direction primarily due to two factors. The first is a small effect and is important only in the initial gaps. Shower particles which are scattered so as to increase their angle of incidence have a longer path length in the argon, and cross the argon gap (on the average) further from the shower axis. Thus the centroid is slightly biased in a direction away from the normal.

A second effect occurs which tends to bend the shower centroid towards the stack normal. Because shower particles that are scattered towards the normal travel through less material by the time they reach a given depth, they suffer less attenuation. Thus the shower 'bends' towards the normal as it propagates through the stack. Figure B.23 plots the deviation of the centroid from the 'expected' position for 500 and 2000 Mev electrons incident at 45 degrees. The deviation decreases as the shower energy increases.

As demonstrated in Figure B.21, the average transverse shower development in the first half of the module is primarily determined by the coil material. As might be guessed from the arguments mentioned above, this contribution to the width grows more quickly than simple scaling would predict. In the deeper regions of the stack, the bending

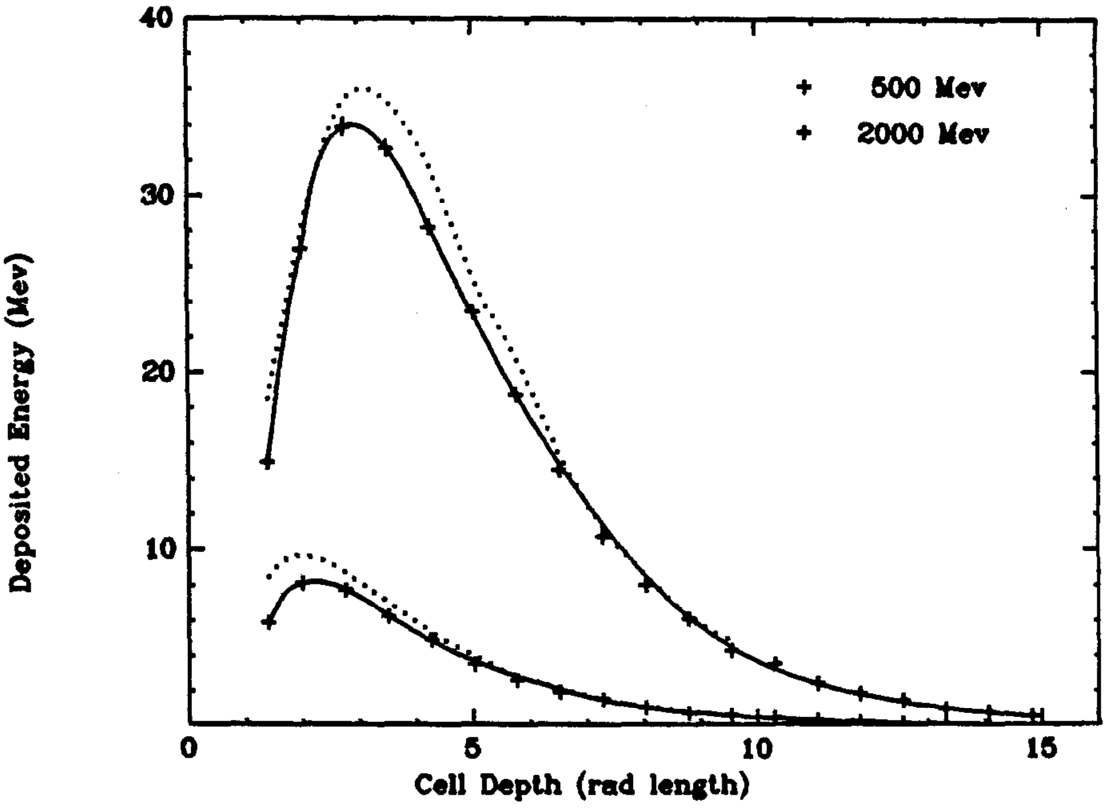

Figure B.22. Longitudinal energy distribution as a function of cell depth for 500 and 2000 MeV showers incident at 45 degrees. The dotted line shows the curve obtained by scaling the measured distribution for normally incident tracks.

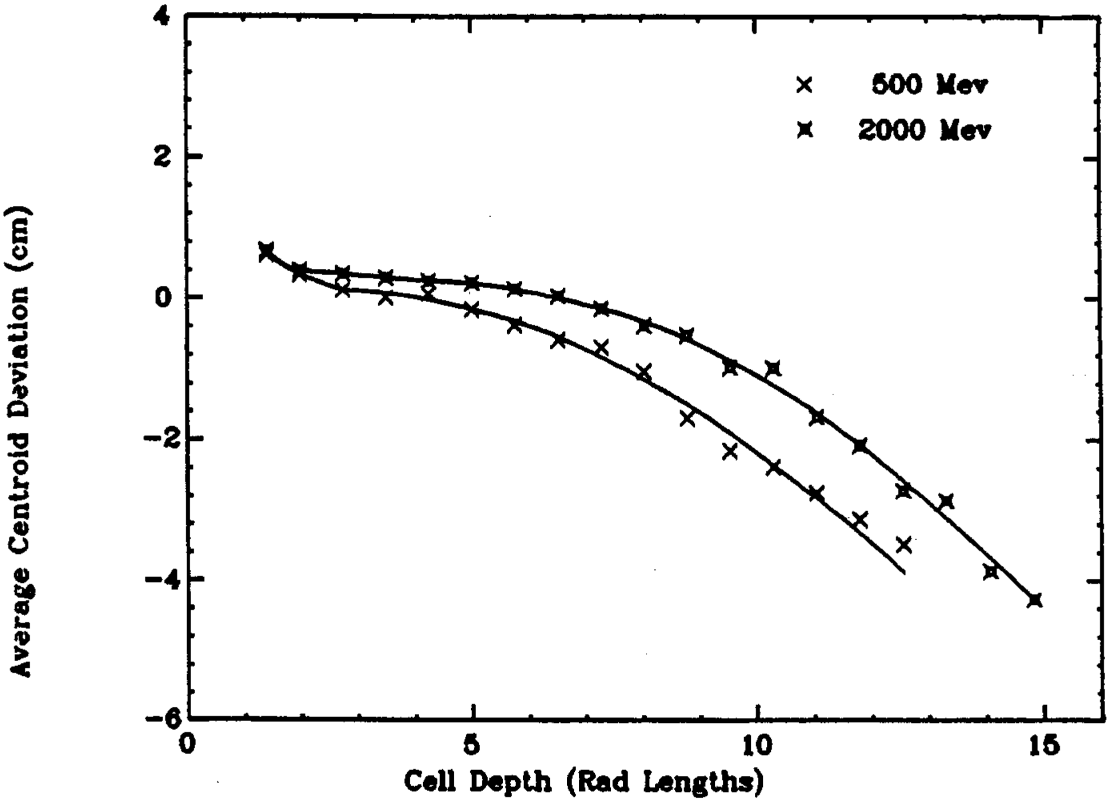

Figure B.23. Average deviation of shower centroid from predicted position as a function of cell depth for showers incident at 45 degrees.

of the shower towards the normal causes the average shower width to grow less quickly than expected. Figure B.24 plots the measured σ_w for 1000 Mev electrons at 45 degrees compared to that expected from simple scaling.

We turn now to the question of individual fluctuations from the average shower response. As regards the overall energy resoultion, a simple argument will illustrate the nature of the fluctuation. Since only a small fraction (1/8) of the total energy is deposited in the liquid argon, fluctuations in this fraction dominate the energy resolution. The energy deposited in the liquid argon is roughly equal to the number of minimum ionizing particles which traverse a gap times the average energy lost by each particle in the gap. We ignore fluctuations in the individual particles' ionization loss. (Note that in certain classes of shower counters, such as those which measure the ionization with proportional tubes, this fluctuation cannot be ignored.) The total number of liquid argon gaps crossed is given by the incident particle's energy divivded by the energy lost by a minimum ionizing particle in traversing one argon gap and one lead plate (9.8 Mev). Because the electrons and positrons are created in pairs, the number of uncorrelated events is less than this by a factor between 1 and 2. So the relative error is given by

$$\Delta E/E = 1/\sqrt{E/(.098\ \mathrm{Gev})/\neg 1.5} = .12/\sqrt{E} \qquad (5)$$

Thus we see the resolution is inversely proportional to the square root of the energy, and is proportional to the square root of the cell thickness. The Monte Carlo yields somewhat better results ($.10/\sqrt{E}$) although it deteriorates at low energy faster than the inverse square root due to large fluctuations in the energy lost in the coil. Because

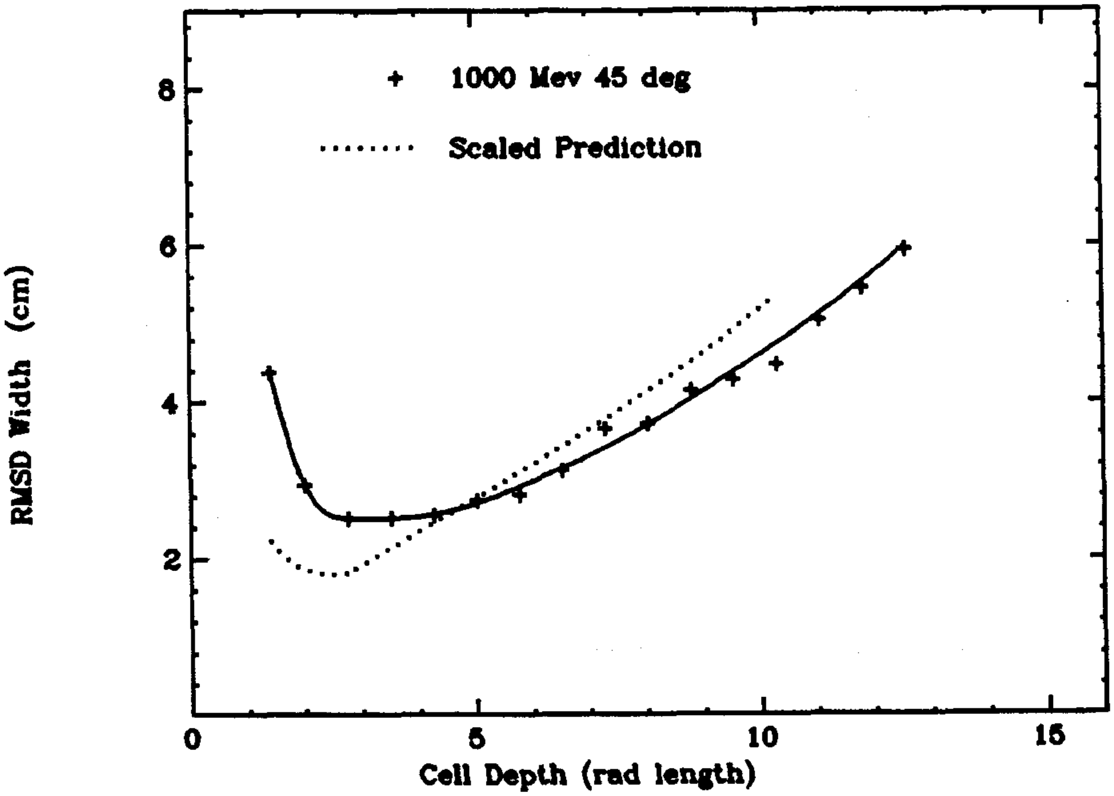

Figure B.24. RMSD width of the average shower transverse distribution as a function of cell depth for 1000 MeV showers incident at 45 degrees. The dotted line shows the curve obtained by scaling the measured widths for normally incident tracks.

the effective gap thickness increases as the inverse cosine of the normal angle, we expect the resolution varies with the angle of incidence like the inverse square root of the cosine. However, the increased effect of the fluctuations in the energy lost in the coil decrease the resolution more quickly than this at large incidence angles.

There are large fluctuations about the average for the energy deposited in any particular cell. Figure B.25 is a plot of the deposited energy distribution in the trigger gaps and 2 stack cells for 750 Mev electrons. We can see the evolution of the shower develpment in these distributions. In the trigger gap distribution, a peak is clearly seen representing a single minimum ionizing particle traversing the argon gap. As we consider deeper cells, the minimum ionization peak become less prominent reflecting the evolving nature of the shower: there are more lower energy electrons which range out as the Compton ionization process becomes increasingly important. As is illustrated in Figure B.25b, the distributions become Poisson in character.

The relative rmsd width of the individual cell energy distribution is plotted in Figure B.26 for several different incident energies. Just as the overall energy resolution is determined by the number of argon gaps traversed by charged shower particles, the individual cell energy resolution is determined by the average number of energy depositing processes, 'events', which occur in an individual cell. Assuming the distributions are Poisson, the measured average energy and rms deviation from the average can be used to determine the average number of 'events' and the mean energy deposited by each 'event' for the cell in question.

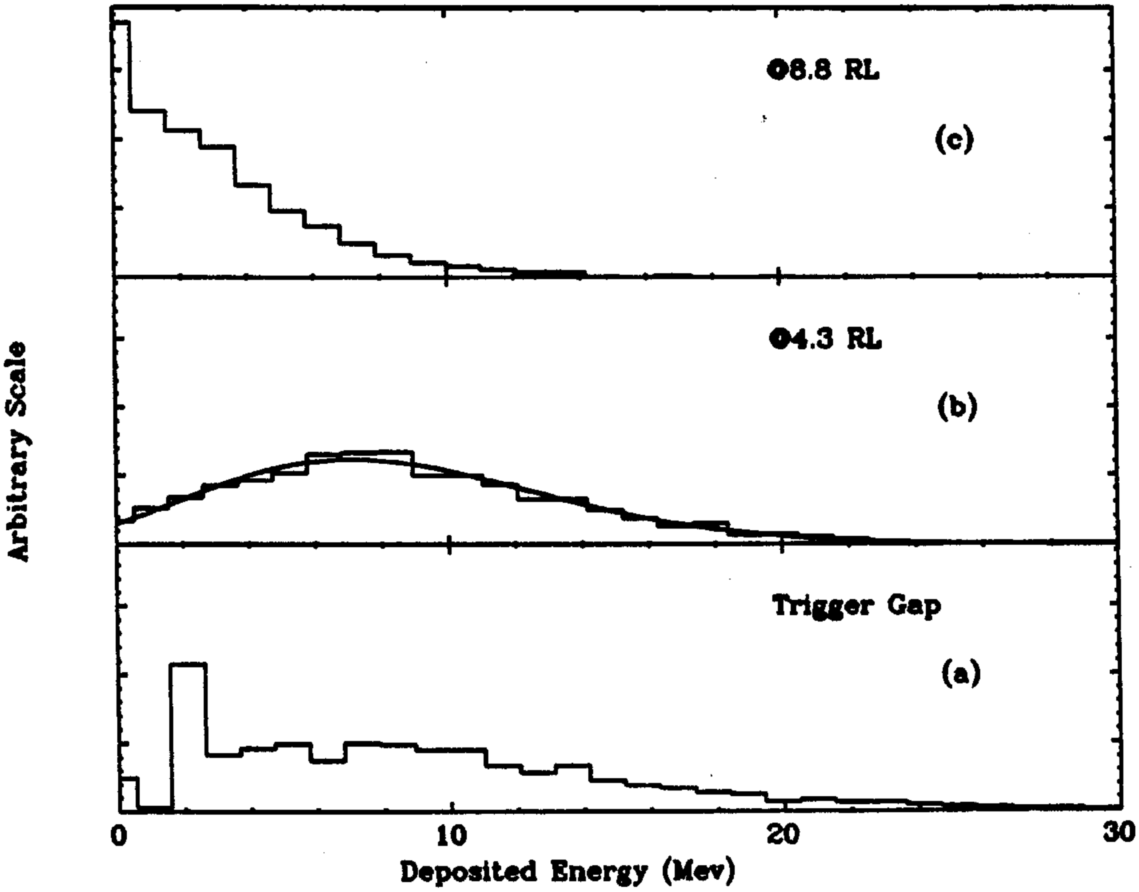

Figure B.25. Deposited energy distribution for 750 MeV showers in the trigger gaps and at two depths in the stack.

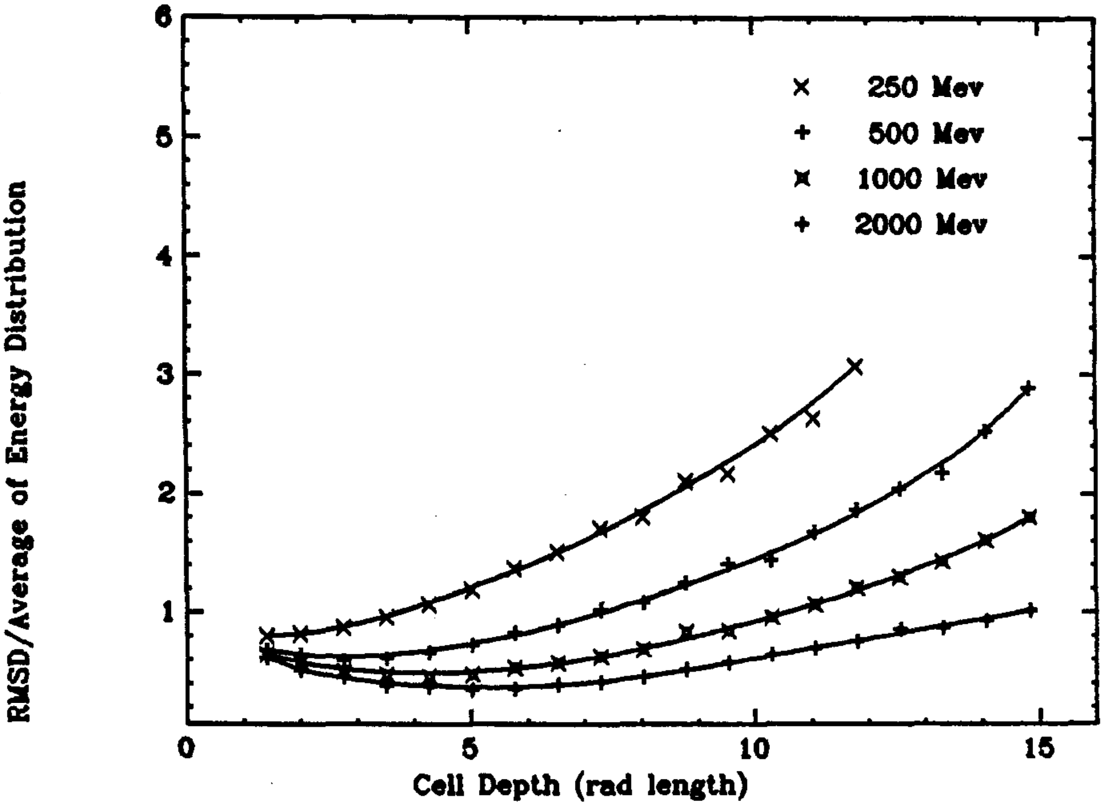

Figure B.26. Relative RMSD width of the individual cell energy distribution as a function of depth in the stack.

In Figure B.27 we have plotted for 750 Mev showers, the average energy per 'event' calculated in this way as a function of cell depth. It is nearly constant except near the rear of the module where it begins to decrease. Another way to interpret this plot is to note that the relative rms deviation of the energy distribution is less than unity whenever the average energy deposited in a cell is greater than this 'event' energy.

There are weak correlations between the deposited energy in different cells. Figure B.28 is a plot of the correlation coefficients between specific cells and the other cells in the counter. The coefficients are generally positive between cells on the same side of shower max, and negative for cells on opposite sides. The correlation is usually strongest between adjacent cells and grows as the shower energy increases. (See Ref. 16 for data at 20 Gev).

The measurement of an individual shower's transverse distribution is a more difficult problem than the corresponding longitudinal measurements particularly at low or moderate energies because one must subdivide an already meager data sample. There are several reasons which make a detailed discription of such measurements with the ideal module of limited value. For example, when the probability of any given cell receiving energy is small, a more useful discription of the shower development can be obtained if the signals from several contiguous cells are added together. However, the transverse response of the ganged cells --as measured by the average of individual shower width or centroid measurements-- cannot be obtained from a knowledge of these quantities for the unganged cells. Also, the transverse energy distribution of an individual shower is not a continuous function, and

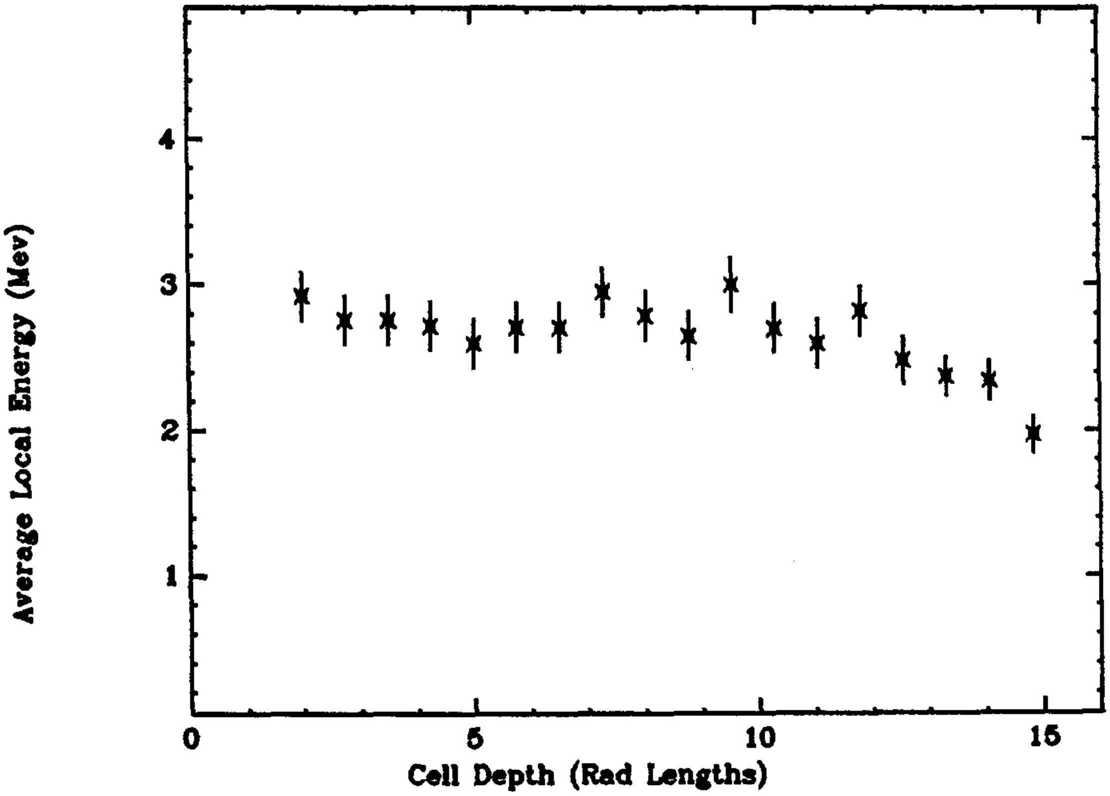

Figure B.27. Average local energy deposited as a function of depth in the stack (see text).

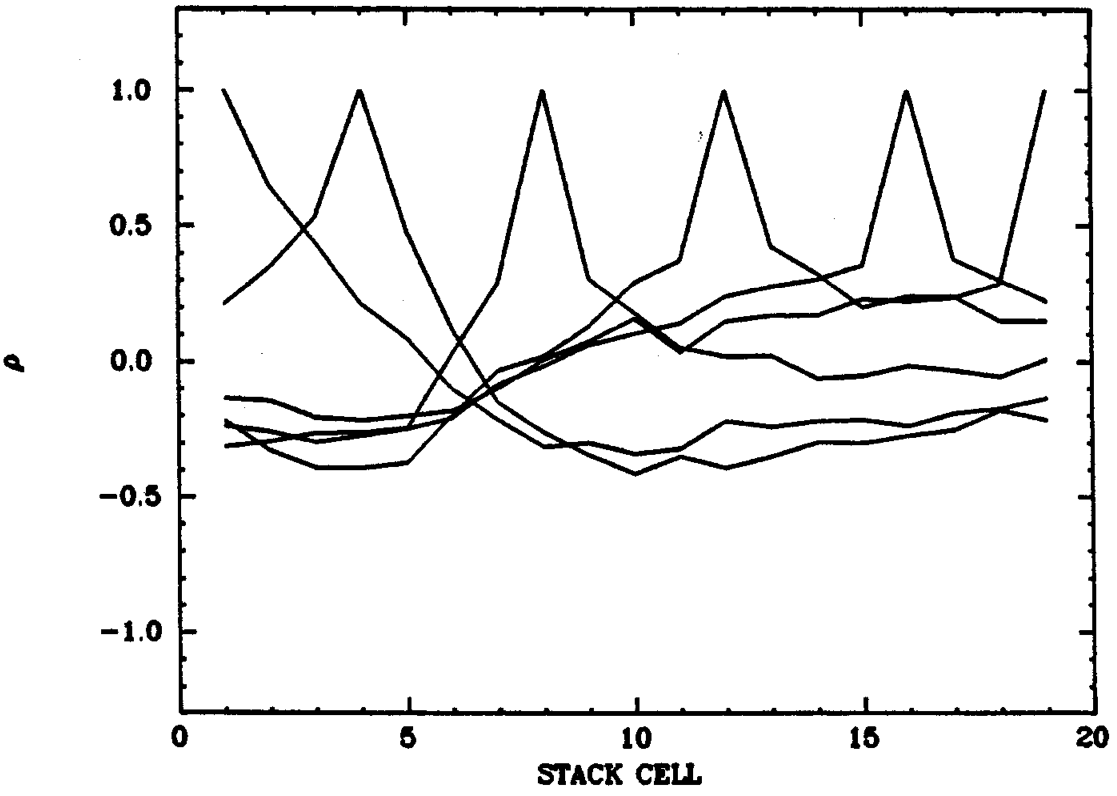

Figure B.28. correlation coefficients for the individual cell deposited energy for 2000 MeV showers.

measurements of it will be affected by the absolute strip width. But a few useful points can be discussed.

One way to get a "feel" for the significance of the transverse width of individual showers without actually defining and measuring individual shower widths, is to compare the distribution of measured shower centroids to the average shower transverse distribution. In Figure B.29 we have plotted the ratio of the rmsd width of these two distributions for showers of several energies. In those cells where in a large fraction of cases only one localized ionization event occurs, the centroid distribution should be nearly the same as the average transverse distribution. As the number of ionization events in the cell grows, the centroid becomes better defined allowing the position resolution to improve. Counting the number of strips in a cell which receive at least a significant fraction of the energy deposited by a minimum ionizing track provides an equivalent measure of this effect as can be seen by comparing Figure B.30 where we have plotted the fraction of events where two or more strips in a cell receive a least 50% of the minimum ionization energy.

The position resolution depends not only on the inherent width of the transverse distribution, but also on the absolute width of the strips and the manner in which the cells are ganged. For very small strips, the position resolution is determined solely by the intrinsic width of the shower (averaged over the ganged cells). The dependence on strip width is weak until the strips become almost as wide as the shower itself. When the shower is contained completely within one wide strip, the centroid measurement is nearly independent of the shower characteristics, but then the center of the strip must be near the

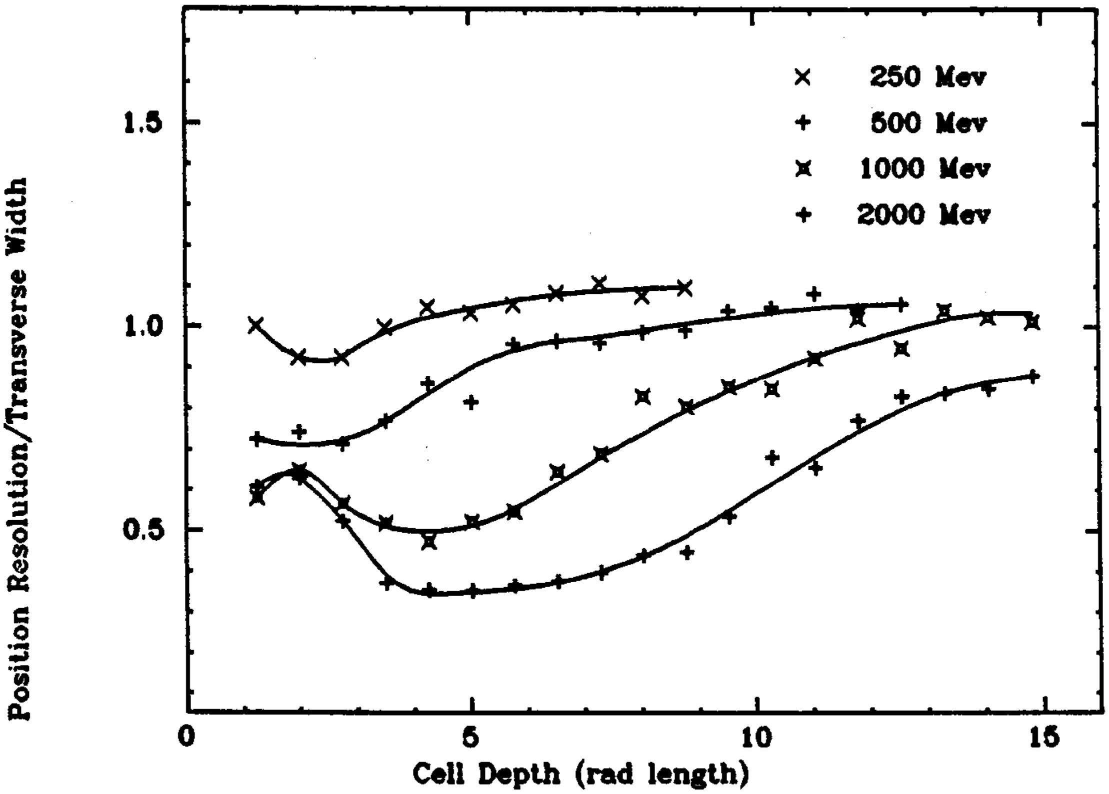

Figure B.29. Ratio of the RMSD width of the measured shower centroid distribution to the RMSD width of the average shower transverse distribution as a function of depth in the stack.

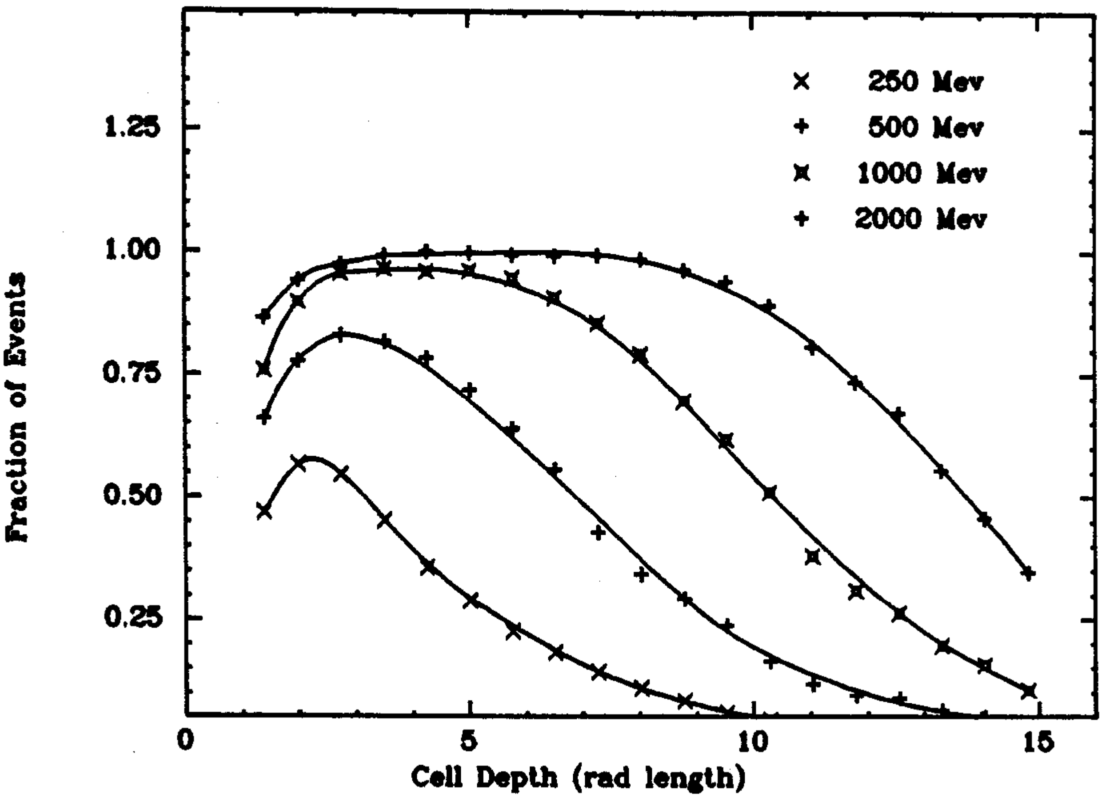

Figure B.30. Fraction of showers where two or more strips in a cell receive at least 50% of the energy deposited by one minimum ionizing particle.

shower centroid, providing the strip is not too wide. When they are very wide, the distribution of the deviation of the shower centroid from the predicted position becomes nearly flat. These points are illustrated in Figure B.31 where we have plotted for 500 Mev showers, the deviation of the shower centroid from the predicted position near shower maximum as measured with strips of 3 different widths. In Figure B.32 is plotted the position resolution measured near shower maximum as a function of strip width for 500 and 2000 Mev showers. The basic module strip width of 3.8 cm negligibly effects the position resolution for 500 Mev showers, but has become the dominant contribution to the resolution at 2 Gev. As the angle of incidence increases, the situation improves.

Measuring the width of the transverse shower distribution could provide another source of information which can be used in particle identifcation schemes. The measured width depends more strongly on the strip width, however, than did the measured shower centroid. In particular, if only one strip is hit (i.e., receives a significant amount of energy) we can only assign an upper limit to the actual shower width. If two strips are hit, again there is little that can be said about the actual shower width. A narrow shower which happens to be at the boundary of two strips will hit them both. The fact that two strips were hit has statistical meaning though in that the fraction of time that this happens will increase with the intrinsic width of the shower. Only when 3 or more strips are hit can we hope to assign a width to the shower which in some sense measures its intrinsic width. A commonly used measure of the width is the rmsd width defined by

$$\sum E_i(X_i-X_0)^2/\sum E_i \qquad (6)$$

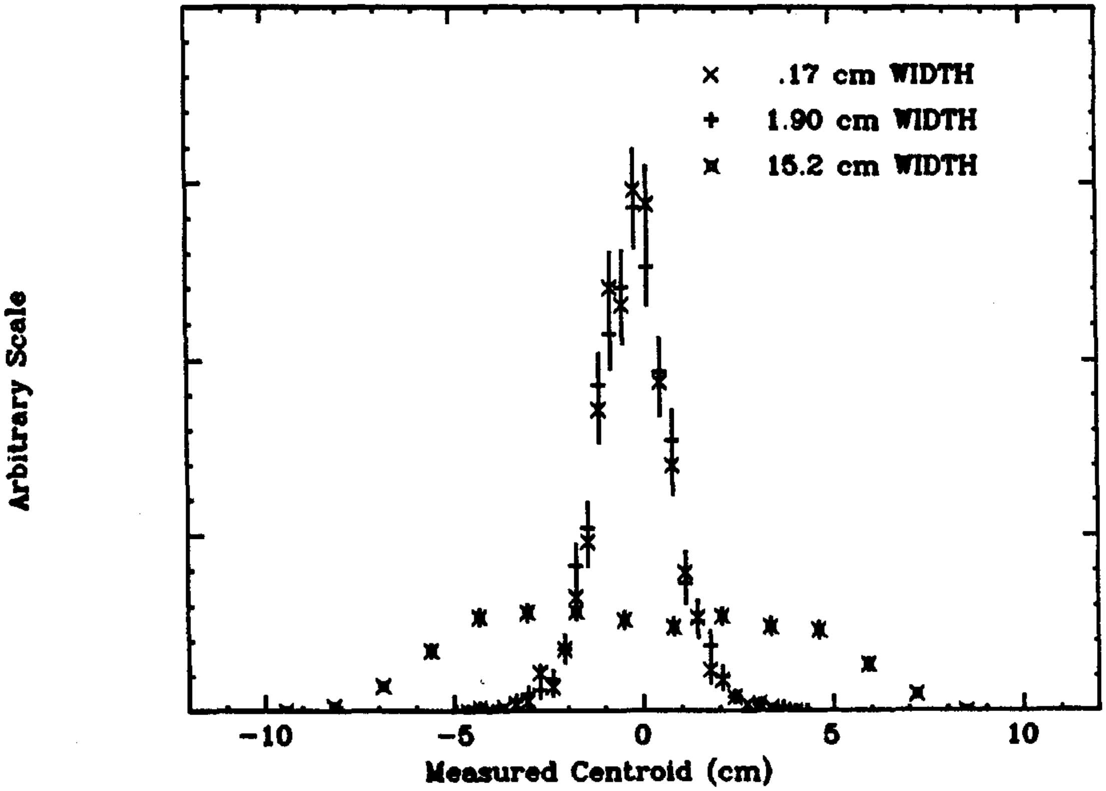

Figure B.31. Distribution of the deviation of the shower centroid from the predicted position measured with strips of three different widths.

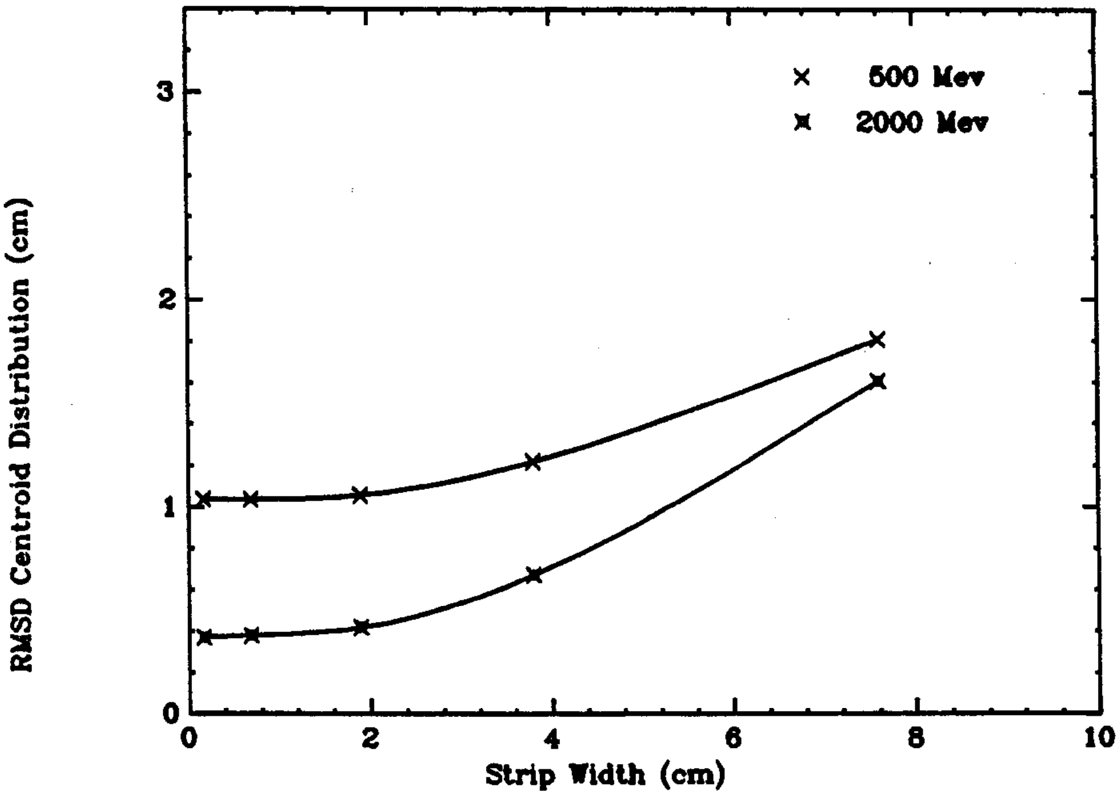

Figure B.32. Position resolution near shower maximum as a function of the strip width.

where X_i represents the center of the i'th strip and X_0 is the shower centroid. If only two adjacent strips are hit, this can be rewritten as $\sigma_w * \sqrt{(f(1-f))}$ where f is the fraction of energy deposited in one strip and σ_w is the strip width. This has a maximum value of $\sigma_w/2$ when each strip receives half the energy. As an illustration, Figure B.33 shows the distribution of rmsd widths near shower maximum as measured with 3.8 cm wide strips. Also shown is the width measured on the same trials with .35 cm strips. The contribution from events where only two adjacent strips are hit is located below the 1.9 cm bin and is clearly visible. When more than 2 adjacent 3.8 cm strips are hit, the widths as measured by both sets are similiar.

Thus we see the quality of the width information depends very strongly on the number of strips which are used to define it. In Figure B.34 is plotted, for 500 and 2000 Mev showers, the fraction of events in layer T1 (ie, near shower max) where more than 1 or more than 2 strips receive an energy larger than 50% of that deposited by a minimum ionizing track as a function of strip width. At either energy with 3.8 cm strips, only a small fraction of events have 3 or more strips hit, while at 500 Mev the fraction where 2 are hit is only 50%. Therefore, we see that only the fraction of events where 2 strips are hit has any meaning as far as the LASC shower counter width information is concerned, and the significance of this information is weakened by electrical noise and the misalignment of the ganged physical layers for non-normally incident showers. Furthermore, for low energy showers the fluctuation in the number of charged particles even near shower maximum is so large that often only a few ionizing tracks are present thus making the transverse shower width a somewhat nebulous concept

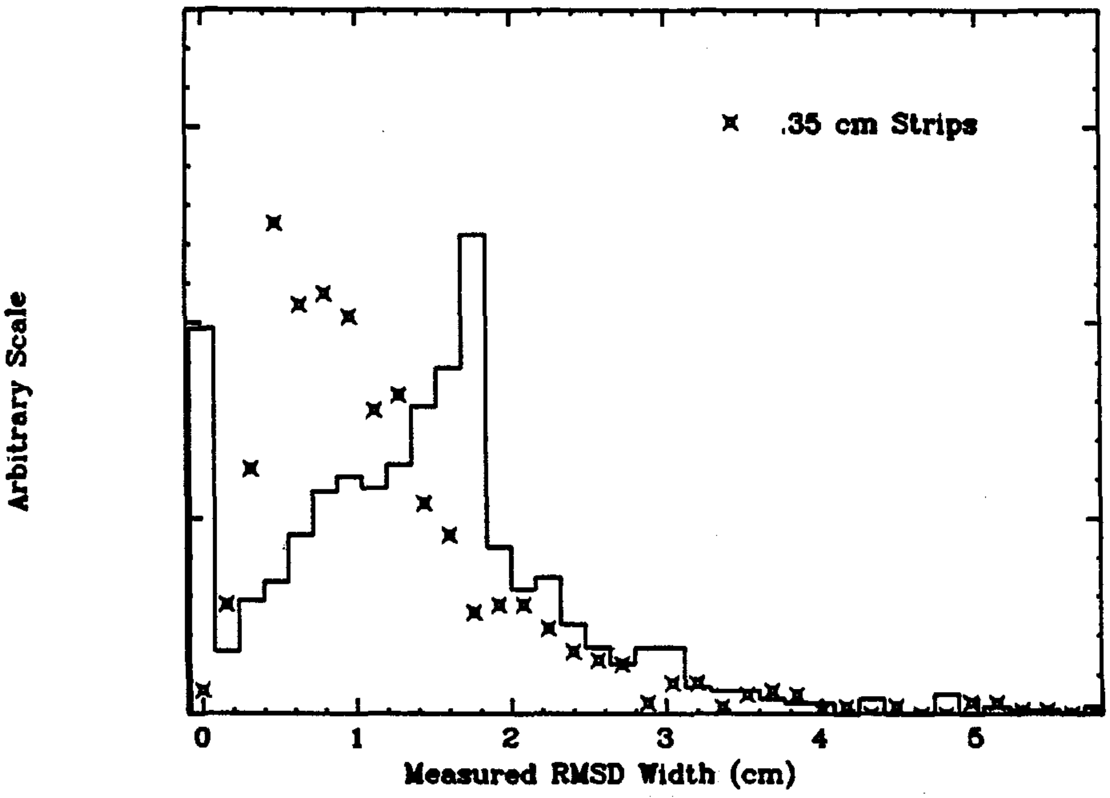

Figure B.33. Distribution of the RMSD width for individual showers measured near shower maximum with 3.8 cm strips. The distribution measured on the same showers with .35 cm wide strips is also shown.

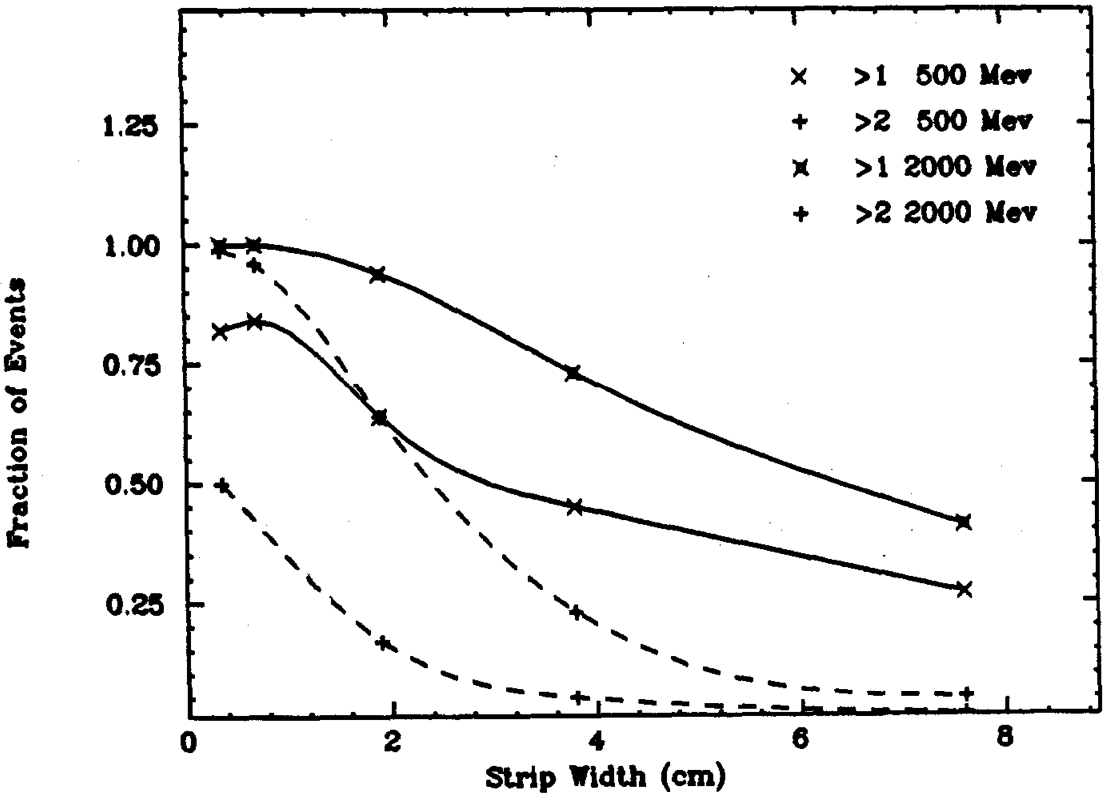

Figure B.34. The fraction of events in layer T1 where more than 1 or more than 2 strips receives an energy larger than 50% of that deposited by a minimum ionizing track as a function of strip width.

independent of the strip width.

References:

1.) H. Messel and D.F. Crawford, Electron-Photon Shower Distribution Function, (Pergamon Press, Oxford, 1970).

2.) T.A. Gabriel and K. Chandler, Part. Acc. 5:161 (1973).

3.) Y.S. Tsai, Rev. of Mod. Phys., 46:815 (1974).

4.) R. Hofstadter et. al., Nature 221:228 (1969).

5.) J.Engler et al., NIM 120:157 (1974);
W.J.Willis and V.Radeka, NIM 120:221 (1974).
See also:
D. Hitlin et al., NIM 137:225 (1976);
C.W. Fabjan et al., NIM 141:61 (1977);
B. Babaev et al., NIM 160:427 (1979);
J.H.Cobb et al., NIM 158:93 (1979).

6.) G.S. Abrams et al., IEEE Trans. Nucl. Sci., NS-25:309, (1978).

7.) W.J. Willis and V. Radeka, NIM 120:221 (1974).

8.) Ibid.

9.) W.P. Jesse and J. Sadaukis, Phys. Rev. 107:766 (1957).

10.) L. Landau, J. Phys. USSR 8:201 (1944).

11.) H. Messel and D.F. Crawford, op. cit.

12.) B. Rossi, High-Energy Particles, (Prentice-Hall, N.J. 1952).

13.) H. Messel and D.F. Crawford, op. cit.

14.) Ibid.

15.) R.L. Ford and W.R. Nelson, SLAC Report #210 (1978).

16.) C. Cerri and F. Sergiampietri, NIM 141:207 (1977).